

OPTICAL AND ELECTRONIC PROPERTIES OF METHYLAMMONIUM LEAD HALIDE PEROVSKITE SOLAR CELLS



By

SEKAI LANA TOMBE

BSc Honours Chemistry, MSc Chemistry (Rhodes University)

A thesis submitted in fulfilment of the requirements for the degree of

PHILOSOPHIAE DOCTOR

UNIVERSITY of the
WESTERN CAPE

In the

Department of Chemistry

Faculty of Science

University of the Western Cape, South Africa

Supervisor: Professor Emmanuel I. Iwuoha

Co-supervisor: Professor Niyazi Serdar Sariciftci

May 2017

ABSTRACT

Organic-inorganic hybrid perovskite solar cells have emerged as promising materials for next-generation photovoltaics with certified efficiency of 22.1%. Despite rapid developments, achieving precise control over the morphologies of the perovskite films, enhanced stability and reproducibility of the devices remains challenging. In this work, we employed a low-temperature solution processing technique to attain high efficiency inverted planar heterojunction devices with device architecture ITO/PEDOT:PSS/Perovskite/PCBM/Al (indium doped tin oxide; poly(3,4-ethylenedioxythiophene) polystyrene sulfonate; [6,6]-phenyl-C₆₁-butyric acid methyl ester; aluminium). A perovskite solar cell fabrication technique is developed and opto-electronic characterization of solution-processed planar heterojunction perovskite solar cells based on methylammonium (MA) lead halide derivatives, MAPbI_{3-x}Y_x (Y = Cl, Br, I) is presented in this thesis work. By employing lead iodide (PbI₂) with various amounts of additional methylammonium halides, perovskite precursor solutions were obtained, which were used in the fabrication of four perovskite systems, MAPbI₃, MAPbI_{3-x}Cl_x and MAPbI_{3-x}Br_x and MAPbBr₃. The absorption and photoluminescence (steady state and temperature-dependent) behavior were explored in this compositional space. In addition, the physical parameters of the mixed halide perovskites such as the exciton binding energy, exciton-phonon interaction and bandgap were determined via temperature-dependent photoluminescence spectroscopy. The effects of the halide ratio in the perovskite formulations processed via a one-step deposition technique, of perovskite processing parameters on film formation, morphology and composition are examined and correlated with perovskite optoelectronic properties and photovoltaic performance. The photovoltaic performance of the devices was found to be greatly dependent on the film morphology, which in turn is dependent on the deposition techniques and subsequent treatments employed. With optimized solution-based film formation, power conversion efficiencies of 9.2, 12.5, 5.4 and 3.2% were obtained for MAPbI₃, MAPbI_{3-x}Cl_x, MAPbI_{3-x}Br_x and MAPbBr₃ devices. The photocurrent-density-voltage (J-V) curves of the perovskite solar cells demonstrate anomalous dependence on the voltage scan and direction. The problem of perovskite solar cell stability is also addressed. MAPbI_{3-x}Cl_x perovskite solar cells exhibited the most promising stability by maintaining ~ 50% of their initial performance over long periods of time in a nitrogen-filled glove box without encapsulation. Through the judicious selection of hole- and electron-transport layers, we achieved a general approach for low-cost solution processing of MAPbI_{3-x}Y_x (Y = Cl, Br, I) in a way to maximize performance and stability.

KEYWORDS

Perovskite

Photovoltaics

Methylammonium lead halide

Photoluminescence

Exciton binding energy

Hysteresis

Power conversion efficiency

Electron transport material

Hole transport material

Microscopy

Morphology

Temperature-dependent photoluminescence spectroscopy



UNIVERSITY *of the*
WESTERN CAPE

ABBREVIATIONS

AM – Air Mass

CaTiO₃ – Calcium Tin Oxide

CdTe – Cadmium Telluride

CIGS - Copper Indium Cadmium Telluride

DSSCs – Dye-Sensitized Solar Cells

EQE – External Quantum Efficiency

ETM – Electron Transport Material

FF – Fill Factor

FTO – Fluorine Tin Oxide

HI – Hydroiodic acid

HOMO – Highest Occupied Molecular Orbital

HTM – Hole Transport Material

IPCE – Incident Photon-to-Current Efficiency

ITO – Indium Tin Oxide

J_{sc} – Short-circuit current density (current per unit area i.e., mA/cm²)

J-V – Current-Voltage

LED – Light Emitting Diode

LiTFSI – Lithium *bis*(trifluoromethane-sulfonyl)imide

LUMO – Lowest Unoccupied Molecular Orbital

MPP – Maximum Power Point

OPV – Organic Photovoltaic

P3HT – Poly(3-hexylthiophene)

PCBM – [6,6]-phenyl-C₆₁-butyric acid methyl ester



PCE – Power Conversion Efficiency

PDI - *N,N*-dialkyl perylenediimide

PL – Photoluminescence

PSC – Perovskite Solar Cell

PTAA – Poly(triarylamine)

PTCDI – *N,N'*-dimethyl-3,4,9,10-perylenetetracarboxylic diimide

PV – Photovoltaic cell (solar cell)

R_s – Series Resistance

R_{sh} – Shunt Resistance

SEM - Scanning Electron Microscopy

Spiro-OMeTAD – 2, 2'-7,7'-tetrakis (*N,N*-di-*p*-methoxyphenylamine)-9,9'-spirofluorene

tBP – 4-*tert*-butyl pyridine

TiO₂ – Titanium dioxide, titania

TPD - *N,N*-bis(3-methyl-phenyl)- *N,N*-diphenylbenzidine

TTF – Tetrathiafulvalene

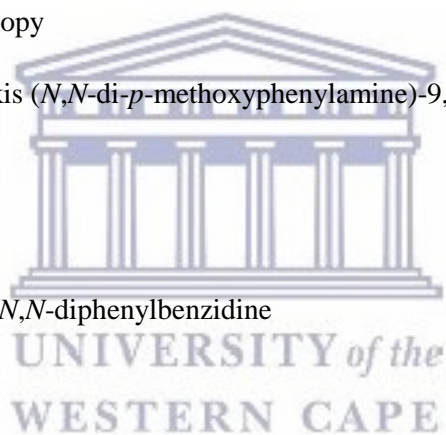
UV-Vis – Ultraviolet-Visible

VASP - Vapor-Assisted Solution Process

V_{oc} – Open-circuit Voltage


XRD- X-ray Diffraction spectroscopy

ZnO – Zinc oxide



DECLARATION

I declare that **Optical and electronic properties of methylammonium lead halide perovskite solar cells** is my own work, that it has not been submitted before for any degree or examination in any other university, and that all the sources I have used or quoted have been indicated and acknowledged as complete references.

Signature 

Sekai Lana Tombe

May 2017



UNIVERSITY *of the*
WESTERN CAPE

DEDICATION

To my late grandparents

Taaziva and Nayisai Tombe

and

Isaac and Shorai Mukaro



**UNIVERSITY *of the*
WESTERN CAPE**

ACKNOWLEDGEMENTS

Lord, You establish peace for us; all that we have accomplished You have done for us (Isaiah 26:12)

This thesis would not have been possible without the guidance and support of several individuals who in one way or another contributed their invaluable assistance in the preparation and completion of this work.

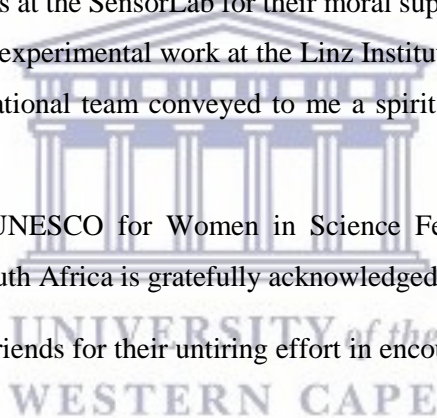
First and foremost, it is with immense gratitude that I acknowledge my supervisor, Professor Emmanuel Iwuoha and co-supervisor Professor Niyazi Serdar Sariciftci for giving me the opportunity to study for a doctorate degree. Their invaluable advice, helpful discussions and guidance are very much appreciated.

It gives me great pleasure to acknowledge Dr Markus Scharber, Dr Getachew Adam, Professor Christopher Arendse, Mr Patrick Denk and Dr Christoph Ulbricht for their invaluable insights on many theoretical and experimental aspects of this thesis.

I would like to thank my colleagues at the SensorLab for their moral support. I consider it a great privilege and honour to have conducted my experimental work at the Linz Institute for Organic Solar Cells (LIOS). Working in such a diverse international team conveyed to me a spirit of adventure regarding scientific research.

Financial support from L'Oréal-UNESCO for Women in Science Fellowship 2013 and the National Research Foundation (NRF) of South Africa is gratefully acknowledged.

Finally, my parents, siblings and friends for their untiring effort in encouraging me to pursue my career in scientific research.



LIST OF PUBLICATIONS

1. **S. Tombe**, G. Adam, H. Heilbrunner, D. H. Apaydin, C. Ulbricht, N. S. Sariciftci, E. Iwuoha, and M. C. Scharber, Wide bandgap solution processed mixed-halide methylammonium lead iodide-bromide perovskite solar cells, 2017, (in preparation)
2. **S. Tombe**, G. Adam, H. Heilbrunner, D. H. Apaydin, C. Ulbricht, N. S. Sariciftci, C. J. Arendse, E. Iwuoha, and M. C. Scharber, Optical and electronic properties of mixed halide (X = I, Cl, Br) methylammonium lead perovskite solar cell, *J. Mater. Chem. C.*, 2017, 5, 1714-1723
3. G. Adam, M. Kaltenbrunner, E. D. Głowacki, D. H. Hazar, M. S. White, H. Heilbrunner, **S. Tombe**, P. Stadler, B. Ernecker, C. W. Klampfl, N. S. Sariciftci and M. C. Scharber, Solution processed perovskite solar cells using highly conductive PEDOT:PSS interfacial layer, *Sol. Energy Mater. Sol. Cells*, 2016, 157, 318-325



UNIVERSITY of the
WESTERN CAPE

TABLE OF CONTENTS

CHAPTER 1-GENERAL INTRODUCTION

1.1 Global energy demand	1
1.2 Photovoltaic effect	3
1.3 Photovoltaic technologies	6
1.4 Summary of aims of thesis	11
1.5 Summary of thesis chapters	11

CHAPTER 2- HALOGENATED-PEROVSKITES FOR SOLAR CELLS

2.1 Introduction	14
2.2 Solid-state perovskite solar cells	17
2.3 Perovskite processing parameters	19
2.3.1 Perovskite precursor composition	19
2.3.2 Deposition methods	19
2.4 Perovskite device architectures	23
2.4.1 Mesoporous architecture	24
2.4.2 Planar architecture	25
2.5 Hysteresis	25
2.6 Stability	29
Conclusion	32

CHAPTER 3- OPTICAL AND ELECTRONIC PROPERTIES OF MIXED HALIDE (X = I, Cl, Br) METHYLAMMONIUM LEAD PEROVSKITE SOLAR CELLS.

3.1 Introduction	41
3.2 Experimental	43
3.2.1 Materials	43

3.2.2 Perovskite precursor solutions	44
3.2.3 Device Fabrication	44
3.2.4 Perovskite film and device characterization	46
3.3 Results and discussion	47
3.3.1 Thin perovskite film morphology	47
3.3.2 Temperature-dependent photoluminescence spectroscopy	51
3.3.3 Photovoltaic characterization	57
Conclusion	71

CHAPTER 4- THE INFLUENCE OF PEROVSKITE PRECURSOR COMPOSITION ON THE STRUCTURAL PROPERTIES AND PHOTOVOLTAIC ACTIVITY OF MIXED HALIDE MAPBI_{3-x}CL_x SOLAR CELLS

4.1 Introduction	75
4.2 Experimental	77
4.3 Results and discussion	78
4.3.1 Effect of perovskite annealing time on MAPbI ₃ solar cells	78
4.3.2 Effect of perovskite precursor composition	81
4.3.3 MAPbI _{3-x} Cl _x perovskite layer morphology	87
4.3.4 Effect of charge transport material on device performance	89
4.3.5 Perovskite solar cell stability	96
Conclusion	

CHAPTER 5- WIDE-BANDGAP SOLUTION PROCESSED MIXED-HALIDE METHYLAMMONIUM LEAD IODIDE-BROMIDE PEROVSKITE SOLAR CELLS

5.1 Introduction	102
5.2 Experimental	104
5.3 Results and discussion	105
5.3.1 Device structure	105

5.3.2 Perovskite film morphology	106
5.3.3 Absorbance and photoluminescence spectroscopy	107
5.3.4 Photoluminescence quenching	108
5.3.5 Temperature-dependent photoluminescence spectroscopy	109
5.3.6 Device characterization	113
5.3.7 Electroluminescence spectroscopy	116
5.3.8 Statistical data analysis	117
Conclusion	
CHAPTER 6- CONCLUSIONS	122



CHAPTER 1

INTRODUCTION

1. Introduction

Global energy demand and dependence on electricity is increasing, as environmental concerns become more pressing. In this chapter, different energy sources are introduced and renewable energy sources are discussed as feasible future alternatives to fossil fuels. Photovoltaics as a renewable energy technology is briefly presented.

1.1 Global energy demand

With worldwide economic development and population growth, global energy demands have increased dramatically. To address the issues of the energy trilemma namely, energy security, equality and environmental sustainability, we need to develop low-emission, cost-effective and efficient energy technologies. There are nine major areas of energy resources and these are divided into non-renewable and renewable energy sources [1,2]. **Figure 1.1** shows the world energy sources with non-renewable resources, fossil fuels accounting for almost 80%.

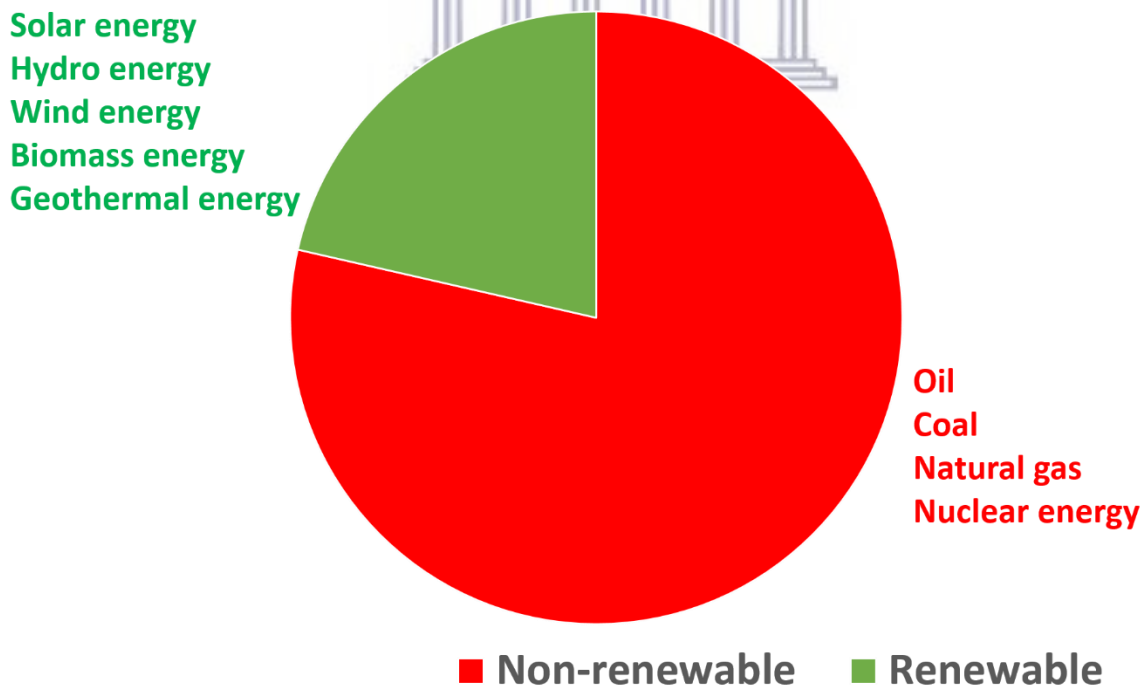


Figure 1.1: World energy sources categorized as non-renewable (petroleum, coal and natural gas) and renewable energy (wind, hydro, biomass, solar etc.) sources [1].

1.1.1 Non-renewable energy resources

Non-renewable energy resources, based on fossil fuels (e.g. oil, coal, natural gas, etc.) are available in limited supplies. Currently the main source of our energy supply is delivered through not only fossil fuels, such as oil, gas, and coal but also nuclear power using ^{235}U [3,4]. Violent conflicts over energy have erupted over the years for example, in Nigeria, South China Sea, Iraq/Syria and Ukraine/Russia. The growing concerns over the finite supply of non-renewable energy sources reflected by the rising prices of oil and gas, the geopolitical climate surrounding fossil fuel production coupled with the environmental consequences such as greenhouse gas emissions and the nuclear catastrophe in Fukushima underscores the urgency of searching for alternative renewable and sustainable energy sources.

1.1.2 Renewable energy resources

Renewable energy resources are naturally replenished on a human timescale and are environmentally and economically clean alternative energy resources. Several technologies are available for the production of clean, efficient and reliable energy from long term renewable energy sources such as wind, sun, water, biomass and biogas, hydrogen and geothermal energy. Among these sources, solar photovoltaic (PV) energy stands out as the only one with sufficient theoretical capacity to meet global electricity needs [3,4]. The sun is champion among all non-renewable and renewable energy sources as it provides the earth with 174 000 TW; solar energy that hits the planet in one hour is more than the total energy consumed by all human activities in an entire year. Renewable energy sources will be successful only if they are delivered at a competitive price compared to conventional energy sources based on fossil fuels.

1.1.2.1 Solar energy

Solar energy in one form or another is the source of nearly all energy on the Earth [4]. Additionally, most renewable energy comes either directly or indirectly from the sun. Hydropower depends on the evaporation of water as a result of solar heating that leads to rain fall and create rivers, biomass converts the sun's energy into a fuel and wind energy uses air currents that are created by solar heated air. Solar energy is harnessed using a range of solar technologies such as solar heating, solar thermal energy, solar architecture, artificial synthesis and photovoltaics. The most commonly used solar technologies are solar water heating, passive solar design for space heating and cooling, and solar photovoltaics for electricity. Another route to harnessing solar energy to produce electricity is using concentrated solar power (CSP) which is beyond the scope of this thesis. Although the sun supplies the Earth with enough energy in one hour to meet global electricity needs for one hour, solar-generated electricity today supplies only around 0.1% of worldwide demand.

1.2 Photovoltaic effect

The physical phenomenon responsible for converting light to electricity, the photovoltaic effect, was first observed in 1839 by Edmund Becquerel. A photovoltaic device/solar cell is based on the photoelectric effect, requiring photogeneration of charge carriers (electron and holes) in a light absorbing material and their separation to conductive contacts that transmit electricity. Solar light energy reaching on Earth is 1 kW/m^2 (100 mW/cm^2) with spectra covering from 280-300 nm to infrared area, which is called 1 sun. The standard spectra of the light are called air mass 1.5 (AM 1.5). Therefore, the standardized light is called AM 1.5 with 1 sun energy density.

1.2.1 Photovoltaic device/solar cell operation

Solar cells are composed of a semiconductor layer and two selective contacts as a basic configuration. Solar cells can be made of only one single layer of light-absorbing material (single-junction) or use multiple physical configurations (multi-junction) to take advantage of various absorption and charge separation mechanisms. The working principle of solar cells is based on the photovoltaic effect, *i.e.* the generation of a potential difference at the junction of two different materials in response to electromagnetic radiation. The photovoltaic effect can be divided into three basic processes:

1. Generation of charge carriers due to the absorption of photons in the materials that form a junction
2. Subsequent separation of the photo-generated charge carriers in the junction
3. Collection of the photo-generated charge carriers at the terminals of the junction

1.2.2 Solar cell parameters/characteristics

Opto-electronic devices like photovoltaic cells are usually characterized by their electrical, optical and thermodynamic parameters.

1.2.2.1 The current density-voltage characteristics

Under illumination, a solar cell generates an electrical voltage and/or electrical current. The external parameters of a solar cell can be extracted by illuminating the solar cell under standard test conditions (100 mW/cm^2 , AM 1.5G) and determining the J - V characteristics, where J is the current density and V is the voltage. A typical example of illuminated and dark J - V curves is shown in **Figure 1.2**. The difference between the dark and the illuminated J - V is the photocurrent. The dark current stems from the random generation of electron-hole pairs within the absorber layer [5].

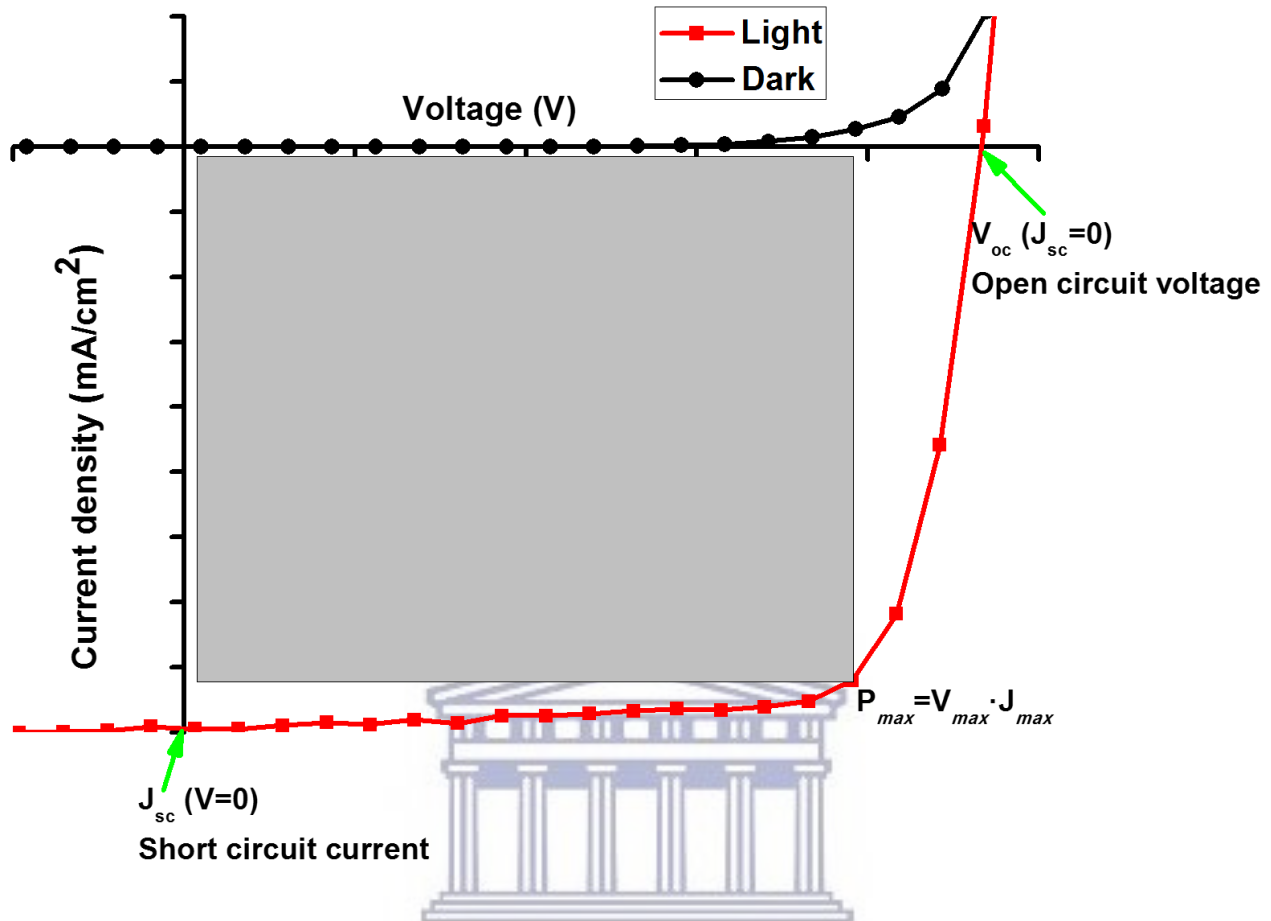


Figure 1.2: Typical solar cell current-voltage (J - V) characteristics showing the open circuit voltage (V_{oc}), short circuit current (J_{sc}) and maximum power point (P_{max}). The PV device in the dark acts as a diode, passing current easily in only one direction.

The J - V curve of a solar cell is the superposition of the J - V curve of the solar cell diode in the dark with the light generated current [6]. There are three important points on the current-voltage curve: the short-circuit current J_{sc} , open-circuit voltage V_{oc} , and the electrical fill factor, FF. The short-circuit current, J_{sc} , is the current through the solar cell when the voltage across the cell is zero. The J_{sc} is due to the generation and collection of light-generated carriers. The open-circuit voltage, V_{oc} , is the maximum voltage available from a solar cell and this occurs at zero current. The fill factor, FF, is the ratio of the device's maximum obtainable power to the product of the V_{oc} and J_{sc} . The fill factor is a key parameter in evaluating performance. Graphically, the fill factor is a measure of the 'squareness' of the solar cell. The FF is illustrated in **Figure 1.2**.

The fill factor of the solar cell is given by the ratio:

$$FF = \frac{J_{MP} \cdot V_{MP}}{J_{sc} \cdot V_{oc}} \quad (1.1)$$

where V_{oc} is the open circuit voltage, J_{sc} is the short circuit current density, J_{MP} and V_{MP} are the current and voltage at maximum power respectively. The fill factor should be as high as possible for commercial solar cells it should be higher than 0.7.

The solar power conversion efficiency (PCE) is given by:

$$\eta = \frac{FF \cdot V_{oc} \cdot J_{sc}}{P_{in}} \quad (1.2)$$

where V_{oc} is the open circuit voltage, FF is the fill factor, J_{sc} is the short circuit current density, and P_{in} is the incident optical power on the device assuming an AM1.5G solar spectrum. Because the J_{sc} is maximized by increasing the external quantum efficiency (EQE) across the absorbance spectrum of the active layer, the PCE takes into account not only the quantum efficiency at zero bias, but also the energetic efficiency of converting a spectrum of photon energies to photocurrent at all potentials. In this article, we will discuss how morphology and fabrication of hybrid organic/inorganic devices affect the photovoltaic parameters and ultimately PCE.

1.2.2.2 External Quantum Efficiency

The external quantum efficiency EQE (λ_0) is the fraction of photons incident on the solar cell that creates electron-hole pairs in the absorber, which are successfully collected. It is wavelength dependent and is usually measured by illuminating the solar cell with monochromatic light of wavelength λ_0 and measuring the photocurrent I_{ph} through the solar cell.

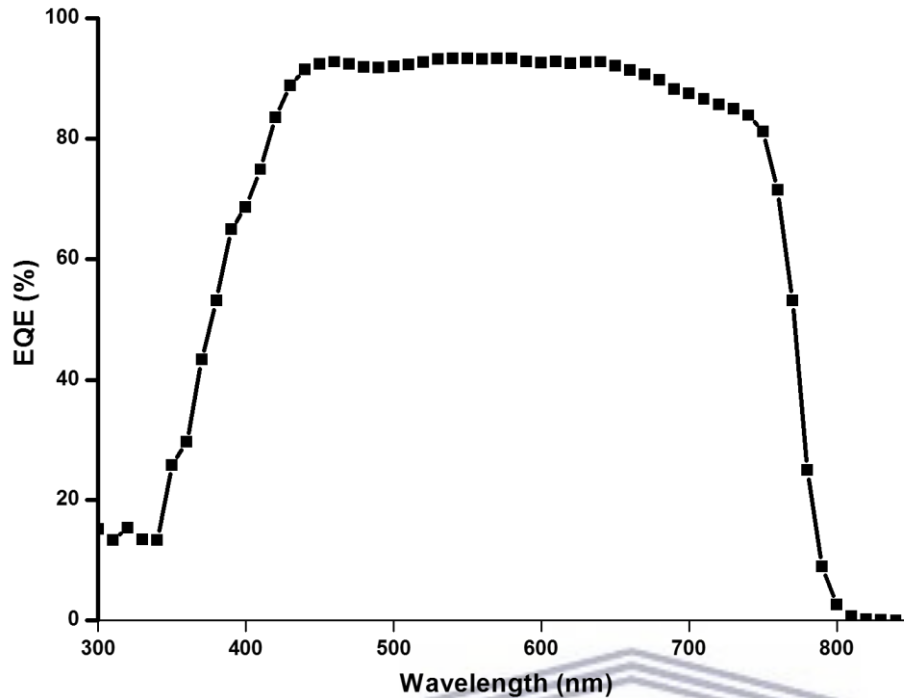


Figure 1.3: External quantum yield (EQE) spectrum of a typical perovskite solar cell.

The external quantum efficiency is then determined as

$$\text{EQE}(\lambda_0) = \frac{I_{ph}(\lambda_0)}{e\Phi_{ph}(\lambda_0)} \quad (1.3)$$

where e is the elementary charge and Φ_{ph} is the photon flux incident on the solar cell. Since I_{ph} is dependent on the bias voltage, the bias voltage must be fixed. The photon flux is usually determined by measuring the EQE of a calibrated photodiode under the same light source.

1.2.2.3 Theoretical limits for solar cell performance

The Shockley-Queisser (SQ) limit describes the maximum solar energy conversion efficiency achievable for a particular material and is the standard by which new photovoltaic technologies are compared. The SQ limit is reached by applying the principle of detailed balance to the particle (photons or electrons) flux into and out of the semiconductor [7]. The maximum possible efficiency is achieved when non-radiative recombination is absent, and all generated carriers are either collected as current in the leads or recombine, emitting a single photon per electron-hole pair. Because an actual cell cannot collect all the light since it has specific band gap that restricts light absorption, the projected efficiency limit is not physically

obtainable and there are currently no photovoltaic materials that meet all the Shockley- Quiesser limit requirements.

1.3 Photovoltaic technologies

Many different photovoltaic technologies are being developed for large-scale solar energy conversion, **Figure 1.4 [8-10]**. Solar cells are typically named after the semiconducting material they are made of and can be classified into first, second and third generation cells.

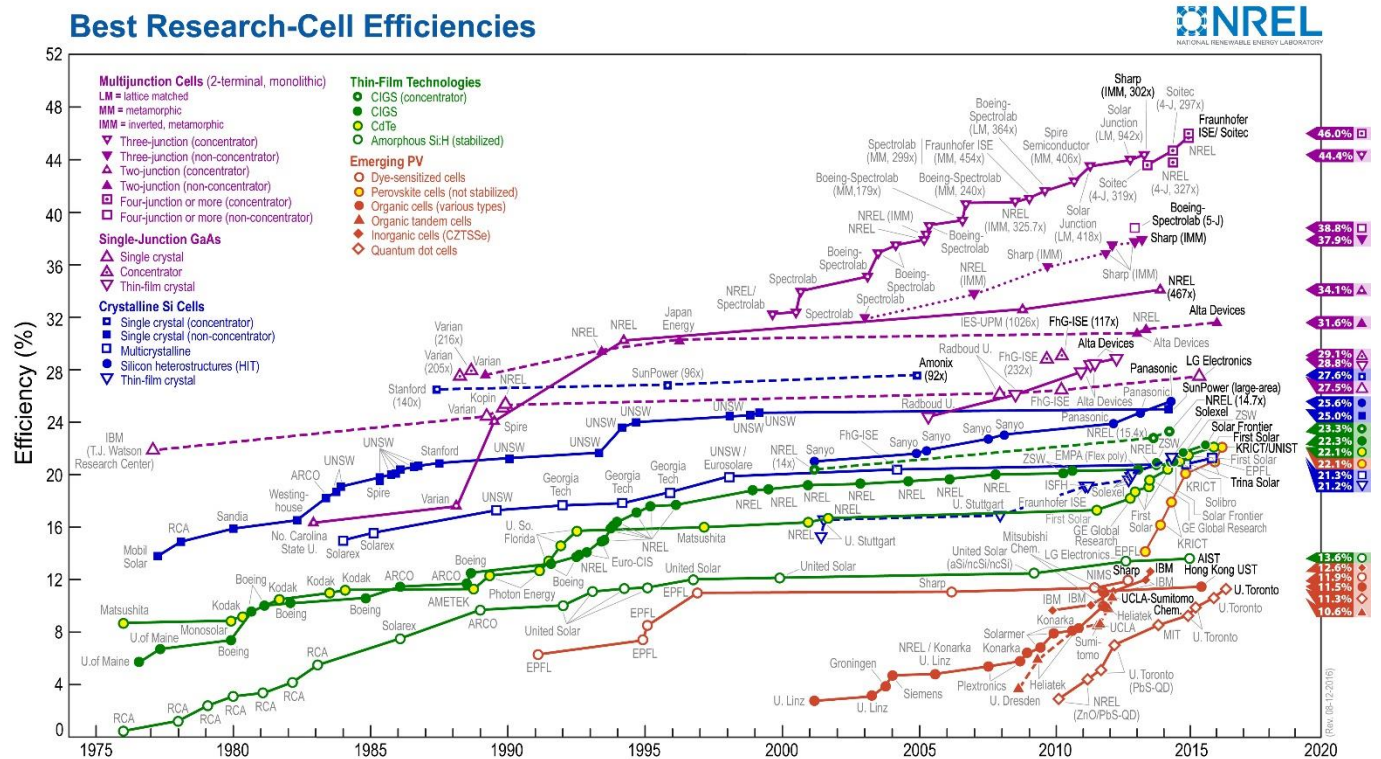


Figure 1.4: A summary of certified efficiencies for various classes of semiconductor materials used in solar cells [8].

1.3.1 First-generation solar cells

The first-generation solar cells are mainly based on silicon wafers and include polysilicon and monocrystalline silicon. Crystalline Si, multi-crystalline Si (mc-Si) and polycrystalline Si (p-Si) are the group of traditional silicon solar cells. Crystalline silicon solar cells have been continuously advancing in efficiency and reducing in cost of fabrication over the last 40 years [9,11] and in some locations in the world at the current prices, they are capable of producing electricity from sunlight at a comparable cost to the

price of electricity generated from fossil fuels [13]. A very high purity (e.g. $\geq 99.9999\%$) is often required for solar-grade silicon as the charge generation and transport in silicon is very sensitive to defects [14]. In addition, due to a large energy difference between the direct gap (~ 3.4 eV) and indirect gap (~ 1.1 eV) of silicon [15], the active layer of silicon solar cells must be thick enough (e.g. typically $300\ \mu\text{m}$) to efficiently absorb incident sunlight. This makes silicon solar cells expensive. Silicon is energetically and economically expensive to produce in bulk and it is also mechanically fragile requiring sheet of strong glass to be used as mechanical support resulting in significant increases in manufacturing costs. There are many other newer solar cell technologies that promise even lower cost solar power, and these range from thin-film vapor deposited semiconductor-based solar cells, for example, CdTe or CIGS [16,17] to solution processed solar cells based on organic semiconductors, hybrid composites, or inorganic semiconductors [10,18-22] often referred to as second- and third-generation photovoltaics respectively.

1.3.2 Second-generation solar cells

All different types of thin-film solar cells form the second generation [23]. Second-generation solar cells are usually called thin-film solar cells because when compared to crystalline silicon based cells they are made from layers of semiconductor materials only nanometers or a few micrometers thick. Second generation solar cells, including amorphous (or nano-, micro-, poly-) silicon, CuInGaSe₂ (CIGS) and CdTe are based on thin film technologies [24]. These thin film solar cells possess some advantages, such as relatively simple manufacturing process, multiple choices of applied materials and the possibility of flexible substrates. However, second generation solar cells face several shortcomings as well such as toxicity (e.g. Cd), and low abundance (e.g. In and Se) of the component materials. Because they are extremely thin, light and flexible, second generation solar cells can be laminated onto windows, skylights, roof tiles and on metal, glass and polymer (plastic) substrates. However what second generation cells gain in flexibility, they lack in efficiency as first-generation solar cells traditional first generation solar cells still outperform them [8].

1.3.3 Third-generation solar cells

The third generation of solar cells includes several thin-film technologies often described as emerging photovoltaics. This photovoltaic technology combines the best features of first and second generation solar cells [25,26]. Like first generation cells, they promise high efficiency and like second generation cells they can be made from a variety of new materials besides 'simple' silicon and can feature multiple junctions (made from multiple layers of different semiconducting materials). And unlike silicon cells, the emerging ones can be fabricated on flexible supports via inexpensive solution-phase techniques common in plastic manufacturing such as roll-to-roll printing.

This new generation of solar cells are being made from assortment of new inexpensive materials, including gallium arsenide [27,28], copper zinc tin sulphide (CZTS) [29,30], silicon wires [31], solar inks using conventional printing press technologies [32], quantum dot solar cells [33-35], organic solar cells [36-39], concentrated solar cells [40,41] and perovskite solar cells [42-44]. Compared with traditional silicon solar cells, emerging photovoltaic technologies promise to be less expensive, thinner, more flexible and amenable to a wide range of lighting conditions, all of which make them suitable for a host of applications beyond rooftop and solar-farm panels-silicon's bailiwick.

1.3.3.1 Organic photovoltaics

Organic photovoltaic devices rely on a mixture of light-sensitive polymers or small molecules and fullerene-like compounds to absorb light and set their electricity-generating events in motion [36-39]. The compounds are typically blended in a nanoscale network known as a bulk heterojunction to mediate efficient charge separation by providing a large area of contact between the organic molecule (an electron donor) and the fullerene (an electron acceptor). Whilst multiple small area devices, fabricated in ideal laboratory settings, have achieved PCEs above 10% [8,36], the demonstrations of large-scale polymer solar modules suffer from low efficiency.

1.3.3.2 Quantum dot solar cells

In quantum dot solar cells, nanocrystals of semiconducting metal chalcogenides- including CdS, CdSe, PbS and PdSe- and other materials function as the light-absorbing material in the device [33-35]. QD nanoparticles having high absorption hold the promise of significantly reducing absorber material. As with other emerging photovoltaic technologies, quantum dot cells can be prepared via low-cost solution-phase chemistry methods and are amenable to high-speed printing techniques. However, quantum dots have size-dependent spectral response and having the right QD sizes, concentration and combination to cover incident spectrum is challenging.

1.3.3.3 Dye-sensitized solar cells

The most developed third generation of solar cells are dye-sensitized solar cells (DSSCs). Dye-sensitized solar cells are hybrid solar cells containing a mesostructured inorganic n-type oxide such as TiO₂ sensitized with an organic or metal complex dye, and infiltrated with an organic or metal complex dye, and infiltrated with an organic p-type hole-conductor [19]. Photons captured by the dye-generally a ruthenium complex-generate pairs of negatively charged electrons and positively charged electron vacancies called holes. The charges separate at the surface of the nanoparticles. Electrons are injected into and transported through the

TiO₂ layer to one electrode and positive charges migrate via the electrolyte to the opposite side of the cell. Although the stability of DSSCs has been extensively evaluated in the laboratory, the long-term durability of semi-commercial DSSC products is still unsatisfactory due mostly to the degradation of organic dyes and the leakage of liquid electrolytes after prolonged illumination [45-47]. Historically, the lower price tag on emerging photovoltaics has gone together with significantly lower performance. In terms of power conversion efficiency, DSSCs, OPVs and quantum dots started at a few percent and have climbed slowly over the years to roughly 12%, where they sit today, **Figure 1.4 [8]**. The value for silicon cells is much higher, in the range of 20-25%.

1.3.3.4 Perovskites

Although the efficiencies of most other emerging photovoltaic technologies sit well below silicon, a new type of material, organic-inorganic metal halide perovskite semiconductors, may soon become a strong competitor of silicon solar cells such that truly low-cost photovoltaic modules may become a reality. Unlike other emerging technologies which debuted at very low efficiencies and crept up slowly over several years to the 10% range, perovskite solar cell efficiencies soared in just a couple of years to more than 22% with the prospect of further improvements towards Shockley-Queisser limit for a single-junction solar cell (~33.5%) [8].

Methylammonium lead trihalide (MAPbX₃) perovskites were initially used to replace the dye molecules in the conventional configuration of dye-sensitized solar cells (DSSCs) based on liquid electrolyte [42,43]. Although first implemented in dye-sensitized solar cells based on mesoporous structures, perovskites have been gradually found to assume all the principal roles of PV operation [48-50].

Perovskite precursor compounds are abundant and inexpensive and their conversion into thin films can be achieved using roll-to-roll compatible methods using both solution [51-53] and vacuum-based techniques [52,54]. Therefore, in principle perovskite photovoltaics can generate electricity at very low cost. The combination of their low cost, low weight, flexibility, thinness and ability to transmit light means the perovskite solar cells could be used for applications outside of silicon's reach. Another advantage of perovskite materials is that it has a direct band gap, which means it can be used to absorb and emit light efficiently. Silicon has an indirect band gap and is so relatively poor at emitting light. Perovskite materials can also be applied to any kind of junction structure. Both the first- and second-generation solar cells are based on single junction devices which must obey the Shockley-Queisser limit with a maximum thermodynamic efficiency of 31-33% when the optimum band gaps fall between about 1.1 and 1.4 eV [55]. Tandems of perovskites on top of silicon (Si) or copper indium gallium diselenide (CIGS) cells are considered a pathway to achieving industry goals of improving efficiency while lowering cost [56,57].

Despite the remarkable progress in record cell efficiency, perovskite optoelectronic materials suffer from several drawbacks that need to be overcome before the technology becomes industrially relevant and hence achieve long-term application. Chief among these are the high cost of the employed charge selective contacts, the formation of pinhole-free films of the highly crystalline semiconductor over large areas and unreliable device performance dictated by the operation history of the device, that is, hysteresis. In addition to this, the stability of perovskite based devices remains an open question and perhaps will determine the fate of this remarkable technology in the longer run.

1.4 Summary of aims of thesis

The general objective of this work is to investigate the material/physical/chemical properties of methylammonium lead halide perovskite materials by fabricating high efficiency planar heterojunction perovskite solar cells using a low-temperature solution processing technique for low-cost production and energy payback time.

The specific objectives of this thesis are:

1. Synthesis of organic/inorganic halide materials: organic halide salts (methylammonium (MA) iodide (MAI) and methylammonium bromide (MABr) organic/inorganic methylammonium lead trihalide MAPbX_3 ($X = \text{I}, \text{Cl}, \text{Br}$) perovskite precursor solutions
2. Solution-processing of defect-free, uniform perovskite thin-films by optimisation of process parameters for methylammonium lead perovskites (MAPbI_3 , $\text{MAPbI}_{3-x}\text{Cl}_x$ and $\text{MAPbI}_{3-x}\text{Br}_x$) such as precursor composition and concentration, spin-coating speed and time, annealing time and temperature.
3. Fabrication of photovoltaic devices with a planar heterojunction architecture of Glass/ITO/PEDOT:PSS/perovskite/PCBM/Al
4. To investigate the effect of the halide ($X = \text{I}, \text{Cl}, \text{Br}$) composition on perovskite; morphology, optoelectronic properties, photovoltaic performance and hysteretic behaviour in methylammonium lead halide perovskites.
5. To investigate the effect of hole- and electron transport materials as device components on the photovoltaic efficiency and stability of the perovskite solar cell.

1.5 Summary of thesis chapters

Starting with a general introduction into perovskite materials, **Chapter 2** addresses several aspects of perovskite solar cells with a special focus on perovskite processing parameters, current-voltage hysteresis and perovskite solar cell stability. The systematic fabrication, characterization and comparison of methylammonium lead triiodide perovskite solar cells and their mixed halide counterparts by the incorporation of chloride or iodide is presented in **Chapter 3**. The effects of chloride incorporation into the methylammonium lead triiodide perovskite and their effects on perovskite morphology and photovoltaic performance are presented in **Chapter 4**. The effect of other device components is also discussed in this chapter. High voltage and larger bandgap perovskite absorber with potential use in tandem solar cells are presented in **Chapter 5**. This chapter also addresses the effect of bromide inclusion in methylammonium lead triiodide perovskite solar cells.

References

- [1] International Energy Agency www.iea.org/outlook
- [2] G. Boyle, B. Everett, J. Ramage, *Energy Systems and Sustainability*, Oxford University Press, 2003, ISBN 0199261792
- [3] E. Dogan and F. Seker, *Renew. Sustainable Energy Rev.*, 2016, 60, 1074-1085
- [4] J. Twiddle and A. D. Weir, *Renewable Energy Sources*, 3rd Ed. 2006, Taylor & Francis, ISBN 978-0-415-58437
- [5] G. Streetman and S. Banerjee, *Solid State Electronic Devices*, 6th Ed, 2000, Upper Saddle River, NJ, Prentice Hall, ISBN 978-0131497269
- [6] F.A. Lindholm, J. G. Fossum, E. L. Burgess, *IEEE Trans. Electron Dev.*, 1979, 26, 165-171
- [7] W. Shockley and H. J. Queisser, *J. Appl. Phys.* 1961, 32, 510-519
- [8] NREL http://www.nrel.gov/ncpv/images/efficiency_chart.jpg
- [9] M. A. Green, K. Emery, Y. Hishikawa, W. Warta, E. D. Dunlop, *Prog. Photovolt*, 2012, 20, 606-614
- [10] M. Graetzel, R. A. J. Janssen, D. B. Mitzi, E. H. Sargent, *Nature*, 2012, 488, 304-312
- [11] M. A. Green, *Prog. Photovolt. Res. Appl.*, 2005, 13, 447-455
- [12] M. A. Green, Silicon Solar-Cells- Evolution, *Semicond. Sci. Technol.*, 1993, 8, 1-12
- [13] K. Branker, M. J. M. Pathak, J. M. Pearce, *Renew. Sustainable Energy Rev.*, 2011, 15, 4470-4482
- [14] A. Yella, H. W. Lee, H. N. Tsao, C. Yi, A. K. Chandiran, M. K. Nazeeruddin, E. W. Diau, C. Y. Yeh, S. M. Zakeeruddin, M. Graetzel, *Science*, 2011, 334, 629
- [15] H. J. Xiang, B. Huang, E. J. Kan, S. H. Wei, X. G. Gong, *Phys. Rev. Lett.*, 2013, 110, 118702
- [16] J. Britt, C. Ferekides, *Appl. Phys. Lett.* 1993, 62, 2851-2852
- [17] I. Repins, M. A. Contreras, B. Egaas, C. DeHart, J. Scharf, C. L. Perkins, B. To, R. Noufi, *Prog. Photovolt*, 2008, 16, 235-239
- [18] J. J. M. Halls, C. A. Walsh, N. C. Greenham, E. A. Marseglia, R. H. Friend, S. C. Moratti, A. B. Holmes, *Nature*, 1995, 376, 498-500
- [19] B. O'Regan, M. Grätzel, *Nature*, 1991, 353, 737-740
- [20] C. W. Tang, *Appl. Phys. Lett.*, 1986, 48, 183-185
- [21] T. K. Todorov, K. B. Reuter, D. B. Mitzi, *Adv. Mater*, 2010, 22, E156
- [22] G. Yu, J. Gao, J. C. Hummelen, F. Wudl, A. J. Heeger, *Science*, 1995, 270, 1789-1791
- [23] K. L. Chopra, P. D. Paulson, V. Dutta, *Prog. Photovolt. Res. Appl.*, 2004, 12, 69-92

- [24] A. G. Aberle, *Thin Film Solids*, 2009, 517, 4706-4710
- [25] M. A. Green, *Prog. Photovolt. Res. Appl.*, 2001, 9, 123-135
- [26] G. Conibeer, *Mater. Today.*, 2007, 10, 42-50
- [27] K. Nakayama, K. Tanabe and H. A. Atwater, *Appl. Phys. Lett.*, 2008, 93, 121904
- [28] S. Moon, K. Kim, Y. Kim, J. Heo and J. Lee, *Sci. Rep.*, 2016, 6, 30107
- [29] K. Ramasamy, M. A. Malik and P. O'Brien, *Chem. Commun.*, 2012, 48, 5703-5714
- [30] Y. A. Jadhav, P. R. Thakur and S. K. Haram, *Sol. Energy Mater. Sol. Cells*, 2016, 155, 273-279
- [31] A. S. Togonal, M. Foldyna, W. Chen, J. X. Wang, V. Neplokh, M. Tchernycheva, J. Nassar, P. R. Cabarrocas and Rusli *J. Phys. Chem. C*, 2016, 120, 2962-2972
- [32] Q. Guo, G. M. Ford, R. Agrawal, H. W. Hillhouse, *Prog. Photovolt.*, 21, 64-71
- [33] E. H. Sargent, *Nat. Photonics*, 2012, 6, 133-135
- [34] P. V. Kamat, *J. Phys. Chem. Lett.*, 2013, 4, 908-918
- [35] A. J. Nozik, M. C. Beard, J. M. Luther, M. Law, R. J. Ellingson, J. C. Johnson, *Chem. Rev.*, 2010, 110, 6873-6890
- [36] B. Kippelen and J.-L. Brédas, *Energy Environ. Sci.*, 2009, 2, 251-261
- [37] S. Ito, S. M. Zakeeruddin, R. Humphry-Baker, P. Liska, R. Charvet, P. Comte, M. K. Nazeeruddin, P. Péchy, M. Takata, H. Miura, S. Uchida and M. Grätzel, *Adv. Mater.*, 2006, 18, 1202-1205
- [38] M. C. Scharber, N.S. Sariciftci, *Prog. Polym. Sci.*, 2013, 38, 1929-1940
- [39] J. Huang, J. H. Carpenter, C.-Z. Li, J.-S. Yu, H. Ade, A. K.-Y. Jen, *Adv. Mater.*, 2016, 28, 967-974
- [40] H. M. Seyf and A. Henry, *Energy Environ. Sci.*, 2016, 9, 2654-2665
- [41] S. A. Bonke, M. Wiechen, D. R. MacFarlane and L. Spiccia, *Energy Environ. Sci.*, 2015, 8, 2791-2796
- [42] A. Kojima, K. Teshima, Y. Shirai and T. Miyasaka, *J. Am. Chem. Soc.*, 2009, 131, 6050
- [43] J.-H. Im, C.-R. Lee, J.-W. Lee, S.-W. Park and N.-G. Park, *Nanoscale*, 2011, 3, 4088
- [44] D. Bi, W. Tress, M. I. Dar, P. Gao, J. Luo, C. Renevier, K. Schenk, A. Abate, F. Giordano, J-P. C. Baena, J-D. Decoppet, S. M. Zakeeruddin, M. K. Nazeeruddin, M. Grätzel and A. Hagfeldt, *Sci. Adv.*, 2016, 2, e1501170
- [45] G. G. Xue, Y. Guo, T. Yu, J. Guan, X. R. Yu, J. Y. Zhang, J. G. Liu, Z. G. Zou, *Int. J. Electrochem. Sci.*, 2012, 7, 1496
- [46] R. Kern, N. Van Der Burg, G. Chmiel, J. Ferber, G. Hasenhiendl, A. Hinsch, R. Kinderman, J. M. Kroon, A. Meyer, R. Niepmann, J. Van Roosmalen, C. Schill, P. M. Sommeling, M. Späth, I. Uhlendorf, *Opto-Electron. Rev.*, 2000, 8, 284
- [47] P. M. Sommeling, M. Späth, H. J. P. Smit, N. J. Bakker, J. M. Kroon, *J. Photochem. Photobiol. A: Chem.*, 2004, 164, 137-144
- [48] S. D. Stranks, G. E. Eperon, G. Grancini, C. Menelaou, M. J. P. Alcocer, T. Leijtens, L.M. Herz, A. Petrozza, H. J. Snaith, *Science*, 2013, 342, 341
- [49] G. Xing, N. Mathews, S. Sun, S.S. Lim, Y. M. Lam, M. Grätzel, S. Mhaisalkar, T. C. Sum, *Science*, 2013, 342, 344
- [50] L. Etgar, P. Gao, Z. Xue, Q. Peng, A. K. Chandiran, B. Liu, M. K. Nazeeruddin, M. Grätzel, *J. Am. Chem. Soc.*, 2012, 134, 17396
- [51] J. Burschka, N. Pellet, S.-J. Moon, R. Humphry-Baker, P. Gao, M. K. Nazeeruddin and M. Grätzel, 2013, *Nature*, 499, 316-319
- [52] M. Liu, M. B. Johnston, H. J. Snaith, *Nature*, 2013, 501, 395-398
- [53] W. Nie, H. Tsai, R. Asadpour, J-C. Blancon, A. J. Neukirch, G. Gupta, J.J. Crochet, M. Chhowalla, S. Tretiak, M.A. Alam, H-L. Wang and A. D. Mohite, *Science*, 2015, 347, 522-525
- [54] O. Malinkiewicz, A. Yell, Y. H. Lee, G. M. Espallargas, M. Grätzel, M. D. Nazeeruddin, H. J. Bolink, *Nature Photon.*, 2014, 8, 128-132

[55] N. S. Lewis, *Science*, 2007, 315, 798-801

[56] T. Todorov, T. Gershon, O. Gunawan, C. Sturdevant, S. Guha, *Appl. Phys. Chem. Phys.* 2015, 17, 1619

[57] Y. M. Yang, Q. Chen, Y. Hsieh; T. Song, N. De Marco, H. Zhou, and Y. Yang, *ACS Nano*, 2015, 9, 7714



UNIVERSITY *of the*
WESTERN CAPE

CHAPTER 2: REVIEW ARTICLE

HALOGENATED-PEROVSKITES FOR SOLAR CELLS

Abstract

Organic-inorganic lead halide perovskites have garnered great interest from academia and industry as photovoltaic materials due to their exceptional optical and electrical properties. Perovskite solar cells (PSCs) are solution-processable and they use only earth-abundant materials making them prime contenders for high efficiency, low-cost solar power generation. In this review, we summarize recent and previous investigations on halide perovskites and provide comparisons with existing theoretical and experimental work. The factors influencing the perovskite processing parameters such as perovskite composition, deposition methods and film treatment will be discussed extensively in this review. A comparison of perovskite device architectures and material selection for the various layers as well as their corresponding impact on the perovskite film and device behaviour will be presented. Critical issues affecting perovskite photovoltaic performance such as hysteresis in the current-voltage measurements and perovskite solar cell stability will be addressed.

2.1 Introduction

The need to develop inexpensive renewable and sustainable energy sources stimulates scientific research for efficient, low-cost photovoltaic devices. Photovoltaic technology is the most attractive future source of energy and many different photovoltaic technologies are being developed for large-scale solar energy conversion [1]. A new material class, organic-inorganic metal halide perovskite semiconductors, is a potential candidate to produce truly low-cost photovoltaic modules. As a result of intensive research, over the past three years [2-5], perovskite solar cells have exhibited unprecedented development with power conversion efficiencies (PCEs) competing with inorganic thin-film solar cells and mainstream multi-crystalline silicon with a certified efficiency of 22.1% [1].

Perovskite was originally the name given to the mineral form of calcium titanium oxide, CaTiO_3 , discovered in the Ural Mountains by German scientist Gustav Rose in 1839. He named it in honour of Count Lev Aleksevich von Perovski, a Russian mineralogist (1792-1856), who first characterized the material. The term is now generally used to describe any substance having the same or a related crystal structure exhibiting the stoichiometry as ABX_3 , where A is aliphatic or aromatic ammonium, B is a divalent metal cation and X is a halogen anion, **Figure 2.1**.

This ambiguity of terminology of the structural family and the mineral was explicitly elucidated Müller and Roy [6]. They sought to address the ambiguity by proposing that the original mineral composition would be enclosed in brackets, thus $[\text{CaTiO}_3]$ represents the perovskite structure and not the composition CaTiO_3 .

Materials with the perovskite structure attracted much attention in the late 1980s and early 1990s due to superconductivity [7,8]. The choice of material combinations is crucial for determining perovskite properties. The electronic and optical properties of perovskites can be tuned by adjusting the composition of A, B and X. Pioneering work by Mitzi *et al.*, [9,10] suggested that perovskite films exhibit composition-/structure-dependent properties, which can be accessed by various processing approaches. The possibility of tuning perovskite optical properties was supported by theoretical modeling, which found agreement between the calculated band structures and the experimental trend of optical band gaps in these perovskite structures [11]. Dependent on which atoms/molecules are used in the structure, perovskites can have an array of properties and exhibit rich physical behaviour such as ferroelectricity, piezoelectricity, thermoelectricity, birefringence and superconductivity [12-16].

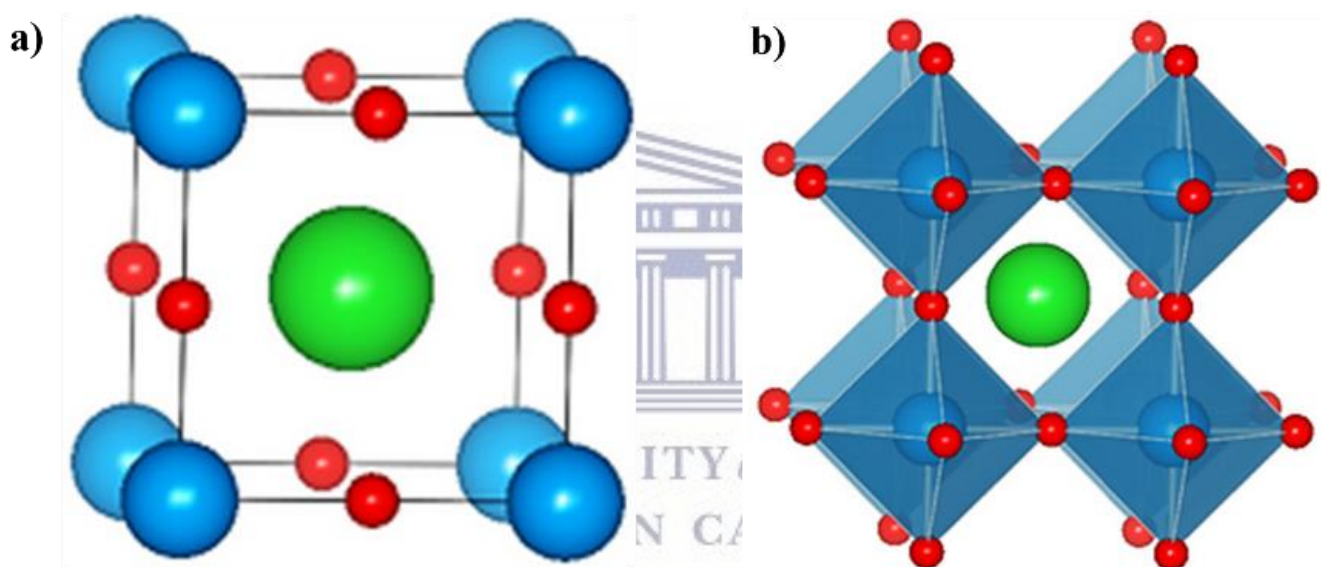


Figure 2.1: a) Schematic figure of the generic ABX_3 , which has the crystal structure of calcium titanium oxide [$CaTiO_3$], A cations (blue), B cations (green) and X cations (red), b) an alternative view depicting B cations assembled around X anions to form BX_6 octahedra, as B-X bonds are responsible for determining optical properties.

The perovskite crystal structure was first described by Victor Goldschmidt in 1926, who devised a tolerance factor to determine the formability of perovskites based on the atomic radii of the constituents [17]. The crystal structure was later published in 1945 from X-ray diffraction (XRD) data on barium titanate by H. D. Megaw [18]. The Goldschmidt tolerance factor is expressed as:

$$t = \frac{[(R_A) + (R_X)]}{[\sqrt{2} (R_B) + (R_X)]} \quad (2.1)$$

where R_A , R_B and R_X are the effective ionic radii for the cations in the cubo-octahedral A and octahedral B sites and corresponding anion.

Many metallic elements are stable in the perovskite structure, if the tolerance factor t is in the range of 0.75-1.0. It was experimentally found that the high-symmetry cubic structure is formed when $0.89 < t < 1.0$ [19] otherwise, the cubic structure will be distorted and crystal symmetry is lowered. When t is below 0.89, the octahedral rotates to form an orthorhombic or rhombohedral structure, whereas above 1 a hexagonal arrangement is adopted.

As illustrated in **Figure 2.1**, perovskites crystallize in the ABX_3 structure consisting of corner-sharing BX_6 with the A component neutralizing total charge. The larger A cation occupies a cubo-octahedral site shared with twelve X anions, while the smaller B cation is stabilized in an octahedral site shared with six X anions. It has been proposed that the organic A cation does not play major role in determining the band structure, and acts to fulfill charge neutrality within the lattice [20]. Nevertheless, the size of the organic cation, A, is important. A larger or smaller A cation can cause the whole lattice to expand or contract. The most widely used A cation for organic-inorganic perovskites is methylammonium ($CH_3NH_3^+$, MA) [2, 21-27]. Other cations that have been explored including ethylammonium cation ($CH_3CH_2NH_3^+$, EA) [28], formamidinium (FA) [26,29,30], cesium (Cs^+) [30-32], 5-aminovaleic acid (5-AVA) [33] and rubidium cations [Rb^+] [34]. Recently, Cs was used to explore more complex cation combinations, *i.e.*, Cs/MA, Cs/FA, Cs/MA/FA and Cs/Rb [30,31,32, 34-37]

The B metal cation sites in organic-inorganic perovskites are occupied by Group IVA metals in a divalent oxidation state (Pb^{2+} , Sn^{2+} , Ge^{2+}). In hybrid perovskite, photovoltaic devices Pb^{2+} [26-41] has proven to be superior in comparison to Sn^{2+} [39,42,43] and Ge^{2+} [44,45] both in terms of performance and stability, thus has been the most widely employed metal cation. The halide anions occupying the X site play an important role in determining the band gap of the perovskites as well as their stability. The X halide anion has been the most effectively varied component of organometallic perovskites with the I^- ion forming the basis of hybrid methylammonium lead halide perovskites. The inclusion of Cl^- [46-50] or Br^- [26,41,51,52] to form mixed halide perovskites resulted in increased device performance due to significantly improved perovskite film morphology [4,22,26] and allowed for effective band gap tunability [11,22] respectively. Changing the B-X bond length has been demonstrated to be important in determination of bandgap [29,53-55]. Given a particular metal and halide, there is a relatively small size range allowed for the A cation since it must fit between the corner-sharing metal halide octahedra. If the A cation is too large *e.g.* ethylammonium cation [56], $C_6H_5C_2H_4NH_3$ [57], the 3D perovskite structure is unfavourable, lower dimensional layered or confined perovskites will be formed [58-60]. If it is too small, the lattice would be too strained to form.

Halide perovskites allow monovalent and divalent cations in the A and B sites, respectively to fulfill charge neutrality.

For the three-dimensional perovskites discussed in this review, A is the CH_3NH_3^+ ($R_A = 0.18$ nm) organic cation [61], B is a divalent Pb^{2+} ($R_B = 0.119$ nm) metal cation [38] and X is a halide ion I ($R_I = 0.220$ nm) with Br^- ($R_{\text{Br}} = 0.196$ nm) and/or Cl^- ($R_{\text{Cl}} = 0.181$ nm) usually in a mixed-halide material. Methylammonium lead triiodide ($\text{CH}_3\text{NH}_3\text{PbI}_3/\text{MAPbI}_3$) crystallizes in tetragonal perovskite structure arising from a distortion of the perovskite lattice under ambient conditions [42,58] because its Goldschmidt tolerance factor, t , is less than the ideal unity ($t \sim 0.83$) [58,62]. The CH_3NH_3^+ cation is suitable for perovskite structure because of its ionic radius of 180 pm [62,63].

In this review, fundamentals of perovskite solar cells in terms of device structure and operation are discussed. Since perovskite film quality is directly related to its photovoltaic performance, effective methods for high performance solar cells using different deposition methods are addressed. In terms of perovskite photovoltaic device architecture, a comprehensive comparison of the regular- and inverted-mesoporous or planar structures is provided. Stability issues such as photo-, moisture- and thermal-stabilities are addressed and methodologies to solve the underlying stability problems are discussed. Further development and possible solutions to the remaining challenges facing the commercialization of perovskite solar cells are discussed within each subject.

2.2 Solid-state perovskite solar cells

Methylammonium lead halide perovskites were initially used as sensitizers to replace the dye molecules in the conventional configuration of dye-sensitized solar cells (DSSCs) based on liquid electrolyte solar cells showing power conversion efficiency of $\sim 4\%$ [21]. However, the unavoidable problem associated with the liquid solar cells was the inherent instability of perovskite sensitizers in the electrolyte. By changing the electrolyte formulation and the deposition method of the perovskite sensitizer on TiO_2 , Park *et al.* improved the PCE to 6.5% [64]. To combat the stability issue, Kim *et al.*, and Lee *et al.*, reported solid-state heterojunction perovskite solar cells using 2, 2'-7,7'-tetrakis (*N,N*-di-*p*-methoxyphenylamine)-9,9'-spirofluorene (Spiro-OMeTAD) as hole transport material (HTM) achieving power conversion efficiencies of 9.2% employing a mesoporous TiO_2 layer [65] and 10.9% employing Al_2O_3 scaffold [66]. Lee *et al.* demonstrated that substituting the TiO_2 substrate with a mesoporous scaffold made of Al_2O_3 produced similar conversion efficiencies, suggesting that perovskites are not only efficient absorbers, but electron transporters as well [66]. At the same time Etgar *et al.* showed that the perovskite could also assume the role of a hole transporter material [67], which prompted the development of new device architectures. Although first implemented in dye-sensitized solar cells based on mesoporous structures [21,64], the perovskites have

been gradually found to assume all the principal roles of photovoltaic operation [22,23,67]. Since the pioneering work by Kojima *et al.*, [21] organohalide lead perovskites have revolutionized the field of emerging photovoltaic technologies, competing with inorganic thin-film solar cells and mainstream multi-crystalline silicon, with various reports of efficiencies of ~20% [26, 41,68-70] and certified 22.1% efficiency [1].

The inorganic-organic lead halide perovskite crystal structure confers exceptional properties to the final photoactive layer in perovskite solar cells [71] including a direct band gap, large and broad absorption spectrum in the visible range (absorption coefficient = $1.5 \times 10^4 \text{ cm}^{-1}$ at 550 nm) [72,73], bandgap tunability [53-55], fast exciton separation with charges rapidly generated within the bulk material [74], long range electron-hole diffusion length ~100 nm for MAPbI₃ and 1 μm for methylammonium lead iodide-chloride (CH₃NH₃PbI_{3-x}Cl_x/MAPbI_{3-x}Cl_x) [22] high carrier mobilities [76,76] and efficient charge-injection into the charge transport layer [22,23,65,77]. The rate of non-radiative recombination in these materials is relatively low, reducing the bandgap-voltage offset, allowing for high open-circuit voltage (V_{oc}) [78-80]. Additionally, ambipolar carrier diffusion within lead halide perovskites further highlights the unique excited state character of this peculiar class of semiconductors [67,81,82]. Solution-processability from inexpensive input materials [49,83-85], compatibility with large-area deposition techniques [86,87], make this material very attractive for solar energy.

The most commonly explored organic-inorganic metal halide perovskite, applied in the field of photovoltaics is MAPbI₃. Currently the highest efficiency devices are Pb-based with mixtures of MA/FA cations and I/Br halides [26,41,51]. Recently, several reports have been published on the effective performance of hole conductor-free perovskite solar cells, demonstrating the potential applications of *p-i-n* homojunctions in solar cells [88-90]. The highest PCE of 13.5% is one of the highest recorded for a hole transport layer (HTL)-free perovskite device [91].

Pioneering work by Pellet *et al.* [92] and Jeon *et al.* [26] has led to high efficiency perovskite using mixtures of the organic cation A and halide anion X. Mixed organic cation perovskites which allow for combination of the strong individual attributes of each organic cation have also been reported *e.g.* (MA)_x(FA)_{1-x}PbI₃ [29,92-94], Cs_x(MA)_{1-x}PbI₃ [31], (Cs)_x(FA)_{1-x}PbI_{3-y}Br_y [35] and (5-MA)_x(MA)_{1-x}PbI₃ [33]. Mixed metal cation perovskites demonstrating band gap tunability *e.g.* MASn_{1-x}Pb_xI₃ have also been explored [39,42,95]. Recently McMeekin *et al.* [52], and Isikgor *et al.* [96] reported high efficiency mixed cation lead mixed halide absorber, [HC(NH₂)₂]_{1-x}Cs_xPb(I_{1-y}Br_y)₃ and MA_{1-x}FA_xPbI_{3-y}Cl_y.

2.3 Perovskite processing parameters

The optimization of film deposition methods has been a key factor behind the outstanding increases in perovskite solar cell device performance. Every aspect of the perovskite solar cell fabrication process, such as the precursor composition [93,97-100] and concentration [101], the addition of certain chemicals that aid film formation [29,98-100,102] and the thermal annealing step [102-105] has a critical influence on the perovskite crystallization rate and therefore on the morphology of the resulting perovskite layer.

2.3.1 Perovskite precursor composition

There are a multitude of different perovskite precursor formulations developed to-date that include mixtures of solvents, halide and molecular ions and solvated metals. All halide perovskite fabrication protocols combine an organic salt with a lead salt to produce a lead halide perovskite thin film. Generally, these precursors either can be combined in a common solution or can be combined from separate solutions. Selecting suitable solvents of the precursor is a very critical step towards the optimization of the perovskite film morphology. Currently, the most commonly used solvent of the perovskite precursor is *N,N*-dimethylformamide (DMF) [27,29,66,77,85] and other solvents include γ -butyrolactone (GBL) [106,107] the homologue of DMF, dimethylacetamide (DMA), [106,108] and dimethylsulfoxide (DMSO) [80], or mixtures thereof. Homogeneous crystal domains of a perovskite film can be produced by certain combinations of these solvents, such as DMF-GBL [109] and GBL-DMSO [110]. Noel *et al.*, [111] recently reported low viscosity and low boiling point acetonitrile (ACN) as a promising alternative solvent of lead halide perovskites to induce rapid crystallization of perovskite films for high-efficiency photovoltaic devices.

2.3.2 Deposition methods

The fabrication processes available for perovskites are robust and a myriad of approaches [3], **Figure 2.2**, has been developed to deposit perovskite films, **Figure 2.3**. Generally, they can be categorized into the solution-process deposition (one-step and two-step sequential deposition techniques), vapor-assisted solution process (VASP) and vacuum deposition. To date, the perovskite layer in these efficient solar cells has generally been fabricated by either vapor deposition or a two-step sequential deposition process.

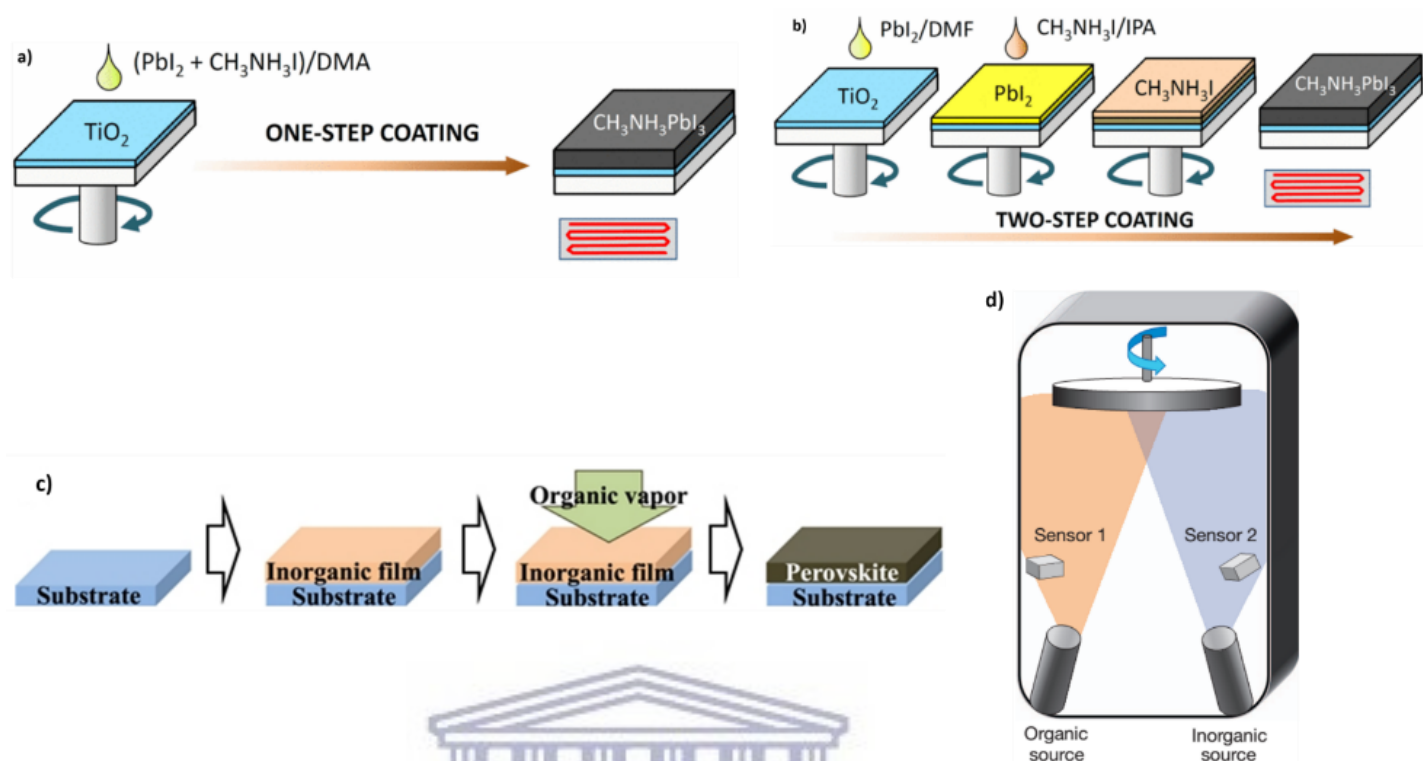
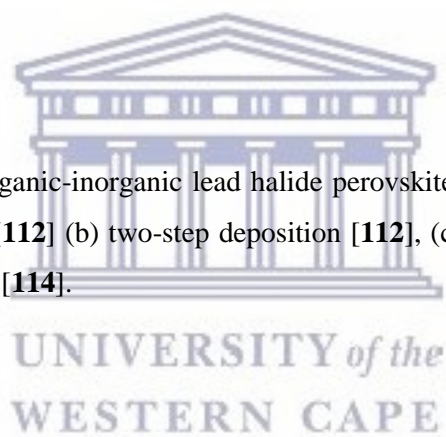


Figure 2.2: The preparation of organic-inorganic lead halide perovskite films using different deposition methods: (a) one-step deposition [112] (b) two-step deposition [112], (c) vapor-assisted solution process [113] and (d) vacuum evaporation [114].



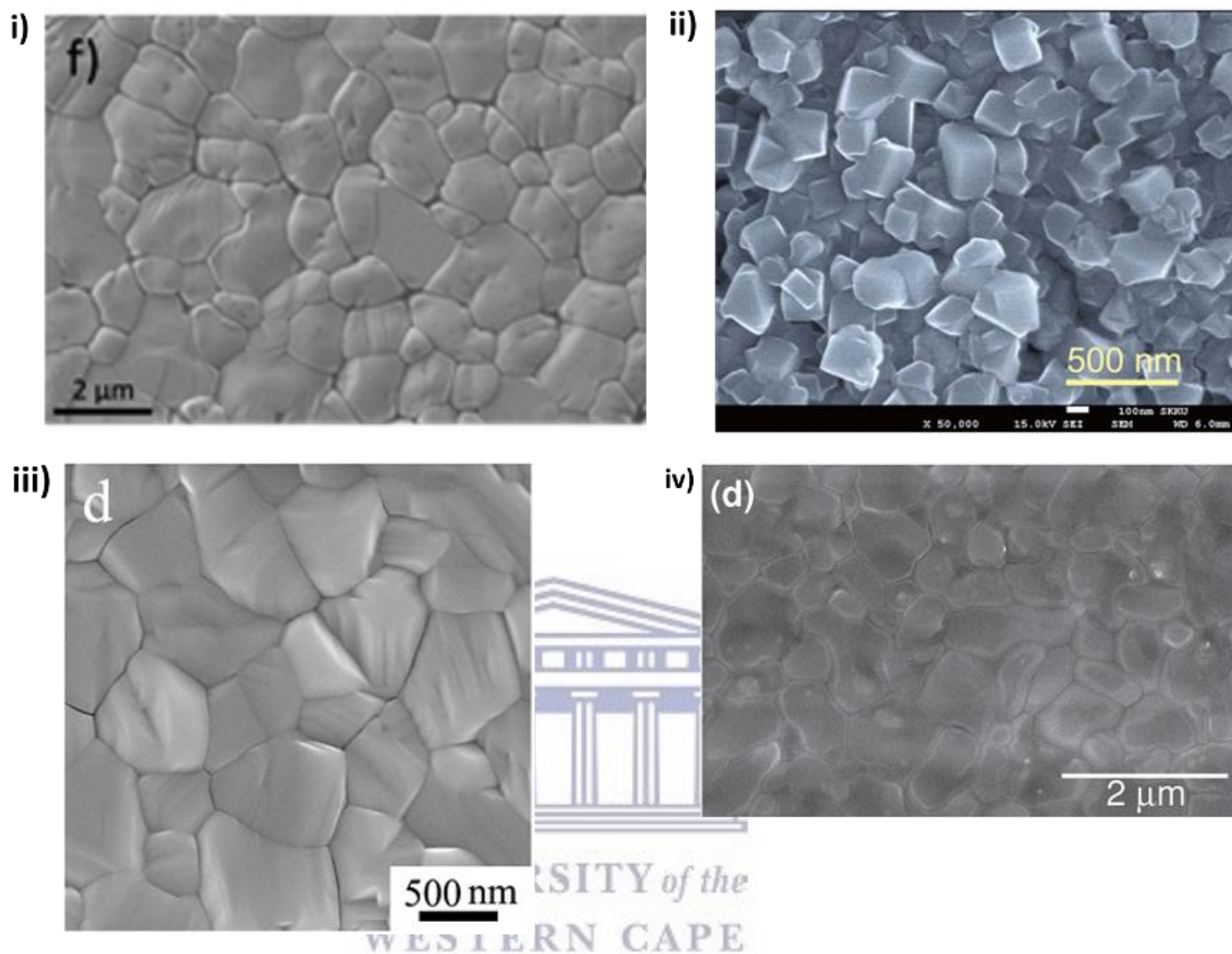


Figure 2.3: Scanning electron microscopy images of perovskite films fabricated using various deposition methods: (i) one-step deposition [85], (ii) two-step deposition [112], (iii) vapour-assisted solution process [113] and (iv) vacuum evaporation [115].

2.3.2.1 One-step deposition technique

The one-step deposition method, **Figure 2.2(a)**, consists of mixing both the organic (RNH_3X) and inorganic (PbX_2) precursors in a single solution (e.g. DMF, DMSO and/or GBL) and casting a film from this solution onto the appropriate substrate. This leads to the formation of a film composed of a solvent-perovskite complex [110] which is then annealed and the precursor components self-assemble into the final perovskite phase, **Figure 2.3(a)**, with the general ABX_3 stoichiometry [77,83,110].

Metal halide precursors and organic cations exhibit very different chemical properties, and as such, often show markedly different solubilities in the same solvent, greatly complicating their deposition using one-

step approaches. Therefore, any change to the precursor mixture affects the whole film formation and crystallization dynamics. Rough and discontinuous films [85] are produced when the perovskite film morphology is not controlled by carefully controlling the solubility of precursors in solution and/or by controlling the humidity of the processing environment. This causes some problems like light-harvesting reduction, charge recombination, film instability and decreased device efficiency.

One-step spin coating remains the simplest and most widely used method in research laboratories. In an effort to improve film morphology, different variations of this deposition technique have been developed, such as the utilization of a variety of lead salt precursors [97,116,117], the addition of a solvent quenching step [110] and the utilization of solvent mixtures [110]. Most recently, a popular approach involved the inclusion of dimethyl sulfoxide (DMSO) in the precursor solution [37,80,118]. Although spin coating is not recognized as the ideal manufacturing methodology, it represents a starting point from which more scalable deposition methods, such as slot-dye coating and ink-jet printing.

2.3.2.2 Two-step deposition technique

The two-step deposition, **Figure 2.2(b)**, involves sequential steps of first depositing the inorganic halide PbI_2 layer with concentrated PbI_2 solution onto a substrate by spin-coating or vacuum evaporation and subsequently converting the PbI_2 layer into the perovskite film, **Figure 2.3(b)**, by reacting with $\text{CH}_3\text{NH}_3\text{I}$ (MAI) [84,107]. Appropriate solvents can be targeted for both the lead precursor and the organic cation and thus almost no additional optimization beyond tuning of temperature and reaction times is required. This deposition technique therefore gives access to many highly crystalline perovskite structures with little effort. Generally, the two-step deposition is favoured due to its easy control over the morphology. But one of the main drawbacks of two-step deposition technique is the difficulty in depositing mixed perovskite films, which have superior transport properties [22].

2.3.2.3 Vapor-assisted solution process (VASP)

In the vapor-assisted solution process (VASP), **Figure 2.2(c)**, the inorganic framework film is formed by depositing the precursor solution on the substrates and subsequently treating with the desired organic vapor [113]. The key step includes the film growth, **Figure 2.3(c)**, via the as-deposited film of PbI_2 *in situ* reacting with the organic halide vapor. Since there is no kinetically favourable van der Waals gap in the inorganic perovskite/perovskite interface where transformation occurs, a long reaction time is required to transform inorganic precursors into perovskite completely.

2.3.2.4 Vacuum evaporation deposition

Like other thin-film PV technologies, (e.g. α -Si, Cu(InGa)S₂, and CdTe), vacuum evaporation is one of the most promising techniques to construct perovskite thin films for planar junctions. In this deposition process, the perovskite is prepared by co-evaporation of the metal halide and organic halide, **Figure 2.2(d)**. Vacuum evaporation allows the precise control of the thickness and smoothness of the thin-film surface, **Figure 2.3(d)** [115]. However, it is often difficult to balance the organic and inorganic evaporation rate, an important criterion for the optimization of perovskite film composition. This technique also demands high vacuum, which is too energy consuming and hinders mass production.

2.4 Perovskite device architectures

Perovskite materials can be applied to any kind of junction structure. The architecture of perovskite solar cells was derived from the dye-sensitized solar cells (DSSC) technology [21,64]. Perovskite optoelectronic devices are generally based on a n-i-p junction, where the intrinsic perovskite material sits between a hole transport material (HTM) and an electron transport material (ETM), **Figure 2.4**.

Mesoporous and planar structures are the main perovskite solar cell architectures currently under investigation. Depending on which transport material is encountered by light first, these architectures can be categorized as either the conventional n-i-p (**Figure 2.4(a,b)**) or the inverted p-i-n structures, (**Figure 2.4 (c,d)**). The inverted planar device structure, derived from organic solar cells, uses p-type and n-type materials as bottom and top charge transport layers, respectively. Wang *et al.*, [119] and Chen *et al.*, [120] recently reported NiO-based mesoscopic p-i-n devices with efficiencies of 9.5% and >13% respectively, **Figure 2.4(d)**.

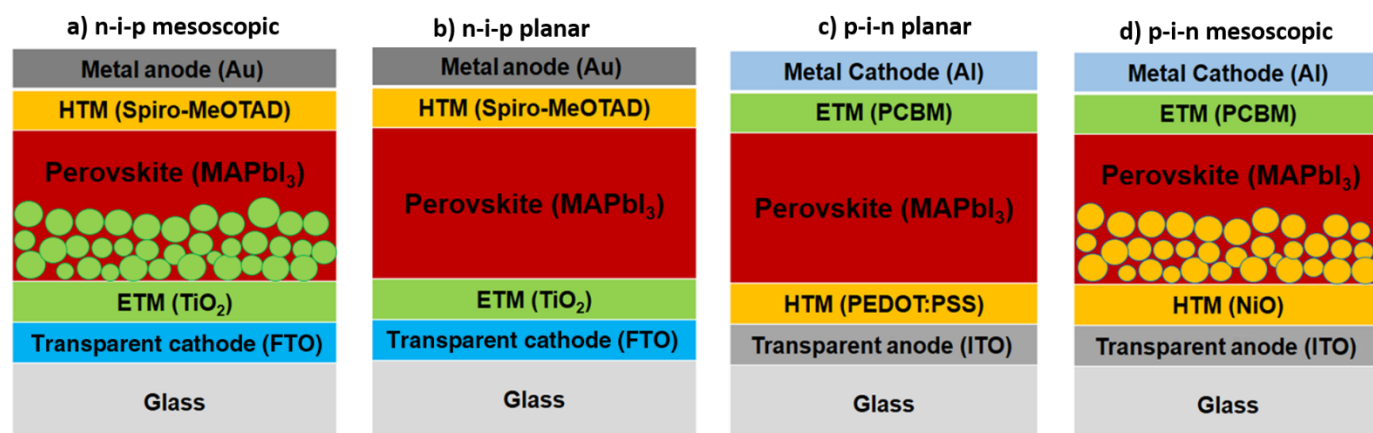


Figure 2.4: Schematic diagrams of different perovskite device architectures showing a) n-i-p mesoscopic, b) n-i-p planar, c) p-i-n planar and d) p-i-n mesoscopic [121].

Hybrid perovskites have demonstrated high power conversion efficiencies both in planar [29,84,113,114,122] and mesoporous device architectures [65,66,77,92,107,123,124], complicating any correlation between device architecture and photovoltaic performance. [1,107]. Varying interpretations of planar and mesoscopic perovskite morphologies have also complicated objective comparisons between the two cell architectures. Additionally, high efficiency PSC devices have been produced through the combination of planar and mesoscopic architectures [84]. Tandems of perovskites, as distinct device architectures on top of silicon (Si) or copper indium gallium diselenide (CIGS) cells have been investigated as a pathway to achieving industry goals of improving efficiency while lowering cost [125,126].

2.4.1 Mesoporous architecture

The mesoporous n-i-p device architecture is the current dominant photovoltaic architecture. Early reports of PSC technologies represent the perovskite material in mesoscopic architectures as a quantum-dot style sensitizer [21,64,65] or as a dense layer coating the mesoporous scaffold [66]. In this device structure, the perovskite layer is either deposited on top of a mesoscopic, **Figure 2.4(a)**, electron-transporting metal oxide and covered with an organic hole-transport layer, or it is sandwiched between a bottom hole-transport material, **Figure 2.4(d)** and a top organic electron-transport layer. Mesostructured semiconducting metal oxides, such as TiO₂ [25,65,107], Al₂O₃ [66,77,123], ZrO₂ [124] and most recently, zinc-doped TiO₂ (Zn-TiO₂) [127,128] have been employed as n-type scaffolds, while the perovskite absorber is infiltrated within the pores. There is wide debate in the PSC community about the exact effect of the scaffold on the perovskite solar cell operation [64,77,129]. It is suggested that the metal oxide scaffold provides pathways for electron extraction as well as limiting the growth and size of perovskite crystals. Regardless of the influence of the metal scaffold on the solar cell, metal oxide scaffolds require high sintering temperatures to maximize transport properties [77,130] limiting application to flexible substrates and increasing production costs. The requirement to reduce the fabrication temperature has been demonstrated by replacing TiO₂ be replaced by ZnO [84,131,132]. Unfortunately, the ZnO/CH₃NH₃PbI₃ interface appears to accelerate the thermal decomposition of the perovskite layer and the film is less thermally stable, when compared to TiO₂ [133,134].

The most commonly used hole transport materials in mesoporous solar cells are 2, 2'-7,7'-tetrakis (*N,N*-di-*p*-methoxyphenylamine)-9,9'-spirofluorene (Spiro-OMeTAD) [25,66,68], poly(3-hexylthiophene) (P3HT) [135,136] and poly(triarylamine) (PTAA) [137,138]. Spiro-OMeTAD material requires an additive, namely *t*-tert-butylpyridine (TBP) or bis(trifluoromethane)sulfonimide lithium salt (Li-TFSI), to improve the conductivity. However, it has been reported that these additives breakdown the perovskite layer, reducing the stability of the device [139]. Liu *et al.* investigated the use of a dopant free HTL material, a tetrathiafulvalene derivative (TTF-1) [140] in a mesoporous perovskite solar cells. This cell achieved an

efficiency higher than undoped Spiro-OMeTAD and P3HT. Gold is the most commonly used electrode material for high efficiency perovskite solar cells [64-67,141]. However, this material is prohibitively expensive so multiple novel applications of carbon electrodes have recently been reported [142-144].

2.4.2 Planar architecture

Planar heterojunction, **Figure 2.4(c,d)** perovskite solar cells in contrast to mesoporous cells, employ a thin film of the perovskite absorber sandwiched between the charge selective contacts [83,97,114,144]. In this configuration, the high temperature sintered mesoporous scaffold can be replaced either by metal oxides prepared at lower temperatures such as ZnO [84,131-134] or by organic contact materials [84]. The planar architecture potentially provides enhanced flexibility for device optimization, multijunction construction and investigation of the underlying device physics, but it requires tremendous effort to fabricate high-quality perovskite films [27,85].

Most reports on planar perovskite architectures use an organic material for the HTL. The most commonly used p-type contact is PEDOT:PSS. Inverted planar perovskite devices using non-oxide PEDOT:PSS have demonstrated efficiencies >16% [145-147], lower temperature processing [27,85,122], flexibility [27,122] and furthermore negligible current-voltage hysteresis effects [85,141,147].

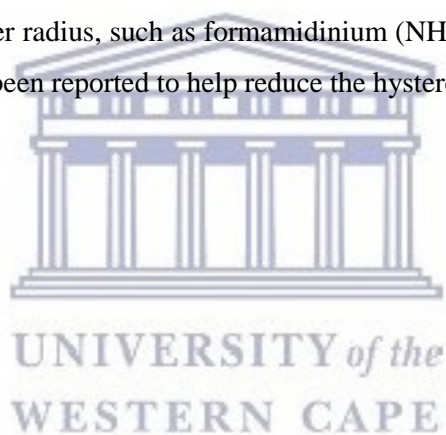
Kim *et al.* incorporated an inorganic HTL, Cu-NiO_x [148]. Such inorganic oxide films display better environmental stability than their organic counterparts; however, generally, organic HTLs have led to higher device efficiency [148]. Zheng *et al.* took a different approach to replace the spiro-OMeTAD. They synthesized a conductive oligothiophene, DR3TBDDT, for use as a HTL in a planar geometry perovskite solar cell [149]. The most commonly used n-type contact is PCBM.

2.5 Hysteresis

Perovskite solar cells suffer from a strong scan rate and/or scan direction hysteresis [25,150,151] in the current-voltage measurements typically conducted under AM1.5G illumination that can lead to an under- or over-estimation of the solar cell device efficiency, **Figure 2.5(a)**. Hysteretic phenomena have been observed for other photovoltaic technologies including CIGS, CdTe and amorphous silicon that exhibit high internal capacitances, which have been attributed to charge carrier accumulation in the depletion layer or neutral region of the junction, existence or formation of defect states and other phenomena such as ion migration [152,153].

Hysteresis has also been reported to be heavily dependent on device architecture, perovskite processing parameters (grain size and boundaries and/or surface imperfections of perovskites) and has been observed in devices utilizing alternative selective contacts, suggesting that the contact interfaces have a big effect on

transients in perovskite absorber devices [150,151]. Hysteresis in perovskite solar cells with a mesoscopic architecture has been reported to be strongly influenced by the perovskite grain size and the structure of the underlying TiO₂ layer which is used as an electron transport layer [25,150,151]. Efforts are now concentrated on generating perovskite films with larger grain sizes to minimize the hysteresis [25,110,115]. Reports have shown C₆₀/fullerene passivation eliminates this kind of photocurrent hysteresis in thin film planar devices. The fullerene was found to interact with halide rich defective regions at the grain boundaries, leading to the passivation of localized trap states [141,165]. The differences in the hysteretic behaviour observed in the mesoscopic and planar devices may be a consequence of differences in stoichiometry or morphology due to the differences in processing however, no conclusive outcomes about the observed differences have been provided as hysteresis-less devices for both devices have been reported, **Figure 2.5 (b,c)**. Several groups have fabricated devices without significant hysteresis, *e.g.* by using mesoporous TiO₂ layers instead of a compact TiO₂ layer (**Figure 2.5(b)**) [110], solvent annealing to obtain large crystalline grains [49] as well as a fullerene passivation method (**Figure 2.5(c)**) [165]. In addition, the replacement of MA⁺ with cations that have a larger radius, such as formamidinium (NH₂CH=NH₂⁺, FA⁺) [94,155] and 5-ammoniumvaleric acid [34] have been reported to help reduce the hysteresis effects.



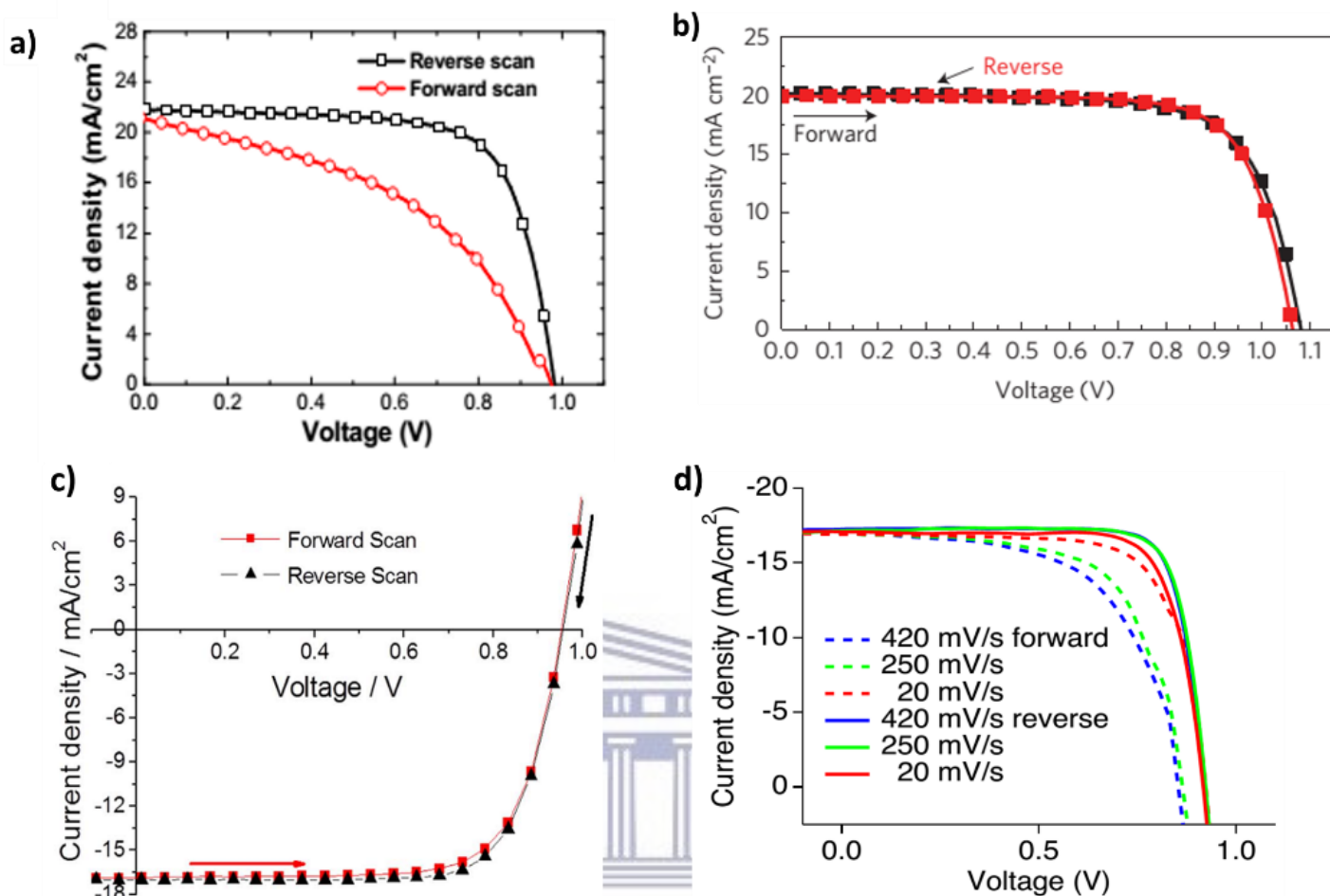


Figure 2.5: Current-voltage (J - V) with forward and reverse scans exhibiting: (a) hysteresis [154] (b) negligible hysteresis for a mesoporous solar cell [26], (c) negligible hysteresis for a planar perovskite solar cells [85] and (d) scan-rate and direction- dependent hysteresis [27].

The origin of hysteresis and its mechanism in perovskite solar cells is a highly-debated topic and has become an area of intense research. Hysteresis effects are generally associated with a high capacitance (of the order of mF cm^{-2}) compared to Si cells (of the order of μF) [25,155-158]. This capacitance effect was hypothesized to originate from the ferroelectricity or the polarization of the perovskite layer [42,150,159-161], changes in absorber or contact conductivity [162], ion migration within the crystal structure of perovskites [150,159,163,164] and/or the trapping/de-trapping of charge carriers [25,42,150,151]. It has also been reported that the degree of observed hysteresis is highly dependent on the interface properties and choice of contact materials, which control interfacial trap density [110,150,165,166]. However, no conclusive outcomes about the origin of this capacitive effect have been provided. Instead it was suggested that this phenomenon must obey an intrinsic property of the perovskite solar cells because perovskite was the common denominator for samples experiencing hysteresis [150].

Hysteresis has also been reported to be heavily dependent on device architecture, perovskite processing parameters (grain size and boundaries and/or surface imperfections of perovskites) and has been observed in devices utilizing alternative selective contacts, suggesting that the contact interfaces have a big effect on transients in perovskite absorber devices [150,151]. Hysteresis in perovskite solar cells with a mesoscopic architecture has been reported to be strongly influenced by the perovskite grain size and the structure of the underlying TiO₂ layer which is used as an electron transport layer [25,150,151]. Efforts are now concentrated on generating perovskite films with larger grain sizes to minimize the hysteresis [25,110,115]. Reports have shown C₆₀/fullerene passivation eliminates this kind of photocurrent hysteresis in thin film planar devices. The fullerene was found to interact with halide rich defective regions at the grain boundaries, leading to the passivation of localized trap states [141,165]. The differences in the hysteretic behaviour observed in the mesoscopic and planar devices may be a consequence of differences in stoichiometry or morphology due to the differences in processing however, no conclusive outcomes about the observed differences have been provided as hysteresis-less devices for both devices have been reported, **Figure 2.5 (b,c)**. Several groups have fabricated devices without significant hysteresis, *e.g.* by using mesoporous TiO₂ layers instead of a compact TiO₂ layer (**Figure 2.5(b)**) [110], solvent annealing to obtain large crystalline grains [49] as well as a fullerene passivation method (**Figure 2.5(c)**) [165]. In addition, the replacement of MA⁺ with cations that have a larger radius, such as formamidinium (NH₂CH=NH₂⁺, FA⁺) [94,155] and 5-ammoniumvaleric acid [34] have been reported to help reduce the hysteresis effects.

The dependence of hysteresis on the scan rate and direction is still controversial, **Figure 2.5(d)**. Snaith and co-workers observed that sweeping voltage from forward bias to short circuit results in higher measured photocurrents and open-circuit voltage values than sweeping in the opposite direction [150]. On the contrary, Dualeh *et al.* [159] and Kaltenbrunner *et al.* [27] reported an opposite dependence of the hysteresis with the scan rate.

Although there are several proposed PSC hysteresis mechanisms, recently more and more attention is focused on the role of ions/vacancies migration under an electrical field [167-169]. Iodine ions were identified as the migrating species by measuring temperature-dependent current-transients and photoelectron spectroscopy [170]. Field-dependent orientation effects of the MA⁺-dipoles and lattice distortion have been proposed to give rise to polarization effects that affect the charge carrier dynamics [42,155,160,161]. In addition, metal halides and metal halide perovskites can exhibit significant halide ion mobilities [163,164] that are often accelerated by photoexcitation. The strong, reversible dependence of hysteresis on light and voltage bias in thin-films, **Figure 2.5(d)** suggest that photo-induced ion migration may play an important role in device hysteresis [151]. Additionally, there is strong direct and indirect evidence that slow drift and diffusion of ionic defects at room temperature is the dominant mechanism

underlying hysteresis in MAPbI₃ solar cells [159,168,170,171]. Recent simulations suggest that *J-V* hysteresis could be reproduced accurately if both ionic migration and recombination via interfacial traps were present in devices [173].

Whereas there is increasing evidence supporting ion migration as the origin of PSC hysteretic behavior, there are speculations against charge trapping and ferroelectric polarization as possible main hysteresis mechanisms. Eames *et al.*, [168] demonstrated that simple trapping and de-trapping of charges at bulk or interface defects is unlikely to be the main mechanism due to the long duration and large magnitude of the current decay although the trapping/de-trapping process associated with migrating defects has been shown to play an important role in hysteresis [167,174].

Hermes *et al.* [175] and Leguy *et al.* [176] proved that ferroelectric polarization is highly unlikely to persist in perovskite materials leading to speculations that ferroelectric polarization may not be a possible hysteresis mechanism. Further development in perovskite device current-voltage characterization depends on understanding the origin and mechanism of device hysteretic behaviour.

2.6 Stability

For practical application and commercialization, not only the power conversion efficiency but also the lifetime of a photovoltaic device is of importance. Perovskite optoelectronic materials suffer from several drawbacks that need to be overcome before the technology becomes industrially relevant and hence achieve long-term application. Environmental stability [75] remains a key challenge to the commercialization of perovskite solar cells. This instability is caused by the intrinsic instabilities of the perovskite absorber, as well extrinsic factors which degrade the device **Figure 2.6**.

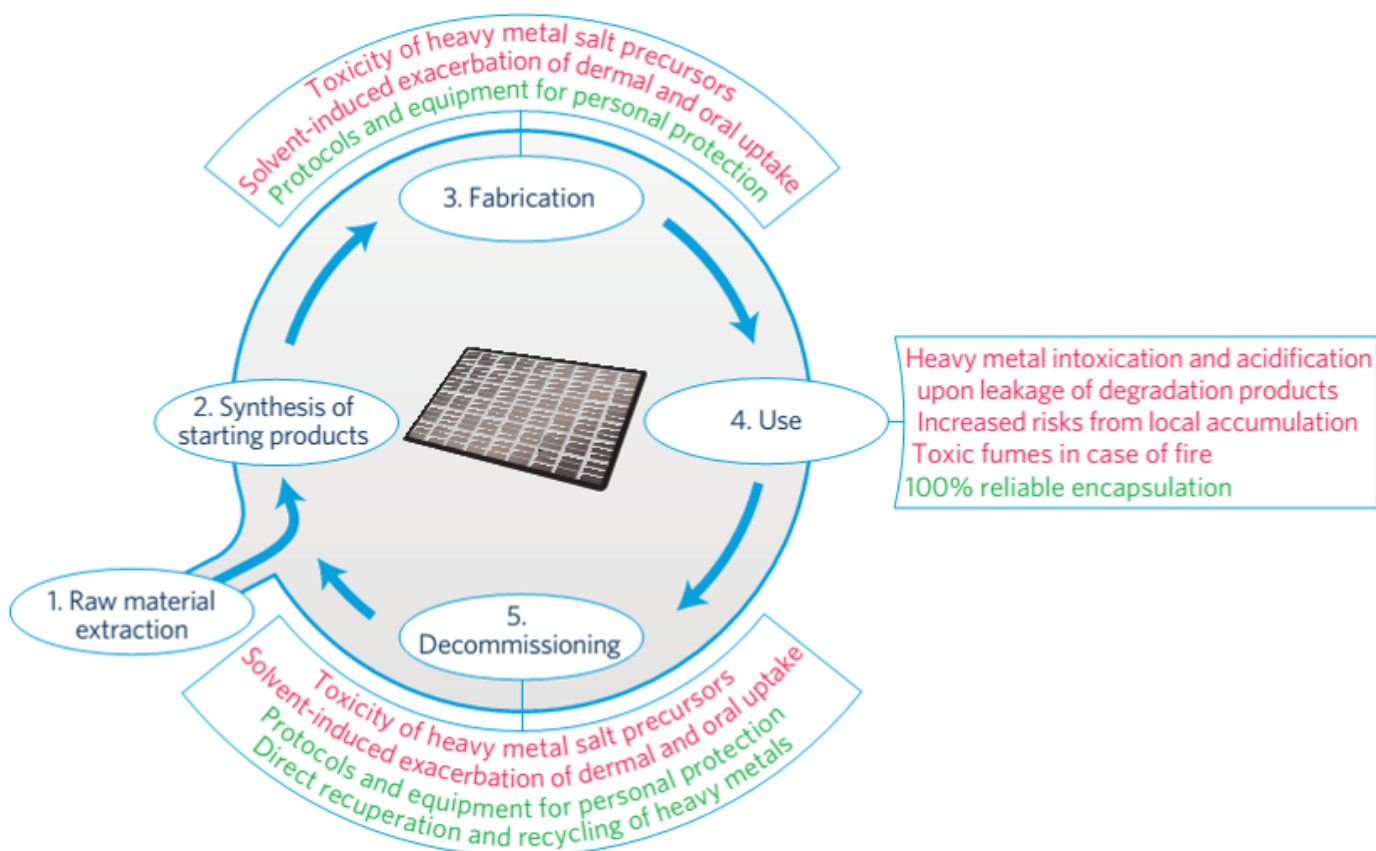


Figure 2.6: Schematic of the life cycle of perovskite solar cells indicating the most important hazards (red) and strategies for their control (green) [177].

Research conducted over the past years indicates that the perovskite is susceptible to moisture ingress [53,178-180], methylammonium iodide egress [181], photodegradation [182] and corrosion of metal electrodes by reaction with halides in the perovskite; however, there are many considerations which must be addressed. Exposure to H_2O and O_2 can dramatically affect the chemical stability of perovskite solar cells, together with the degradation of the perovskite layer, associated with a color change from dark brown to yellow **Figure 2.7(a)**, owing to hydrolysis of the perovskite, incurring a loss in photovoltaic performance **Figure 2.7(b)** [160,178].

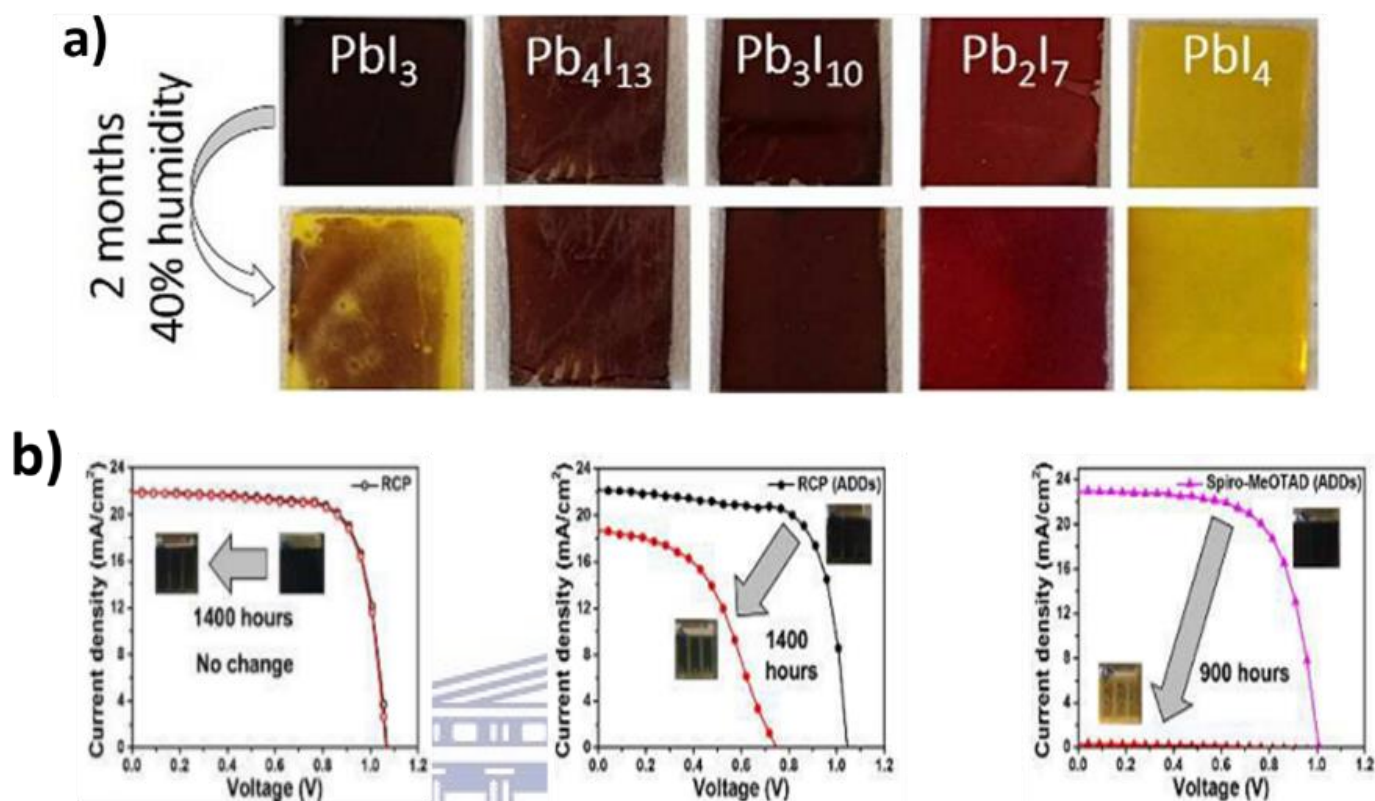


Figure 2.7: a) Perovskite films before and after exposure to humidity [183] and b) current-voltage scans over time showing loss of photovoltaic performance because of perovskite degradation [184].

The inherent toxicity of the lead halide perovskites poses another potential barrier to commercialization, relating to the toxicological issues of lead [177,185,186]. The desire for non-toxic, solution-processable solar cells has led researchers to consider alternatives to lead within the perovskite structure [187-189]. The most appropriate element to replace lead is tin (Sn). However, Sn^{2+} is less stable than Pb^{2+} , which causes significant stability problems for perovskites containing Sn [190]. Hao *et al.* reported perovskite solar cells incorporating Sn halides, with an efficiency of almost 6% for $CH_3NH_3Sn(I Br_2)$ perovskites [39]. Regarding the ecotoxicity of lead, conjecture still remains about its actual impact on the environment.

Several solutions have been proposed so far to improve the stability of perovskite solar cells under ambient conditions [53,178,191]. Amongst them are, the replacement of $MAPbI_3$ with a mixed-halide $MAPbI_{3-x}Br_x$ [53,192], the use of single-walled carbon nanotubes [178], carbon-based hole-transport layers and the introduction of poly(methyl) methacrylate (PMMA) [178] or Al_2O_3 [191] as hydrophobic buffer layers and the use of TiO_2 as a scaffold layer to reduce the O_2^- [193,194], the substitution of MA^+ with FA^+ [26,29,30], the inclusion of heterojunction contacts or an additional encapsulation layer to prevent moisture ingress [33,75,195] and/or a pinhole-free metal oxide layer to prevent metal-halide interaction [196]. Recent studies

show that perovskite solar cells are relatively stable up to 1000 h in accelerated degradation tests [33]. Graphene and graphene-related materials, known for their applications as protective layers are currently being investigated to protect perovskite solar cells from atmospheric degradation [197-199]. Agresti *et al.*, demonstrated an 18.2% efficiency cell that retained more than 88% of its efficiency after 16 h of prolonged sun exposure by employing a graphene-doped mesoporous TiO₂ as the electron-transport photoelectrode [198].

The degradation mechanisms of perovskites have been a topic under intense investigation [192-194]. At present, little is understood about the degradation mechanisms of perovskite photovoltaic devices. Previous research on MAPbI₃ perovskite films brought about the conclusion that the gas products of thermal degradation of this material were hydrogen iodide (HI) and methylamine (CH₃NH₂) [50,200]. However recent research revealed that the main gas products of degradation are ammonia (NH₃) and methyl iodide (CH₃I) [201,202]. Fully understanding the PSC degradation pathways is crucial to develop effective strategies to improve stability and thus achieve market standards.

Conclusion

Owing to its complex structure, it is challenging to attribute the perovskite device photovoltaic performance to any one of the different components that constitute the device. Based on the issues addressed in this review, there is an urgent need to assess the impact of each device component on the widespread application of perovskite solar technology. Advances of optoelectronic devices based on methylammonium lead halide perovskites heavily depends on understanding their photovoltaic hysteretic behaviour and environmental stability, whether it is marginal as in inorganic semiconductors or crucial like in organics. The realization of practical goals such as commercialization will be strongly determined by an understanding of the roles played by perovskite architecture, the effects of processing parameters and key materials employed in perovskite device layers and until a clear consensus on the environmental stability of perovskite solar cells is reached or a high-efficiency non-toxic alternative is found, the safe deployment of perovskite photovoltaic technology relies on adopting precautionary measures against contamination and potential poisoning at each stage of the device's lifecycle, from fabrication to disposal.

References

- [1] NREL http://www.nrel.gov/ncpv/images/efficiency_chart.jpg
- [2] H. J. Snaith, *J. Phys. Chem. Lett.*, 2013, 4, 3623-3630
- [3] M. A. Green, A. Ho-Baillie and H. J. Snaith, *Nat. Photon.*, 2014, 8, 506-514
- [4] P. Gao, M. Grätzel and M. K. Nazeeruddin, J. Maier and M. Grätzel, *Energy Environ. Sci.*, 2014, 7, 2448-2463
- [5] S. D. Stranks and H. J. Snaith, *Nat. Nanotechnol.*, 2015, 10, 391-402
- [6] O. Müller and R. Roy, *Cryst. Chem. Non-Metallic Mater.*, Springer-Verlag, Berlin, Heidelberg, 1974
- [7] R. J. Cava, B. Batlogg, G. P. Espinosa, A. P. Ramirez, J. J. Krajewski, W. F. Peck, L.W. Rupp, A. S. Cooper., *Nature*, 1989, 339, 291-293
- [8] A. Schilling, M. Cantoni, J. D. Guo, H. R. Ott, *Nature*, 1993, 363, 56-58
- [9] C. Kagan, D. Mitzi, C. Dimitrakopoulos, *Science*, 1999, 286, 945
- [10] D. B. Mitzi, *Prog. Inorg. Chem.*, 2007, 48,1
- [11] E. Mosconi, A. Amat, M. K. Nazeeruddin, M. Grätzel, F. D. Angelis, *J. Phys. Chem. C*, 2013, 117, 13902-13913
- [12] I. Grinberg, D. V. West, M. Torres, G. Gou, D. M. Stein, L. Wu, G. Chen, E. M. Gallo, A. R. Akbashev, P. K. Davies, J. E. Spanier and A. M. Rappe, *Nature*, 2013, 503, 509-512
- [13] Y. Guo, K.-I. Kakimoto and H. Ohsato, *Mater. Lett.*, 2005, 59, 241-244
- [14] Y. Maeno, H. Hashimoto, K. Yoshida, S. Nishizaki, T. Fujita, J. G. Bednorz and F. Lichtenberg, *Nature*, 1994, 372, 532-534
- [15] T. Ogasawara, T. Kimura, T. Ishikawa, M. Kuwata-Gonokami and Y. Tokura, *Phys. Rev. B.*, 2001, 63, 113105
- [16] A. Weidenkaff, R. Robert, M. Aguire, L. Bocher, T. Lippert, S. Canulescu, *Renew. Energy.*, 2008, 33, 342-347
- [17] V. Goldschmidt, Die Gesetze der Krystallochemie, Die Naturwissenschaften, 1926, 21, 477
- [18] H. D. Megaw, Crystal Structure of Barium Titanate, 1945, 155, 484-485
- [19] M. Johnsson and P. Lemmens. "Crystallography and Chemistry of Perovskites." In Handbook of Magnetism and Advanced Magnetic Materials. John Wiley & Sons, Ltd, 2007
- [20] I. Boriello, G. Cantele and D. Ninno, *Phys. Rev. B: Condens. Matter Mater. Phys.*, 2008, 77, 235214
- [21] A. Kojima, K. Teshima, Y. Shirai, T. Miyasaka, *J. Am. Chem. Soc.* 2009, 131, 6050
- [22] S. D. Stranks, G.E. Eperon, G. Grancini, C. Menelaou, M. J. P. Alcocer, T. Leijtens, L. M. Herz, A. Petrozza, H. J. Snaith, *Science*, 2013, 342, 341-344
- [23] G. Xing, N. Mathews, S. Sun, S. S. Lim, Y. M. Lam, M. Grätzel, S. Mhaisalkar, T.C. Sum, *Science*, 2013, 342, 344-347
- [24] C. Wehrenfennig, G.E. Eperon, M. B. Johnston, H. J. Snaith, L. M. Herz, *Adv. Mater.* 2014, 26, 1584-1589
- [25] H.-S. Kim and N.-G. Park, *J. Phys. Chem. Lett.*, 2014, 5, 2927-2934
- [26] N. J. Jeon, J. H. Noh, W. S. Yang, Y. C. Kim, S. Ryu, J. Seo, S. I. Seok, *Nature*, 2015, 517, 476-480
- [27] M. Kaltenbrunner, G. Adam, E. D. Głowacki, M. Drack, R. Schwödiauer, L. Leonat, D. H. Hazar, H. Groiss, M. C. Scharber, M. S. White, N. S. Sariciftci and S. Bauer, *Nat. Mater.*, 2015, 14, 1032-1039
- [28] J.-H. Im, I. Chung, S.-J. Kim, N.-G. Park, *Nanoscale Res. Lett.*, 2012, 7, 353-359
- [29] G. E. Eperon, S. D. Stranks, C. Menelaou, M.B. Johnston, L.M. Herz and H. J. Snaith, *Energy Environ. Sci.*, 2014, 7, 983-988
- [30] J.-W. Lee, D.-H. Kim, H.-S. Kim, S.-W. Seo, S. M. Cho, N.-G. Park, *Adv. Energy Mater.*, 2015, 5, 1501310

- [31] H. Choi, J. Jeong, H.-B. Kim, S. Kim, B. Walker, G.-H. Kim, J. Y. Kim, *Nano Energy*, 2014, 7, 80-85
- [32] S. Sun, D. Yuan, Y. Xu, A. Wang and Z. Deng, *ACS Nano*, 2016, 10, 3648-3657
- [33] A. Mei, X. Li, L. Liu, Z. Ku, T. Liu, Y. Rong, M. Xu, M. Hu, J. Chen, Y. Yang, M. Grätzel, H. Han, *Science*, 2014, 345, 295-298
- [34] M. Saliba, T. Matsui, K. Domanski, J.-Y. Seo, A. Ummadisingu, S. M. Zakeeruddin, J.-P. Correa-Baena, W. Tress, A. Abate, A. Hagfeldt, M. Grätzel, *Science*, 2016, 354, 206-209
- [35] C. Yi, J. Luo, S. Meloni, A. Boziki, N. Ashari-Astani, C. Grätzel, S. M. Zakeeruddin U. Rothlisberger and M. Grätzel, *Energy Environ. Sci.*, 2016, 9, 656-662
- [36] Z. Li, M. Yang, J.-S. Park, S.-H. Wei, J. J. Berry, K. Zhu, *Chem. Mater.*, 2016, 28, 284-292
- [37] M. Saliba, T. Matsui, J.-Y. Seo, K. Domanski, J.-P. Correa-Baena, M. K. Nazeeruddin, S. M. Zakeeruddin, W. Tress, A. Abate, A. Hagfeldt, M. Grätzel, *Energy Environ. Sci.*, 2016, 9, 1989-1997
- [38] P. Umari, E. Mosconi, F. D. Angelis, *Sci Rep.*, 2014, 4, 4467
- [39] F. Hao, C. C. Stoumpos, D. H. Cao, R. P. H. Chang and M. G. Kanatzidis, *Nat. Photon.*, 2014, 8, 489-494
- [40] A. Kojima, M. Ikegama, K. Teshima and T. Miyasaka, *Chem. Lett.*, 2012, 41, 397-399
- [41] X. Li, D. Bi, C. Yi, J. D. Décoppet, J. Luo, S. M. Zakeeruddin, A. Hagfeldt, M. Grätzel, *Science*, 2016, 353, 58-62
- [42] C. C. Stoumpos, C. D. Malliakas, M. G. Kanatzidis, *Inorg. Chem.*, 2013, 52, 9019-9038
- [43] C. Bernal and K. Yang, *J. Phys. Chem. C.*, 2014, 118, 24383-24388
- [44] A. S. Ionkin, W. J. Marshall, B. M. Fish, *Organometallics*, 2006, 25, 4170-4178
- [45] S. P. R. D. Madan, *Mod. Inorg. Chem.*, 1987, 207-212
- [46] E. L. Unger, A. R. Bowring, C. J. Tassone, V. L. Pool, A. Gold-Parker, R. Cheacharoen, K. H. Stone, E. T. Hoke, M. F. Toney, M. D. McGehee, *Chem. Mater.*, 2014, 26, 7158-7165
- [47] M. I. Dar, N. Arora, P. Gao, S. Ahmad, M. Grätzel and M. K. Nazeeruddin, *Nano Lett.*, 2014, 14, 6991-6996
- [48] X. Li, M. I. Dar, C. Yi, J. Luo, M. Tschumi, S. M. Zakeeruddin, M. K. Nazeeruddin, H. Han and M. Grätzel, *Nat. Chem.*, 2015, 7, 703-711
- [49] W. Nie, H. Tsai, R. Asadpour, J.-C. Blancon, A. J. Neukirch, G. Gupta, J.J. Crochet, M. Chhowalla, S. Tretiak, M.A. Alam, H.-L. Wang and A. D. Mohite, *Science*, 2015, 347, 522-525
- [50] D. P. Nenon, J. A. Christians, L. M. Wheeler, J. L. Blackburn, E. M. Sanehira, B. Dou, M. L. Olsen, K. Zhu, J. J. Berry and J. M. Luther, *Energy Environ. Sci.*, 2016, 9, 2072-2082
- [51] M. Saliba, S. Orlandi, T. Matsui, S. Aghazada, M. Cavazzini, J.-P. Correa-Baena, P. Gao, R. Scopelliti, E. Mosconi, K.-H. Dahmen, F. De Angelis, A. Abate, A. Hagfeldt, G. Pozzi, M. Grätzel and M. K. Nazeeruddin, *Nat. Energy.*, 2016, 1, 15017
- [52] D. P. McMeekin, G. Sadoughi, W. Rehman, G. E. Eperon, M. Saliba, M. T. Hörantner, A.-A. Haghighirad, N. Sakai, L. Korte, B. Rech, M. B. Johnston, L. M. Herz and H. J. Snaith, *Science*, 2016, 351, 151-155
- [53] J. H. Noh, S. H. Im, J. H. Heo, T. N. Mandal and S.I Seok, *Nano Lett.*, 2013, 13, 1764-1769
- [54] S. A. Kulkarni, T. Baikie, P. P. Boix, N. Yantara, N. Mathews and S. G. Mhaisalkar, *J. Mater. Chem. A.*, 2014, 2, 9221-9225
- [55] S. M. H. Qaid, M. S. Al Sobaie, M. A. M. Khan, I. M. Bedja, F. H. Alharbi, M. K. Nazeeruddin and A. S. Aldwayyan, *Mater. Lett.*, 2016, 164, 498-501
- [56] J.-H. Im, J. Chung, S.-J. Kim and N.-G. Park, *Nanoscale Res. Lett.*, 2012, 7, 353
- [57] M. Era, S. Morimoto, T. Tsutsui and S. Saito, *Appl. Phys. Lett.*, 1994, 65, 676

- [58] D. B. Mitzi, Synthesis, structure, and properties of organic-inorganic perovskites and related materials. In: *Progress in Inorganic Chemistry*. Karlin K. D. ed John Wiley & Sons. New York, 1999, 48: 1-121
- [59] Z. Cheng and J. Lin, *CrystEngComm*, 2010, 12, 2646-2662
- [60] X.-H. Zhu, N. Mercier, P. Frère, P. Blanchard, J. Roncali, C. Pasquier and A. Riou, *Inorg. Chem.*, 2003, 42, 5330-5339
- [61] N. K. McKinnon, D. C. Reeves, and M. H. Akabas, *J. Gen. Physiol.*, 2011, 138, 453-466
- [62] H. S. Kim, S. H. Im, N.-G. Park, *J. Phys. Chem. C*, 2014, 118, 5615-5625
- [63] B. E. Cohen, C. Labarca, N. Davidson, H. A. Lester, *J. Gen. Physiol.*, 1992, 138, 453
- [64] J.-H. Im, C.-R. Lee, J.-W. Lee, S.-W. Park and N.-G. Park, *Nanoscale*, 2011, 3, 4088-4093
- [65] H. S. Kim, C. R. Lee, J. H. Im, K. B. Lee, T. Moehl, A. Machioro, S. J. Moon, R. Humphry-Baker, J. H. Yum, J. E. Moser, M. Grätzel, N. G. Park, *Sci. Rep.* 2012, 2, 591
- [66] M. M. Lee, J. Teuscher, T. Miyasaka, T. N. Murakami, H. J. Snaith, *Science*, 2012, 338, 643-647
- [67] L. Etgar, P. Gao, Z. Xue, Q. Peng, A. K. Chandiran, B. Liu, M. K. Nazeeruddin and M. Grätzel, *J. Am. Chem. Soc.*, 2012, 134, 17396-17399
- [68] H. Zhou, Q. Chen, G. Li, S. Luo, T.-B. Song, H.-S. Duan, Z. Hong, J. You, Y. Liu and Y. Yang, *Science*, 2014, 345, 542-546
- [69] F. Giordano, A. Abate, J.-P. C. Baena, M. Saliba, T. Matsui, S. H. Im, S. M. Zakeeruddin, M. K. Nazeeruddin, A. Hagfeldt, M. Grätzel, *Nat. Commun.* 2016, 7, 10379
- [70] W. S. Yang, J. H. Noh, Nam J. Jeon, Y. C. Kim, S. Ryu, J. Seo and S. I. Seok, *Science*, 2015, 348, 1234-1237
- [71] W.-J. Yin, J.-H. Yang, J. Kang, Y. Yan, S.-H. Wei, *J. Mater. Chem. A.*, 2015, 3, 8926
- [72] M. Shiriyama, H. Kadowaki, T. Miyadera, T. Sugita, M. Tamakoshi, M. Kato, T. Fujiseki, D. Murata, S. Hara, T. N. Murakami, S. Fujimoto, M. Chikamatsu, H. Fujiwara, *Phys. Rev. Appl.*, 2016, 5, 1
- [73] P. Löper, M. Stuckelberger, B. Niesen, J. Werner, M. Filipič, S.-J. Moon, J.-H. Yum, M. Topič, S. De Wol, C. Ballif, *J. Phys. Chem. Lett.*, 2014, 6, 66
- [74] A. M. Askar and K. Shankar, *J. Nanosci. Nanotechnol.*, 2016, 16, 5890
- [75] T. Leijtens, G. E. Eperon, N. K. Noel, S. N. Habisreutinger, A. Petrozza and H. J. Snaith, *Adv. Energy Mater.*, 2015, 5, 1500963
- [76] T. Leijtens, S. D. Stranks, G. E. Eperon, R. Lindblad, E. M. J. Johansson, I. J. McPherson, H. Rensmo, J. M. Ball, M. M. Lee and H. J. Snaith, *ACS Nano*, 2014, 8, 7147-7155
- [77] J. M. Ball, M. M. Lee, A. Hey and H. J. Snaith, *Energy Environ. Sci.*, 2013, 6, 1739-1743
- [78] E. Edri, S. Kirmayer, D. Cahen, G. Hodes, *J. Phys. Chem. Lett.*, 2013, 4, 897-902
- [79] S. Ryu, J. H. Noh, N. J. Jeon, Y. C. Kim, W. S. Yang, J. Seo, S. I. Seok, *Energy Environ. Sci.*, 2014, 7, 2614
- [80] J. P. Correa Baena, L. Steier, W. Tress, M. Saliba, S. Neutzner, T. Matsui, F. Giordano, T. J. Jacobsson, A. R. S. Kandada, S. M. Zakeeruddin, A. Petrozza, A. Abate, M. K. Nazeeruddin, M. Grätzel, A. Hagfeldt, *Energy Environ. Sci.* 2015, 8, 2928-2934
- [81] G. Giorgi, J.-I. Fujisawa, H. Segawa and K. Yamashita, *J. Phys. Chem. Lett.*, 2013, 4, 4213-4216
- [82] W. A. Laban and L. Etgar, *Energy Environ. Sci.*, 2013, 6, 3249-3253
- [83] G. E. Eperon, V. M. Burlakov, P. Docampo, A. Goriely and H. J. Snaith, *Adv. Funct. Mater.*, 2014, 24, 151-157
- [84] D. Liu and T. L. Kelly, *Nat. Photonics*, 2014, 8, 133-138
- [85] G. Adam, M. Kaltenbrunner, E. D. Glowacki, D. H. Hazar, M. S. White, H. Heilbrunner, S. Tombe, P. Stadler, B. Ernecker, C. W. Klampfl, N. S. Sariciftci and M. C. Scharber, *Sol. Energy Mater. Sol. Cells*, 2016, 157, 318-325

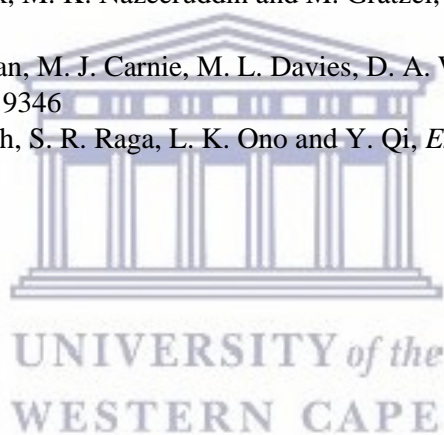
- [86] K. Hwang, Y.-S. Jung, Y.-J. Heo, F. H. Scholes, S. E. Watkins, J. Subbiah, D. J. Jones, D.-Y. Kim, D. Vak, *Adv. Mater.*, 2015, 27, 1241-1247
- [87] Z. Wei, H. Chen, K. Yan, S. Yang, *Angew. Chem.*, 2014, 53, 13239-13243
- [88] K.-W. Tsai, C.-C. Chueh, S. T. Williams, T.-C. Wen and A. K. Y. Jen, *J. Mater. Chem. A.*, 2015, 3, 9128-9132
- [89] Y. Zhang, X. Hu, L. Chen, Z. Huang, Q. Fu, Y. Liu, L. Zhang and Y. Chen, *Org. Electron.*, 2016, 30, 281-288
- [90] Q. Ma, S. Huang, X. Wen, M. A. Green, A. W. Y. Ho-Baillie, *Adv. Energy Mater.*, 2016, 6, 1502202
- [91] H. Wei, J. Xiao, Y. Yang, S. Lv, J. Shi, X. Xu, J. Dong, Y. Luo, D. Li, Q. Meng, *Carbon*, 2015, 93, 861-868
- [92] N. Pellet, P. Gao, G. Gregori, T.-Y. Yang, M. K. Nazeeruddin, J. Maier and M. Grätzel, *Angew. Chem. Int. Ed.*, 2014, 53, 3151-3157
- [93] S. Pang, H. Hu, J. Zhang, S. Lv, Y. Yu, F. Wei, T. Qin, H. Xu, Z. Liu and G. Cui, *Chem. Mater.*, 2014, 26, 1485-1491
- [94] J.-W. Lee, D.-J. Seol, A.-N. Cho, N.-G. Park, *Adv. Mater.*, 2014, 4991-4998
- [95] X. Li, W. Cao, W. Wang, B. Xu, S. Liu, H. Dai, S. Chen, K. Wang and X. W. Sun, *Nano Energy*, 2016, doi:10.1016/j.nanoen.2016.10.039
- [96] F. H. Isikgor, B. Li, H. Zhu, Q. Xu, *J. Mater. Chem. A.*, 2016, 4, 12543-1255
- [97] W. Zhang, M. Saliba, D. T. Moore, S. K. Pathak, M. T. Hörantner, T. Stergiopoulos, S. D. Stranks, G. E. Eperon, J. A. Alexander-Webber, A. Abate, A. Sadhanala, S. Yao, Y. Chen, R. H. Friend, L. A. Estroff, U. Wiesner, H. J. Snaith, *Nat. Commun.*, 2015, 6, 6142
- [98] C.-Y. Chang, C.-Y. Chu, Y.-C. Huang, C.-W. Huang, S.-Y. Chang, C.-A. Chen, C.-Y. Chao and W.-F. Su, *ACS Appl. Mater. Interfaces*, 2015, 7, 4955-4961
- [99] C. Sun, Q. Xue, Z. Hu, Z. Chen, F. Huang, H.-L. Yip and Y. Cao, *Small*, 2015, 11, 3344-3350
- [100] X. Song, W. Wang, P. Sun, W. Ma and Z.-K. Chen, *Appl. Phys. Lett.*, 2015, 106, 033901
- [101] T. Leitjens, B. Lauber, G. E. Eperon, S. D. Stranks, H. J. Snaith, *J. Phys. Chem. Lett.*, 2014, 5, 1096-1102
- [102] J. H. Heo, D. H. Song and S. H. Im, *Adv. Mater.*, 2014, 26, 8179-8183
- [103] J. Troughton, C. Charbonneau, M. J. Carnie, M. L. Davies, D. A. Worsley and T. M. Watson, *J. Mater. Chem. A.*, 2015, 3, 9123-9127
- [104] M. Saliba, K. W. Tan, H. Sai, D. T. Moore, T. Scott, W. Zhang, L. A. Estroff, U. Wiesner, and H. J. Snaith, *J. Phys. Chem. C.*, 2014, 118, 17171-17177
- [105] A. Dualeh, N. Tétreault, T. Moehl, P. Gao, M. K. Nazeeruddin and M. Grätzel, *Adv. Funct. Mater.*, 2014, 24, 3250-3258
- [106] D. Shen, X. Yu, X. Cai, M. Peng, Y. Ma, X. Su, L. Xiao, D. Zou, *J. Mater. Chem. A.*, 2014, 2, 20454-20461
- [107] J. Burschka, N. Pellet, S.-J. Moon, R. Humphry-Baker, P. Gao, M. K. Nazeeruddin and M. Grätzel, *Nature*, 2013, 499, 316-319
- [108] M. Lv, X. Dong, X. Fang, B. Lin, S. Zhang, J. Ding, N. Yuan, *RSC Adv.*, 2015, 5, 20521-20529
- [109] H. B. Kim, H. Choi, J. Jeong, S. Kim, B. Walker, S. Song and J. Y. Kim, *Nanoscale*, 2014, 6, 6679
- [110] N. J. Jeon, J. H. Noh, Y. C. Kim, W. S. Yang, S. Ryu and S. I. Seok, *Nat. Mater.*, 2014, 13, 897-903
- [111] N. K. Noel, S. N. Habisreutinger, B. Wenger, M. T. Klug, M. T. Hörantner, M. B. Johnston, D. T. Moore, and H. J. Snaith, *Energy Environ. Sci.*, 2016, doi: 10.1039/C6EE02373H
- [112] J.-H. Im, H.-S. Kim and N.-G. Park, *APL Mater.*, 2014, 2, 081510
- [113] Q. Chen, H. Zhou, Z. Hong, S. Luo, H.-S. Duan, H.-H. Wang, Y. Liu, G. Li and Y. Yang, *J. Am. Chem. Soc.*, 2014, 136, 622-625

- [114] M. Liu, M. B. Johnston, H. J. Snaith, *Nature*, 2013, 501, 395-398
- [115] C.-W. Chen, H.-W. Kang, S.-Y. Hsiao, P.-F. Yang, K.-M. Chiang and H.-W. Lin, *Adv. Mater.*, 2014, 26, 6647-6652
- [116] F. K. Aldibaja, L. Badia, E. Mas-Marza, R. S. Sanchez, E. M. Barea, I. Mora-Sero, *J. Mater. Chem. A.*, 2015, 3, 9194-9200
- [117] D. T. Moore, H. Sai, K. W. Tan, D. M. Smilgies, H. J. Snaith, U. Wiesner and L. A. Estroff, *J. Am. Chem. Soc.*, 2015, 137, 2350-2358
- [118] A. Abate, S. Paek, F. Giordano, J. P. Correa-Baena, M. Saliba, P. Gao, T. Matsui, J. Ko, S. M. Zakeeruddin, K. H. Dahmen, A. Hagfeldt, M. Grätzel and M. K. Nazeeruddin, *Energy Environ Sci.*, 2015, 8, 2946-2953
- [119] K.-C. Wang, J.-Y. Jeng, P.-S. Shen, Y.-C. Chang, E. W.-G. Diau, C.-H. Tsai, T.-Y. Chao, H.-C. Hsu, P.-Y. Lin, P. Chen, T.-F. Guo and T.-C. Wen, *Sci. Rep.*, 2014, 4, 4756
- [120] W. Chen, Y. Wu, J. Liu, C. Qin, X. Yang, A. Islam, Y.-B. Cheng and L. Han, *Energy Environ. Sci.*, 2015, 8, 629-640
- [121] Z. Song, S. C. Wathage, A. B. Phillips and M. J. Heben, *J. Photon. Energy.*, 2016, 6, 022001
- [122] J. You, Z. Hong, Y. M. Yang, Q. Chen, M. Cai, T.-B. Song, C.-C. Chen, S. Lu, Y. Liu, H. Zhou and Y. Yang, *ACS Nano*, 2014, 8, 1674-1680
- [123] J. T.-W. Wang, J. M. Ball, E. M. Barea, A. Abate, J. A. Alexander-Webber, J. Huang, M. Saliba, I. Mora-Sero, J. Bisquert, H. J. Snaith and R. J. Nicholas, *Nano Lett.*, 2014, 14, 724-730
- [124] D. Bi, S.-J. Moon, L. Häggman, G. Boschloo, L. Yang, E. M. J. Johansson, M. K. Nazeeruddin, M. Grätzel and A. Hagfeldt, *RSC Adv.*, 2013, 3, 18762
- [125] T. Todorov, T. Gershon, O. Gunawan, C. Sturdevant, S. Guha, *Appl. Phys. Chem. Phys.* 2015, 17, 1619
- [126] Y. M. Yang, Q. Chen, Y. Hsieh, T. Song, N. De Marco, H. Zhou, and Y. Yang, *ACS Nano*, 2015, 9, 7714
- [127] M. C. Wu, S.-H. Chan, M.-H. Jao and W. F. Su, *Sol. Energy Mater. Sol. Cells*, 2016, 157, 447-453
- [128] M. Lv, W. Lv, X. Fang, P. Sun, B. Lin, S. Zhang, X. Xu, J. Ding and N. Yuan, *RSC Adv.*, 2016, 6, 35044-35050
- [129] V. Roiati, E. Mosconi, A. Listorti, S. Colella, G. Gigli and F. De Angelis, *Nano Lett.*, 2014, 14, 2168-2174
- [130] P. Docampo, S. Guldin, U. Steiner and H. J. Snaith, *J. Phys. Chem. Lett.*, 2013, 4, 698-703
- [131] M. H. Kumar, N. Yantara, S. Dharani, M. Graetzel, S.G. Mhaisalkar, M. Graetzel, S. G. Mhaisalkar, and N. Mathews, *Chem. Commun.*, 2013, 49, 11089-11091
- [132] Y. Dkhissi, S. Meyer, D. Chen, H. C. Weerasinghe, L. Spiccia, L. Spiccia, R. A. Caruso, *ChemSusChem*, 2016, 9, 687-695
- [133] J. Yang, B. D. Siempelkamp, E. Mosconi, F. De Angelis, T. L. Kelly, *Chem. Mater.*, 2015, 27, 4229-4236
- [134] Q. Hu, J. Wu, C. Jiang, T. Liu, X. Que, R. Zhu, Q. Gong, *ACS Nano*, 2014, 8, 10161-10167
- [135] F. Di Giacomo, S. Razza, F. Matteocci, A. D'Epifanio, S. Licocchia, T. M. Brown, A. Di Carlo, *J. Power Sources*, 2014, 251, 152-156
- [136] M. Zhang, M. Q. Lyu, H. Yu, J. H. Yun, Q. Wang and L. Z. Wang, *Chem-Eur. J.* 2015, 21, 434-439
- [137] T. Matsui, I. Petrikyte, T. Malinauskas, K. Domanski, M. Daskeviciene, W. Tress, J.-P. Correa-Baena, A. Abate, A. Hagfeldt, M. Grätzel, M. K. Nazeeruddin, M. Saliba, *ChemSusChem*, 2016, 9, 2567-2571
- [138] J. H. Heo, S. H. Im, J. H. Noh, T. N. Mandal, C.-S. Lim, J. A. Chang, Y. H. Lee, H.-J. Kim, A. Sarkar, M. K. Nazeeruddin, M. Grätzel, S. I. Seok, *Nat. Photon.*, 2013, 7, 486-491
- [139] W. Li, H. Dong, L. Wang, N. Li, X. Guo, J. Li, Y. Qiu, *J. Mater. Chem. A.*, 2014, 2, 13587-13592

- [140] J. Liu, Y. Wu, C. Qin, X. Yang, T. Yasuda, A. Islam, K. Zhang, W. Peng, W. Chen, L. Han, *Energy Environ. Sci.*, 2014, 7, 2963-2967
- [141] J. Xu, A. Buin, A. H. Ip, W. Li, O. Voznyy, R. Comin, M. Yuan, S. Jeon, Z. Ning, J. J. McDowell, P. Kanjanaboos, J. P. Sun, X. Lan, L. N. Quan, D. H. Kim, I. G. Hill, P. Maksymovych, E. H. Sargent, *Nat. Commun.*, 2015, 6, 7081
- [142] R. Li, X. Xiang, X. Tong, J. Zou, Q. Li, *Adv. Mater.*, 2015, 27, 3831-3835
- [143] Z. Li, S. A. Kulkarni, P. P. Boix, E. Shi, A. Cao, K. Fu, S. K. Batabyal, J. Zhang, Q. Xiong, L. H. Wong, N. Mathews, S. G. Mhaisalkar, *ACS Nano*, 2014, 8, 6797-6804
- [144] P. Docampo, J. M. Ball, M. Darwich, G. E. Eperon and H. J. Snaith, *Nat. Commun.*, 2013, 4, 2761
- [145] J. Y. Jeng, K. C. Chen, T. Y. Chiang, P.-Y. Lin, T. D. Tsai, Y. C. Chang, T. F. Guo, P. Chen, T. C. Wen and Y. J. Hsu, *Adv. Mater.*, 2014, 26, 4107-4113
- [146] J. H. Heo, H. J. Han, D. Kim, T. K. Ahn, S. H. Im, *Energy Environ. Sci.*, 2015, 8, 1602-1608
- [147] J. H. Heo, D. H. Song, H. J. Han, S. Y. Kim, Jun Ho Kim, Dasom Kim, H. W. Shin, T. K. Ahn, C. Wolf, T.-W. Lee and S. H. Im, *Adv. Mater.*, 2015, 27, 3424-3430
- [148] J. H. Kim, P. W. Liang, S. T. Williams, N. Cho, C. C. Chueh, M. S. Glaz, D. S. Ginger, A. K. Jen, *Adv. Mater.*, 2015, 27, 695-701
- [149] L. Zheng, Y. H. Chung, Y. Ma, L. Zhang, L. Xiao, Z. Chen, S. Wang, B. Qu, Q. Gong, *Chem. Commun.*, 2014, 50, 11196-11199
- [150] H. J. Snaith, A. Abate, J. M. Ball, G. E. Eperon, T. Leijtens, N. K. Noel, S. D. Stranks, J. T.-W. Wang, K. Wojciechowski, W. Zhang, *J. Phys. Chem. Lett.*, 2014, 5, 1511-1515
- [151] E. L. Unger, E. T. Hoke, C. D. Bailie, W. H. Nguyen, A. R. Bowring, T. Heumüller, M. G. Christoforo, M. D. McGehee, *Energy Environ. Sci.*, 2014, 7, 3690-3698
- [152] J. A. del Cueto, C.A. Deline, D. S. Albin, S. R. Rummel and A. Anderberg, *Proc. SPIE 7412, Reliab. Photovolt. Cells, Modul. Components, Syst. II*, 2009, 741204
- [153] M. Herman, M. Jankovec and M. Topic, *Int. J. Photoenergy*, 2012, 2012, 151452
- [154] S. Ryu, J. Seo, S. S. Shin, Y. C. Kim, N. J. Jeon, J. H. Noh and S. I. Seok, *J. Mater. Chem. A*, 2015, 3, 3271-3275
- [155] R. S. Sanchez, V. Gonzalez-Pedro, J.-W. Lee, N.-G. Park, Y. S. Kang, I. Mora-Sero, and J. Bisquert, *J. Phys. Chem. Lett.*, 2014, 5, 2357-2363
- [156] H. M. Tian, J. Y. Zhang, X. Y. Wang, T. Yu and Z. G. Zou, *Measurement*, 2011, 44, 1551-1555
- [157] E. J. Juarez-Perez, R. S. Sanchez, L. Badia, G. Garcia-Belmonte, Y.S. Kang, I. Mora-Sero and J. Bisquert, *J. Phys. Chem. Lett.*, 2014, 5, 2390-2394
- [158] H.-S. Kim, I. Mora-Sero, V. Gonzalez-Pedro, F. Fabregat-Santiago, E. J. Juarez-Perez, N.-G. Park, J. Bisquert, *Nat. Commun.*, 2013, 4, 2242
- [159] A. Dualeh, T. Moehl, N. Tétreault, J. Teuscher, P. Gao, M. K. Nazeeruddin and M. Grätzel, *ACS Nano*, 2014, 8, 362-373
- [160] J. M. Frost, K. T. Butler, F. Brivio, C. H. Hendon, M. van Schilfgaarde, A. Walsh, *Nano Lett.*, 2014, 14, 2584-2590
- [161] F. Brivio, A. Walker, A. Walsh, *APL Mater.*, 2013, 1, 042111
- [162] D. L. Staebler and C. R. Wronski, *J. Appl. Phys.*, 1980, 51, 3262
- [163] J. Mizusaki, K. Arai and K. Fueki, *Solid State Ionics*, 1983, 11, 203-211
- [164] K. Yamada, K. Isobe, E. Tsuyama, T. Okuda and Y. Furukawa, *Solid State Ionics*, 1995, 79, 152-157
- [165] Y. Shao, Z. Xiao, C. Bi, Y. Yuan, J. Huang, *Nat. Commun*, 2014, 5, 5784
- [166] W. Tress, J. P. Correa Baena, M. Saliba, A. Abate, M. Graetzel, *Adv. Energy Mater.*, 2016, 6, doi:10.1002/aenm.201600396
- [167] T.-Y. Yang, G. Gregori, N. Pellet, M. Grätzel, J. Maier, *Angew. Chem. Int. Ed.*, 2015, 54, 7905

- [168] C. Eames, J. M. Frost, P.R.F. Barnes, B.C. O'Regan, A. Walsh, M.S. Islam, *Nat. Commun.*, 2015, 6, 7497
- [169] W. Tress, N. Marinova, T. Moehl, S. M. Zakeeruddin, M. K. Nazeeruddin and M. Grätzel, *Energy Environ. Sci.*, 2015, 8, 995-1004
- [170] C. Li, S. Tscheuschner, F. Paulus, P. E. Hopkinson, J. Kießling, A. Köhler, Y. Vaynzof, S. Huettner, *Adv. Mater.*, 2016, 28, 2446-2454
- [171] S. Meloni, T. Moehl, W. Tress, M. Franckevičius, M. Saliba, Y. H. Lee, P. Gao, M. K. Nazeeruddin, S. M. Zakeeruddin, U. Rothlisberger and M. Graetzel, *Nat Commun.*, 2016, 7, doi:10.1038/ncomms10334
- [172] Y. Shao, Y. Fang, T. Li, Q. Wang, Q. Dong, Y. Deng, Y. Yuan, H. Wei, M. Wang, A. Gruverman, J. Shield and J. Huang, *Energy Environ. Sci.*, 2016, 9, 1752-1759
- [173] S. van Reenen, M. Kemerink and H. J. Snaith, *J. Phys. Chem. Lett.*, 2015, 6, 3808-3814
- [174] H.-S. Duan, H. Zhou, Q. Chen, P. Sun, S. Luo, T.-B. Song, B. Bob and Y. Yang, *Phys. Chem. Chem. Phys.*, 2015, 17, 112
- [175] I. M. Hermes, S. A. Bretschneider, V. W. Bergmann, D. Li, A. Klasen, J. Mars, W. Tremel, F. Laquai, H.-J. Butt, M. Mezger, R. Berger, B. J. Rodriguez, S. A. L. Weber, *J. Phys. Chem. C*, 2016, 120, 5724-5731
- [176] A. M. A. Leguy, J. M. Frost, A. P. McMahon, V. G. Sakai, W. Kockelmann, C. Law, X. Li, F. Foglia, A. Walsh, B. C. O'Regan, J. Nelson, J. T. Cabral, P. R. F. Barnes, *Nat Commun.*, 2015, 6, 7124
- [177] A. Babayigit, A. Ethirajan, M. Muller and B. Conings, *Nat. Mater.*, 2016, 15, 247-251
- [178] S. N. Habisreutinger, T. Leitjens, G. E. Eperon, S. D. Stranks, R. J. Nicholas, H. J. Snaith, *Nano Lett.*, 2014, 14, 5561-5568
- [179] A. M. A. Leguy, Y. Hu, M. Campoy-Quiles, M. I. Alonso, O. J. Weber, P. Azarhoosh, M. van Schilfgaarde, M. T. Weller, T. Bein, J. Nelson, P. Docampo, P. R. F. Barnes, *Chem. Mater.*, 2015, 27, 3397-3407
- [180] J. A. Christians, P. A. Miranda Herrera and P. V. Kamat, *J. Am. Chem. Soc.*, 2015, 137, 1530-1538
- [181] B. Conings, J. Drijkoningen, N. Gauquelin, A. Babayigit, J. D'Haen, L. D'Olieslaeger, A. Ethirajan, J. Verbeeck, J. Manca, E. Mosconi, F. De Angelis, H.-G. Boyen, *Adv. Energy Mater.*, 2015, 5, 1500477
- [182] W. Nie, J. Blancon, A. J. Neukirch, K. Appavoo, H. Tsai, M. Chhowalla, M.A. Alam, C. Katan, J. Even, S. Tretiak, J. J. Crochet, G. Gupta and A. D. Mohite, *Nat Commun.*, 2016, 7, 11574
- [183] D. H. Cao, C. C. Stoumpos, O. K. Farha, J. T. Hupp and Mercouri G. Kanatzidis, *J. Am. Chem. Soc.*, 2015, 137, 7843
- [184] G.-W. Kim, G. Kang, J. Lim, G.-Y. Lee, H. I. Kim, L. Pyeon, J. Lee, T. Park, *Energy Environ. Sci.*, 2016, 9, 2326-2333
- [185] P. Singh, P. J. S. Rana, P. Dhingra and P. Kar, *J. Mater. Chem. C.*, 2016, 4, 3101-3105
- [186] A. Babayigit, D. D. Thanh, A. Ethirajan, J. Manca, M. Muller, H.-G. Boyen and B. Conings, *Sci. Rep.*, 2016, 6, 18721
- [187] S. J. Lee, S. S. Shin, Y. C. Kim, D. Kim, T. K. Ahn, J. H. Noh, J. Seo and S. I. Seok, *J. Am. Chem. Soc.*, 2016, 138, 3974-3977
- [188] M. H. Kumar, S. Dharani, W. L. Leong, P. P. Boix, R. R. Prabhakar, T. Baikie, C. Shi, H. Ding, R. Ramesh, M. Asta, M. Graetzel, S. G. Mhaisalkar and N. Mathews, *Adv. Mater.*, 2014, 26, 7122-7127
- [189] L. Serrano-Luján, N. Espinosa, T. T. Larsen-Olsen, A. Urbina and F. C. Krebs, *Adv. Energy Mater.*, 2015, 5, 1501119
- [190] N. K. Noel, S. D. Stranks, A. Abate, C. Wehrenfennig, S. Guarnera, A.-A. Haghighirad, A. Sadhanala, G. E. Eperon, M. B. Johnston, A. Petrozza, L. M. Herz and H. J. Snaith, *Energy Environ. Sci.*, 2014, 7, 3061-3068

- [191] X. Dong, X. Fang, M. Lv, B. Lin, S. Zhang, J. Ding, N. Yuan, *J. Mater. Chem. A*, 2015, 3, 5360-5367
- [192] R. K. Misra, S. Aharon, B. Li, D. Mogiöyansky, I. Visoly-Fisher, L. Etgar and E. A. Katz, *J. Phys. Chem. Lett.*, 2015, 6, 326-330
- [193] N. Aristidou, I. Sanchez-Molina, T. Chotchuangchutchaval, M. Brown, L. Martinez, T. Rath and S. A. Haque, *Angew. Chem. Int. Ed.*, 2015, 54, 8208-8212
- [194] D. Bryant, N. Aristidou, S. Pont, I. Sanchez-Molina, T. Chotchuangchutchaval, S. Wheeler, J. R. Durrant and S. A. Haque, *Energy Environ. Sci.*, 2016, 9, 1655-1660
- [195] X. Li, M. Tschumi, H. Han, S. S. Babkair, R. A. Alzubaydi, A. A. Ansari, S. S. Habib, M. K. Nazeeruddin, S. M. Zakeeruddin and M. Grätzel, *Energy Technol.* 2015, 3, 551
- [196] J. You, L. Meng, T.-B. Song, T.-F. Guo, Y. Yang, W.-H. Chang, Z. Hong, H. Chen, H. Zhou, Q. Chen, Y. Liu, N. De Marco, Y. Yang, *Nat. Nanotechnol.* 2015, 11, 75
- [197] M. Acik and S. B. Darling, *J. Mater. Chem. A.*, 2016, 4, 6185-6235
- [198] A. Agresti, S. Pescetelli, B. Taheri, A. E. Del Rio Castillo, L. Cinà, F. Bonaccorso and A. Di Carlo, *ChemSusChem*, 2016, 9, 2609-2619
- [199] S. Feng, Y. Yang, M. Li, J. Wang, Z. Cheng, J. Li, G. Li, G. Yin, F. Song, Z. Wang, J. Li, X. Gao, *ACS Appl. Mater. Interfaces.*, 2016, 8, 14503-14512
- [200] A. Dualeh, P. Gao, S. I. Seok, M. K. Nazeeruddin and M. Grätzel, *Chem. Mater.*, 2014, 26, 6160-6164
- [201] A. E. Williams, P. J. Holliman, M. J. Carnie, M. L. Davies, D. A. Worsley and T. M. Watson, *J. Mater. Chem. A.*, 2014, 2, 19338-19346
- [202] E. J. Juarez-Perez, Z. Hawash, S. R. Raga, L. K. Ono and Y. Qi, *Energy Environ. Sci.*, 2016, doi:10.1039/C6EE2016J



CHAPTER 3

OPTICAL AND ELECTRONIC PROPERTIES OF MIXED HALIDE (X = I, Cl, Br) METHYLAMMONIUM LEAD PEROVSKITE SOLAR CELLS.

Abstract

The fabrication and opto-electronic characterization of solution-processed planar heterojunction perovskite solar cells based on methylammonium (MA) lead halide derivatives, $\text{MAPbI}_{3-x}\text{Y}_x$ (Y = I, Cl, Br) is presented in this work. Three different perovskite photovoltaic devices; MAPbI_3 , $\text{MAPbI}_{3-x}\text{Cl}_x$ and $\text{MAPbI}_{3-x}\text{Br}_x$ were made independently by varying the halide ratios. The effect of the halide ratios (I, Cl, Br) on perovskite optoelectronic properties and their influence on photovoltaic performance was investigated by means of a systematic analysis of devices fabricated via a one-step deposition technique. The perovskite film morphology, temperature-dependent photoluminescence properties, hysteresis behaviour in current-voltage characteristics and the photovoltaic performance as a function of chemical composition were investigated using microscopic, spectroscopic and photovoltaic techniques. Power conversion efficiency was found to be dependent on $\text{MAPbI}_{3-x}\text{Y}_x$ (Y = I, Cl, Br) perovskite film morphology. By controlling perovskite precursor composition and stoichiometry, highest power conversion efficiencies of 9.2, 12.5 and 5.4 % were obtained for MAPbI_3 , $\text{MAPbI}_{3-x}\text{Cl}_x$ and $\text{MAPbI}_{3-x}\text{Br}_x$ devices respectively. Additionally, the physical parameters of the mixed halide perovskites such as the exciton binding energy, exciton-phonon interaction and bandgap were determined via temperature-dependent photoluminescence spectroscopy. Exciton binding and optical phonon energies of $\text{MAPbI}_{3-x}\text{Y}_x$ (Y = I, Cl, Br) were found to be in the ranges of 49-68 meV and 29-32 meV respectively. The solution-processed MA lead halide derivatives form highly crystalline materials with chemical versatility allowing the tuning of their optical and electronic properties depending on the nature and the ratio of the halides employed.

3.1 Introduction

There is worldwide focus on the development of PV technologies based on organic-inorganic solar cells which offer the prospect of significantly improved performance and/or low cost manufacture, thus helping to accelerate commercial exploitation and large scale deployment. Photovoltaic cells based on organic-inorganic hybrid materials have shown rapid improvements over the past decade comparing favourably with existing inorganic semiconductor technology on energy, scalability and cost associated with manufacture. Hybrid organic-inorganic perovskite materials are currently among the most competitive candidates for semiconductor materials and have experienced the fastest increase in reported efficiencies ever obtained for any PV technology [1-12].

The development of metal halide perovskite solar cells was triggered by the reports of Kojima *et al.*, [1] and Im *et al.* [2] on liquid electrolyte-based on liquid electrolyte-based dye-sensitized solar cells. Perovskite solar cell devices have shown tremendous advancement in energy conversion efficiency starting from 3.8% in 2009 [1] to reaching 21% to date [6]. The certificated PCE of 22.1% is higher than the certificated record PCE of polycrystalline silicon solar cells [4], indicating a competitive advantage. The reason for the rapid increase in PCE of PSCs is that perovskite materials possess most of the properties required to be excellent absorbers: sharp absorption edge as a function of composition, superior light absorption coefficient ($\sim 10^5 \text{ cm}^{-1}$), long electron and hole diffusion lengths to suppress the recombination of photoexcited charges, high carrier mobility and apparent tolerance of defects [7-12].

Pioneering work suggested that perovskite films exhibit composition-/structure-dependent properties, which can be accessed by various processing approaches [13]. Noh *et al.* [7], showed that chemical modification of MAPbI₃ by substituting I with Br can tune the bandgaps to range between 1.5 eV and 2.3 eV by incorporating MAPbBr₃. By substituting iodine with chlorine and bromine, wavelength-tunable emissions from ultra-violet to near infrared were achieved. [14]. Controlling perovskite morphology and composition has been found critical to developing high-performance perovskite solar cells [15-17]. Many methods have been developed for the deposition of perovskite films including the solution-process, dual-source vapour deposition and vapour-assisted solution process (VASP). To date, the perovskite layer in these efficient solar cells has generally been fabricated by either vapour deposition or a two-step sequential deposition process. Solution processed devices have the potential to ultimately yield lower production costs. Several successful perovskite device architectures have been reported. Hybrid perovskites have demonstrated high power conversion efficiencies both in thin film device architectures [18-22] and meso-structured device architectures comprising meso-scopic alumina [23-25], zirconia [26] and titania [27-29]. It is yet unclear whether perovskite-absorber devices of different architecture types perform equally well or if certain architectures will prove beneficial over others [4, 28].

Despite the remarkable progress in record cell efficiency, many fundamental questions remain that need to be addressed at both the material and device levels. The fundamental questions are centred on perovskite material/device development and characterization, perovskite materials' structural and electronic properties, perovskite composition control with band gap tuning, device operation principles (e.g. hysteresis), the nature of photogenerated excitations (*i.e.* charge-carrier-phonon interactions) and long term stability. Advances in methylammonium lead halide photovoltaic devices depend on understanding the nature of photogenerated excitations (*i.e.* charge carrier-phonon interactions) and the role of excitons. However, a consensus on charge carrier-phonon interactions and their temperature-dependence is still lacking.

Motivated by the high PCE achieved with perovskites and with the desire to find a better simplified processing alternative to both mesoporous TiO_2 and Al_2O_3 scaffolds and vapour-deposition approaches reported previously, and aiming at fabricating stable, bandgap tunable high efficiency and cost-effective solid-state solar cells, we investigated the use of solution-processed planar heterojunction perovskite solar cells by a systematic study of mixed halide composition in methylammonium lead iodide based perovskite solar cells.

In this work, three different perovskite compositions; MAPbI_3 , $\text{MAPbI}_{3-x}\text{Cl}_x$ and $\text{MAPbI}_{3-x}\text{Br}_x$, were made independently by varying the halide ratio. We found a correlation between photovoltaic device performance and perovskite thin film morphology. Power conversion efficiencies in $\text{MAPbI}_{3-x}\text{Y}_x$ ($\text{Y} = \text{I}, \text{Cl}, \text{Br}$) were found to vary over a wide range indicating that small changes in perovskite precursor composition can have a significant effect on device performance. The lowest efficiencies were found for mixed-halide perovskites with bromide content and the highest were found for highly crystalline mixed-halide perovskites with chloride content. The physical parameters of the $\text{MAPbI}_{3-x}\text{Y}_x$ ($\text{Y} = \text{I}, \text{Cl}, \text{Br}$) perovskites such as the exciton binding energy, exciton-phonon interaction and bandgap were elucidated via temperature-dependent photoluminescence spectroscopy. The exciton binding energy (E_B) of $\text{MAPbI}_{3-x}\text{Y}_x$ ($\text{Y} = \text{Cl}, \text{Br}, \text{I}$), which greatly impacts the efficiency of exciton dissociation and charge transfer, was found to be 68.3 ± 4.7 , 49.7 ± 6.2 and 58.3 ± 4.0 meV for MAPbI_3 , $\text{MAPbI}_{3-x}\text{Cl}_x$ and $\text{MAPbI}_{3-x}\text{Br}_x$, respectively.

3.2 Experimental

3.2.1 Materials

Chemicals and solvents were used as received from commercial suppliers, if not stated otherwise. Pre-patterned indium doped tin oxide (ITO) coated glass (15 ohm/cm^2), PbI_2 (99.9%, Sigma Aldrich), PbCl_2 (99.9%, Sigma Aldrich), dimethylformamide (DMF, anhydrous, Sigma Aldrich), poly(3,4-ethylenedioxythiophene) polystyrene sulfonate (PEDOT:PSS) Clevios PH 1000 and Clevios PVP (Al 4083), Zonyl[®]FS-300 fluorosurfactant (40% in H_2O , Fluka), dimethyl sulfoxide (DMSO, AnalR, VWR Chemicals), [6,6]-phenyl-C₆₁-butyric acid methyl ester (PCBM; SolenneBV), chlorobenzene (GPR, VWR Chemicals) chloroform (AnalR, VWR Chemicals), chloroform (AnalR, VWR Chemicals) and isopropanol (AnalR, Fisher Chemicals), methylamine (in absolute ethanol, 33 wt%), hydrobromic acid (HBr) (aqueous, 48 wt%) (Sigma Aldrich), diethyl ether, hydroiodic acid (aqueous, 57 wt %), ethanol (absolute) and methylammonium chloride ($\text{CH}_3\text{NH}_3\text{Cl}/\text{MACl}$) (VWR, Riedel de Haën and MERCK), respectively were used. Organic halide salts, methylammonium iodide ($\text{CH}_3\text{NH}_3\text{I}/\text{MAI}$) and methylammonium bromide ($\text{CH}_3\text{NH}_3\text{Br}/\text{MABr}$) were synthesized according to reported literature procedures [3]. The chemical structures of the materials used in the perovskite solar cells are shown in **Figure 3.1**.

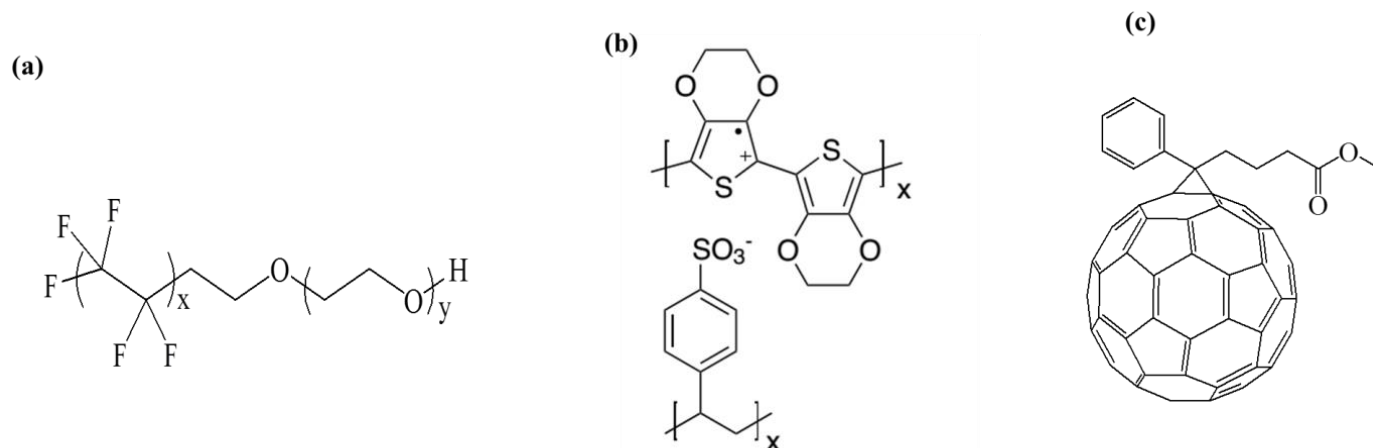


Figure 3.1: Chemical structures of materials used in the fabrication of $\text{MAPbI}_{3-x}\text{Y}_x$ ($\text{Y} = \text{I}, \text{Cl}, \text{Br}$) perovskite solar cells, a) Zonyl, b) PEDOT:PSS and c) PCBM.

3.2.2 Perovskite precursor solutions

A variety of precursor compositions were explored to observe the role of precursor chemistry in the photovoltaic performance of the MAPbI_3 , $\text{MAPbI}_{3-x}\text{Cl}_x$ and $\text{MAPbI}_{3-x}\text{Br}_x$ perovskite solar cells. Systematic analysis was undertaken using precursor solutions with varying ratios of methylammonium iodide (MAI), methylammonium chloride (MACl) and methylammonium bromide (MABr). This range of initial precursor stoichiometries was designed to contrast pure triiodide and mixed halide (iodide-chloride and iodide-bromide) derived films while elucidating the role Cl plays. The precursor solutions exhibiting the best photovoltaic performances were employed for further study and prepared as follows:

Precursor mixed halide solutions were prepared in DMF by overnight stirring at room temperature. The precursor mixed halide solutions with molar ratios were: MAPbI_3 (1 PbI_2 :2MAI) (222 mg/mL), $\text{MAPbI}_{3-x}\text{Cl}_x$ (1 PbI_2 :1MAI:1MACl) (638 mg/mL) and $\text{MAPbI}_{3-x}\text{Br}_x$ (1 PbI_2 :1MAI:0.2MABr) (598 mg/mL). The solutions were then filtered with a 0.45 μm PTFE filter. The final stoichiometry of the perovskites in terms of either iodide/chloride or iodide/bromide content was not evaluated. The denoted stoichiometry of compositional perovskites employed in this work was defined according to the stoichiometry of the precursors. The absence of Cl in $\text{MAPbI}_{3-x}\text{Cl}_x$ films was confirmed by EDX hence the term $\text{MAPbI}_{3-x}\text{Cl}_x$ refers only to the method of synthesis and not the outcome. The exact composition of perovskites originating from mixed halide precursor solutions is an ongoing subject of debate.

3.2.3 Device Fabrication

Planar heterojunction perovskite solar cells with a layer configuration of ITO/PEDOT:PSS/Perovskite/PCBM/Al were prepared in a fully solution-based process. The glass /ITO

substrates were first cleaned with acetone, and isopropanol successively in an ultrasonic bath, then PEDOT:PSS is spin coated at 1000 rpm for 1 min and annealed first at 120°C for 10 min and rinsed with isopropanol and then annealed for another 10 min at 120°C, then the perovskite precursor solution, $\text{MAPbI}_{3-x}\text{Y}_x$ ($\text{Y} = \text{I}, \text{Cl}, \text{Br}$) is deposited by spin coating at 1800 rpm for 20 s and 2000 rpm for 5 s. PCBM solution (20 mg/mL in 1:1 ratio of chlorobenzene and chloroform) was spin coated at 1500 rpm for 30 s on top of the perovskite film. Finally, 110 nm of aluminium cathode was thermally evaporated in a vacuum chamber on top of the PCBM layer. The fabrication procedure resulted in a 130-150 nm thick PEDOT:PSS layer, 380-420 nm thick perovskite absorber and a 50-80 nm thick PCBM layer. In the fabrication of the three different devices (i.e. MAPbI_3 , $\text{MAPbI}_{3-x}\text{Cl}_x$ and $\text{MAPbI}_{3-x}\text{Br}_x$) all other experimental parameters were held constant and only the PEDOT:PSS was changed. MAPbI_3 and $\text{MAPbI}_{3-x}\text{Br}_x$ perovskite solar cells were fabricated on low conductivity PEDOT:PSS, Clevis PVP Al 4083 (0.7% Zonyl) whereas $\text{MAPbI}_{3-x}\text{Cl}_x$ was fabricated on high conductivity PEDOT:PSS, Clevis PH 1000 (5% DMSO, 0.7% Zonyl) according to a previously reported procedure [30]. The perovskite crystal structure and device configuration are shown in **Figure 3.2**.

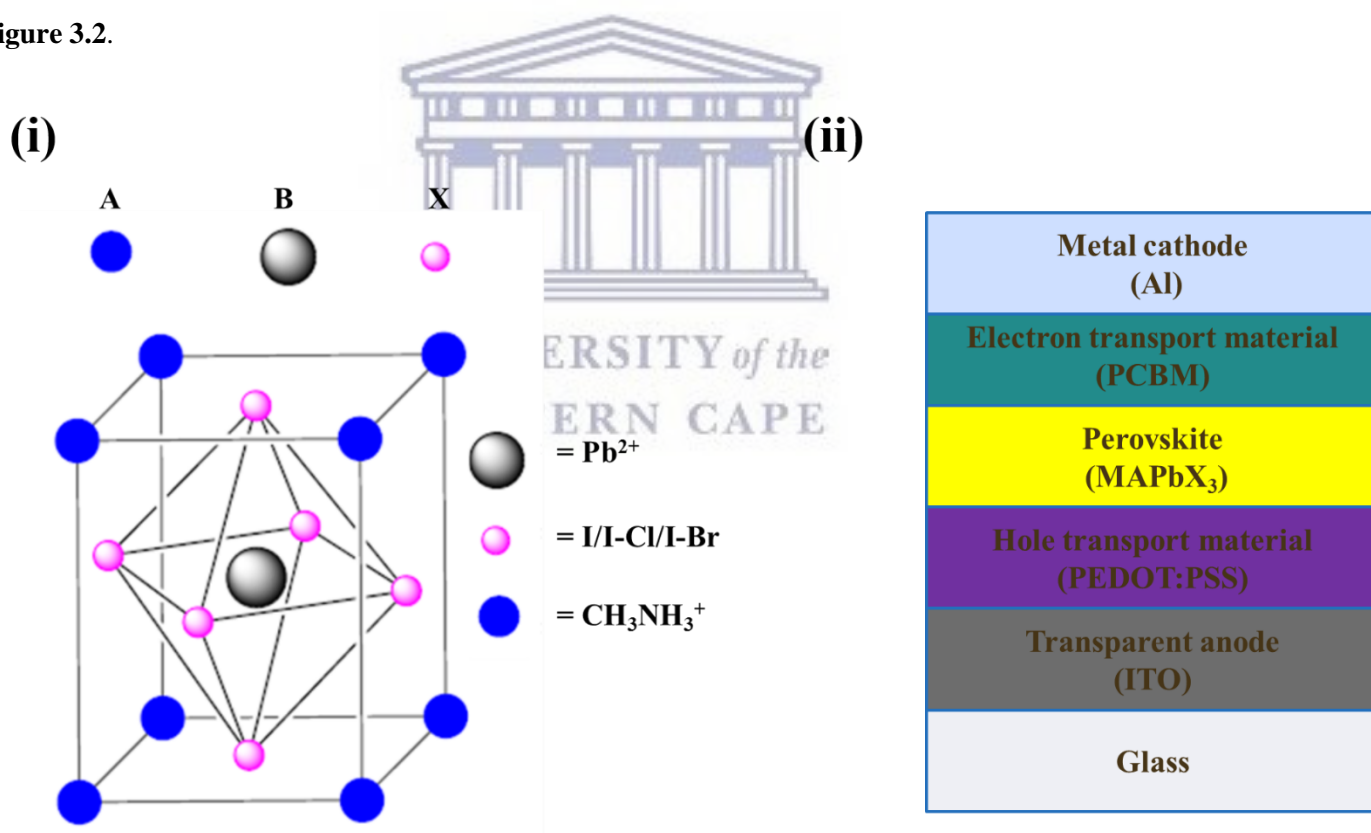


Figure 3.2: Crystal structure of the perovskite absorber adopting the ABX_3 form, where A is methylammonium, B is Pb and X is I (i) and a schematic of the device layer structure (ii).

Figure 3.2 illustrates the device architecture used in this study where ITO, PEDOT:PSS, perovskite, PCBM and Al are incorporated as electrode (anode), the hole transport material, photoactive layer, electron transport material and the electrode (cathode) respectively.

3.2.4 Perovskite film and device characterization

Perovskite film morphology investigations were performed using Atomic Force Microscopy (AFM) Dimension 3100 system (Digital instruments Santa Barbara CA) operating in tapping mode. Surface scanning electron microscopy (SEM) measurements and energy dispersive X-ray spectroscopy (EDX) were made using a ZEISS 1540XB CrossBeam Scanning microscope equipped with a focused ion-beam (FIB) unit and an EDX-unit. Perovskite thin films for UV-VIS optical absorption and photoluminescence measurements studies were prepared by spin coating on clean glass substrate from 50% diluted solution of the precursor solution at 4000 rpm. UV-VIS absorption spectra of perovskite films were recorded using a double beam UV-VIS spectrometer (Perkin Elmer 1050) equipped with an integrating sphere. Microscopic images of films were taken by using Nikon Eclipse LV100ND. A Bruker Dektak XT profilometer was used to measure layer thicknesses. Photoluminescence spectra of various devices were measured using a Shamrock SR-303i monochromator and an Andor iDus Si-CCD. Samples were excited at 473 nm (5 mW) using a solid-state laser or a supercontinuum light source (NKT EXB6) connected to a VIS-NIR SuperK Select Box. A set of long-pass filters was used to avoid any distortion of the recorded spectra by the laser light.

The finished solar cells with an active area of $\sim 0.17 \text{ cm}^2$ as defined by the overlapping area of Al and the patterned ITO substrate were tested on a LOT-QD solar simulator (LS0821). The radiation intensity was adjusted using a reference silicon diode to 100 mW/cm^2 . The power conversion efficiency of the prepared solar cells was determined as follows: The illuminated area of the solar cell was defined using a shadow mask (0.13 cm^2). In a first step the current-voltage curve was recorded with a Keithley 2400 source-measurement unit under illumination (solar simulator). The voltage was increased slowly (20 mV/s) and the current-voltage curve was determined close to steady state-conditions. To check for hysteresis a reverse voltage scan was performed decreasing the voltage by 20 mV/s . In a second step the short circuit current was recorded (steady state value) with a Keithley 2400.

External quantum efficiencies (EQEs) were recorded by using a lock-in amplifier (SR830, Stanford Research Systems) and a Jaissle 1002 potentiostat functioning as a preamplifier. The potentiostat operated in the 2-electrode configuration is a high performance current amplifier with a variable gain ranging from 10 to 10^8 V/A . In addition, the potentiostat allows measuring the EQE-spectra at different applied voltages. The devices were illuminated by monochromatic light from a xenon lamp passing through a monochromator (Oriol Cornerstone) with typical intensities in the range of 10 to $100 \mu\text{W}$. A filter wheel

holding long-pass filters and a mechanical chopper was mounted between the Xenon lamp and the monochromator. Chopping frequencies in the range of 10–200 Hz were used. A calibrated silicon diode (Hamamatsu S2281) was used as a reference. A halogen lamp (Philips 50 W, 12 V) provided a variable white light bias to the solar cells while the EQE was measured. The short circuit current calculated using the EQE-data allowed the determination of the spectral mismatch factor (MM) of our solar simulator. Values > 0.95 were found for the investigated devices. This mismatch factor was used to correct the maximum power point measurement.

3.3 Results and discussion

3.3.1 Thin perovskite film morphology

Because the optoelectronic properties of perovskite films are closely related to film quality, deposition of uniform pinhole free films is crucial for fabricating high performance perovskite solar cells, it is thus necessary to investigate perovskite film formation by solution processing [31].

Figure 3.3 shows the diascopic optical microscopy images of the perovskite films deposited on glass and Glass/ITO/PEDOT:PSS substrates. Perovskite films on glass substrates show non-uniform, discontinuous thin films whereas uniform and continuous pinhole-free films are observed on Glass/ITO/PEDOT:PSS substrates.

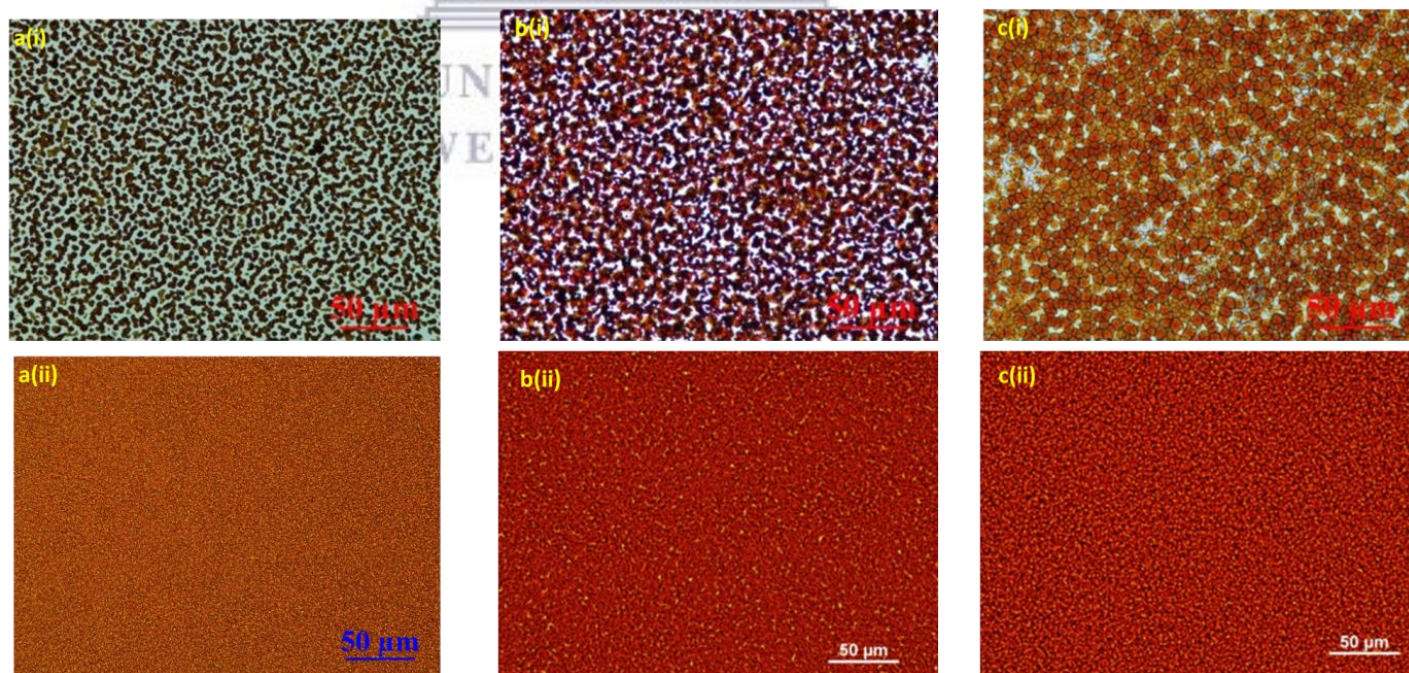


Figure 3.3: Diascopic illumination optical microscopy images on (a) Glass/ITO of (i) MAPbI_3 , (ii) $\text{MAPbI}_{3-x}\text{Cl}_x$ and (iii) $\text{MAPbI}_{3-x}\text{Br}_x$ and on (b) Glass/ITO/ PEDOT.PSS.

Perovskites film morphology was further examined by scanning electron microscopy (SEM) and atomic force microscopy (AFM). Variations in perovskite crystal size and grain boundaries were observed in perovskite films as shown in **Figure 3.4** in the SEM (**Figures 3.4a-c (i)**) and the corresponding AFM images (**Figures 3.4a-c (ii)**).



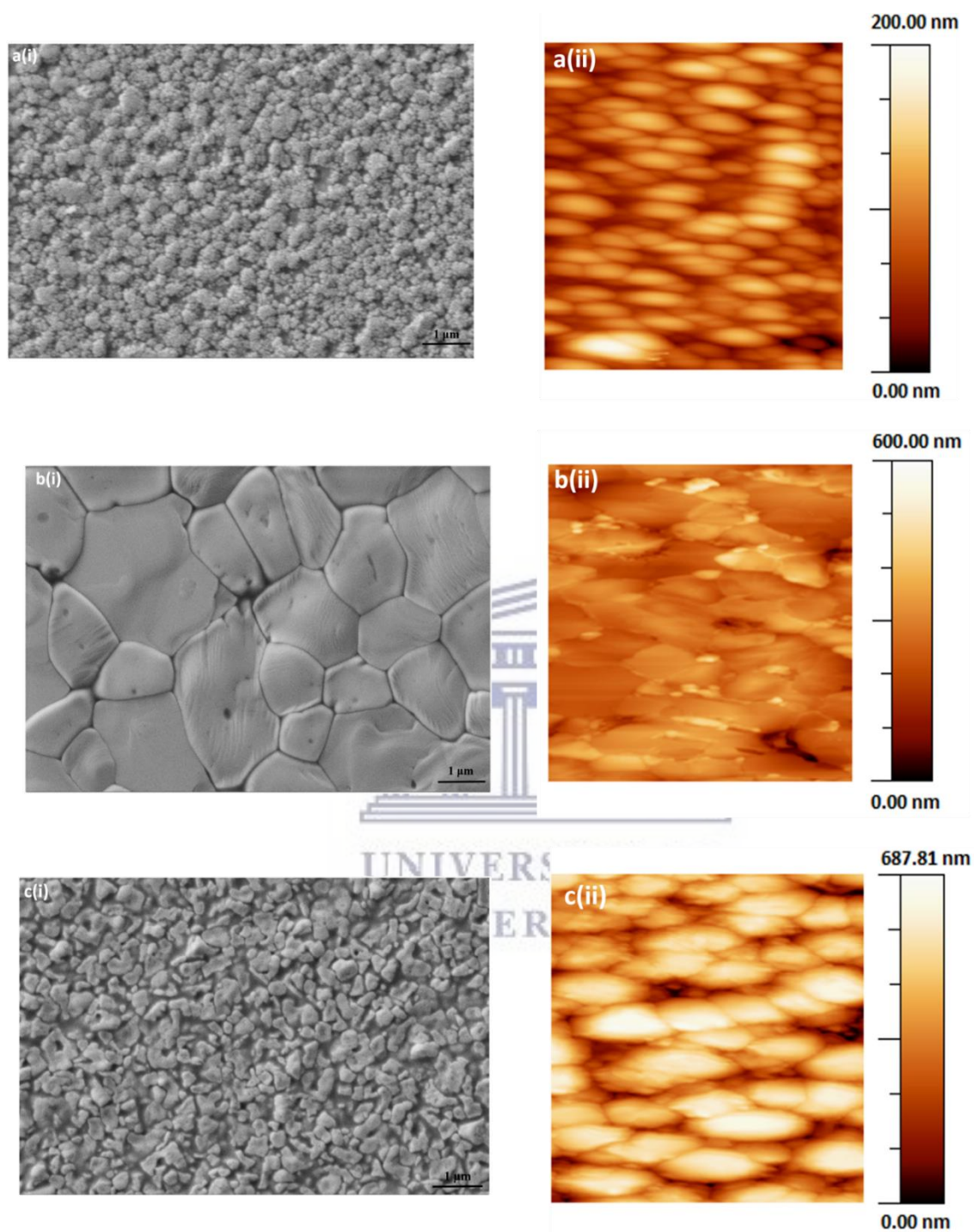


Figure 3.4: Microscopic characterization of perovskite films. Scanning electron microscopy images (i) on Glass/ITO/ PEDOT.PSS of (a) MAPbI_3 , (b) $\text{MAPbI}_{3-x}\text{Cl}_x$ and (c) $\text{MAPbI}_{3-x}\text{Br}_x$ and their respective atomic force microscopy images (ii).

The SEM and AFM images reveal tightly packed crystallites of several micrometres in size in the case of $\text{PbMAI}_{3-x}\text{Cl}_x$ (**Figure 3.4b (i)**) whereas PbMAI_3 (**Figure 3.4a (i)**) and $\text{PbMAI}_{3-x}\text{Br}_x$ (**Figure 3.4c (i)**) show

smaller crystallites. SEM images of the $\text{PbMAI}_{3-x}\text{Cl}_x$ (**Figure 3.4b (i)**) perovskite film reveals large crystal grain sizes of several micrometres with minimal grain boundaries, whereas as PbMAI_3 (**Figure 3.4a (i)**) and $\text{PbMAI}_{3-x}\text{Br}_x$ (**Figure 3.4c (i)**) show a large number of smaller of several nanometres crystallites with many grain boundaries. These differences might be due to slower crystallization in $\text{PbMAI}_{3-x}\text{Cl}_x$ perovskite film formation compared to PbMAI_3 and $\text{PbMAI}_{3-x}\text{Br}_x$ [32]. These results are direct evidence that perovskite morphology is dependent on perovskite composition. AFM images (**Figures 3.4a-c (ii)**) of the same perovskite films deposited on PEDOT:PSS films show perovskite crystallites consistent with the SEM images.

The exact effect of Cl in terms of modifying the crystallinity of the perovskite morphology is not known [33]. To confirm the presence and content of chlorine within the $\text{MAPbI}_{3-x}\text{Cl}_x$ films, energy dispersive X-ray spectroscopy (EDX) measurements were conducted, **Figure 3.5**.

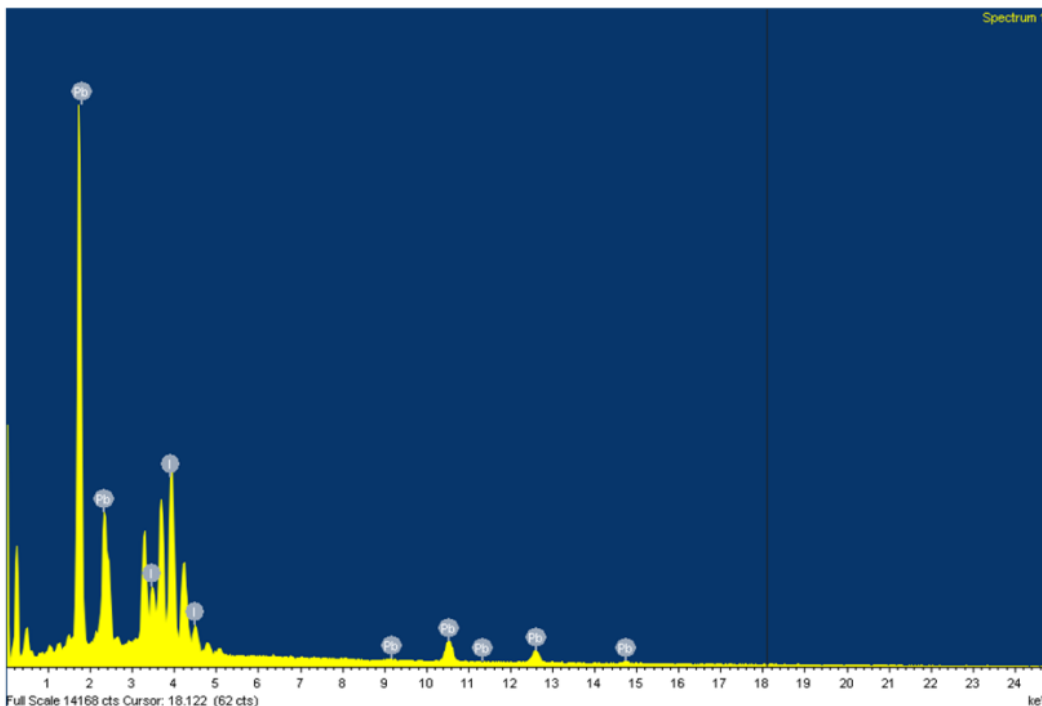


Figure 3.5: EDX spectra of thin film of perovskite ($\text{MAPbI}_{3-x}\text{Cl}_x$) on glass substrate coated with high conductivity PEDOT:PSS (PH1000) containing 5% v/v (DMSO).

Figure 3.5 indicates that the Cl content in the perovskite film is below the detection limit of EDX and the morphological evolution may be attributable to slow crystallization induced by the replacement of Cl^- with I^- during perovskite formation as stated above.

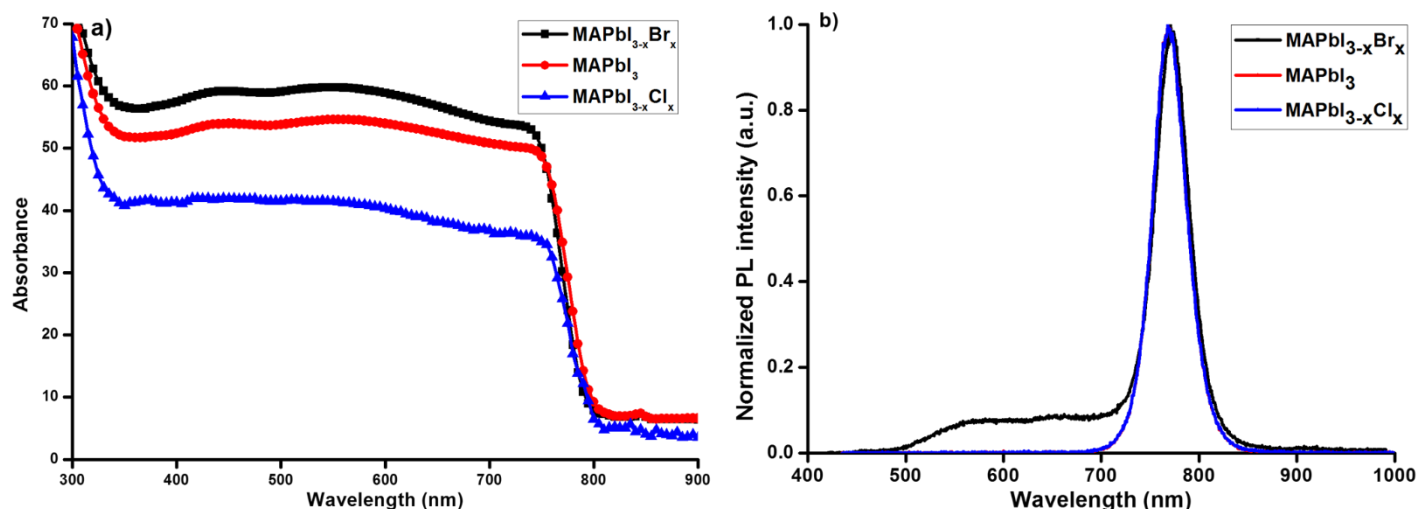


Figure 3.6: Absorbance (a) and photoluminescence (b) spectra of $\text{MAPbI}_{3-x}\text{Y}_x$ ($\text{Y} = \text{I}, \text{Cl}, \text{Br}$) perovskite films on glass.

Figure 3.6 shows the room temperature absorbance (**Figure 3.6a**) and photoluminescence spectra (**Figure 3.6b**) of $\text{MAPbI}_{3-x}\text{Y}_x$ ($\text{Y} = \text{Cl}, \text{Br}, \text{I}$). With x being small in $\text{MAPbI}_{3-x}\text{Cl}_x$ (small amount of Cl from EDS, **Figure 3.5**) and $\text{MAPbI}_{3-x}\text{Br}_x$ ($x = 0.2$), the absorption onset for all 3 systems is ~ 800 nm which is consistent with previously reported data on thin films of solution-processed mixed halide perovskites [34-36]. Substitution of iodine with chlorine or bromine atoms is expected to increase the band gap of perovskites [37]. In our case, the observed PL peak position is still close to that of MAPbI_3 , [38], consistent with the low chlorine or bromine content in the films. The similarity of the observed trends in **Figure 3.6** suggests that the ratio of intercalated halide ions is like that of the dissolved ions in the precursor solutions.

Because the electrical buffer layers, PEDOT:PSS as hole transport layer and PCBM as electron transport layer, free carriers can be extracted and dissociate excitons into free charges, we measure charge generation of the PSCs by photoluminescence spectroscopy. A significant quenching effect was observed from the photoluminescence data in **Figure 3.7**, when the perovskite layer establishes contact with either the PEDOT:PSS or PCBM layer.

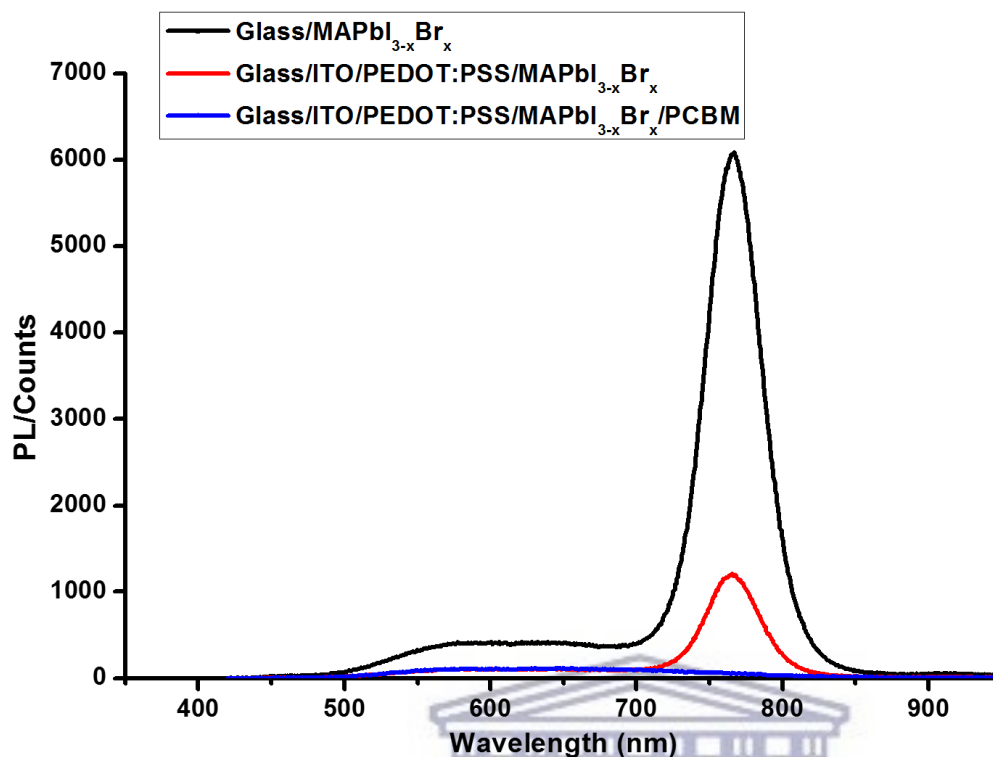


Figure 3.7: Photoluminescence quenching in perovskite samples.

Charge separation is possible at both the PEDOT:PSS and PCBM interfaces as evidenced by the significant quenching in the glass/ITO/PEDOT:PSS/perovskite and evidenced by complete quenching in the glass/ITO/PEDOT:PSS/perovskite/PCBM film with carrier generation at the perovskite/ PEDOT:PSS interface less than the perovskite/PCBM interface.

3.3.2 Temperature-dependent photoluminescence spectroscopy

Charge-carrier-phonon interactions of $\text{MAPbI}_{3-x}\text{Y}_x$ ($\text{Y} = \text{Cl}, \text{Br}, \text{I}$) which greatly impacts the efficiency of exciton dissociation and charge transfer, were elucidated via temperature-dependent photoluminescence (PL) spectroscopy. Temperature-dependent PL measurements from 77 to 293 K of perovskite samples on glass substrates were carried out and the data are summarized in **Figure 3.8**. $\text{MAPbI}_{3-x}\text{Y}_x$ ($\text{Y} = \text{Cl}, \text{Br}, \text{I}$) perovskite systems in **Figure 3.8**, show a decrease in emitted photoluminescence intensity with increasing temperature, which is attributed to temperature-activated exciton dissociation [9,39,40]. All three materials show continuous shifts of photoluminescence peak towards higher energy with increasing temperature. The shifts in peak energy at various temperatures are associated with phase transitions commonly found in lead halide perovskites [41-43]. Significant peak broadening with increasing temperature is also observed in **Figure 3.8** with MAPbI_3 (**Figure 3.8a**) and $\text{MAPbI}_{3-x}\text{Cl}_x$ (**Figure 3.8b**) showing similar results, with the

effect being more pronounced in the $\text{MAPbI}_{3-x}\text{Br}_x$ film (**Figure 3.8c**). The broadening of the peaks intensifies at higher temperatures because of stronger exciton-phonon interaction [39, 44].

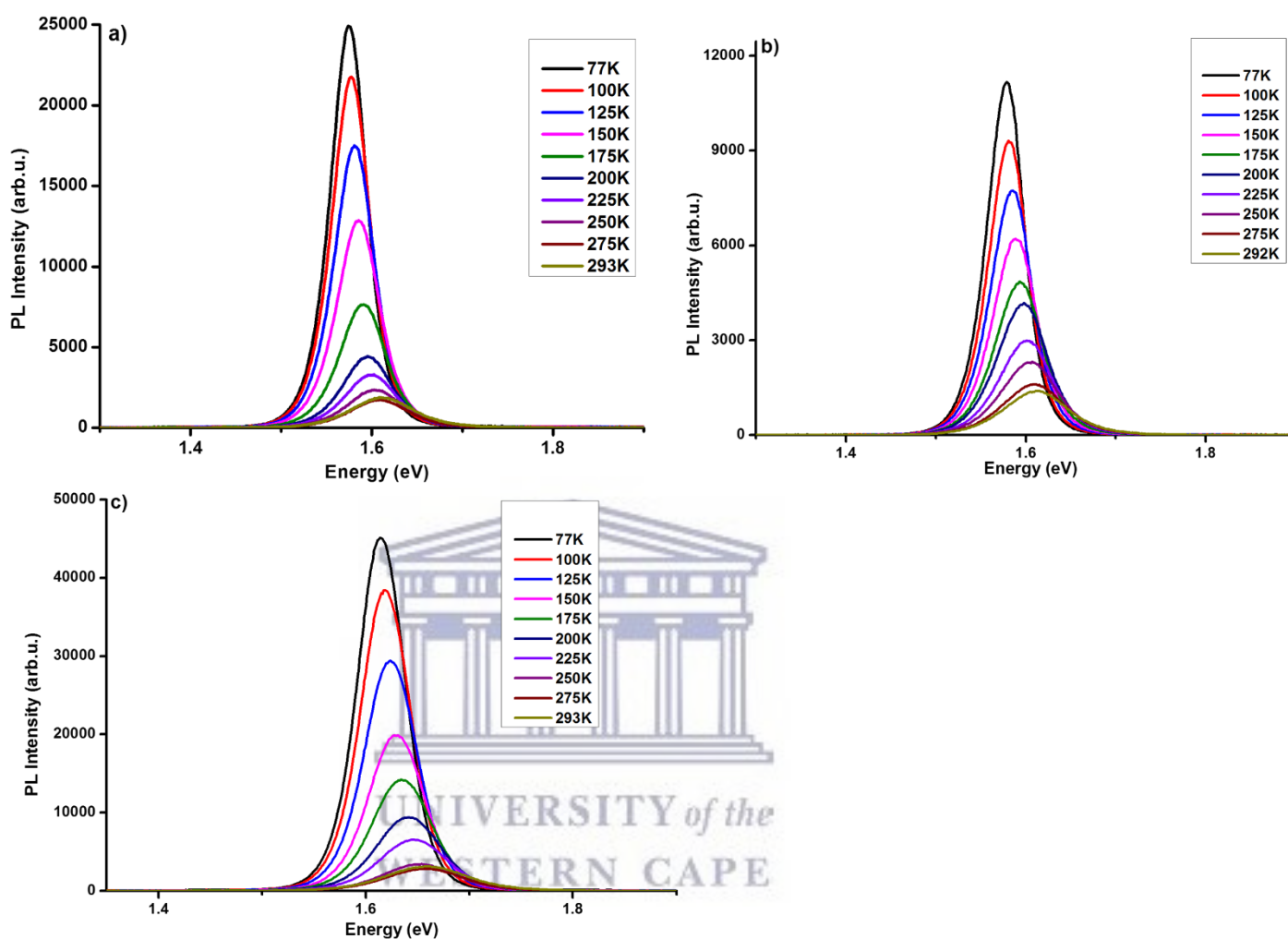


Figure 3.8: Temperature-dependent photoluminescence spectra from 77 K to 293 K of (a) MAPbI_3 (b) $\text{MAPbI}_{3-x}\text{Cl}_x$ (c) and $\text{MAPbI}_{3-x}\text{Br}_x$.

Several groups have reported multi-peak emission behaviour in methylammonium lead halide at temperatures below 150 K [40,45- 49]. The origin of this multi-peak behaviour is not fully understood. Such behaviour was not observed in our $\text{MAPbI}_{3-x}\text{Y}_x$ ($\text{Y} = \text{Cl}, \text{Br}, \text{I}$) perovskites as shown in **Figure 3.8**.

Analysis of temperature-dependent photoluminescence data in **Figure 3.8** was used to assess the linewidth parameters of $\text{MAPbI}_{3-x}\text{Y}_x$ ($\text{Y} = \text{Cl}, \text{Br}, \text{I}$) perovskites, and extracted fitting parameters are shown in **Figure 3.9 (i-iii)**.

As shown in **Figure 3.9 a-c (i)**, the peak energy changes almost linearly with temperature. Bandgap energies of 1.56, 1.56 and 1.6 eV were extracted for MAPbI₃, MAPbI_{3-x}Cl_x and MAPbI_{3-x}Br_x respectively in good agreement with previous and current reports [3, 50, 51].

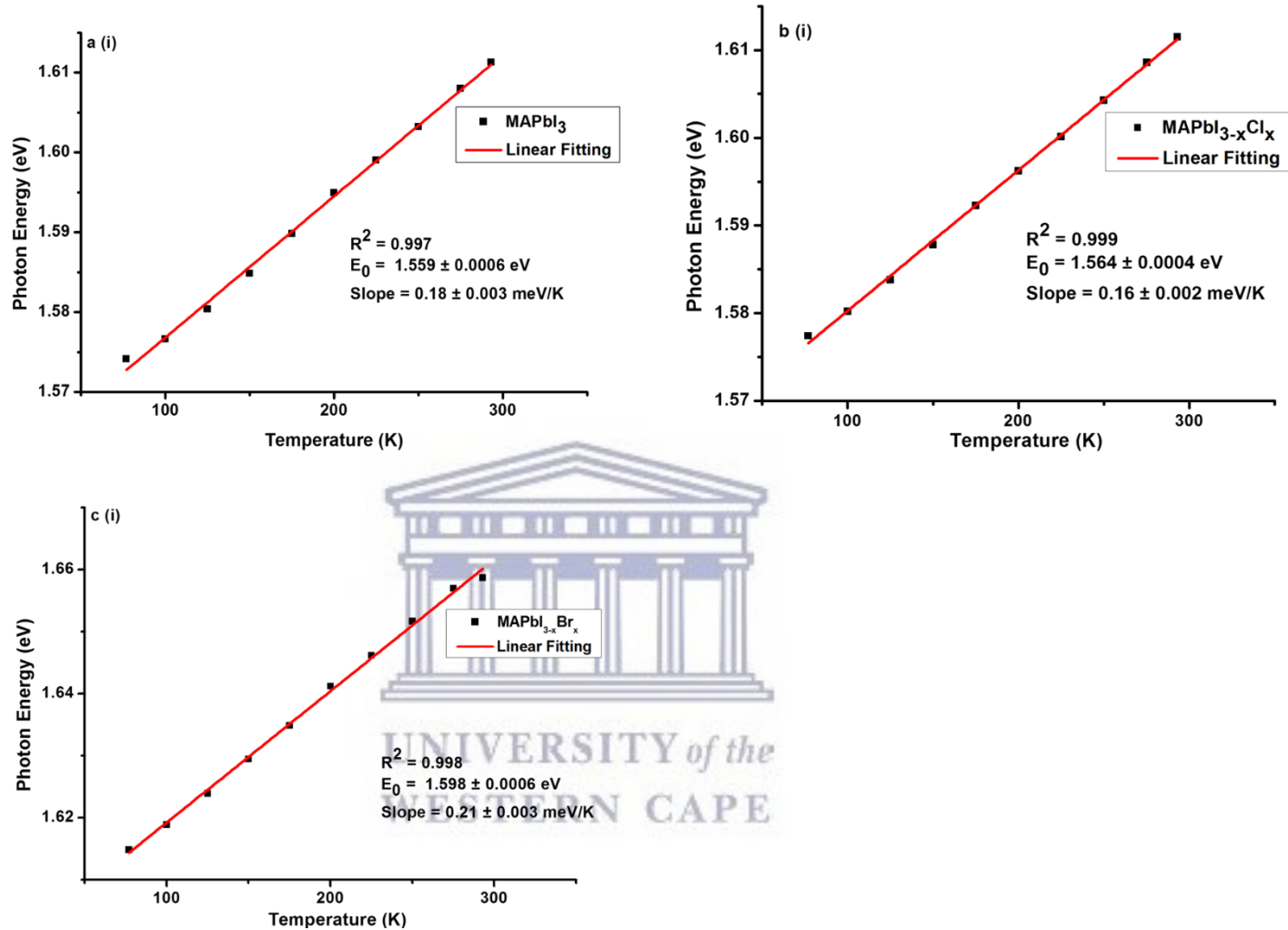


Figure 3.9(i): Temperature-dependent photoluminescence linewidth parameters of MAPbI_{3-x}Y_x (Y = Cl, Br, I) perovskite films: a) MAPbI₃, MAPbI_{3-x}Cl_x and MAPbI_{3-x}Br_x, showing peak energy.

Figure 3.9 (a-c ii) shows a plot of photoluminescence intensity as a function of temperature. The temperature-dependent photoluminescence intensity plotted in **Figure 3.9 (a-c ii)**, was fitted using the Arrhenius equation [39,52], **Equation 3.1**,

$$I(T) = \frac{I_0}{1 + Ae^{-\frac{E_B}{k_B T}}} \quad (3.1)$$

in which I₀ is the intensity at 0 K, E_B the binding energy and k_B the Boltzmann constant.

In general, substitution doping of Cl or Br into MAPbI₃ may hinder collective molecular motions, leading to larger exciton binding energy. However, our results, **Figure 3.9 (a-c ii)**, show a decrease in exciton binding energy in both the mixed halide perovskites in comparison to MAPbI₃. From the plots in **Figure 3.9 (a-c ii)**, a fit of the data points using **Equation 3.1**, extracts exciton binding energies (E_B) of 68.3 ± 4.7 , 49.7 ± 6.2 and 58.3 ± 4.0 meV for MAPbI₃, MAPbI_{3-x}Cl_x and MAPbI_{3-x}Br_x, which are within the range of previously reported values [53,54]. Similar exciton binding values were reported by Tanaka *et al.* (~50 meV for MAPbI₃) [53], D'Innocenzo *et al.* (55 ± 20 meV for MAPbI_{3-x}Cl_x) [54], Wu *et al.* (62.3 ± 8.9 meV for MAPbI_{3-x}Cl_x) [40]. Other studies using the same Boltzmann activation approach to fit data extracted exciton binding energies of 19 meV [9] and 32 meV [39] for MAPbI₃ and 62 meV [40] for MAPbI_{3-x}Cl_x. To the best of our knowledge exciton binding energy values have only been reported for methylammonium lead tribromide (MAPbBr₃) perovskites and not for methylammonium lead iodide-bromide perovskites. Exciton binding energies of 60 meV [55] have been reported for MAPbBr₃.



UNIVERSITY of the
WESTERN CAPE

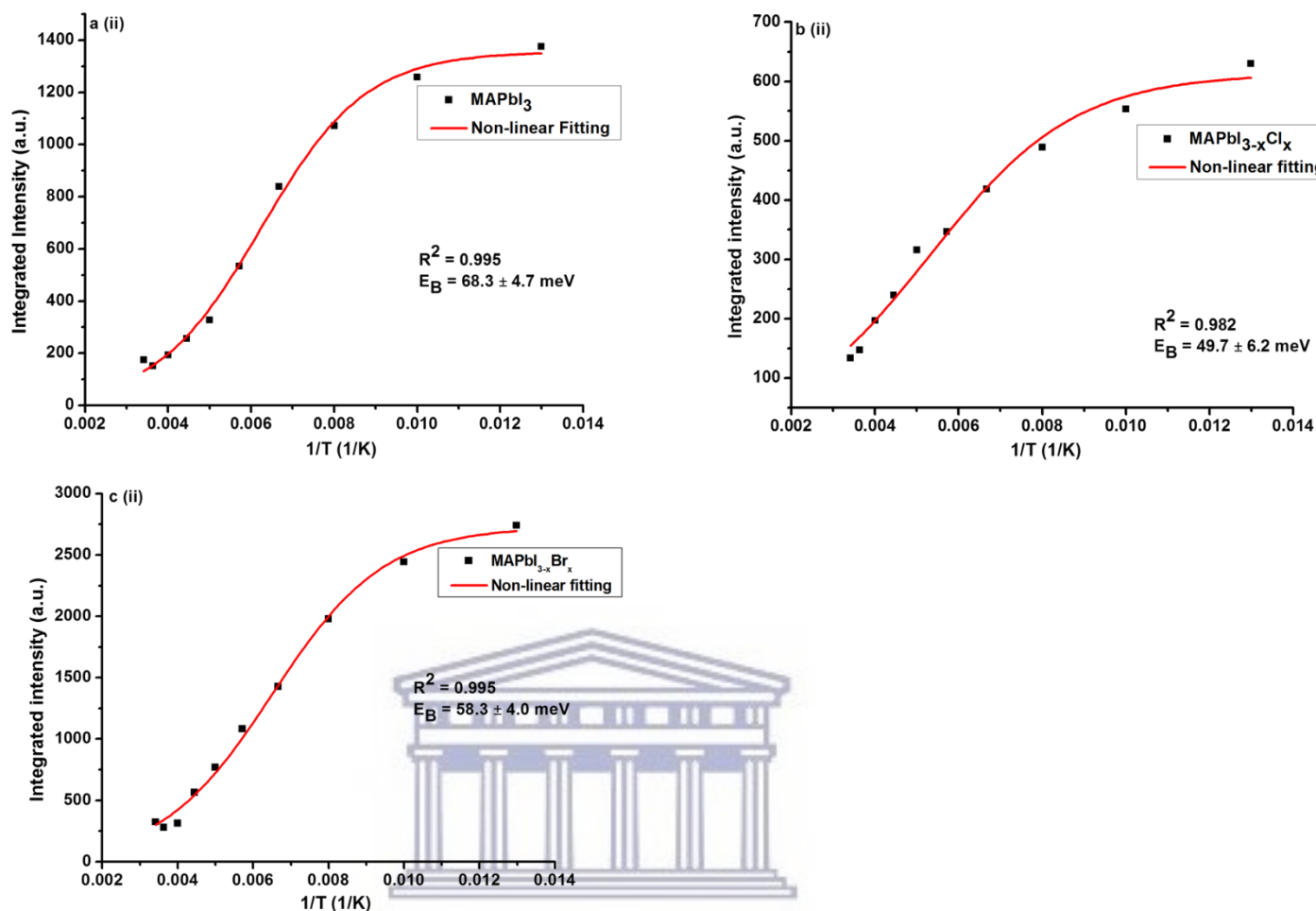


Figure 3.9(ii): Temperature-dependent photoluminescence linewidth parameters of $\text{MAPbI}_{3-x}\text{Y}_x$ ($\text{Y} = \text{Cl}, \text{Br}, \text{I}$) perovskite films: a) MAPbI_3 , $\text{MAPbI}_{3-x}\text{Cl}_x$ and $\text{MAPbI}_{3-x}\text{Br}_x$, showing the integrated intensity.

However, exciton binding energies reported in literature cover a broad range from 2 to 55 meV [9, 53-60]. This rather large variation in exciton binding energy in organic halide lead perovskites is not well understood from fundamental principles. These variations suggest that the exciton characteristics of hybrid perovskites are sensitive to the synthesis, composition and morphology as shown in our results.

To assess the contributions from acoustic and optical phonon modes, the temperature-dependent of the full width at half maximum (FWHM) was analyzed and fitted with a Gaussian function, Figures 3.9 a-c (iii).

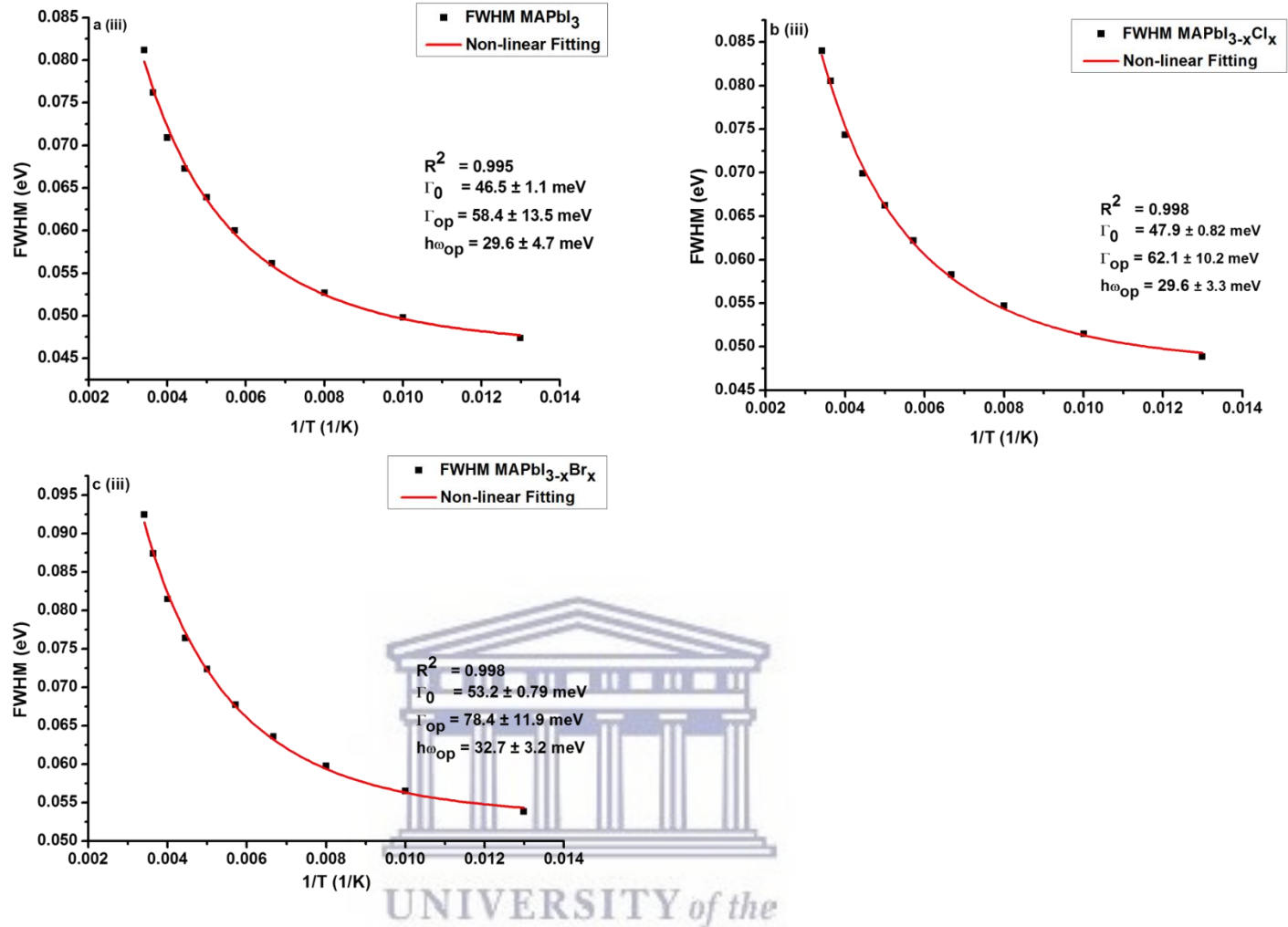


Figure 3.9(iii): Temperature-dependent photoluminescence linewidth parameters of MAPbI_{3-x}Y_x (Y = Cl, Br, I) perovskite films: a) MAPbI₃, MAPbI_{3-x}Cl_x and MAPbI_{3-x}Br_x, showing the temperature-dependent full width at half maximum (FWHM).

From the non-linear fittings of **Figures 3.9 a-c (iii)**, the gradient of the FWHM versus temperature approaches zero at low temperatures, suggesting negligible exciton-acoustic contribution, $\sigma = 0$. The temperature-dependent peak-width broadening is plotted in **Figure 3.9 (a-c iii)** and fitted using the independent Boson model, **Equation 3.2 [61]**:

$$\Gamma(T) = \Gamma_0 + \sigma T + \frac{\Gamma_{op}}{e^{-\frac{\hbar\omega_{op}}{k_B T}} - 1} \quad (3.2)$$

in which Γ_0 is the inhomogeneous broadening contribution, σ and Γ_{op} are the exciton-acoustic phonon interaction and the exciton-optical phonon contribution to the line width broadening respectively, and $\hbar\omega_{op}$ is the optical-phonon energy.

Assuming no exciton-acoustic phonon interaction, as in previous temperature-dependent photoluminescence studies [40,62] and that photoexcitations result only in radiative luminescence or in charge carriers, fitting of the temperature-dependent photoluminescence data parameters, enabled us to deduce the charge yield, as a function of temperature given by the solid line in **Figure 3.9 (a-c iii)**.

The inhomogeneous broadening contributions, Γ_0 , for MAPbI₃, MAPbI_{3-x}Cl_x and MAPbI_{3-x}Br_x were found to be 46.5 ± 1.1 , 47.9 ± 0.82 and 53.2 ± 0.79 meV respectively; the exciton-optical phonon contributions, Γ_{op} , were found to be 58.4 ± 13.5 , 62.1 ± 10.2 and 78.4 ± 11.9 meV respectively and the optical-phonon energies, $\hbar\omega_{op}$, were found to be 29.6 ± 4.7 , 29.6 ± 3.3 and 32.7 ± 3.2 . The values of temperature-dependent FWHM we extracted from our data for MAPbI_{3-x}Br_x perovskites are somewhat higher than those for MAPbI₃, MAPbI_{3-x}Cl_x. This is attributed to stronger electron-phonon coupling in the bromide perovskite than in the iodide and chloride perovskites [44]. Our inhomogeneous broadening contributions, exciton-optical phonon contribution and optical-phonon energy values are within the range of values reported by Wu *et al.* [40] and Quarti *et al.* (25-42 meV) [63]. Although charge-carrier-phonon interactions in methylammonium lead halide perovskites are still a matter of debate, our results provide a link between composition and charge-carrier-phonon interactions.

3.3.3 Photovoltaic characterization

3.3.3.1 Current density-voltage (J-V) characteristics and external quantum efficiencies (EQE)

The photovoltaic performance of the planar perovskite solar cells employing different halides in MAPbI_{3-x}Y_x (Y = I, Cl, Br) were characterized and compared. To probe the effect of halide ions (Y = I, Cl, Br), devices were prepared by spin coating perovskite precursor solutions with varying halide concentration (I, I/Cl, I/Br). Perovskite solar cells with different halide compositions were characterized by measuring their current-voltage (*J-V*) characteristics under standard air mass 1.5 Global (AM 1.5G) illumination and EQE spectra, **Figure 3.10**. External quantum efficiency (EQE) measurements are commonly carried out under short-circuit conditions, and integration of the EQE with respect to the AM1.5G spectrum should amount to a similar current density as determined from *J-V* measurements.

Figure 3.10 depicts the *J-V* curves (**Figure 3.10(a-ci)**) and the corresponding EQE spectra (**Figure 3.10(a-cii)**) for perovskite devices with different halide ratios under reverse bias with results for MAPbI_{3-x}Y_x perovskite solar cell devices employing varying methylammonium iodide (**Figure 3.10a**), methylammonium chloride (**Figure 3.10b**) and methylammonium bromide (**Figure 3.10c**) ratios respectively. The efficiency of the subsequent devices was found to vary with halide ion concentration and care was taken to ensure that the processing conditions were reproduced as consistently as possible.

The photocurrent and external quantum efficiency spectra of devices with different $\text{PbI}_2:x\text{MAI}$ molar ratios of 0.8 (1.25 M), 0.6 (1.5 M), 0.5 (2 M), 0.4 (2.5 M) and 0.3 (3 M) are shown in **Figures 3.10a** and tabulated in **Table 3.1**. It was found that a non-stoichiometric precursor solution is critical for the formation of MAPbI_3 films and a $\text{PbI}_2:\text{MAI}$ molar ratio of 0.5 resulted in the best performing device.

Results in **Figure 3.10a**, indicate that excess MAI acts deleteriously in the MAPbI_3 device as evidenced by the poor photovoltaic performance of cells with high MAI concentration. The integrated EQE was in good agreement with the short-circuit photocurrent density determined from J-V measurements at the steady state photocurrent. The trend in PCE as a function of x shows that J_{sc} decreases from 15.7 mA/cm^2 (at $x = 2$) to 2.2 mA/cm^2 (at $x = 3$). In this range V_{oc} increases from 0.98 V to 1.14 V. Based on these results, the MAPbI_3 solar cell device fabrication was optimized with x fixed at 2 to enhance the photovoltaic performance of the solar cells.



UNIVERSITY of the
WESTERN CAPE

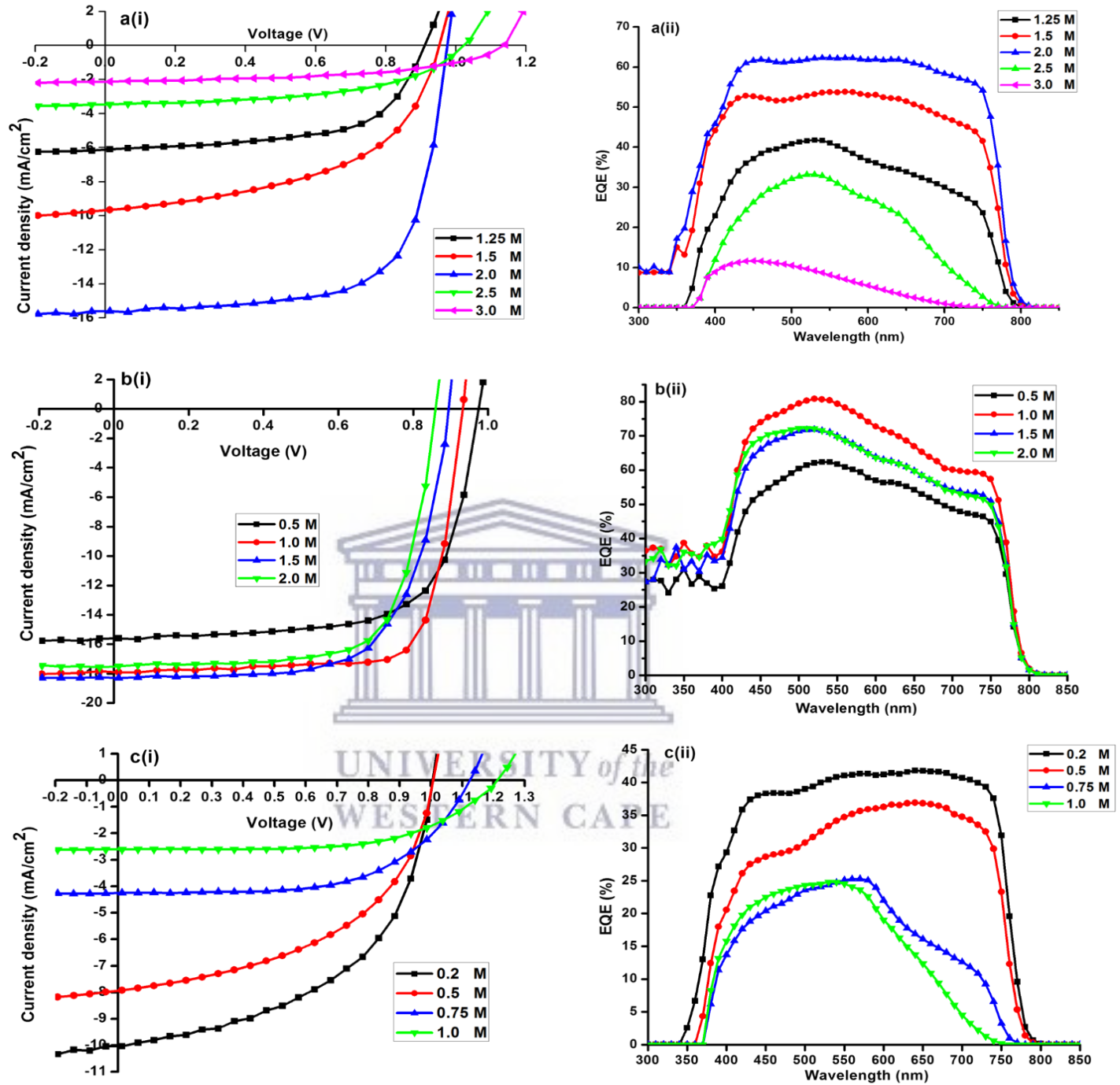


Figure 3.10: Current density-voltage (J-V) characteristics and the corresponding EQE spectra of (a) MAPbI₃ (MAI = 1.25, 1.5, 2.0, 2.5, 3.0 M), (b) MAPbI_{3-x}Cl_x (MACl = 0.5, 1.0, 1.5 and 2.0 M) and (c) MAPbI_{3-x}Br_x (MABr = 0.25, 0.5, 0.75 and 1.0 M) perovskite solar cells under AM1.5G illumination and their corresponding EQE spectra.

The photocurrent and external quantum efficiency spectra of devices with different MAI: x MACl molar ratios of 2 (0.5 M), 1 (1 M), 0.6 (1.5 M) and 0.5 (2 M) are shown in **Figures 3.10b (i) and (ii)**. **Figure 3.10b** shows the J-V curves for different MAPbI_{3-x}Cl_x systems. The trend in PCE as a function of x shows that J_{sc} decreases from 17.8 mA/cm² (at $x = 1$) to 15.6 mA/cm² (at $x = 0.5$). Short-circuit currents from J-V measurements are in good agreement with the calculated J_{sc} obtained by integrating the external quantum efficiency (EQE), **Table 3.1**. In this range V_{oc} increases from 0.940 V to 0.978 V. Based on these results, the MAPbI_{3-x}Cl_x solar cell device fabrication was optimized with x fixed at 1 to enhance the photovoltaic performance of the solar cells. During the rise of V_{oc} with a decrease in x (**Figure 3.10b (i)**), J_{sc} maintains a relatively large value in comparison to MAPbI₃ (**Figure 3.10a**). It was found that overstoichiometric MACl does not strongly influence the optical properties and photovoltaic performance of the MAPbI_{3-x}Cl_x in comparison to MAPbI₃. The broader profile and higher values of EQE are consistent with the higher J_{sc} measured in the solar cells.

Figure 3.10c shows the J-V curves for different MAPbI_{3-x}Br_x systems. The photocurrent and external quantum efficiency spectra of devices with different MAI: x MABr molar ratios of 4 (0.25 M), 1 (1 M), 0.6 (1.5 M) and 0.5 (2 M) are shown in **Figures 3.10b (i) and (ii)**. **Figure 3.10b** shows the J-V curves for different MAPbI_{3-x}Cl_x systems. Data in **Figure 3.10c (i)** exhibits considerably low J_{sc} , V_{oc} , and FF with an increase in x . The trend in PCE as a function of x shows that J_{sc} decreases from 9.6 mA/cm² (at $x = 0.25$) to 2.8 mA/cm² (at $x = 1$). In this range V_{oc} increases from 0.98 V to 1.22 V. A significant decrease in cell efficiency is observed by increasing the Br content due to a decrease in the J_{sc} , which is ascribed to the blue shift of the absorption band-edge observed in **Figure 3.10c(ii)**. For $x > 0.8$, the device performance deteriorates considerably.

Table 3.1: Effect of perovskite precursor halide composition on short-circuit current density (J_{sc}), open-circuit voltage (V_{oc}), fill factor (FF) and power conversion efficiency (PCE) of $\text{MAPbI}_{3-x}\text{Y}_x$ ($\text{Y} = \text{I}, \text{Cl}, \text{Br}$) solar cells.

Perovskite	MAY ($\text{Y} = \text{I}, \text{Cl}, \text{Br}$)	V_{oc} (V)	J_{sc} (mA/cm^2) (EQE)	FF	PCE (%)	E_g (eV) (estimated)
MAPbI₃						
MAI	$x = 1.25$	0.912	6.1	0.60	3.4	1.57
	$x = 1.5$	0.929	9.6	0.62	5.5	1.57
	$x = 2.0$	0.980	15.7	0.68	9.2	1.57
	$x = 2.5$	1.023	3.5	0.53	1.9	1.63
	$x = 3.0$	1.138	2.2	0.52	1.3	1.72
MAPbI_{3-x}Cl_x						
MACl	$x = 0.5$	0.978	13.3	0.68	8.6	1.57
	$x = 1.0$	0.940	17.8	0.75	12.5	1.57
	$x = 1.5$	0.898	15.4	0.67	9.0	1.57
	$x = 2.0$	0.870	15.6	0.70	9.1	1.57
MAPbI_{3-x}Br_x						
MABr	$x = 0.25$	1.016	9.64	0.55	5.4	1.57
	$x = 0.50$	1.018	7.94	0.50	4.0	1.57
	$x = 0.75$	1.126	4.25	0.60	2.9	1.61
	$x = 1$	1.217	2.78	0.60	2.0	1.65

The best performing halide ratios were compared employing ITO/PEDOT:PSS/Perovskite/PCBM/Al planar heterojunction architecture. Representative photovoltaic parameters showing the J-V curves of typical solar cells measured in the dark and under illumination AM1.5 conditions for MAPbI_3 , $\text{MAPbI}_{3-x}\text{Cl}_x$ and $\text{MAPbI}_{3-x}\text{Br}_x$ are shown in **Figure 3.11**. The corresponding semi-logarithmic current-voltage characteristics are shown in **Figure 3.12**. Power conversion efficiencies of 9.2, 12.5 and 5.4 % were obtained for MAPbI_3 , $\text{MAPbI}_{3-x}\text{Cl}_x$ and $\text{MAPbI}_{3-x}\text{Br}_x$ respectively. Even if the material bandgap remains

substantially unchanged, **Table 3.1**, the Cl doping dramatically improves the charge transport within the perovskite layer, explaining the outstanding performances.

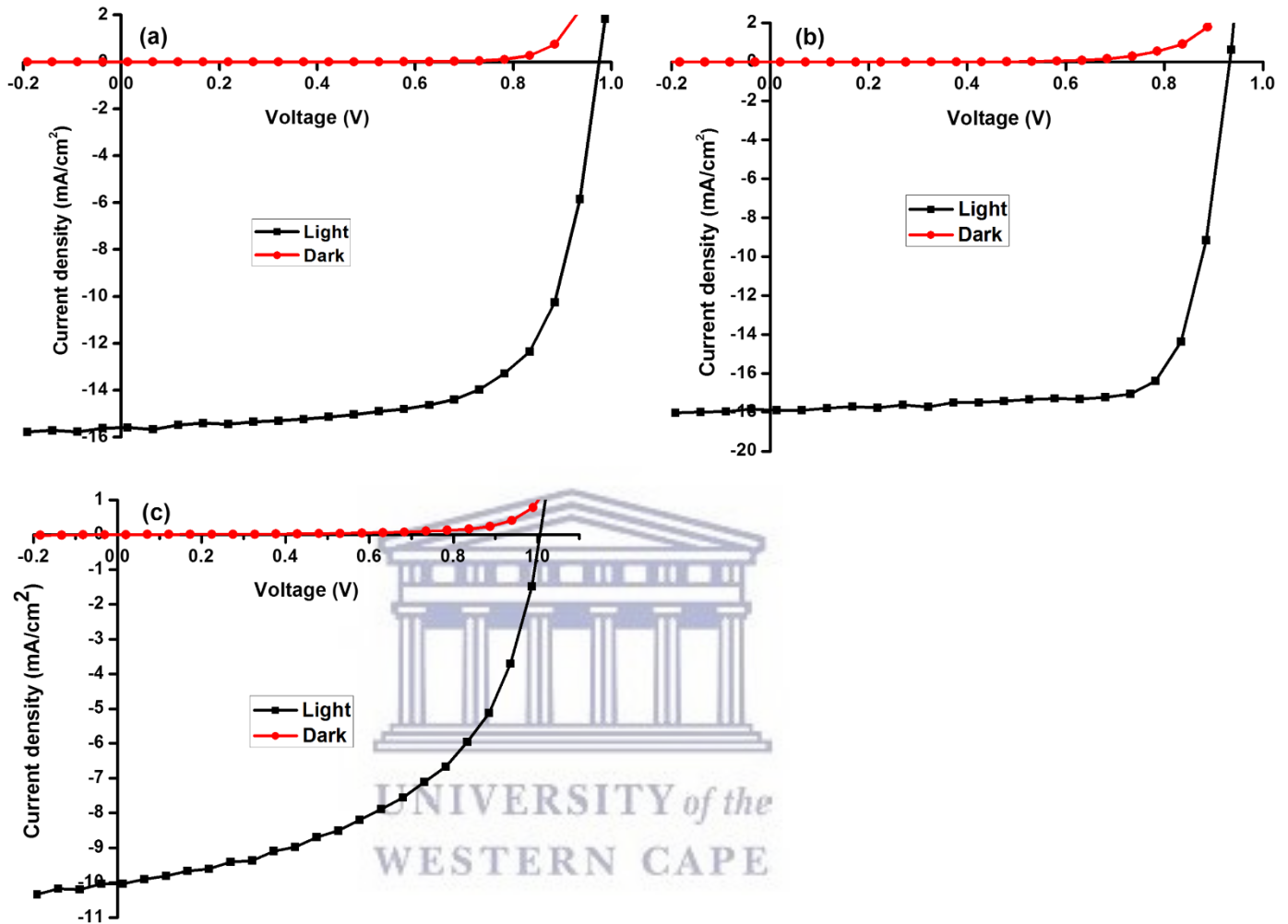


Figure 3.11: Current density-voltage (J-V) curves of a typical solar cell measured in the dark and under AM1.5 conditions (a) MAPbI_3 (b) $\text{MAPbI}_{3-x}\text{Cl}_x$ (c) and $\text{MAPbI}_{3-x}\text{Br}_x$.

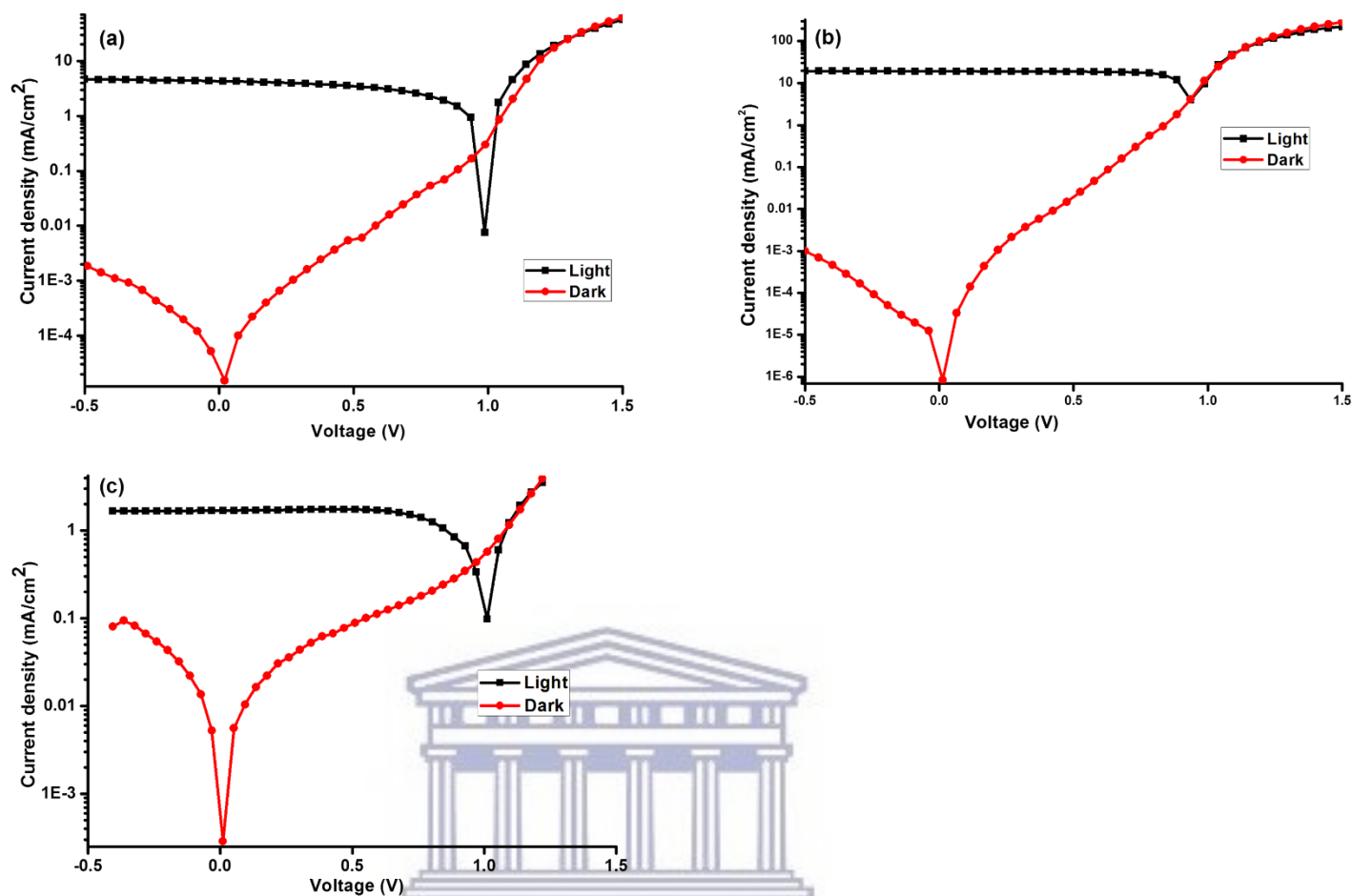


Figure 3.12: Semi-logarithmic current-voltage characteristics (a) MAPbI_3 , (b) $\text{MAPbI}_{3-x}\text{Cl}_x$ and (c) $\text{MAPbI}_{3-x}\text{Br}_x$

Despite the high open circuit voltages, **Figure 3.11**, in MAPbI_3 and $\text{MAPbI}_{3-x}\text{Br}_x$ perovskite solar cells, device efficiencies in comparison to $\text{MAPbI}_{3-x}\text{Cl}_x$ are hampered by significantly lower short circuit currents and fill factors. Higher series resistances were observed in MAPbI_3 and $\text{MAPbI}_{3-x}\text{Br}_x$ devices compared to $\text{MAPbI}_{3-x}\text{Cl}_x$ devices. The high FF in $\text{MAPbI}_{3-x}\text{Cl}_x$ indicates that the charge transport and collection is more efficient, corroborating results obtained in the temperature-dependent photoluminescence spectroscopy. There is also a correlation between perovskite morphology and solar cell performance. The observed correlation of photovoltaic performance with the mean crystallite size is likely since larger perovskite crystallites exhibit a reduced area of grain boundaries and consequently lower overall density of defect states.

3.3.3.2 Hysteresis

Methylammonium lead halide perovskites are ionic crystals, therefore frequency-dependent electrical polarization and ionic drift currents may affect potentiodynamic measurements [64, 65]. The effect of scan rate and direction on hysteretic behaviour is shown in **Figure 3.13**.

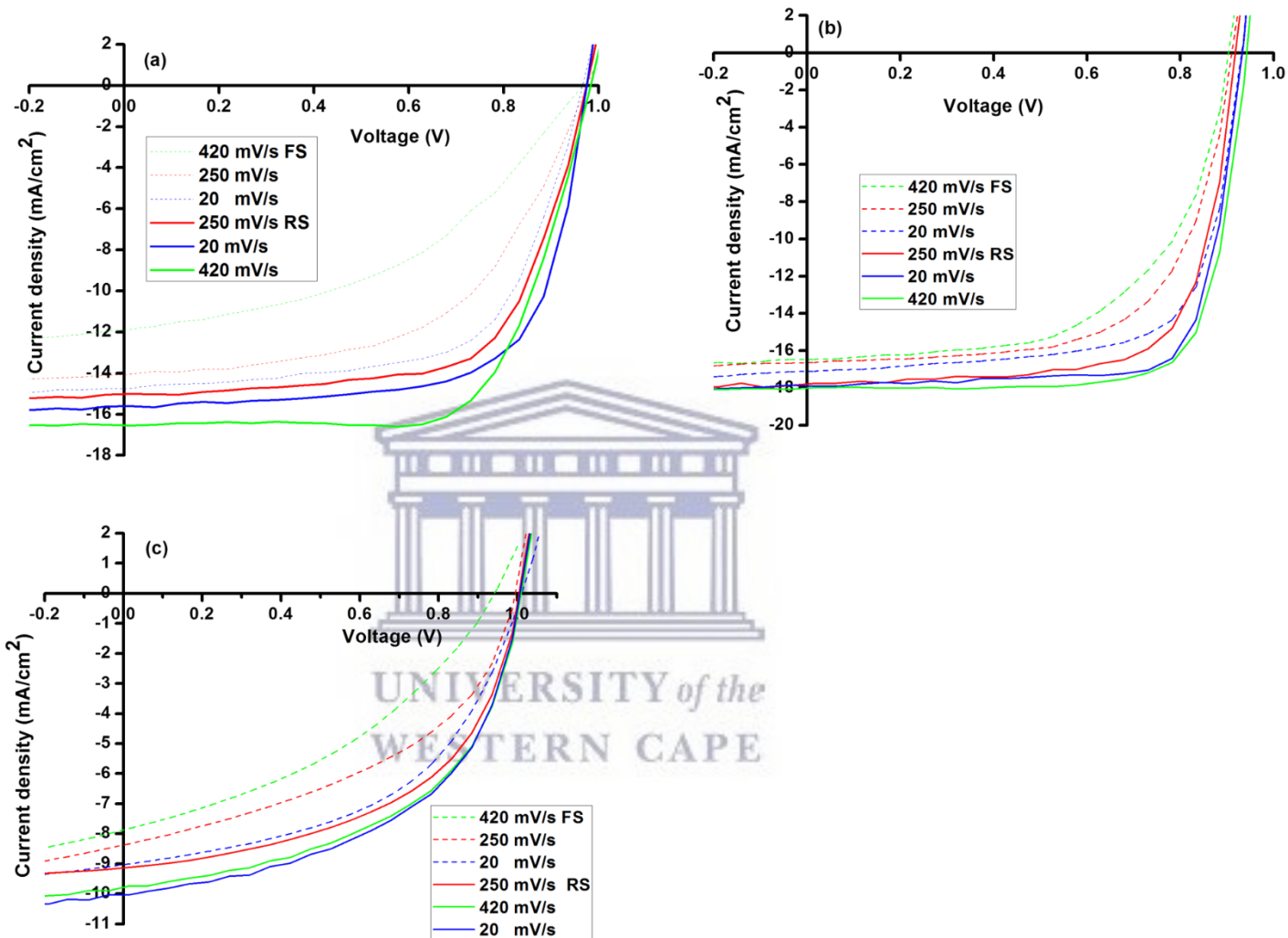


Figure 3.13: Scan rate- and direction dependent forward and reverse J-V scans of ITO/PEDOT:PSS/MAPbX₃/PCBM/Al solar cells (a) PbMAI₃, (b) PbMAI_{3-x}Cl_x and (c) PbMAI_{3-x}Br_x.

A general trend was observed concerning the influence of the scan rate on hysteresis. Specifically, our results show that the hysteresis is enhanced at high sweep rates and the PCE under reverse scan increases with increases in scan rate, whereas the efficiency under forward scan decreases with the scan rate. Furthermore, the magnitude of the hysteresis event is clearly sensitive to the precursors utilized for the perovskite growth as it is minimal in MAPbI_{3-x}Cl_x solar cells in comparison to their MAPbI₃ and MAPbI₃.

$x\text{Br}_x$ counterparts. The reduced current density-voltage (J-V) hysteresis in $\text{MAPbI}_{3-x}\text{Cl}_x$ with respect to the scan rate and scan direction could be attributed to a more balanced electron flux (J_e) and hole flux (J_h) and a reduced number of surface traps. The differences in the hysteretic behaviour that we observed may be a consequence of differences in stoichiometry or perovskite film morphology.

Dualeh *et al.*, [66] observed that the magnitude of the hysteretic effect increased with an increase in scan rate, in agreement with our observations. On the other contrary, Snaith *et al.*, [67] reported an opposite dependence of the hysteresis with the scan rate. However, hysteresis is significantly reduced by using a sufficiently low scan as shown in **Figure 3.14**.

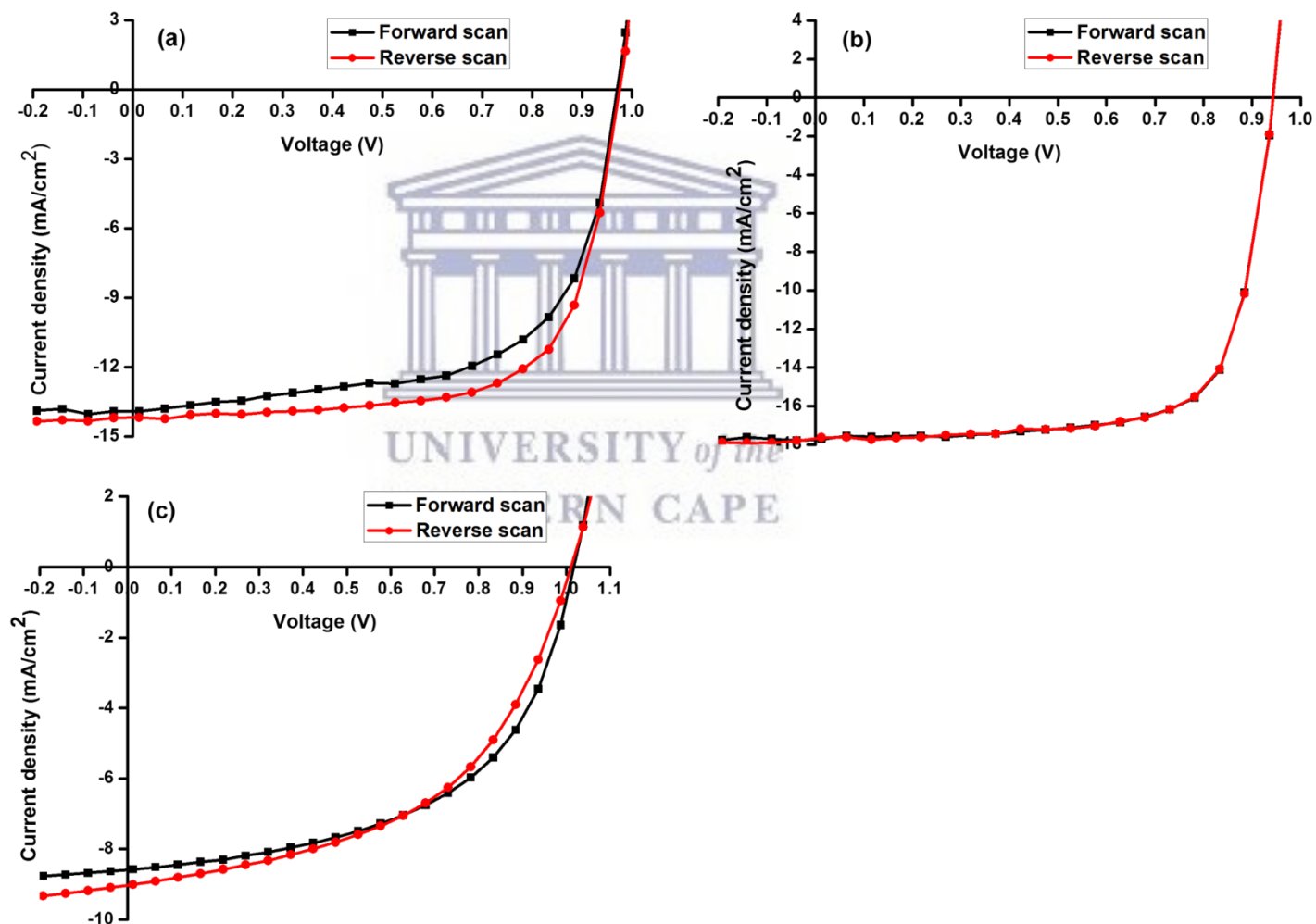


Figure 3.14: Current-voltage curve of the perovskite solar cell, forward and reverse scan 20 mV/s showing minimum hysteretic behaviour.

Hysteresis in perovskite-absorber devices has been speculated to originate from ion migration [66-68]. Since ion migration is particularly sensitive to the concentration of mobile vacancies, this would suggest that the hysteretic behaviour of perovskite devices should be influenced by the stoichiometry of the perovskite material, as well as the degree of crystallinity and the size of crystalline domains. We therefore investigated concentration-dependent hysteretic behaviour, **Figure 3.15**, of the prepared perovskite solar cells.

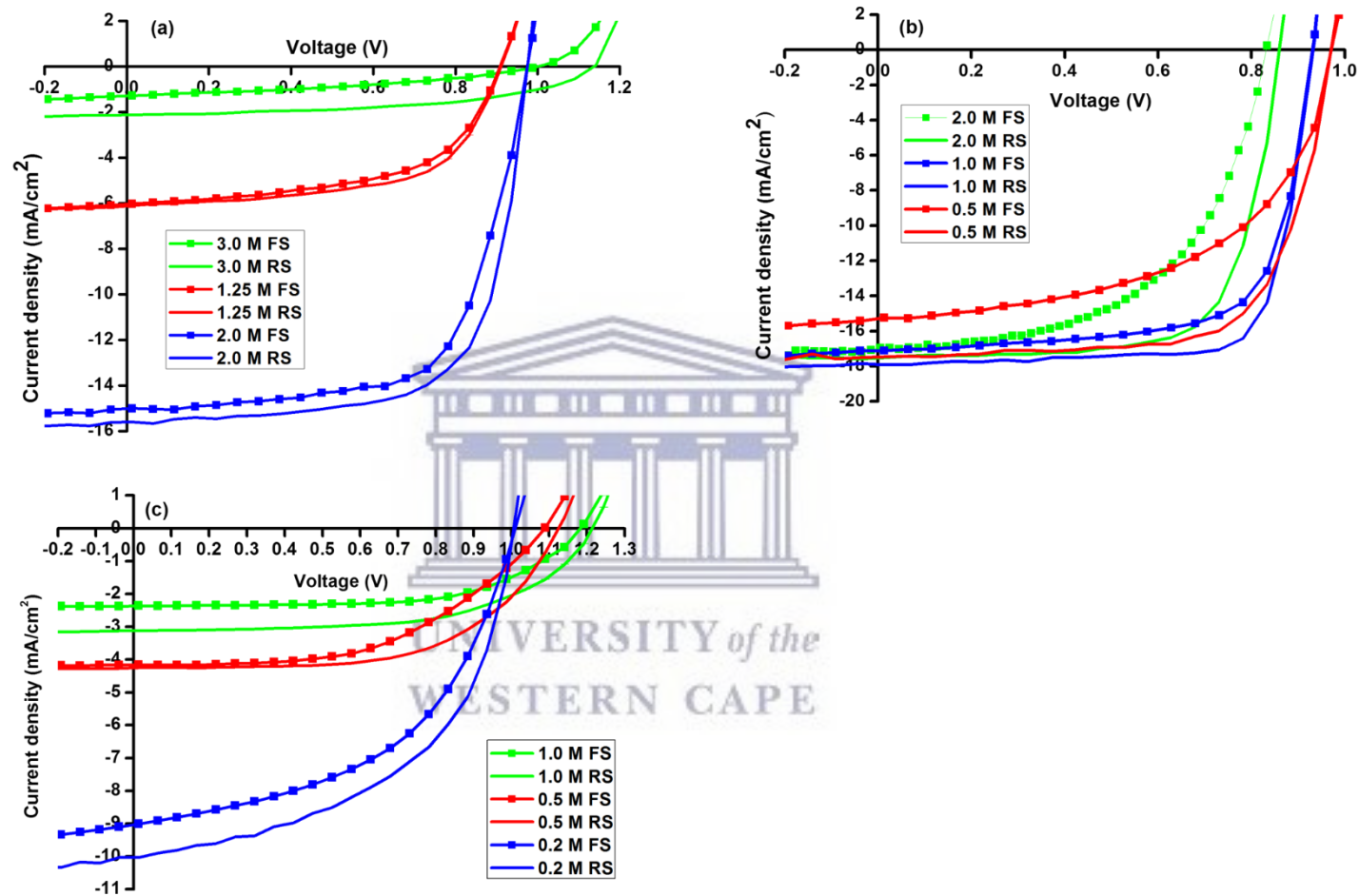


Figure 3.15: Concentration-dependent forward and reverse J-V scans of ITO/PEDOT:PSS/MAPbX₃/PCBM/Al solar cells (a) PbMAI₃, (b) PbMAI_{3-x}Cl_x and (c) PbMAI_{3-x}Br_x.

Though the intermediate hysteretic behaviour is not clear, our results in **Figure 3.15**, show that hysteresis is most severe at high MAX concentrations with less hysteresis in MAPbI_{3-x}Cl_x in comparison to MAPbI₃ and MAPbI_{3-x}Br_x devices. However, the origin of the J-V hysteresis is still under debate and there are challenges associated with the proposed mechanisms.

To elucidate the reproducibility of the perovskite fabrication process, 150 devices were fabricated using the same process and parameters. The photovoltaic parameters of these devices are shown in **Figures 3.16(i-iii)**, together with the corresponding standard deviations summarized in **Table 3.2**. **Figure 3.16(i)**, **Figure 3.16(ii)**, and **Figure 3.16(iii)** show the statistical device parameters for PbMAI_3 , $\text{PbMAI}_{3-x}\text{Cl}_x$ and $\text{PbMAI}_{3-x}\text{Br}_x$ devices respectively. Not only are deviations observed among the three different perovskite composition systems but also within the same batches. It is plausible that other variables, such as processing temperature which may have changed during fabrication, handling techniques such as transfer from the thermal evaporator to the solar simulator and environmental conditions such as humidity may affect the perovskite device parameters as well.



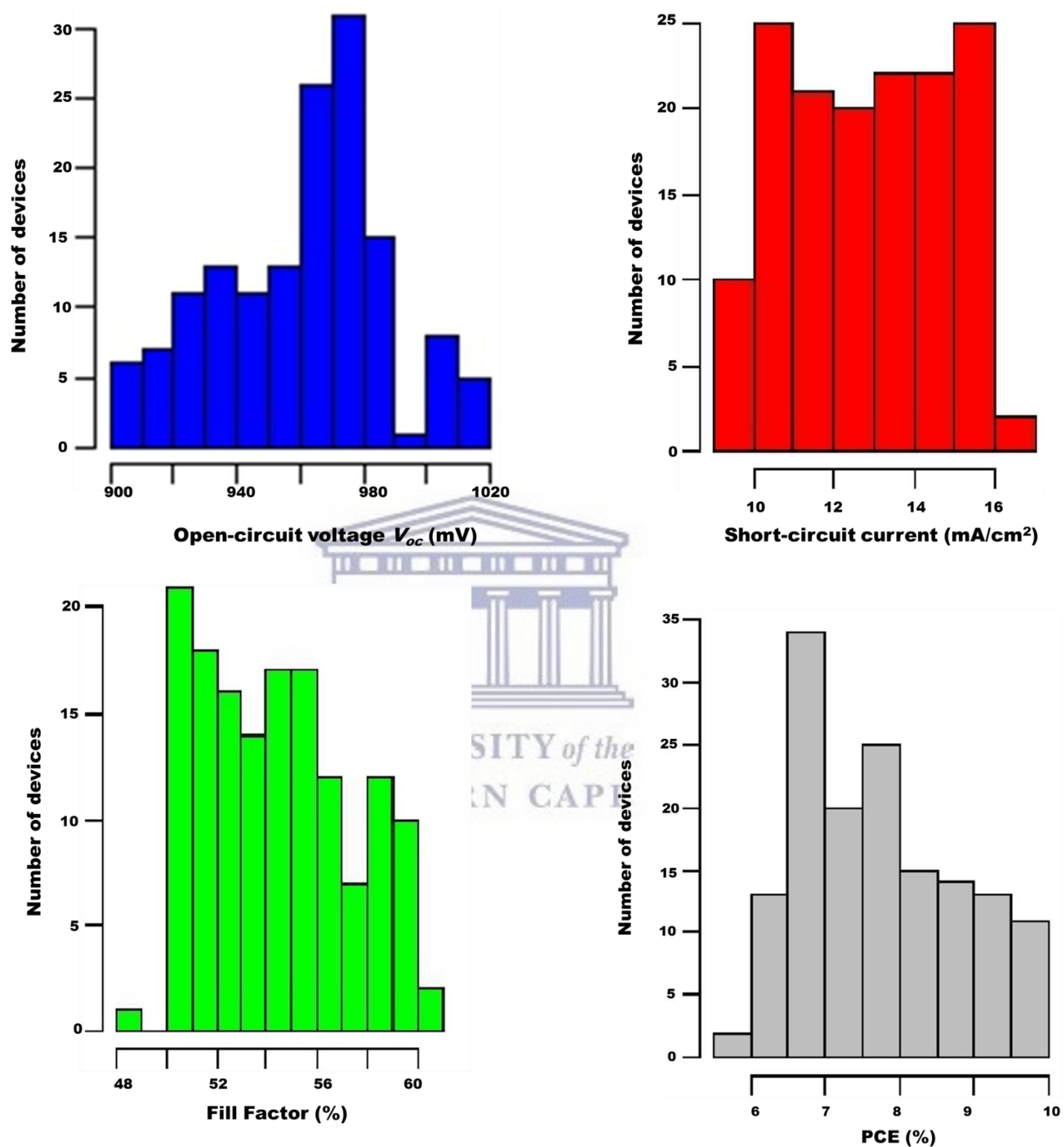


Figure 3.16(i): Histograms of device parameters (V_{oc} , J_{sc} , FF and PCE) for 100 separate PbMAI₃.

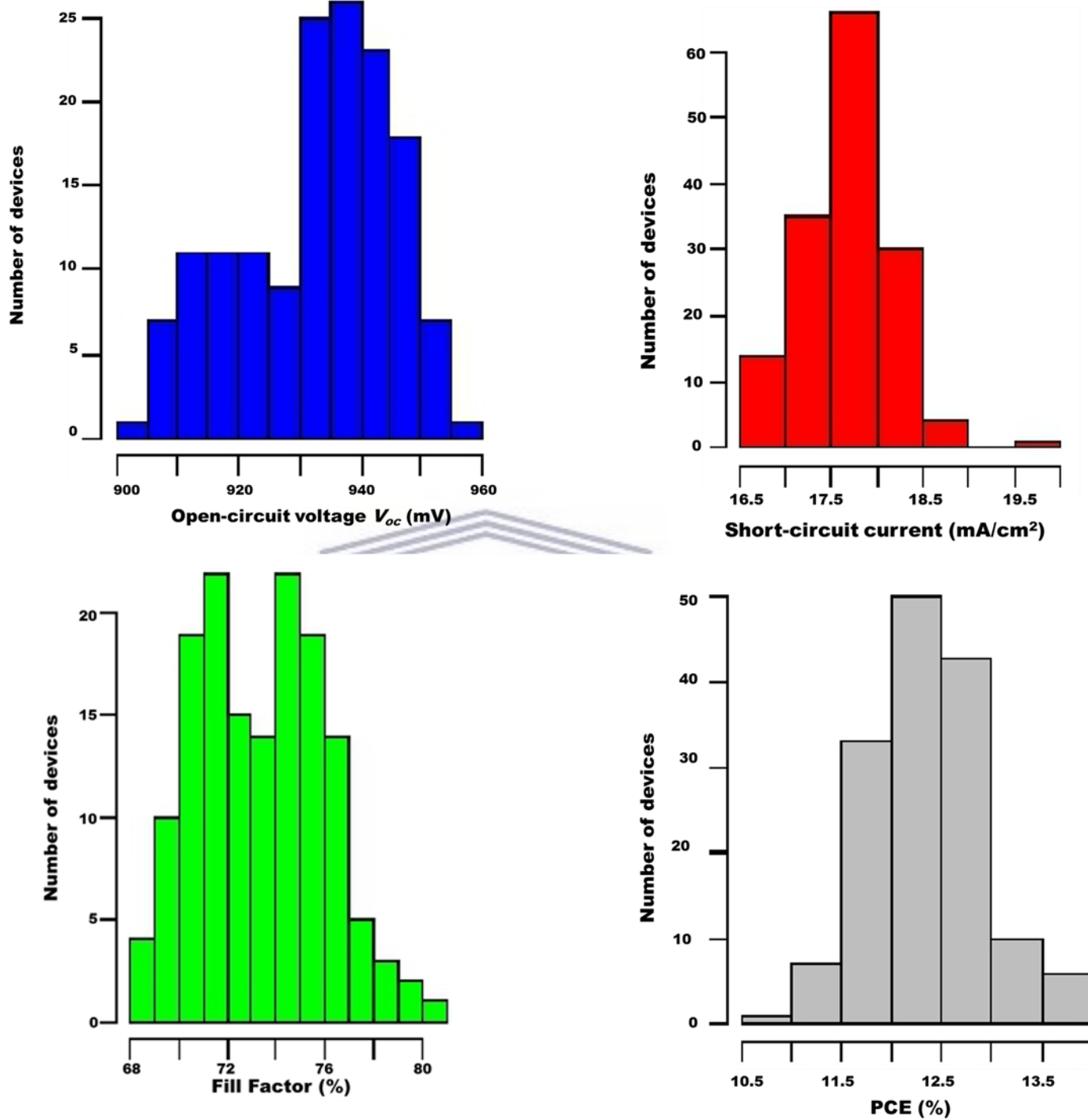


Figure 3.16(ii): Histograms of device parameters (V_{oc} , J_{sc} , FF and PCE) for 100 separate PbMAI_{3-x}Cl_x.

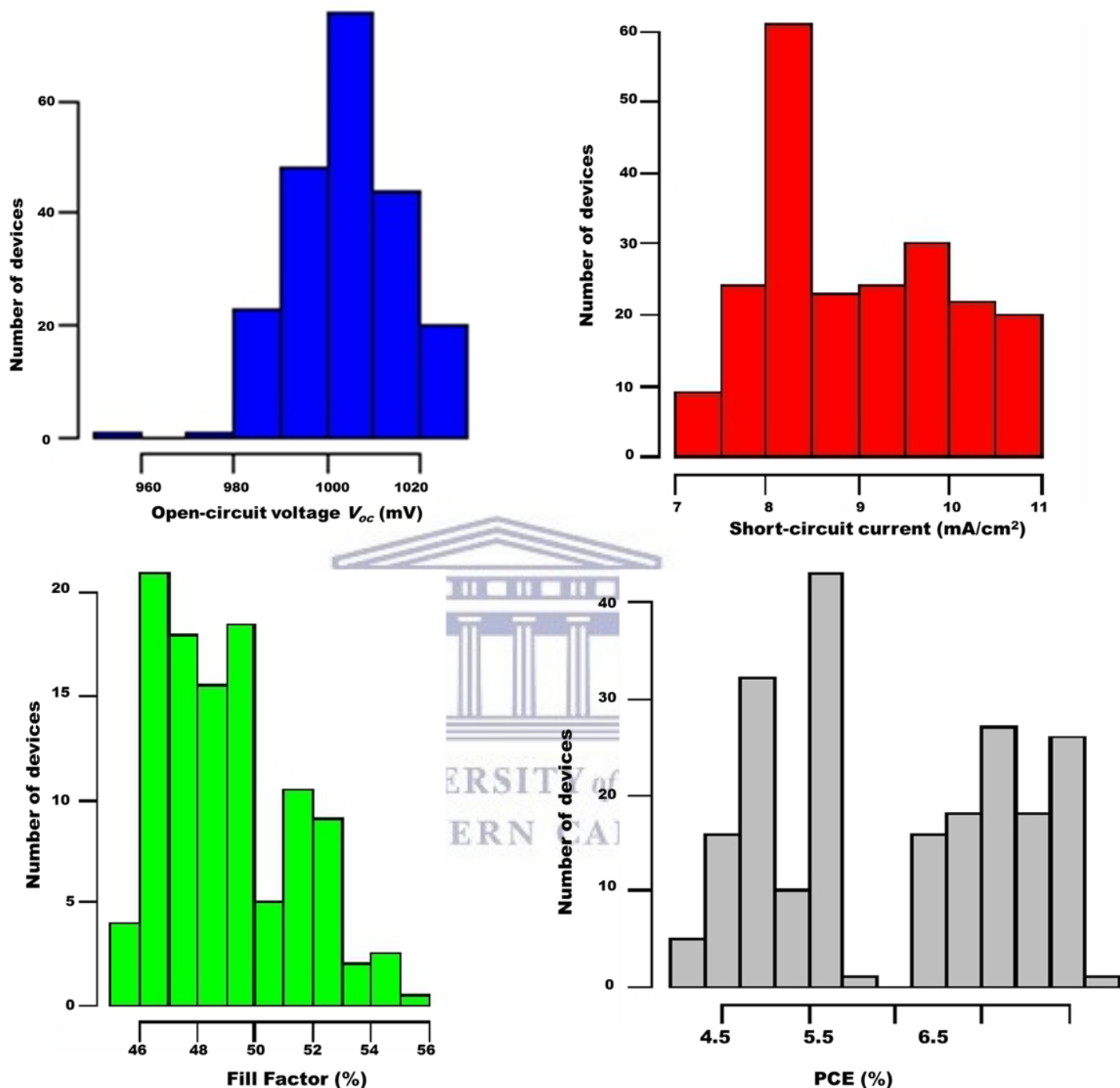


Figure 3.16(iii): Histograms of device parameters (V_{oc} , J_{sc} , FF and PCE) for 100 separate $\text{PbMAI}_{3-x}\text{Br}_x$ devices.

Although MAPbI_3 and $\text{PbMAI}_{3-x}\text{Br}_x$ devices exhibit relatively high V_{oc} , **Figure 3.16(i)**, device performance was mainly affected by the fill factor. The $\text{PbMAI}_{3-x}\text{Cl}_x$, **Figure 3.16(ii)**, solar cells demonstrate consistent

photovoltaic performance as proven by the relatively small standard deviations of the performance parameters in comparison to both PbMAI_3 , **Figure 3.16(i)** and $\text{PbMAI}_{3-x}\text{Br}_x$ devices, **Figure 3.16(iii)**.

Table 3.2: Statistical data for photovoltaic device parameters (V_{oc} , J_{sc} , FF and PCE) for MAPbI_3 , $\text{MAPbI}_{3-x}\text{Cl}_x$ and $\text{MAPbI}_{3-x}\text{Br}_x$ devices.

Perovskite	V_{oc} (mV)	J_{sc} (mA/cm ²)	FF	PCE (%)
PbMAI_3	961 ± 26	12.8 ± 2.0	54.4 ± 2.9	7.7 ± 1.1
$\text{PbMAI}_{3-x}\text{Cl}_x$	933 ± 13	17.6 ± 0.5	73.4 ± 2.6	12.3 ± 0.6
$\text{PbMAI}_{3-x}\text{Br}_x$	1005 ± 12	9.0 ± 1.0	49.0 ± 2.3	5.5 ± 0.7

Table 3.2 shows that $\text{MAPbI}_{3-x}\text{Cl}_x$ exhibit much better reproducibility in performance than MAPbI_3 and $\text{MAPbI}_{3-x}\text{Br}_x$ devices which can be attributed to the improved morphology of the perovskite film upon introduction of MAI as shown in the morphology results in **Figure 3.4**.

3.4 Conclusion

In summary, low-cost planar heterojunction perovskite solar cells which offer a wide tunability on composition and structure by adjusting the metal halide framework were fabricated and their optical and electronic properties were investigated to develop a fundamental understanding of perovskite material properties and device operation principles. This work shows that methylammonium lead halide perovskites exhibit composition-/structure-dependent properties. Although the exact values for exciton binding energies in methylammonium lead halide perovskites are still a matter of debate, the results fall into the range of reported values and provide a link between composition and charge carrier-phonon interactions. Whether the opto-electrical and photovoltaic performance differences between the single halide (tri-iodide) and mixed halide (I/Cl and I/Br) perovskite materials are as a result of crystal orientations or different photogenerated excitations, requires more research.

References

- [1] A. Kojima, K. Teshima, Y. Shirai and T. Miyasaka, *J. Am. Chem. Soc.*, 2009, 131, 6050-6051
- [2] J.-H. Im, C.-R. Lee, J.-W. Lee, S.-W. Park and N.-G. Park, *Nanoscale*, 2011, 3, 4088-4093
- [3] W.S. Yang, J. H. Noh, N. J. Jeon, Y. C. Kim, S. Ryu, J. Seo, S. I. Seok, *Science*, 2015, 348, 1234-1237
- [4] NREL http://www.nrel.gov/ncpv/images/efficiency_chart.jpg
- [5] H. J. Snaith, *J. Phys. Chem. Lett.*, 2013, 4, 3623-3630
- [6] D. Bi, W. Tress, M. I. Dar, P. Gao, J. Luo, C. Renevier, K. Schenk, A. Abate, F. Giordano, J-P. C. Baena, J-D. Decoppet, S. M. Zakeeruddin, M. K. Nazeeruddin, M. Grätzel and A. Hagfeldt, *Sci. Adv.*, 2016; 2:e1501170
- [7] J. H. Noh, S. H. Im, J. H. Heo, T. N. Mandal and S.I Seok, *Nano Lett.*, 2013, 13, 1764-1769
- [8] T. C. Sum and N. Mathews, *Energy Environ. Sci.*, 2014, 7, 2518-2534
- [9] S. Sun, T. Salim, N. Mathews, M. Duchamp, C. Boothroyd, G. Xing, T. C. Sum and Y. M. Lam, *Energy Environ. Sci.*, 2014, 7, 399-407
- [10] S. D. Stranks, G. E. Eperon, G. Grancini, C. Menelaou, M. J. Alcocer, T. Leijtens, L. M. Herz, A. Petrozza and H. J. Snaith, *Science*, 342, 341-344
- [11] G. Xing, N. Mathews, S. Sun, S. S. Lim, Y. M. Lam, M. Grätzel, S. Mhaisalkar, T. C. Sum, *Science*, 2013, 342, 344-347
- [12] Q. Dong, Y. Fang, Y. Shao, P. Mulligan, J. Qui, L. Cao, J. Huang, *Science*, 2015, 347. 967-970.
- [13] D. B. Mitzi, *Prog. Inorg. Chem.* 2007, 48, 1
- [14] G. Xing, N. Mathews, S. S. Lim, N. Yantara, X. Liu, D. Sabba, M. Grätzel, S. Mhaisalkar, T. C. Sum, *Nat. Mater.*, 2014, 13, 476-480
- [15] A. Sharenko and M. F. Toney, *J. Am. Chem. Soc.*, 2016, 138, 463-470.
- [16] H. Tsai, W. Nie, P. Cheruku, N. H. Mack, P. Xu, G. Gupta, A. D. Mohite and H.-L. Wang, *Chem. Mater.*, 2015, 27, 5570-5576.
- [17] F. Matsumoto, S. M. Vorpahl, J. Q. Banks, E. Sengupta and D. S. Ginger, *J. Phys. Chem. C.*, 2015, 119, 20810-20816
- [18] M. Liu, M. B. Johnston and H. J. Snaith, *Nature*, 2013, 501, 395-398
- [19] D. Liu and T. L. Kelly, *Nat. Photonics*, 2013, 8, 133-138
- [20] G. E. Eperon, S. D. Stranks, C. Menelaou, M. B. Johnston, L. Herz and H. J. Snaith, *Energy Environ. Sci.*, 2014, 7, 982-988
- [21] J. You, Z. Hong, Y. M. Yang, Q. Chen, M. Cai, T.-B. Song, C.-C. Chen, S. Lu, Y. Liu, H. Zhou and Y. Yang, *ACS Nano*, 2014, 8, 1674-1680
- [22] Q. Chen, H. Zhou, Z. Hong, S. Luo, H.-S. Duan, H.-H. Wang, Y. Liu, G. Li and Y. Yang, *J. Am. Chem. Soc.*, 2014, 136, 622-625
- [23] M. M. Lee, J. Teuscher, T. Miyasaka, T. N. Murakami, H. J. Snaith, *Science*, 2012, 338, 643-647
- [24] J. M. Ball, M. M. Lee, A. Hey and H. J. Snaith, *Energy Environ. Sci.*, 2013, 6, 1739
- [25] J. T.-W. Wang, J. M. Ball, E. M. Barea, A. Abate, J. A. Alexander-Webber, J. Huang, M. Saliba, I. Mora-Sero, J. Bisquert, H. J. Snaith and R. J. Nicholas, *Nano Lett.*, 2014, 14, 724-730
- [26] D. Bi, S.-J. Moon, L. Häggman, G. Boschloo, L. Yang, E. M. J. Johansson, M. K. Nazeeruddin, M. Grätzel and A. Hagfeldt, *RSC Adv.*, 2013, 3, 18762
- [27] H.-S. Kim, C.-R. Lee, J.-H. Im, K.-B. Lee, T. Moehl, A. Marchioro, S.-J. Moon, R. Humphry-Baker, J.-H. Yum, J. E. Moser, M. Grätzel and N.-G. Park, *Sci. Rep.*, 2012, 2, 591
- [28] J. Burschka, N. Pellet, S.-J. Moon, R. Humphry-Baker, P. Gao, M. K. Nazeeruddin and M. Grätzel, *Nature*, 2013, 499, 316-319
- [29] N. Pellet, P. Gao, G. Gregori, T.-Y. Yang, M. K. Nazeeruddin, J. Maier and M. Grätzel, *Angew. Chem. Int. Ed. Engl.*, 2014, 53, 3151-3157
- [30] G. Adam, M. Kaltenbrunner, E. D. Glowacki, M. S. White, H. Heilbrunner, S. Tombe, P. Stadler, B. Ernecker, C. W. Klampfl, N. S. Sariciftci and M. C. Scharber, *Solar Energ. Mat. Sol. Cells*, 2016, 157, 318-325

- [31] H. Zhou, Q. Chen, G. Li, S. Luo, T. Song, H.-S. Duan, Z. Hong, J. You, Y. Liu and Y. Yang, *Science*, 2014, 345, 542-546
- [32] D. T. Moore, H. Sai, K. W. Tan, D.-M. Smilgies, W. Zhang, H. J. Snaith, U. Wiesner and L. A. Estroff, *J. Am. Chem. Soc.*, 2015, 137, 2350-2358
- [33] E. Edri, S. Kirmayer, A. Henning, S. Mukhopadhyay, K. Gartsman, Y. Rosenwaks, G. Hodes and D. Cahen, *Nano Lett*, 2014, 14, 1000-1004
- [34] S. Colella, E. Mosconi, P. Fedeli, A. Listorti, F. Gazza, F. Orlandi, P. Ferro, T. Besagni, A. Rizzo, G. Calestani, G. Gigli, F. De Angelis and R. Mosca, *Chem. Mater.*, 2013, 25, 4613-4618
- [35] F. Deschler, M. Price, S. Pathak, L. E. Klintberg, D.-D. Jarausch, R. Higler, S. Hüttner, T. Leitjens, S. D. Stranks, H.J. Snaith, M. Atatüre, R.T. Phillips, R. H. Friend, *J. Phys. Chem. Lett.*, 2014, 5, 1421-1426
- [36] T. Baikie, *J. Mater. Chem. A*, 2013, 1, 5628-5641
- [37] P. Gao, M. Grätzel and M. K. Nazeeruddin, J. Maier and M. Grätzel, *Energy Environ. Sci.*, 2014, 7, 2448-2463
- [38] Y. Yasuhiro, N. Toru, E. Masaru, W. Atsushi and Y. Yoshihiko, *Appl. Phys. Express*, 2014, 7, 032302
- [39] T. J. Savenije, C. S. Ponseca, L. Kunneman, M. Abdellah, K. Zheng, Y. Tian, Q. Zhu, S. E. Canton, I. G. Scheblykin, T. Pullerits, A. Yartsev and V. Sundström, *J. Phys. Chem. Lett.*, 2014, 5, 2189-2194
- [40] K. Wu, A. Bera, C. Ma, Y. Du, Y. Yang, L. Li and T. Wu, *Phys. Chem. Chem. Phys.*, 2014, 16, 22476].
- [41] C. C. Stoumpos, C. D. Malliakas, M. G. Kanatzidis, *Inorg. Chem.*, 2013, 52, 9019-9038
- [42] H.-H. Fang, F. Wang, S. Adjokitse, N. Zhao, J. Even and M. A. Loi, *Light Sci. Appl*, 2016, 5, e16056
- [43] N. Onoda-Yamamuro, T. Matsuo and H. Suga, *J. Phys. Chem. Solids*, 1990, 51, 1383-1395
- [44] A. D. Wright, C. Verdi, R. L. Milot, G. E. Eperon, M. A. Pérez-Osorio, H. J. Snaith, F. Giustino, M. B. Johnston and L. M. Herz, *Nat. Commun.*, 2016, 7, doi:10.1038/ncomms11755
- [45] R. L. Milot, G. E. Eperon, H. J. Snaith, M. B. Johnston and L. M. Herz, *Adv. Funct. Mater.*, 2015, 25, 6218-6227
- [46] M. Karakus, S. A. Jensen, F. D'Angelo, D. Turchinovich, M. Bonn and M. Cánovas, *J. Phys. Chem. Lett.*, 2015, 6, 4991-4996
- [47] H.-H. Fang, R. Raissa, M. Abdu-Aguye, S. Adjokitse, G. R. Blake, J. Even and M. A. Loi, *Adv. Funct. Mater.*, 2015, 25, 2378-2385
- [48] X. Wu, M. T. Trinh, D. Niesner, H. Zhu, Z. Norman, J. S. Owen, O. Yaffe, B. J. Kudisch and X.-Y. Zhu, *J. Am. Chem. Soc.*, 2015, 137, 2089-2096
- [49] D. Priante, I. Dursun, M. S. Alias, D. Shi, V. A. Melnikov, T. K. Ng, O. F. Mohammed, O. M. Bakr and B. S. Ooi, *Appl. Phys. Lett.*, 2015, 106, 081902
- [50] S. A. Kulkarni, T. Baikie, P. P. Boix, N. Yantara, N. Mathews and S. G. Mhaisalkar, *J. Mater. Chem. A.*, 2014, 2, 9221
- [51] S. M. H. Qaid, M. S. Al Sobaie, M. A. M. Khan, I. M. Bedja, F. H. Alharbi, M. K. Nazeeruddin and A. S. Aldwayyan, *Mater. Lett*, 2016, 164, 498-501
- [52] Z. Chen, C. Yu, K. Shum, J. J. Wang, W. Pfenninger, N. Vockic, J. Midgley and J. T. Kenney, *J. Lumin.*, 2012, 132, 345-349
- [53] K. Tanaka, T. Takahashi, T. Ban, T. Kondo, K. Uchida and N. Miura, *Solid State Commun.*, 2003, 127, 619-623
- [54] V. D'Innocenzo, G. Grancini, M.J.P. Alcocer, A. R. S. Kandada, S.D. Stranks, M. M. Lee, G. Lanzani, H. J. Snaith, A. Petrozza, *Nat. Commun.* 2014, 5, 3586
- [55] N. Sestu, M. Cadelano, V. Sarritzu, F. Chen, D. Marongiu, R. Piras, M. Mainas, F. Quochi, M. Saba, A. Mura, G. Bongiovanni, *J. Phys. Chem. Lett*, 2015, 6, 4566-4572
- [56] M. Hirasawa, T. Ishihara, T. Goto, K. Uchida and N. Miura, *Physica B*, 1994, 201, 427-430
- [57] E. Menéndez-Proupin, P. Palacios, P. Wahnón and J. C. Conesa, *Phys. Rev. B.*, 2014, 90, 045207
- [58] J. Even, L. Pedesseau and C. Katan, *J. Phys. Chem. C.*, 2014, 118, 11566-11572

- [59] A. Miyata, A. Mitioglu, P. Plochocka, O. Portugall, J. T.-W. Wang, S. D. Stranks and R. J. Nicholas, *Nature Phys*, 2015, 11, 582-587
- [60] L. M. Herz, *Annu. Rev. Phys. Chem*, 2016, 67, doi:10.1146/annurec-physchem-040215-112222
- [61] S. Rudin, T. L. Reinecke and B. Segall, *Phys. Rev. B: Condens. Mater. Phys.*, 1990, 42, 11218-11231
- [62] B. Zhang, T. Taliercio, S. Kolliakos, P. Lefebvre, *J. Phys.: Condens. Matter*, 2001, 13, 7053-7074
- [63] C. Quarti, G. Grancini, E. Mosconi, P. Bruno, J. M. Ball, M. M. Lee, H. J. Snaith, A. Petrozza, and F. De Angelis, *J. Phys. Chem. Lett.*, 2013, 5, 279-284
- [64] J. Wei, Y. C. Zhao, H. Li, G. B. Li, J. L. Pan, D. S. Xu, Q. Zhao, D. P. Yu, , *J. Phys. Chem. Lett.*, 2014, 5, 3937-3945
- [65] B. C. O'Regan, P. R. F. Barnes, X. Li, C. Law, E. Palomares and J. M. Marin-Beloqui, *J. Am. Chem. Soc.*, 2015, 137, 5087-5099
- [66] A. Dualeh, T. Moehl, N. Tétreault, J. Teuscher, P. Gao, M. K. Nazeeruddin and M. Grätzel, *ACS Nano*, 2014, 8, 362-373
- [67] H. J. Snaith, A. Abate, J. M. Ball, G. E. Eperon, T. Leitjens, N. K. Noel, S. D. Stranks, J. T.-W. Wang, K. Wojciechowski, W. Zhang, *J. Phys. Chem. Lett*, 2014, 5, 1511-1515
- [68] E. L. Unger, E. T. Hoke, C. D. Bailie, W. H. Nguyen, A. R. Bowring, T. Heumüller, M. G. Christoforo, M. D. McGehee, *Energy Environ. Sci.*, 2014, 7, 3690



UNIVERSITY of the
WESTERN CAPE

CHAPTER 4

THE INFLUENCE OF PEROVSKITE PRECURSOR COMPOSITION ON THE STRUCTURAL PROPERTIES AND PHOTOVOLTAIC ACTIVITY OF MIXED HALIDE MAPbI_{3-x}Cl_x SOLAR CELLS**Abstract**

To observe the role of precursor chemistry in the crystallization and photovoltaic activity of MAPbI_{3-x}Cl_x solar cells and correlate precursor composition to film morphology and photovoltaic activity, a variety of perovskite precursor compositions were explored. Detailed analysis was undertaken using the precursor solutions, 3:1 MAI:PbCl₂, 1:1:4 PbI₂:PbCl₂:MAI and 1:1:1 PbI₂:MAI:MAcI with varying ratios of methylammonium iodide (MAI). Perovskite thin film of 1:1:4 PbI₂:PbCl₂:MAI and 1:1:1 PbI₂:MAI:MAcI demonstrate high crystallinity and a large and compact micrometer-sized crystal domain. To highlight the relevance of the study of the effect of additives (DMSO, Zonyl) in the hole transport material on perovskite morphology and the effect of different electron transport materials (*bis*-PCBM, PCBM and PTCDI) to solar cell operation, findings are correlated with photovoltaic device performance. By using PCBM as the electron transport layer, the device yields the highest hysteresis-free power conversion efficiency (12.8%). The PTCDI-based devices exhibit power conversion efficiency of 8.4%, superior to that of *bis*-PCBM-based devices (6%). The stability of MAPbI₃ and MAPbI_{3-x}Cl_x under inert conditions reveal that degradation is primarily due to loss of fill factor and is more pronounced in the single halide MAPbI₃ in comparison to MAPbI_{3-x}Cl_x. The effect of annealing time on the prototype methylammonium lead iodide perovskite, MAPbI₃, with PEDOT:PSS and PCBM acting as hole and electron selective contacts respectively is briefly discussed. It was concluded that the lead halide perovskite morphology and photovoltaic activity are extremely sensitive to the environmental and experimental conditions at each step of the fabrication process.

4.1 Introduction

Three-dimensional organic-inorganic lead halide perovskites have recently emerged as high-performance photovoltaic materials in the next generation photovoltaic technology due to their high efficiency and the low cost of fabrication [1-4]. Solution-processability, compatibility with large-area deposition techniques, inexpensive input materials, desirable material properties such as bandgap tunability [5], high open-circuit voltage (V_{oc}) [6], strong absorption [7], large absorption coefficients [8] and high carrier mobility [9,10] make this material very attractive for solar energy. Additionally, ambipolar carrier diffusion within lead halide perovskites further highlights the unique excited state character of this peculiar class of semiconductors [11-13]. The versatility in perovskite processing using roll-to-roll compatible methods

including both solution [14-16] and vacuum-based techniques [15,17] potentially enables large flexibility in device design at low fabrication cost.

Besides their extremely low cost and ease of fabrication, perovskite materials offer a wide tunability on composition and structure by adjusting the metal halide framework and the intercalated organic species. The general formula of organic-inorganic halide perovskite is ABX_3 , where A is aliphatic or aromatic ammonium, B is a divalent metal cation (such as Sn^{2+} or Pb^{2+}) and X is a halide anion (I, Cl, or Br⁻). Recently investigated halide perovskites mostly involved Cs^+ [18,19], $CH_3NH_3^+$ [11-16] or $NH_2CHNH_2^+$ [20-22] as A, Pb^{2+} or Sn^{2+} as B and single or mixed halides as X. The choice of material combinations is crucial for determining both the optical and electronic properties (e.g. bandgap, absorption spectra, mobility, diffusion lengths) [23-25]. The most commonly explored organic-inorganic metal halide perovskite, applied in the field of photovoltaics is $CH_3NH_3PbI_3$. This consists of a large organic cation, methylammonium ($CH_3NH_3^+$), Pb^{2+} as the metal cation and I as the halogen anion. Variations of this compound such as $MAPbI_{3-x}Cl_x$ [26,27] and $MAPbI_{3-x}Br_x$ [28-30] have also been investigated.

Perovskite solar cells can be fabricated with a n-i-p or p-i-n heterojunction structure, depending on the position of the electron or hole conducting layer in front of incident light. Currently the two main perovskite solar cell (PSC) architectures are being investigated: mesoporous [2,3,31,32] and planar [15,33-35]. To date all high-efficiency perovskite solar cells reported make use of a (mesoscopic) metal oxide, such as Al_2O_3 , TiO_2 or ZrO_2 which requires a high-temperature sintering process which render these solar cells incompatible with low-cost, lightweight and flexible plastic substrates [34,36,37] and multijunction device architectures [38]. Despite their good performance, metal oxides suffer from a large degree of electronic disorder, resulting in a significant number of sub-bandgap states below the conduction band edge which may limit the maximum voltage attainable by the system and have an impact on the hysteresis [39-41]. TiO_2 usually requires high calcination temperatures (>450 °C) to form high quality crystallization which limits printable applications and may result in the appearance of unfavourable current-density (*J-V*) hysteresis [42,43]. The current high-efficiency perovskite photovoltaic devices also employ hole transporting layer (HTL), 2,2'-7,7'-tetrakis(*N,N*-di-*p*-methoxyphenylamine)-9,9'-spirofluorene (Spiro-OMeTAD) [1,2,44,45]. However, since Spiro-OMeTAD possess low charge carrier mobility, doping of the organic hole transporter with lithium bis(trifluoromethane-sulfonyl)imide (LiTFSI) or with cobalt complexes is necessary to enhance the conductivity, increasing production costs. The high temperature sintering processing of the metal oxides and doping of the hole transport material in mesoporous perovskite devices increase production cost and energy payback time significantly. Hence, it is of great significance to explore new processes for the low-temperature fabrication of organic-inorganic perovskites and provide an understanding of some fundamental material/physical/chemical properties of these materials. In addition

to this, the stability of perovskite based devices remains an open question and perhaps will determine the fate of this remarkable technology in the longer run.

In this study, a low-temperature solution processable planar heterojunction p-i-n structure, ITO/PEDOT:PSS/Perovskite/PCBM/Al, was employed by using the bottom conducting polymer, PEDOT:PSS, not only as the hole-selective transport layer but also the electrode, eliminating the conducting metal oxide electrodes that are usually employed. Low temperature processing offers a wide selection of potential substrates and electrode materials that could be used in devices. Planar architecture potentially provides enhanced flexibility for device optimization, multijunction construction, and investigation of the underlying device physics. Initial focus of the study was on MAPbI₃ and then three different perovskite precursor compositions of the mixed lead halide perovskite, MAPbI_{3-x}Cl_x. All perovskite compositions were synthesized using DMF as a solvent. In the first part of MAPbI_{3-x}Cl_x work, emphasis was placed on the chemical composition of three different compositions specifically on the source of chlorine, which was either an organic source (MACl) or an inorganic source (PbCl₂). Critical to achieving high efficiency devices in high yield is the subsequent deposition of a conformal and chemically inert electron-transporting material to complement the underlying PEDOT:PSS, therefore the efficiency of three electron-transport materials, *bis*-PCBM, PCBM and PTCDI as n-type materials in the fabricated solar cells was explored. Through the judicious selection and optimization of hole- and electron transport layers, a general approach for low-cost solution processing of MAPbI₃ in a way to maximize performance and stability was achieved. Halide mixtures formed by the addition of chloride to the iodide-based lead perovskites were found have beneficial effects on the resulting perovskite morphology and hence device efficiency.

4.2 Experimental

Perovskite precursor solutions

A variety of precursor compositions were explored to observe the role of precursor composition chemistry in the photovoltaic performance of the MAPbI_{3-x}Cl_x perovskite solar cells. For this study, a different batch of solar cells was fabricated to minimize processing parameters variability. Systematic analysis was undertaken using precursor solutions with varying ratios of methylammonium iodide (MAI) and methylammonium chloride (MACl). The range of initial precursor stoichiometries was designed to elucidate the role of Cl⁻ when added as either PbCl₂ or MACl. The precursor solutions exhibiting the best photovoltaic performances were employed for further study and prepared as follows:

The precursor mixed halide solutions with molar ratios were: 3:1 MAI:PbCl₂ (670 mg/mL), 1:1:4 PbI₂:PbCl₂:MAI (640 mg/mL) and 1:1:1 PbI₂:MAI:MACl (638 mg/mL). DMF was employed as the

solvent. The solutions were then filtered with a 0.45 μm PTFE filter. The final stoichiometry of the perovskites in terms of iodide/chloride content was not evaluated.

Note that the denoted stoichiometry of compositional perovskites was defined according to the stoichiometry of the precursors. For further studies, only perovskite samples processed under ambient conditions were employed since the objective of this work is the fabrication of solution-processed efficient solar cells in air.

Perovskite solar cells were fabricated following the procedure reported in Chapter 3. Different volumes of PEDOT:PSS (Clevios PH), DMSO and Zonyl were mixed to investigate the influence of additives in the hole transport material, PEDOT:PSS. The formulated dispersions were filtered through a 0.45 μm RC filter and spin coated at 1000 rpm for 1 min. PCBM, *bis*-PCBM and PTCDI solutions (20 mg/ml in 1:1 ratio of chlorobenzene and chloroform) were spin coated at 1500 rpm for 30 s on top of the perovskite film.

The instrumentation used for these studies was the same as that reported in Chapter 3. Cross section scanning electron microscopy (SEM) measurements were made using a ZEISS 1540XB CrossBeam Scanning microscope equipped with a focused ion-beam (FIB) unit.

4.3 Results and discussion

4.3.1 Effect of perovskite annealing time on MAPbI_3 solar cells

To fabricate efficient perovskite solar cells, several basic components including the fabrication process, key materials of the device interfaces and architecture should be optimized. Film formation is crucial to fabricate planar heterojunctions in most thin-film photovoltaic techniques, it is thus necessary to understand the underlying kinetic and thermodynamic mechanism of perovskite film formation by solution processing.

Thermal annealing parameters are critical in determining film quality and subsequently the performance of the perovskite devices. The optimization process involved annealing of MAPbI_3 films formed from a PbI_2 :2MAI precursor composition at 110 $^\circ\text{C}$ for different annealing times. Diascopic illumination optical microscopy images, **Figure 4.1**, show that thermal annealing is required for the formation of a crystalline perovskite film. The MAPbI_3 perovskite film surface in **Figure 4.1**, changes strikingly as reaction time increases from homogenous films (**Figure 4.1 c-f**) to inhomogeneous films (**Figure 4.1 g-h**) at longer annealing.

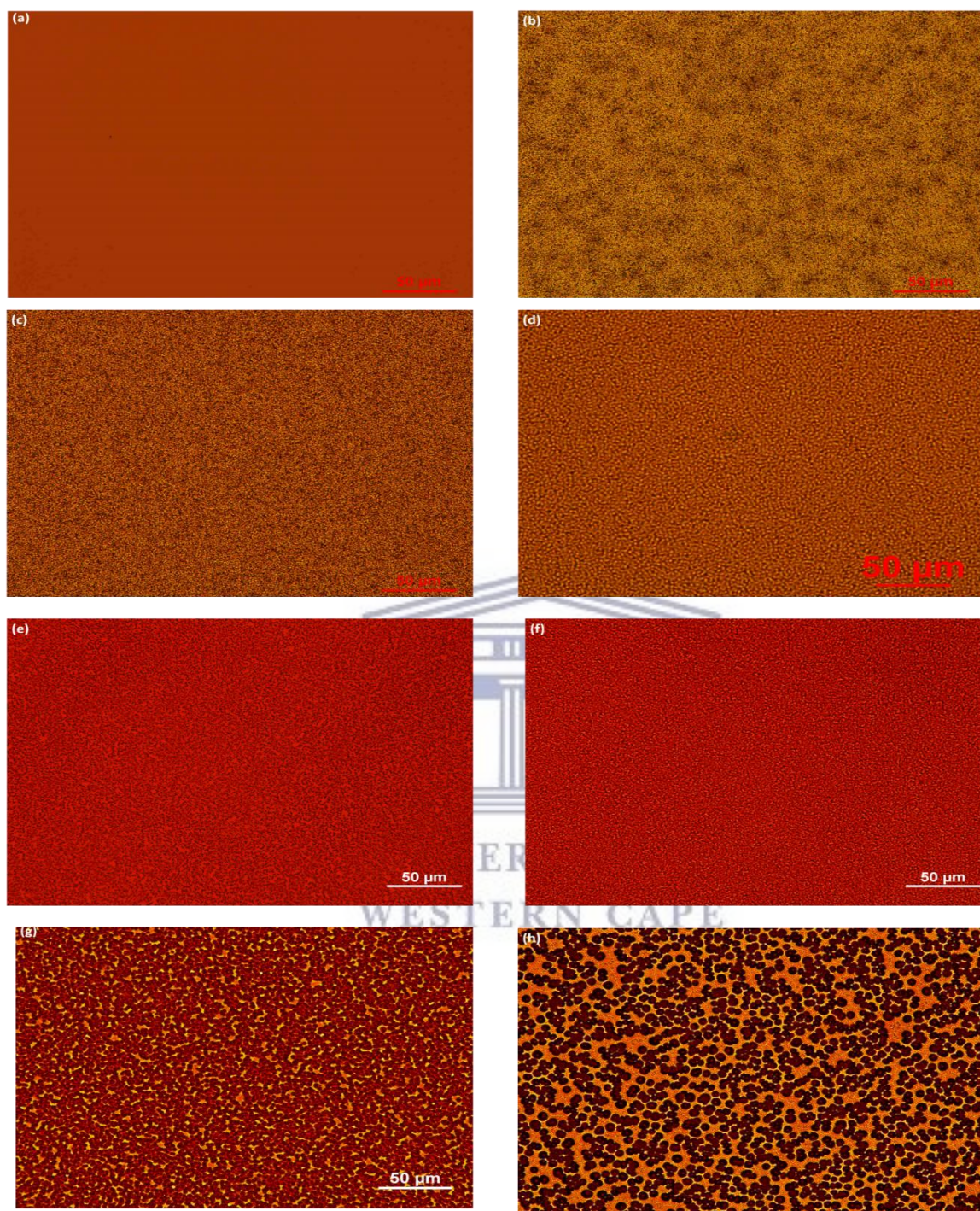


Figure 4.1: Diascopic illumination optical microscopy images of the thermal annealing of MAPbI₃ films for a) 10 min, b) 20 min, c) 30 min, d) 40 min, e) 50 min, f) 60 min, g) 120 min and h) 240 min.

The *J-V* curves of the corresponding devices are shown in **Figure 4.2**. Devices annealed for less than 10 mins hardly showed any photovoltaic activity. Annealing times between 40 and 60 mins resulted in the most efficient devices with 60 mins thermal annealing time leading to the best-performing device, **Table**

4.1. Annealing times longer than 60 mins were detrimental to photovoltaic performance resulting in a significant loss of fill factor. Thermal annealing for 4 h led to the formation of PbI_2 , indicating that the annealing parameters required to form the perovskite film also lead to thermal driven decomposition, although the presence of PbI_2 , caused only a slight reduction in device performance, **Figure 4.2**.

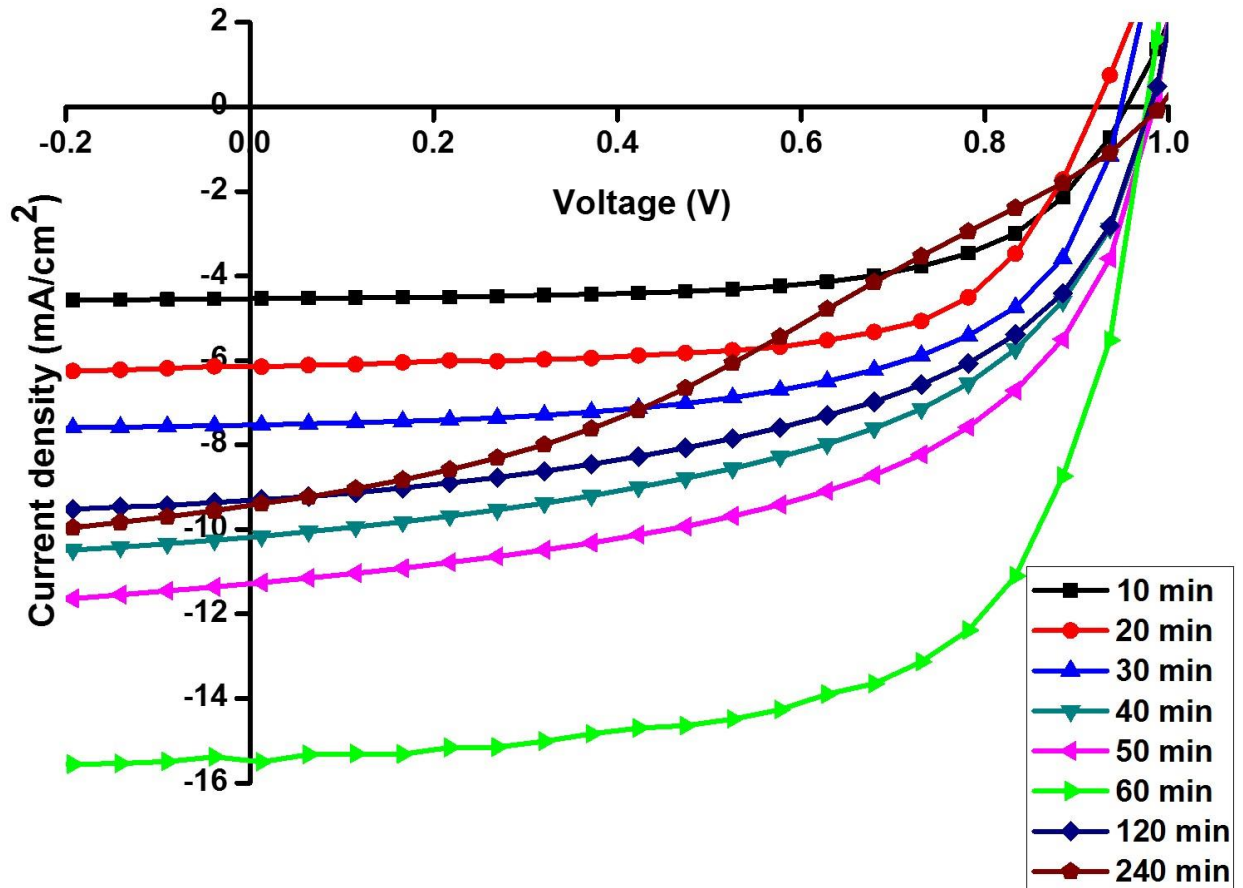


Figure 4.2: Current density-voltage (J - V) characteristics of MAPbI_3 solar cells at different perovskite thermal annealing times under AM1.5G illumination.

Table 4.1: Effect of perovskite thermal annealing times on short-circuit current density (J_{sc}), open-circuit voltage (V_{oc}), fill factor (FF) and power conversion efficiency (PCE) of MAPbI₃ solar cells.

Perovskite annealing time (min)	V_{oc} (V)	J_{sc} (mA/cm ²)	FF	PCE (%)
10	0.956	4.54	0.64	3.4
20	0.951	7.53	0.60	5.4
30	0.982	9.32	0.53	6.0
40	0.985	11.29	0.54	7.5
50	0.995	12.76	0.63	8.0
60	0.980	15.49	0.64	9.7
120	0.983	10.2	0.52	6.5
240	0.978	9.33	0.30	3.4

The dependence of J_{sc} on the annealing time has a similar tendency of temperature-dependent V_{oc} change which can probably be attributed to the relationship;

$$V_{oc} = \left(\frac{k_b T}{q}\right) \ln \left(\frac{J_{sc}}{J_0} + 1\right) \quad (4.1)$$

where V_{oc} is the open circuit voltage, k_b is the Boltzmann constant, T is the temperature, q is the elementary charge, J_{sc} is the short circuit current and J_0 is the reverse saturation current density due to radiative and non-radiative recombination.

Consequently, PCE increases with increasing annealing time. Our results reveal that the annealing conditions of the perovskite layers are critical for the photovoltaic performance of the final device in agreement with previous reports [33,46-48].

4.3.2. Effect of perovskite precursor composition

All lead halide perovskite fabrication protocols combine an organic salt with a lead salt to produce a lead halide perovskite thin film. Multiple solution-based fabrication methodologies to form lead halide perovskite materials have been reported. In this work, a one-step fabrication protocol consisting of mixing different compositions of both the organic (MAI and/or MACl) and inorganic (PbI₂ and/or PbCl₂) precursors in a single solution, using DMF as a solvent, is employed to cast perovskite films and subsequent annealing to drive complete formation of the perovskite phase. MAPbI_{3-x}Cl_x precursor solutions consisting of PbCl₂:3MAI, PbCl₂:PbI₂:4MAI and PbI₂:MAI:MACl molar ratios were prepared and the resulting

morphologies of the different compositions are presented in the diascopic illumination optical microscopy and SEM images in **Figure 4.3**.

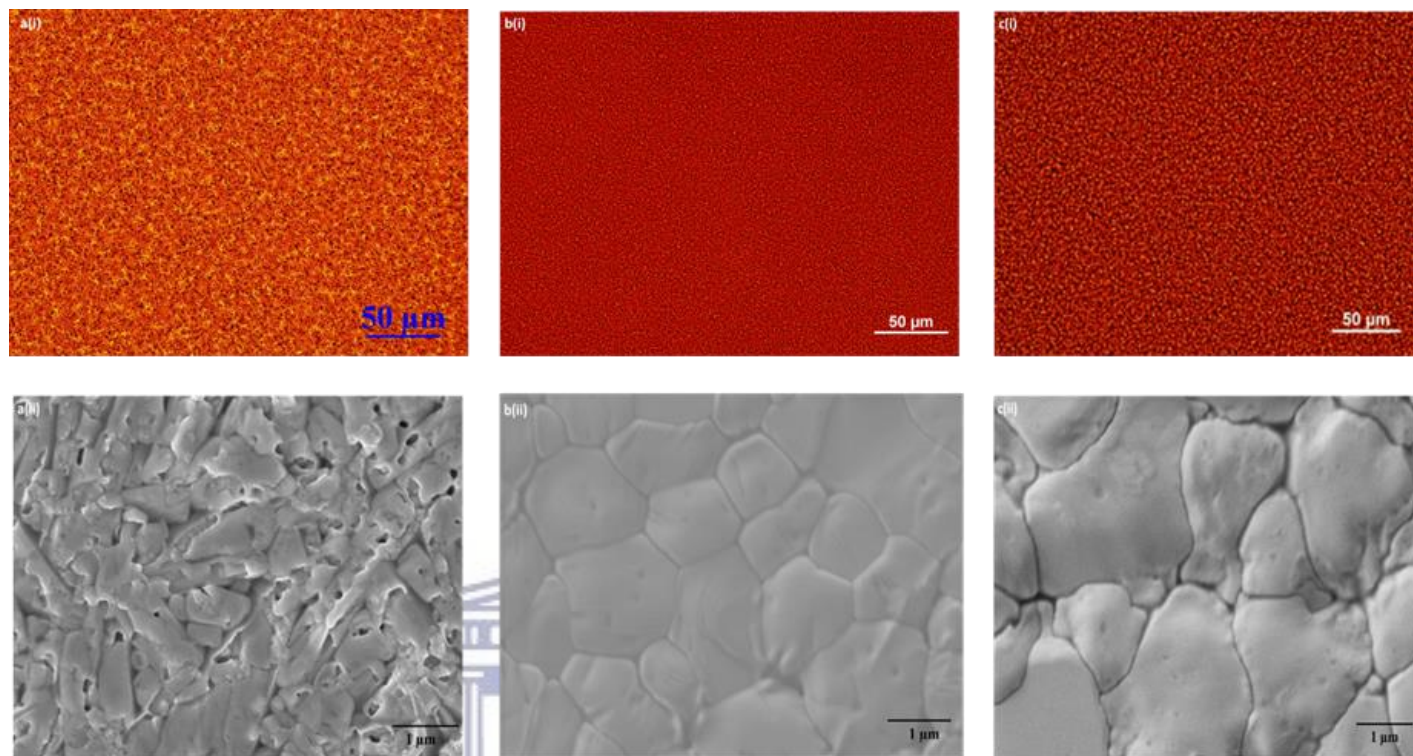


Figure 4.3: (i) Diascopic illumination optical microscopy images on glass and (ii) SEM images on Glass/ITO/PEDOT:PSS substrates of (a) MAPbI_{3-x}Cl_x (PbCl₂:3MAI), (b) MAPbI_{3-x}Cl_x (PbCl₂:PbI₂:4MAI) and (c) MAPbI_{3-x}Cl_x (PbI₂:MAI:MACl) processed under ambient conditions.

In comparison to PbCl₂:3MAI (**Figure 4.3a**), PbCl₂:PbI₂:4MAI (**Figure 4.3b**) and PbI₂:MAI:MACl (**Figure 4.3c**), exhibits higher crystallinity and increased interfacial area for exciton dissociation, all of which lead to an enhancement of device performance. The chloride ions and the excess of organic cations slow down the crystallization rate, leading to the growth of large, continuous crystal domains within the film and high degree of surface coverage. **Figure 4.3** shows that each fabrication protocol produces a different perovskite morphology (grain size/shape, film roughness and surface coverage), and in turn these different morphologies influence photovoltaic device performance, **Figure 4.4** and **Table 4.2**. PbCl₂:3MAI perovskite films are extremely moisture-sensitive until fully crystallized, so the films were processed in a dry nitrogen-filled glovebox. Exposure of the perovskite film to air was found to be detrimental to device performance as shown in **Figure 4.4**. Perovskite compositions, PbCl₂:PbI₂:4MAI and PbI₂:MAI:MACl exhibited similar photovoltaic performance parameters. In comparison to the single-halide MAPbI₃, the mixed halide MAPbI_{3-x}Cl_x, **Figure 4.4**, exhibits superior photovoltaic performance.

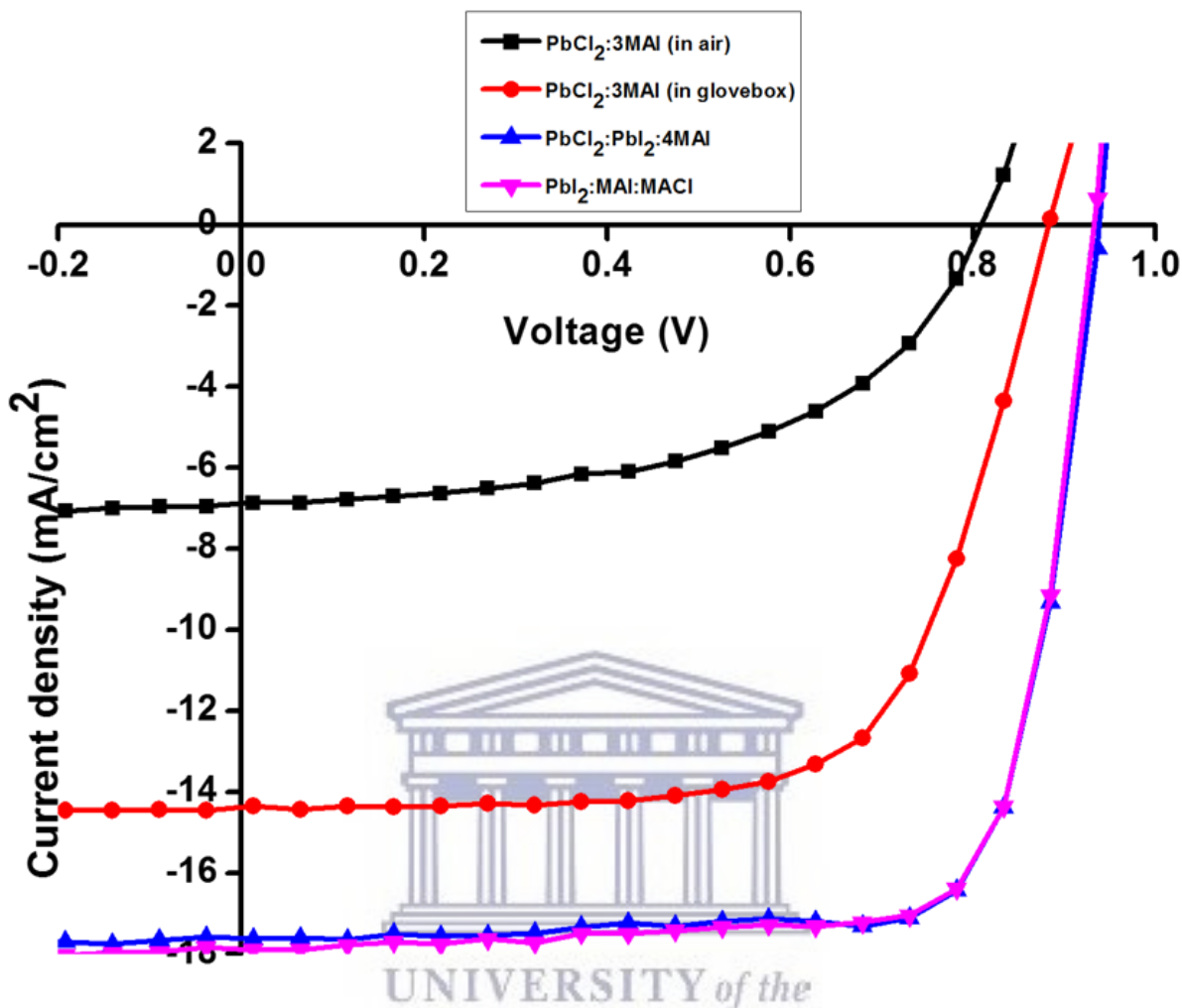


Figure 4.4: Current density-voltage (J - V) characteristics of different perovskite precursor compositions of $\text{MAPbI}_{3-x}\text{Cl}_x$ solar cells under AM1.5G illumination.

Table 4.2: Photovoltaic performance parameters of different perovskite precursor compositions of $\text{MAPbI}_{3-x}\text{Cl}_x$ solar cells.

$\text{MAPbI}_{3-x}\text{Cl}_x$ precursor composition	Perovskite annealing	V_{oc} (V)	J_{sc} (mA/cm^2)	FF	PCE (%)
$\text{PbCl}_2:3\text{MAI}$	in air	0.811	6.88	0.53	2.9
$\text{PbCl}_2:3\text{MAI}$	in glovebox	0.881	14.31	0.68	8.6
$\text{PbCl}_2:\text{PbI}_2:4\text{MAI}$	in air	0.936	17.63	0.78	12.9
$\text{PbI}_2:\text{MAI}:\text{MACl}$	in air	0.939	17.88	0.77	12.8

A previous work of our group focused on a detailed spectroscopic, microscopic and photovoltaic performance of $\text{MAPbI}_{3-x}\text{Cl}_x$ ($\text{PbCl}_2 + \text{PbI}_2 + 4\text{MAI}$) [49], so in the following studies we concentrate on $\text{PbCl}_2:3\text{MAI}$ and $\text{PbI}_2:\text{MAI}:\text{MACl}$.

The J - V curves of the best-performing $\text{PbCl}_2:3\text{MAI}$ and $\text{PbI}_2:\text{MAI}:\text{MACl}$ solar cells measured in the dark and under one sun illumination (100 mW/cm^2) at AM1.5 conditions and the corresponding semi-logarithmic current-voltage characteristics and external quantum efficiencies (EQE) are shown in **Figure 4.5**. Both precursor compositions allowed the fabrication of diodes with excellent rectification and low-reverse-bias dark currents, **Figure 4.5a(i,ii)** and **Figure 4.5b(i,ii)**.



UNIVERSITY of the
WESTERN CAPE

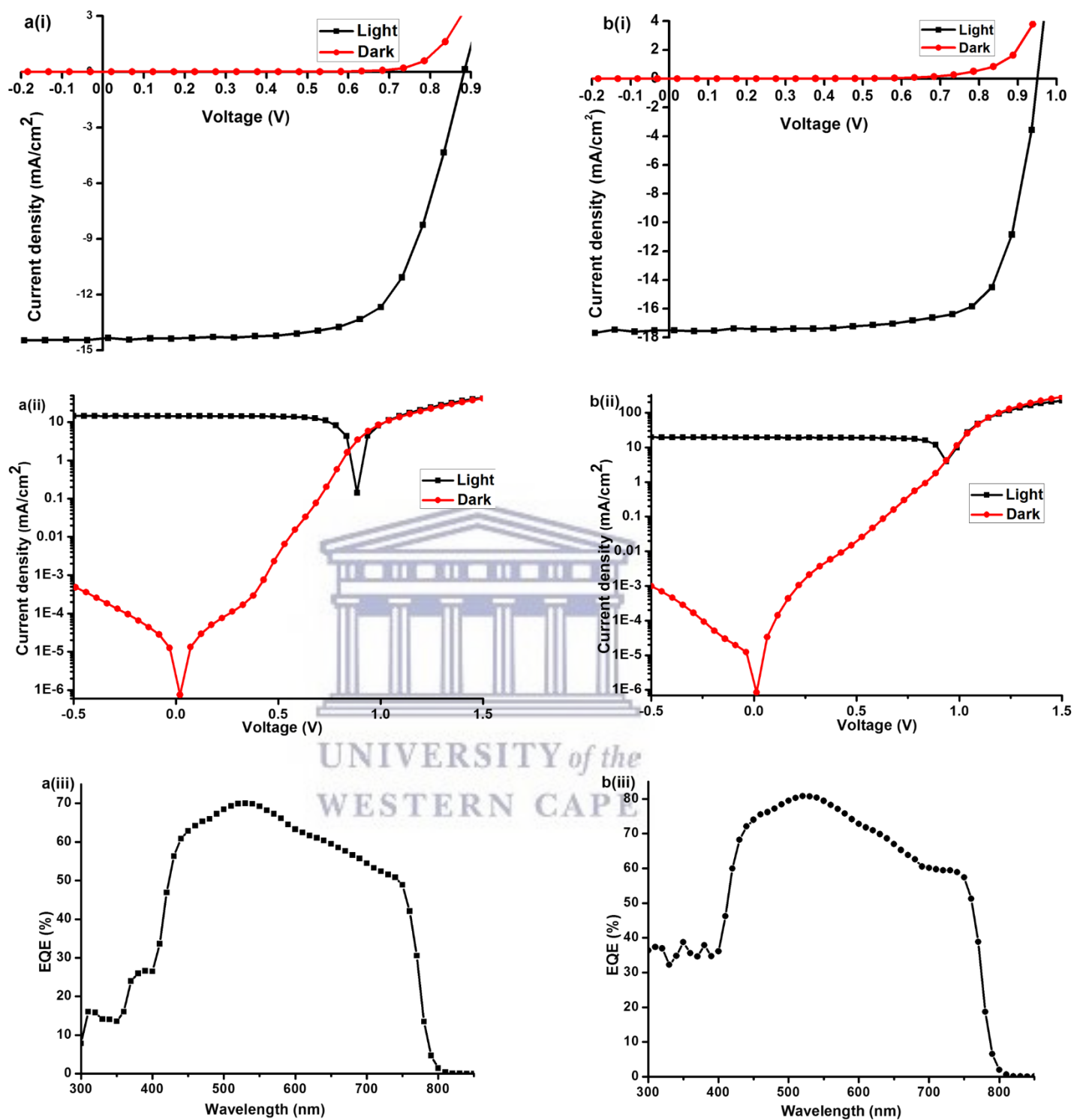


Figure 4.5: i) J - V characteristics, ii) the corresponding semi-logarithmic current-voltage characteristics and iii) external quantum efficiency (EQE) spectra of a) PbCl₂:3MAI and b) PbI₂:MAI:MACl.

The EQE spectra of the PbCl₂:3MAI and PbI₂:MAI:MACl devices illuminated by monochromatic light are shown in **Figure 4.5a(iii)** and **Figure 4.5b(iii)**. The absorption onset in EQE is identical regardless of the

change in precursor composition indicating no change in bandgap. The EQE peaks around 550 nm reaching a maximum external quantum efficiency of $\sim 70\%$ and 80% for $\text{PbCl}_2:3\text{MAI}$ and $\text{PbI}_2:\text{MAI}:\text{MACl}$ respectively. In the blue (300-450 nm) and the near-IR (650-800 nm) the spectral response is substantially smaller leading to a significant photocurrent reduction. This loss can be attributed to parasitic absorption in the ITO and PEDOT:PSS layer as well as the poor reflectance of the metal back electrode (aluminum). The integrated short circuit currents based on EQE were 14.25 and 17.83 mA/cm^2 which were well matched with the J_{sc} from the solar simulators, **Table 4.2**. Power conversion efficiencies of 8.2 and 12.3% were obtained for the $\text{PbCl}_2:3\text{MAI}$ and $\text{PbI}_2:\text{MAI}:\text{MACl}$ devices respectively. Hysteresis effects during current-voltage measurements have been reported for perovskite solar cells. **Figure 4.6** shows the hysteresis behavior at 20 mV/s . The hysteresis in $\text{MAPbI}_{3-x}\text{Cl}_x$ solar cells is clearly sensitive to the precursors utilized for the perovskite growth as it is negligible in $\text{PbI}_2:\text{MAI}:\text{MACl}$ solar cells in comparison to $\text{PbCl}_2:3\text{MAI}$ as exhibited in **Figure 4.6**.

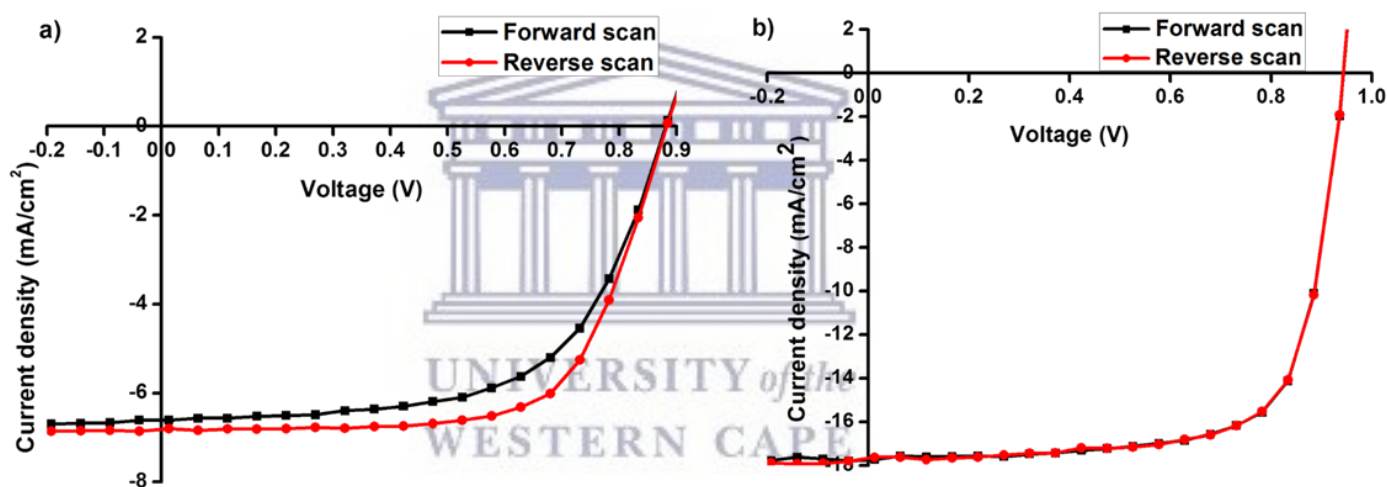


Figure 4.6: Scan rate- and direction-dependent forward and reverse J - V scans of a) $\text{PbCl}_2:3\text{MAI}$ and b) $\text{PbI}_2:\text{MAI}:\text{MACl}$ solar cells.

The differences in the hysteretic behaviour that we observed may also be a consequence of differences perovskite film morphology as shown in **Figure 4.3**. The defects and crystal grain boundaries of the $\text{PbCl}_2:3\text{MAI}$ perovskite crystallites act as traps of carriers which would aggravate the charge recombination. The hysteresis effect, which causes the inaccuracy in evaluating cell efficiency has been reported to be [50-53] related to the crystallinity and interfaces of the perovskite in agreement with our observations. Since our aim was to fabricate low-temperature solution-processable perovskite solar cells in air, the following studies were carried out on $\text{MAPbI}_{3-x}\text{Cl}_x$ ($\text{PbI}_2:\text{MAI}:\text{MACl}$) solar cells which are stable for processing under ambient conditions.

4.3.3 MAPbI_{3-x}Cl_x perovskite layer morphology

4.3.3.1 Scanning electron microscopy (SEM)

The ITO/PEDOT:PSS/MAPbI_{3-x}Cl_x/PCBM/Al planar solar cells employed in this work are effectively a distributed heterojunction. Indium tin oxide (ITO) has good moisture barrier properties, prevents the egress of the methylammonium iodide and has been reported to greatly slow down or completely prevent some degradation mechanisms in perovskite devices [54]. A layer of conducting polymer, PEDOT:PSS forms the oxide-free and low-temperature processable hole-transport material. PEDOT:PSS has high transparency, high conductivity and appropriate energy levels making it a suitable transparent electrode for various photovoltaic applications [55]. In comparison to metal oxides, the fullerene (C₆₀) employed in our device as the electron transport material does not require high-temperature treatment and thus opens the possibility of low-temperature processing on flexible substrates [36,56]. Moreover, the fullerene layer can passivate the charge trap states, which leads to hysteresis-less, high power conversion efficiencies for lead-based perovskite solar cells with p-i-n architectures [57,58]. A typical cross-sectional MAPbI_{3-x}Cl_x perovskite solar cell SEM image is shown in **Figure 4.7**.

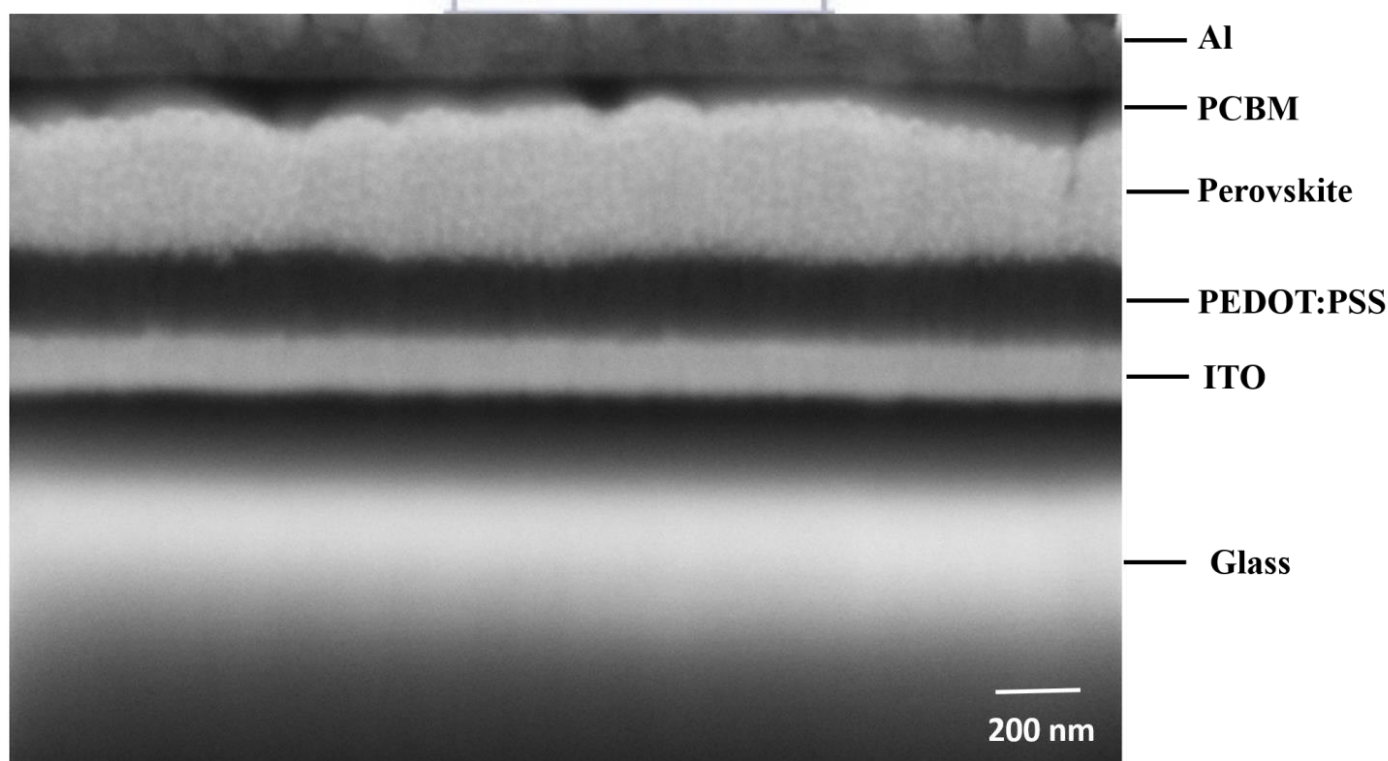


Figure 4.7: Cross-sectional SEM image of solution processed MAPbI_{3-x}Cl_x planar heterojunction perovskite solar cell.

In **Figure 4.7**, distinct layers with different features and contrast are exhibited, confirming that the fabricated devices indeed have a planar heterojunction architecture where the perovskite absorber layer is well implemented into the device with intimate contact to adjacent layers. Film thicknesses from **Figure 4.7** were in good agreement with the thicknesses measured using a surface profilometer.

4.3.3.2 X-ray diffraction spectroscopy (XRD)

To probe the influence of PEDOT:PSS on the $\text{MAPbI}_{3-x}\text{Cl}_x$ structure, X-ray diffraction spectroscopy (XRD) measurements were carried out. $\text{MAPbI}_{3-x}\text{Cl}_x$ perovskite films were spin-coated on Glass/ITO/ PEDOT:PSS substrates. **Figure 4.8** presents the XRD pattern of the $\text{MAPbI}_{3-x}\text{Cl}_x$ film deposited on substrates. Characteristic perovskite diffraction peaks at about 15.4° , 29.5° and 43.4° can be assigned to (110), (220) and (330) planes of crystalline $\text{MAPbI}_{3-x}\text{Cl}_x$, respectively.

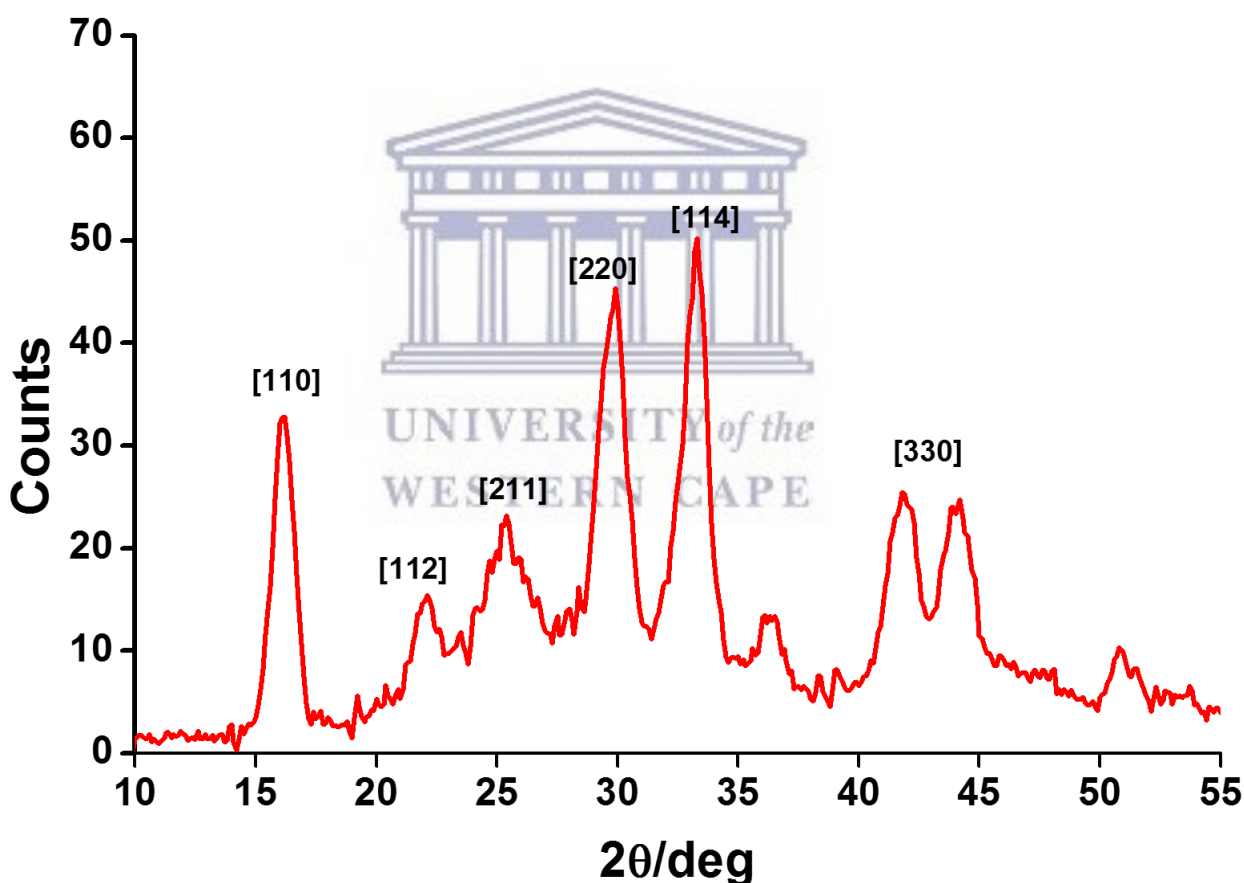


Figure 4.8: X-ray diffraction (XRD) spectrum of a $\text{CH}_3\text{NH}_3\text{PbI}_{3-x}\text{Cl}_x$ film prepared by spin-coating of the precursor solution on a Glass/ITO/PEDOT:PSS substrate and annealing at 110°C .

X-ray diffraction evidences the formation of a tetragonal perovskite phase [59] in agreement with previously reported XRD data [15,50,60]. According to Liu *et al.*, [15] there is often a tiny signature peak

at 12.65° , corresponding to a low-level impurity of PbI_2 . The absence of the aforementioned peak, indicating no secondary phase, in the present perovskite film suggests complete consumption of PbI_2 via solution-processing.

4.3.4 Effect of charge transport material on device performance

Generally, hole selective and electron selective layers are used between the perovskite layer and the electrodes, not only to extract the charges selectively, but also to maximize the photovoltaic performance of the solar cells [61,62]. In this we investigate the effect of the hole-and electron-transport materials on perovskite film morphology and device performance.

4.3.4.1. Effect of additives in hole transport material on perovskite morphology and photovoltaic performance

A different approach to ensure the formation of homogeneous films is the use of additives in the spin-coating solution that affect the crystallization and formation of the perovskite layer. In this work the hole transport material, PEDOT:PSS, will be employed as an alternative to spiro-OMeTAD. The effect of additives, DMSO and Zonyl, in PEDOT:PSS composition is investigated and the results are shown in **Figure 4.9** and **Figure 4.10**. The quality of the resultant perovskite films strongly correlates with the content of DMSO added to the PEDOT:PSS as is apparent from the diascopic (transmitted) illumination optical microscopy images, **Figure 4.9** and scanning electron microscopy images, **Figure 4.10**.

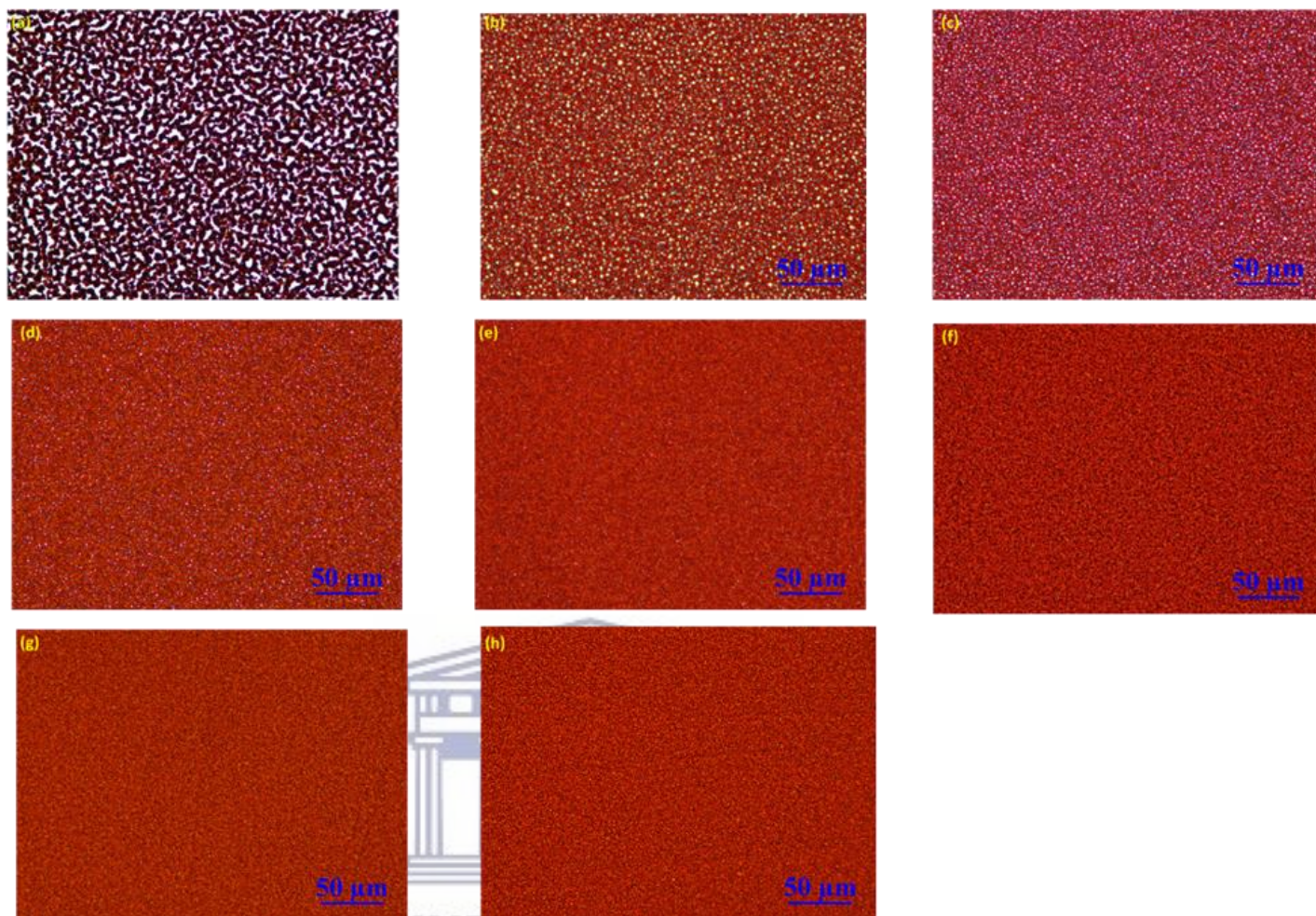


Figure 4.9: Diascopic illumination optical microscopy images of additives in PEDOT:PSS of $\text{MAPbI}_{3-x}\text{Cl}_x$ on a) Glass/ITO and on PEDOT:PSS (Clevios 1000) processed with (b) 0% DMSO, 0% Zonyl[®] FS-300; (c) 0% DMSO, 0.7% Zonyl[®] FS-300; (d) 2.5% v/v DMSO, 0.7% Zonyl[®] FS-300; (e) 5% v/v DMSO, 0% Zonyl[®] FS-300; (f) 5% v/v DMSO, 0.7% Zonyl[®] FS-300; (g) 10% v/v DMSO, 0.7% Zonyl[®] FS-300; (h) 20% v/v DMSO, 0.7% Zonyl[®] FS-300.

Figure 4.9 shows that unfavourable interactions between the substrate (Glass/ITO or Glass/ITO/PEDOT:PSS) and the perovskite precursor mixture can lead to the formation of non-uniform films with pinholes and low substrate area coverage. Perovskite layers processed on either Glass/ITO or on neat PEDOT:PSS show many defects in the form of pinholes (**Figures 4.9a and b**). The addition of DMSO and/or Zonyl reduces the number and size of these defects in the perovskite films (**Figure 4.9c-e**). By using both additives and adding $\geq 5\%$ DMSO continuous layers of uniform pinhole-free polycrystalline films are formed (**Figure 4.9 f-h**). The corresponding SEM images showing a profound effect of additives on the morphology of the perovskite thin films are shown in **Figure 4.10**.

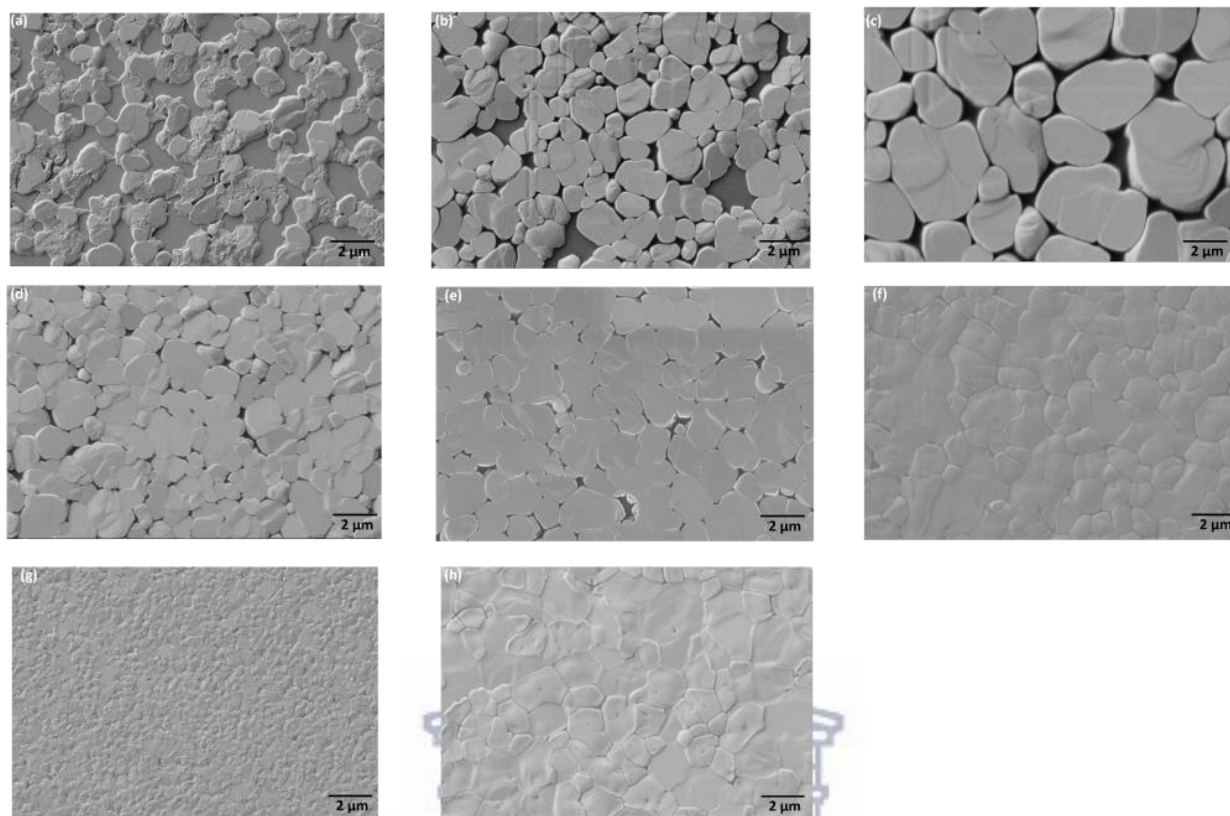


Figure 4.10: SEM images of additives in PEDOT:PSS of $\text{MAPbI}_{3-x}\text{Cl}_x$ on a) Glass/ITO and on PEDOT:PSS (Clevios 1000) processed with (b) 0% DMSO, 0% Zonyl[®] FS-300; (c) 0% DMSO, 0.7% Zonyl[®] FS-300; (d) 2.5% v/v DMSO, 0.7% Zonyl[®] FS-300; (e) 5% v/v DMSO, 0% Zonyl[®] FS-300; (f) 5% v/v DMSO, 0.7% Zonyl[®] FS-300; (g) 10% v/v DMSO, 0.7% Zonyl[®] FS-300; (h) 20% v/v DMSO, 0.7% Zonyl[®] FS-300.

Figure 4.9 and **Figure 4.10** prove that additives can participate in the perovskite formation and play a role in modulating the dynamics of perovskite crystal growth. To highlight the relevance of our study of the effect of additives on perovskite morphology to solar cell operation, we correlated our findings with the performance of the matching devices. The discontinuous films with micrometer-sized pinholes between island-like perovskite clusters because of the de-wetting of the precursor solution from the substrate, **Figure 4.10(a-c)**, leads to shunting via direct contact between the n- and p-type layers and consequently reduce the device performance, **Figure 4.11** and **Table 4.3**.

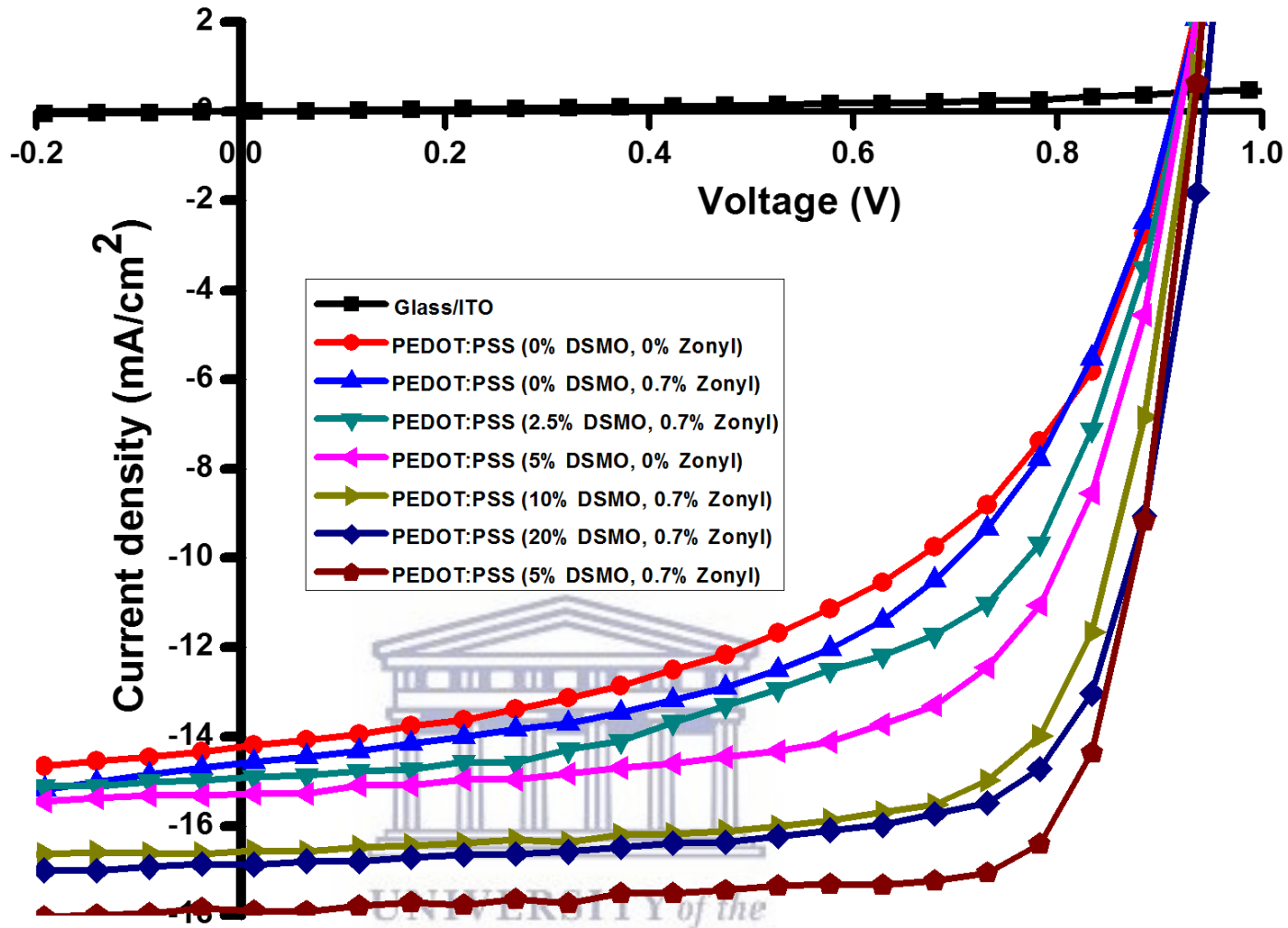


Figure 4.11: J - V characteristics of effect of additives in PEDOT:PSS on of $\text{MAPbI}_{3-x}\text{Cl}_x$ solar cells under AM1.5G illumination.

The defects and crystal grain boundaries of the perovskite crystallites in **Figure 4.10a-e** act as traps of carriers which aggravate the charge recombination. Larger homogeneous grains result in fewer grain boundaries and thus fewer trap states and recombination centers [63]. The presence of DMSO in the conductive film aid in the nucleation of the perovskite crystallites, leading to the formation of a pinhole-free perovskite layer. **Figure 4.11** shows that elimination of heterogeneity in perovskite films is crucial to maximizing device performance.

Table 4.3: The effect of PEDOT:PSS additives on the photovoltaic performance of MAPbI_{3-x}Cl_x perovskite solar cells.

Substrate	DMSO (% v/v)	Zonyl (% v/v)	V_{oc} (V)	J_{sc} (mA/cm ²)	FF	PCE (%)
Glass/ITO	-	-	-	-	-	-
Glass/ITO/PEDOT:PSS	0	0	0.914	14.23	0.51	6.6
Glass/ITO/PEDOT:PSS	0	0.7	0.915	14.59	0.54	7.2
Glass/ITO/PEDOT:PSS	2.5	0.7	0.920	14.91	0.59	8.5
Glass/ITO/PEDOT:PSS	5	0	0.923	15.28	0.65	9.1
Glass/ITO/PEDOT:PSS	5	0.7	0.939	17.88	0.76	12.8
Glass/ITO/PEDOT:PSS	10	0.7	0.931	16.57	0.71	10.9
Glass/ITO/PEDOT:PSS	20	0.7	0.948	16.86	0.73	11.5

The correlation of data in **Figure 4.9** and **Figure 4.10** to device performance parameters, **Table 4.3**, shows that highly ordered perovskite crystals lead to higher short circuit currents on average, and more reproducible devices. The full surface coverage of the films provides more absorption to contribute to the high J_{sc} . Upon doping with additives, PEDOT:PSS conductivity increases, and the overall performance of the device improves, especially the fill factor and J_{sc} .

The role of the additives DMSO and Zonyl is still not fully understood and is currently under investigation. DMSO acts as a solvent of perovskite precursors and mediates the nucleation and crystallization at the PEDOT:PSS and Zonyl is often used to improve the wettability of the PEDOT:PSS dispersion on hydrophobic substrates [64]. Savagatrup *et al.*, [65] reported that the mechanical properties and the surface nano-morphology of PEDOT:PSS layers can be altered by DMSO and Zonyl additives. Though the role of additives is still not fully understood, this study supports the logical conclusion that maximizing surface coverage by incorporating additives is a successful strategy to maximize device performance.

4.3.4.2. Effect of electron transport material on perovskite photovoltaic performance

Critical to achieving high efficiency devices in high yield is the subsequent deposition of a conformal and chemically inert electron-transporting material to complement the underlying PEDOT:PSS. In this work, we optimized the photovoltaic performance of planar heterojunction MAPbI_{3-x}Cl_x perovskite solar cells using three different solution-processed electron transporter materials, PCBM, *bis*-PCBM and PTCDI. As electron transport materials, other than C₆₀, many kinds of perylene tetracarboxylic diimide (PTCDI) have been used due to their n-type property and the tenability of their electronic and optical properties by

functionalization [66,67]. PTCDI is a low-cost commercial pigment, highly resistant to degradation/bleaching and supports electron transport [66,67]. The energy level alignment diagrams and the J - V characteristics of the respective devices are shown in **Figure 4.12** and **Figure 4.13**.

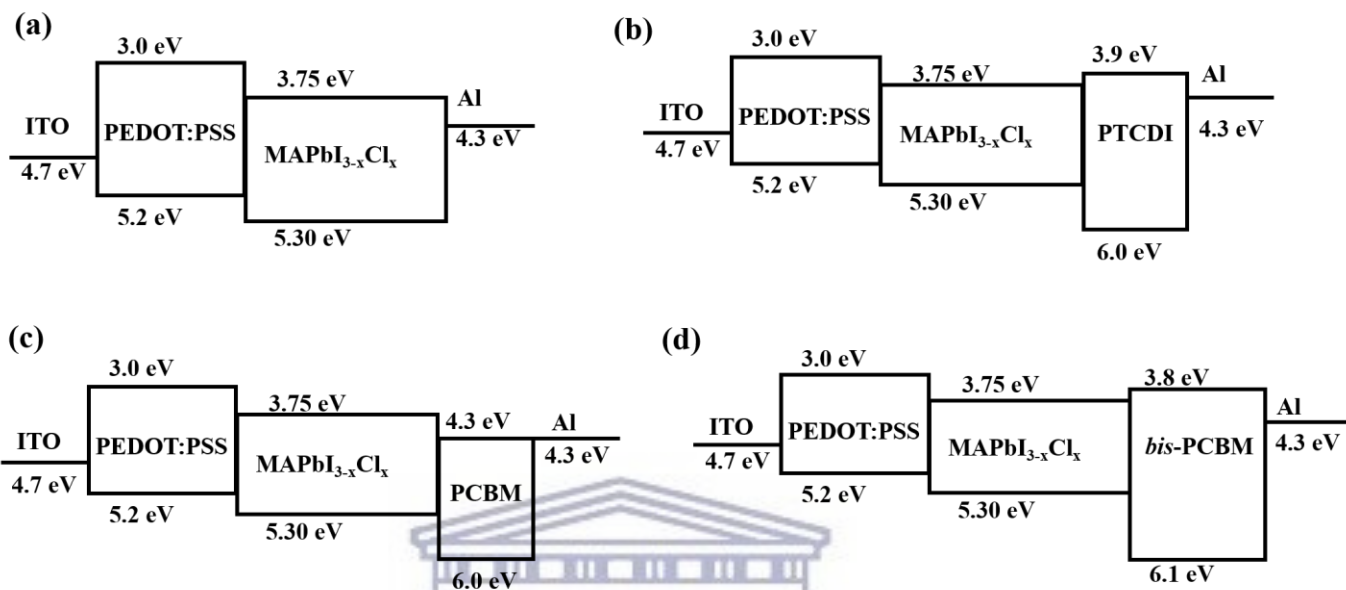


Figure 4.12: Schematic of energy level alignment for different materials acting as electron transport layers in perovskite $\text{MAPbI}_{3-x}\text{Cl}_x$ solar cells: a) $\text{MAPbI}_{3-x}\text{Cl}_x$ b) PTCDI [67] c) PCBM and d) *bis*-PCBM [68].

Figure 4.12 shows that the three materials all possess deep highest occupied molecular orbital (HOMO) levels, which is anticipated to result in effective hole-blocking and hence optimal photovoltaic performance. The short-circuit current density (J_{sc}), open-circuit voltage (V_{oc}), fill factor (FF) and power conversion efficiency (PCE) and the corresponding EQE spectra are shown in **Figure 4.13**. All devices with PCBM, *bis*-PCBM or PTCDI as electron transport layers show typical photovoltaic behavior, **Figure 4.13** and the photovoltaic performance metrics are tabulated in **Table 4.1**.

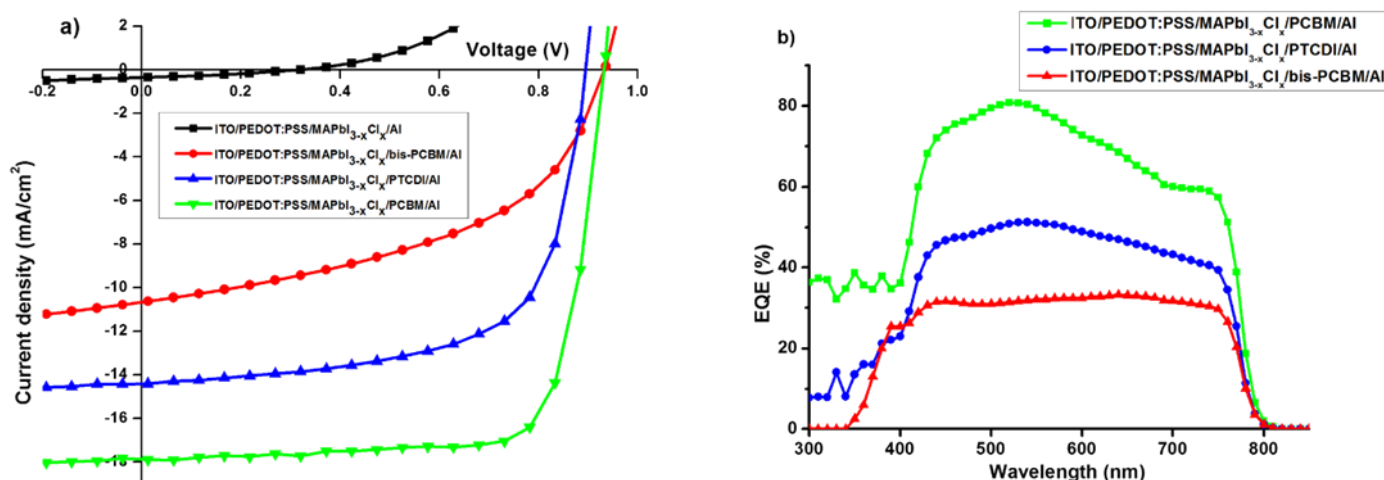


Figure 4.13: J - V characteristics of MAPbI_{3-x}Cl_x devices employing PCBM, *bis*-PCBM and PTCDI as electron transport materials (a) and their corresponding EQE spectra (b).

Table 4.4: Performance parameters of perovskite solar cells with different electron transport materials.

Device structure	V_{oc} (V)	J_{sc} (mA/cm ²)	FF	PCE (%)
Glass/ITO/PEDOT:PSS/ MAPbI _{3-x} Cl _x /Al	0.25	0.29	0.31	0.02
Glass/ITO/PEDOT:PSS/MAPbI _{3-x} Cl _x / <i>bis</i> -PCBM/Al	0.934	10.67	0.48	6.0
Glass/ITO/PEDOT:PSS/MAPbI _{3-x} Cl _x /PTCDI/Al	0.897	14.43	0.65	8.4
Glass/ITO/PEDOT:PSS/MAPbI _{3-x} Cl _x /PCBM/Al	0.940	17.92	0.76	12.8

The photovoltaic performance of the solar cells employing the different electron transport materials decreases in the order, PCBM>PTCDI>*bis*-PCBM because of significantly improved J_{sc} and FF, **Figure 4.12a**. This is corroborated with the EQE data showing a gradual decrease in intensity, **Figure 4.12b**. **Figure 4.12** and **Figure 4.13** show that ITO/PEDOT:PSS/MAPbI_{3-x}Cl_x/PCBM/Al results in overall better energy alignment with the perovskite conduction band than both *bis*-PCBM and PTCDI resulting in the highest device efficiency. In organic/polymer solar cells, it has been reported that in comparison to *mono*-adducts, *bis*-adducts can afford higher V_{oc} , J_{sc} and FF due to their higher LUMO levels [69-71].

No enhancement of photovoltaic parameters was observed in our work as shown in **Table 4.4**, instead the opposite effect was observed. Devices employing *bis*-PCBM mainly suffer from low FF. This is attributed to incomplete coverage of the perovskite layer hence the electrode layer, Al, will be in direct contact with the perovskite absorber layer resulting in poor photovoltaic performance. Kaltenbrunner *et al.*, [56] reported efficient planar heterojunction MAPbI_{3-x}Cl_x solar cells using PTCDI as an electron transporting material.

However vacuum sublimation was used for PTCDI deposition unlike spin-coating that was used in this work. Vacuum depositions are incompatible with low manufacturing costs.

To determine the feasibility of PCBM as an electron acceptor in our planar heterojunction architecture, we compared MAPbI_{3-x}Cl_x perovskite devices with and without PCBM where the MAPbI_{3-x}Cl_x perovskite acts as not only the photoactive absorber layer but also the electron transport material. In the absence of PCBM, the ITO/PEDOT:PSS/ MAPbI_{3-x}Cl_x /Al device does not exhibit any meaningful power that could be extracted from the fourth quadrant of the light current density-voltage curve, **Figure 4.13**. The fact that there is no significant photovoltaic performance observable in ITO/PEDOT:PSS/MAPbI_{3-x}Cl_x/Al devices despite the reported ambipolar characteristics of organic-inorganic halide perovskites and their use as n-transporters [1,72,73] suggest that the PEDOT:PSS/MAPbI_{3-x}Cl_x interface is less efficacious in promoting exciton dissociation and charge transfer, correlating with the energy misalignment of the electronic levels of the device components, **Figure 4.12**, being unfavourable for both charge transport and collection. The lack of efficient exciton dissociation interfaces in the ITO/PEDOT:PSS/ MAPbI_{3-x}Cl_x /Al compared to the other devices is mainly responsible for the remarkable difference in device performance of the four types of devices presented in **Figure 4.13**. It is worth mentioning that the PCBM layer thickness is very critical for achieving high performance.

4.3.5 Perovskite solar cell stability

For practical applications, not only the power conversion efficiency but also the stability and lifetime of the photovoltaic device is of importance. The environmental stability of perovskite solar cells is mainly affected by the intrinsic instabilities of the perovskite absorber, as well extrinsic factors which degrade the device as a whole and remains a key challenge to the commercialization of perovskite solar cells. The stability of unencapsulated MAPbI₃ and MAPbI_{3-x}Cl_x solar cells under inert conditions in a nitrogen-filled glovebox was monitored for 6 months and the *J-V* performance parameters are shown in **Figure 4.14** and tabulated in **Table 4.5** and **Table 4.6**.

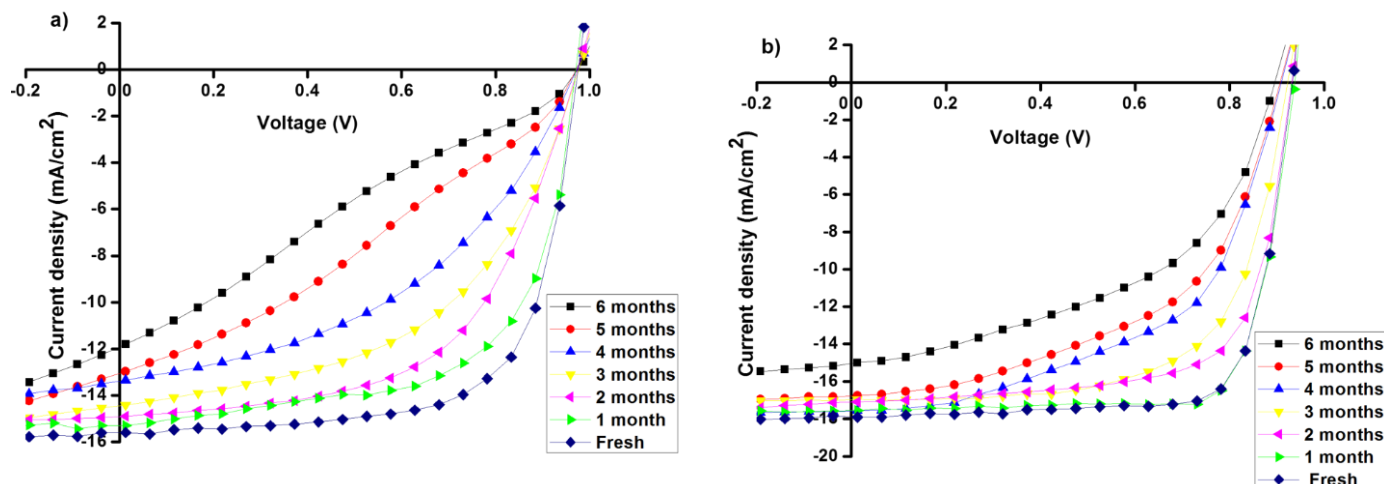


Figure 4.14: J-V response and photovoltaic performance parameters for typical freshly-prepared and aged (a) MAPbI₃ and (b) MAPbI_{3-x}Cl_x perovskite solar cells under simulated AM 1.5G in an inert atmosphere.

In comparison to MAPbI₃, **Figure 4.14a** and **Table 4.5**, MAPbI_{3-x}Cl_x devices, **Figure 4.14b** and **Table 4.6**, show high performance metrics and enhanced stability under inert conditions. This stability is attributed to doping with chloride ions in the crystal structure. After 6 months, the MAPbI₃ device retained 33% of its original power conversion efficiency whereas the MAPbI_{3-x}Cl_x device retained 50% due to a reduction in both J_{sc} and FF because of oxidation, **Table 4.5** and **Table 4.6**. This is indicative of the hygroscopic nature of PEDOT:PSS which degrades the ITO electrode and decomposes the perovskite absorber layer. It is interesting that the V_{oc} is not too much influenced by the degradation, while the reduced J_{sc} and FF are affecting the final performance much more in both MAPbI₃ and MAPbI_{3-x}Cl_x devices.

Table 4.5: J-V performance parameters of aged MAPbI₃ devices under one sun illumination (100 mW/cm², AM 1.5G).

MAPbI ₃ age (months)	V_{oc} (V)	J_{sc} (mA/cm ²)	FF	PCE (%)
0 (freshly-made)	0.978	15.74	0.68	10.5
1	0.974	15.29	0.62	9.3
2	0.974	14.92	0.57	8.3
3	0.977	14.44	0.50	7.1

The perovskite is susceptible to moisture ingress [73,74], methylammonium iodide egress [75], and corrosion of metal electrodes by reaction with halides in the perovskite. Early work performed on stabilizing the perovskite, included the use of a pinhole-free metal oxide layer to prevent metal-halide interaction [76].

The formation of defect-free polycrystalline $\text{MAPbI}_{3-x}\text{Cl}_x$ perovskite films is a possible cause of the enhanced stability observed in $\text{MAPbI}_{3-x}\text{Cl}_x$ devices.

Solar cells with Al in direct contact with the n-type buffer layer, PCBM, degraded immediately on exposure to ambient atmosphere. The ingress of H_2O into the perovskite film results in the perovskite crystal structure degrading with immediate hydrated phases forming, culminating in the reformation of PbI_2 [77,78]. Generation of HI, followed by formation of iodide/iodide, has been suggested as the primary root of degradation [79].

Conclusion

In summary, it was demonstrated that every aspect of the perovskite device fabrication process, such as the thermal annealing step, the precursor composition, addition of certain chemicals that aid the film formation and the substrate have a critical influence on the perovskite crystallization rate and therefore the morphology of the resulting perovskite layer. Given the correlation between improved device performance and perovskite grain size, micrometer-sized grains seem to be an important morphological feature for high efficiency perovskite solar cells. Besides homogeneous morphology of the perovskite layer, high performance perovskite solar cells were achieved by exclusively using an electron transport layer and a hole transport layer which are critically necessary for photovoltaic performance because of their energetically favourable contact of the front and back electrode to promote effective carrier separation and charge recombination reduction. It was shown that perovskite photovoltaic performance is clearly sensitive to the choice of fullerene and replacing PCBM with another C_{60} -based or non-PCBM fullerene decreases device efficiency. In contrast to the single halide, MAPbI_3 , the high photovoltaic performances in the mixed-halide $\text{MAPbI}_{3-x}\text{Cl}_x$, are achieved via the formation of optimum perovskite film morphology that contains highly crystalline perovskite domains. The polymer crystallinity and thus excellent hole transport ability combined with sufficiently pure domains, are the main reasons why exhibit $\text{MAPbI}_{3-x}\text{Cl}_x$ superior performance. It was therefore concluded that maximizing perovskite film surface coverage proves to be a successful strategy to maximize device performance.

References

- [1] M. M. Lee, J. Teuscher, T. Miyasaka, T. N. Murakami, H. J. Snaith, *Science*, 2012, 338, 643-647
- [2] H.-S. Kim, C.-R. Lee, J.-H. Im, K.-B. Lee, T. Moehl, A. Marchioro, S.-J. Moon, R. Humphry-Baker, J.-H. Yum, J. E. Moser, M. Grätzel and N.-G. Park, *Sci. Rep.*, 2012, 2, 591
- [3] J. Burschka, N. Pellet, S.-J. Moon, R. Humphry-Baker, P. Gao, M. K. Nazeeruddin and M. Grätzel, *Nature*, 2013, 499, 316-319
- [4] W. S. Yang, J. H. Noh, N. J. Jeon, Y. C. Kim, S. Ryu, J. Seo and S. I. Seok, *Science*, 2015, 348, 1234-1237
- [5] J. H. Noh, S. H. Im, J. H. Heo, T. N. Mandal and S. I. Seok, *Nano Lett*, 2013, 13, 1764-1769
- [6] J. P. Correa Baena, L. Steier, W. Tress, M. Saliba, S. Neutzner, T. Matsui, F. Giordano, T. J. Jacobsson, A. R. Srimath Kandada, S. M. Zakeeruddin, A. Petrozza, A. Abate, M. K. Nazeeruddin, M. Grätzel, A. Hagfeldt, *Energy Environ. Sci.*, 2015, 8, 2928
- [7] P. Löper, M. Stuckelberger, B. Niesen, J. Werner, M. Filipič, S.-J. Moon, J.-H. Yum, M. Topič, S. De Wol, C. Ballif, *J. Phys. Chem. Lett.*, 2014, 6, 66
- [8] A. Kojima, I. Masashi, T. Kenyiro, M. Totsumo, *Chem. Lett.*, 2012, 41, 397-399
- [9] C. R. Kagan, D. B. Mitzi and C. D. Dimitrakopoulos, *Science*, 1999, 286, 945-947
- [10] D. B. Mitzi, C. A. Field, Z. Schlesinger and R. B. Laibowitz, *J. Solid State Chem.*, 1995, 114, 159-163
- [11] L. Etgar, P. Gao, Z. Xue, Q. Peng, A. K. Chandiran, B. Liu, M. K. Nazeeruddin and M. Grätzel, *J. Am. Chem. Soc.*, 2012, 134, 17396-17399
- [12] G. Giorgi, J.-I. Fujisawa, H. Segawa and K. Yamashita, *J. Phys. Chem. Lett.*, 2013, 4, 4213-4216
- [13] W. A. Laban and L. Etgar, *Energy Environ. Sci.*, 2013, 6, 3249-3253
- [14] J. Burschka, N. Pellet, S.-J. Moon, R. Humphry-Baker, P. Gao, M. K. Nazeeruddin and M. Grätzel, 2013, *Nature*, 499, 316-319
- [15] M. Liu, M. B. Johnston, H. J. Snaith, *Nature*, 2013, 501, 395-398
- [16] W. Nie, H. Tsai, R. Asadpour, J.-C. Blancon, A. J. Neukirch, G. Gupta, J. J. Crochet, M. Chhowalla, S. Tretiak, M. A. Alam, H.-L. Wang and A. D. Mohite, *Science*, 2015, 347, 522-525.
- [17] O. Malinkiewicz, A. Yell, Y. H. Lee, G. M. Espallargas, M. Grätzel, M. D. Nazeeruddin, H. J. Bolink, *Nature Photon.*, 2014, 8, 128-132
- [18] S. Sun, D. Yuan, Y. Xu, A. Wang and Z. Deng, *ACS Nano*, 2016, 10, 3648-3657
- [19] J.-W. Lee, D.-H. Kim, H.-S. Kim, S.-W. Seo, S. M. Cho, N.-G. Park, *Adv. Energy Mater.*, 2015, 5, 1501310
- [20] Z. Yang, C.-C. Chueh, P.-W. Liang, M. Crump, F. Lin, Z. Zhu and A. K.-Y. Jen, *Nano Energy*, 2016, 22, 328-337
- [21] G. E. Eperon, S. D. Stranks, C. Menelaou, M. B. Johnston, L. M. Herz and H. J. Snaith, *Energy Environ. Sci.*, 2014, 7, 983-988
- [22] A. Binek, F. C. Hanusch, P. Docampo, T. Bein, *J. Phys. Chem. Lett.*, 2015, 6, 1249-1253]
- [23] N. J. Jeon, J. H. Noh, W. S. Yang, Y. C. Kim, S. Ryu, J. Seo, S. I. Seok, *Nature*, 2015, 517, 476-480
- [24] S. A. Kulkarni, T. Baikie, P. P. Boix, N. Yantara, N. Mathews and S. G. Mhaisalkar, *J. Mater. Chem. A.*, 2014, 2, 9221
- [25] S. M. H. Qaid, M. S. Al Sobaie, M. A. M. Khan, I. M. Bedja, F. H. Alharbi, M. K. Nazeeruddin and A. S. Aldwayyan, *Mater. Lett*, 2016, 164, 498-501
- [26] N. Sakai, S. Pathak, H.-W. Chen, A. A. Haghighirad, S. D. Stranks, T. Miyasaka and H. J. Snaith, *J. Mater. Chem. A*, 2016, 4, 4464-4471
- [27] E. L. Unger, A. R. Bowring, C. J. Tassone, V. L. Pool, A. Gold-Parker, R. Cheacharoen, K. H. Stone, E. T. Hoke, M. F. Toney, M. D. McGehee, *Chem. Mater.*, 2014, 26, 7158-7165
- [28] K. Cao, H. Li, S. Liu, J. Cui, Y. Shen and M. Wang, *Nanoscale*, 2016, 8, 8839-8846

- [29] A. Sadhanala, S. Ahmad, B. Zhao, N. Giesbrecht, P. M. Pearce, F. Deschler, R. L. Z. Hoye, K. C. Gödel, T. Bein, P. Docampo, S. E. Dutton, M. F. L. De Volder, R. H. Friend, *Nano Lett.*, 2015, 15, 6095-6101
- [30] S. Aharon, B. E. Cohen and L. Etgar, *J. Phys. Chem. C*, 2014, 118, 17160-17165
- [31] J.-H. Im, I.-H. Jang, N. Pellet, M. Grätzel and N.-G. Park, *Nat. Nanotechnol.*, 2014, 9, 927-932
- [32] F. Giordano, A. Abate, J.-P. C. Baena, M. Saliba, T. Matsui, S. H. Im, S. M. Zakeeruddin, M. K. Nazeeruddin, A. Hagfeldt, M. Grätzel, *Nat. Commun.* 2016, 7, 10379
- [33] G. E. Eperon, V. M. Burlakov, P. Docampo, A. Goriely and H. J. Snaith, *Adv. Funct. Mater.*, 2014, 24, 151-157
- [34] P. Docampo, J. M. Ball, M. Darwich, G. E. Eperon and H. J. Snaith, *Nat. Commun.*, 2013, 4, 2761
- [35] W. Zhang, M. Saliba, D. T. Moore, S. K. Pathak, M. T. Hörantner, T. Stergiopoulos, S. D. Stranks, G. E. Eperon, J. A. Alexander-Webber, A. Abate, A. Sadhanala, S. Yao, Y. Chen, R. H. Friend, L. A. Estroff, U. Wiesner, H. J. Snaith, *Nat. Commun.*, 2015, 6, 6142
- [36] C. Roldán-Carmona, O. Malinkiewicz, A. Soriano, G. Mínguez Espallargas, A. Garcia, P. Reinecke, T. Kroyer, M. I. Dar, M. K. Nazeeruddin and H. J. Bolink, *Energy. Environ. Sci.*, 2014, 7, 994-997
- [37] S. Sun, T. Salim, N. Mathews, M. Duchamp, C. Boothroyd, G. Xing, T. C. Sum and Y. M. Lam, *Energy. Environ. Sci.*, 2014, 7, 399-407
- [38] Z. M. Bailey, M. D. McGehee, *Energy Environ. Sci.* 2012, 5, 9173-9179
- [39] P. Docampo, S. Guldin, U. Steiner and H. J. Snaith, *J. Phys. Chem. Lett.*, 2013, 4, 698-703
- [40] P. Docampo, S. Guldin, T. Leitjens, N. K. Noel, U. Steiner and H. J. Snaith, *Adv. Mater.*, 2014, 26, 4013-4030
- [41] A. K. Jena, H.-W. Chen, A. Kogo, Y. Sanehira, M. Ikegami and T. Miyasaka, *ACS Appl. Mater. Interfaces*, 2015, 7, 9817-9823
- [42] H. J. Snaith, A. Abate, J. M. Ball, G. E. Eperon, T. Leitjens, N. K. Noel, S. D. Stranks, J. T.-W. Wang, K. Wojciechowski, W. Zhang, *J. Phys. Chem. Lett.*, 2014, 5, 1511-1515
- [43] B.C. O'Regan, P. R. F. Barnes, X. Li, C. Law, E. Palomares and J. M. Marin-Belouqui, *J. Am. Chem. Soc.*, 2015, 137, 5087-5099
- [44] H. Zhou, Q. Chen, G. Li, S. Luo, T.-b. Song, H.-S. Duan, Z. Hong, J. You, Y. Liu and Y. Yang, *Science*, 2014, 345, 542-546
- [45] N. J. Jeon, H. G. Lee, Y. C. Kim, J. Seo, J. H. Noh, J. Lee, and S. I. Seok, *J. Am. Chem. Soc.*, 2014, 136, 7837-7840
- [46] A. Dualeh, N. Tétreault, T. Moehl, P. Gao, M. K. Nazeeruddin and M. Grätzel, *Adv. Funct. Mater.*, 2014, 24, 3250-3258
- [47] J.-W. Lee, D.-J. Seol, A.-N. Cho and N.-G. Park, *Adv. Mater.*, 2014, 4991-4998
- [48] M. Saliba, K. W. Tan, H. Sai, D. T. Moore, T. Scott, W. Zhang, L. A. Estroff, U. Wiesner, and H. J. Snaith, *J. Phys. Chem. C.*, 2014, 118, 17171-17177
- [49] G. Adam, M. Kaltenbrunner, E. D. Głowacki, D. H. Hazar, M. S. White, H. Heilbrunner, S. Tombe, P. Stadler, B. Ernecker, C. W. Klampfl, N. S. Sariciftci and M. C. Scharber, *Sol. Energy Mater. Sol. Cells*, 2016, 157, 318-325
- [50] J. Kim, M. A. Teridi, A. R. bin Mohd Yusoff and J. Jang, *Sci. Rep.*, 2016, 6, 27773
- [51] H. Yu, H. Lu, F. Xie, S. Zhou and N. Zhao, *Adv. Funct. Mater.*, 2016, 26, 1411-1419
- [52] Y. Chen, T. Chen and L. Dai, *Adv. Mater.*, 2015, 27, 1053-1059
- [53] H.-S. Kim and N.-G. Park, *J. Phys. Chem. Lett.*, 2014, 5, 2927-2934
- [54] K. A. Bush, C. D. Bailie, Y. Chen, Andrea R. Bowring, W. Wang, W. Ma, T. Leitjens, F. Moghadam and M. D. McGehee, *Adv. Mater.*, 2016, 28, 3937-3943
- [55] S. K. M. Jönsson, J. Birgersson, X. Crispin, G. Greczynski, W. Osikowicz, A. W. Denier van der Gon, W. R. Salaneck and M. Fahlman, *Synth. Met.*, 2003, 139, 1-10
- [56] M. Kaltenbrunner, G. Adam, E. D. Głowacki, M. Drack, R. Schwödiauer, L. Leonat, D. H. Hazar, H. Groiss, M. C. Scharber, M. S. White, N. S. Sariciftci and S. Bauer, *Nat. Mater.*, 2015, 14, 1032-1039

- [57] J. Xu, A. Buin, A. H. Ip, W. Li, O. Voznyy, R. Comin, M. Yuan, S. Jeon, Z. Ning, J. J. McDowell, P. Kanjanaboos, J. P. Sun, X. Lan, L. N. Quan, D. H. Kim, I. G. Hill, P. Maksymovych, E. H. Sargent, *Nat. Commun.*, 2015, 6, 7081
- [58] Y. Shao, Z. Xiao, C. Bi, Y. Yuan, J. Huang, *Nat. Commun.*, 2014, 5, 5784
- [59] A. Poglitsch, D. Weber, *J. Chem. Phys.*, 1987, 87, 6373-6378
- [60] P.-W. Liang, C.-Y. Liao, C.-C. Chueh, F. Zuo, S. T. Williams, X.-K. Xin, J. Lin, A. K. Y. Jen, *Adv. Mater.*, 2014, 26, 3748-3754
- [61] S. Ryu, J. H. Noh, N. J. Jeon, Y. C. Kim, W. S. Yang, J. Seo, S. I. Seok, *Energy Environ. Sci.*, 2014, 7, 2614-2618
- [62] J. H. Heo, S. H. Im, J. H. Noh, T. N. Mandal, C.-S. Lim, J. A. Chang, Y. H. Lee, H.-J. Kim, A. Sarkar, M. K. Nazeeruddin, M. Grätzel, S. I. Seok, *Nat. Photonics*, 2013, 7, 486-491
- [63] W. Nie, H. Tsai, R. Asadpour, J.-C. Blancon, A. J. Neukirch, G. Gupta, J. J. Crochet, M. Chhowalla, S. Tretiak, M. A. Alam, H.-L. Wang and A. D. Mohite, *Science*, 2015, 347, 522-525.
- [64] M. M. Voigt, R. C. I. Mackenzie, C. P. Yau, P. Atienzar, J. Dane, P.E. Keivanidis, D. D. C. Bradley. J. Nelson, *Sol. Energy Mater. Sol. Cells*, 2011, 95, 731-734
- [65] S. Savagatrup, E. Chan, S. M. Renteria-Garcia, A. D. Printz, A. V. Zaretski, T. F. O'Connor, D. Rodriguez, E. Valle, D. J. Lipomi, *Adv. Funct. Mater.*, 2015, 25, 427-436
- [66] X. Zhan, A. Facchetti, S. Barlow, T. J. Marks, M. A. Ratner, M. R. Wasielewski, *Adv. Mater.*, 2011, 23, 268-284
- [67] C. Huang, S. Barlow, S. R. Marder, *J. Org. Chem.*, 2011, 76, 2386-2407
- [68] L. Ye, S. Zhang, D. Qian, Q. Wang and J. Hou, *J. Phys. Chem. C*, 2013, 117, 25360-25366
- [69] Y. He, Y. Li, *Phys. Chem. Chem. Phys.*, 2011, 13, 1970-1983
- [70] M. Lenes G. J. A. H. Wetzelaer, F. B. Kooistra, S. C. Veenstra, J. C. Hummelen, P. W. M. Blom, *Adv. Mater.*, 2008, 20, 2116-2119
- [71] G. D. Han, A. Maurano, J. G. Weis, V. Bulovic, T. M. Swager, *Org. Electron.*, 2016, 31, 48-55
- [72] J. M. Ball, M. M. Lee, A. Hey and H. J. Snaith, *Energy Environ. Sci.*, 2013, 6, 1739
- [73] J. H. Noh, S. H. Im, J. H. Heo, T. N. Mandal and S. I. Seok, *Nano Lett*, 2013, 13, 1764-1769
- [74] S. N. Habisreutinger, T. Leitjens, G. E. Eperon, S. D. Stranks, R. J. Nicholas, H. J. Snaith, *Nano Lett.*, 2014, 14, 5561-5568
- [75] B. Conings, J. Drijkoningen, N. Gauquelin, A. Babayigit, J. D'Haen, L. D'Olieslaeger, A. Ethirajan, J. Verbeeck, J. Manca, E. Mosconi, F. De Angelis, H.-G. Boyen, *Adv. Energy Mater.*, 2015, 5, 1500477
- [76] You, L. Meng, T.-B. Song, T.-F. Guo, Y. Yang, W.-H. Chang, Z. Hong, H. Chen, H. Zhou, Q. Chen, Y. Liu, N. De Marco, Y. Yang, *Nat. Nanotechnol.* 2015, 11, 75
- [77] J. A. Christians, P. A. Miranda Herrera and P. V. Kamat, *J. Am. Chem. Soc.*, 2015, 137, 1530-1538
- [78] A. M. A. Leguy, Y. Hu, M. Campoy-Quiles, M. I. Alonso, O. J. Weber, P. Azarhoosh, M. Van Schifgaarde, M. T. Weller, T. Bein, J. Nelson, P. Docampo, P. R. F. Barnes, *Chem. Mater.*, 2015, 27, 3397-3407
- [79] J. M. Frost, K. T. Butler, F. Brivio, C. H. Hendon, M. van Schilfgaarde and A. Walsh, *Nano Lett*, 2014, 14, 2584-259

CHAPTER 5

WIDE-BANDGAP SOLUTION PROCESSED MIXED-HALIDE METHYLAMMONIUM LEAD IODIDE-BROMIDE PEROVSKITE SOLAR CELLS

Abstract

We report the optical and electronic properties of wide bandgap planar heterojunction mixed-halide $\text{MAPbI}_{3-x}\text{Br}_x$ ($0 \leq x \leq 3$) perovskite solar cells fabricated by a one-step solution deposition technique as promising low-cost alternatives for application in tandem or multi-junction photovoltaics. The morphologies of $\text{MAPbI}_{3-x}\text{Br}_x$ ($x = 1$) and MAPbBr_3 perovskite materials are characterized and the differences in their photoluminescence behaviour are demonstrated. Temperature-dependent photoluminescence properties of the $\text{MAPbI}_{3-x}\text{Br}_x$ perovskites films were studied by using steady-state photoluminescence. It was found that photoluminescence intensities of $\text{MAPbI}_{3-x}\text{Br}_x$ ($x = 1$) decreased gradually with increasing temperature, while those of MAPbBr_3 dropped rapidly and were almost quenched at 293 K. The methylammonium lead trihalide perovskites exhibited thermal quenching in the temperature range 77-293 K. Exciton binding energies extracted from the temperature dependence of the free exciton peak intensity were 61 and 103 meV respectively. We show that chemical modification of methylammonium lead iodide perovskites by substitution of iodide with bromide can tune the bandgaps to range between 1.5 and 2.3 eV resulting in colour variation and perovskite power conversion efficiency modulation. A maximum overall power conversion efficiency of 3.2% under AM 1.5G, 100 mW/cm^2 illumination was achieved with the optimized mixed-halide cell.

5.1 Introduction

Recently the power conversion efficiency (PCE) of lead halide perovskite-based thin film photovoltaic devices has skyrocketed from 3.8% to a certified 22.1% record efficiency [1-4]. Perovskite absorber materials have proven to be versatile materials for incorporation into highly efficient low-cost solar cells due to their simplified device architecture, low-temperature processing, the variety of processing techniques (e.g. spin-coating, dip-coating, vapour deposition *etc.*) and the availability of many other metal and organic salts that could form a perovskite structure [5-9].

One attractive attribute of hybrid perovskites as photovoltaic absorbers is the ability to tune their optical and electronic properties by changes in the chemical composition (changes in the alkyl group, metal atom and/or halide) [10-14]. Since Kojima *et al.*, [1] reported solution-processable organic-inorganic hybrid perovskite-sensitized solar cells, perovskite solar cells based on solid-state single- and mixed-halides have been demonstrated [9,13-17]. The most extensively studied single-halide methylammonium lead triiodide,

MAPbI₃ perovskites with a reported bandgap of 1.5 eV have never reached efficiencies larger than 20% despite the numerous attempts made since the early days of research in the field [1,6,13-17].

A key target for the photovoltaics community has been to find a wider-bandgap highly efficient ‘top cell’ to enable the next step in improving the performance of crystalline silicon and existing second-generation thin-film solar cells. Previous reports have demonstrated that large bandgap perovskite solar cells can serve as efficient top sub-cells in high-performance tandem solar cells with crystalline silicon (1.12 eV) employed as the bottom sub-cell [18-20].

As a consequence of the possibility to tune bandgap, high voltage mesoscopic MAPbBr₃ perovskite solar cells were demonstrated with open circuit voltages (V_{oc}) of 1.15 V [21], 1.3 V [11], 1.4 V [22] and 1.5 V [23] using poly[*N*-9-heptadecanyl-2,7-carbazole-*alt*-3,6-bis-(thiophen-5-yl)-2,5-dihydropyrrolo[3,4-]pyrrole-1,4-dione] (PCBTDDPP), *N,N*-dialkyl perylenediimide (PDI) and poly(indenofluoren-8-triarylamine) (PIF8-TAA) as hole transport materials respectively. Edri *et al.*, reported a 1.5 V mixed-halide CH₃NH₃PbBr_{3-x}Cl_x using 4'-bis(*N*-carbazolyl)-1,1'-biphenyl (CBP) as the hole conductor [24]. Recently 1.5 V formamidinium (FA) lead tribromide FAPbBr₃ was reported by Arora *et al.*, using fluorene-dithiophene derivatives as hole-transporting materials [25]. Photovoltaic devices containing MAPbI_{3-x}Br_x have demonstrated power conversion efficiencies of 4-16% for a wide range of halide ratios [26-30]. Using a one-step deposition technique, Seok *et al.* showed colourful, efficient perovskite solar cells using different Br concentrations in the perovskite achieving PCE of 12.3% using poly(triarylamine) (PTAA) as the hole conductor [27].

Solar cells that use only the high-energy part of the solar spectrum and yield high open-circuit voltage are needed to make more efficient use of the high-energy part of the solar spectrum and can serve as the front cell in tandem cells or in a general spectral splitting system. Currently, GaInP photovoltaic devices are used as top cell in inorganic tandem systems, with $V_{oc} \sim 1.45$ V [31].

However, these devices are expensive, and therefore, although they increase the overall efficiency of a tandem system, they also increase the cost per watt. A low-cost way for possible large scale cell fabrication is through low temperature solution methods.

In this work, we combine two important properties of the perovskite absorbers, low-cost solution processability and perovskite bandgap tunability by incorporating bromide into planar heterojunction ITO/PEDOT:PSS/MAPbI₃/PCBM/Al solar cells with the aim to produce high voltage solar cells. We examine the optical properties of MAPbI_{3-x}Br_x ($0 \leq x \leq 3$) with a focus on only the high voltage MAPbI_{3-x}Br_x ($x \geq 1$) and MAPbBr₃, to understand the effect of iodide-bromide composition on perovskite morphology and photovoltaic device performance. Solution deposition was conducted by directly

depositing different molar ratios of PbI_2 , MAI and MABr to form $\text{MAPbI}_{3-x}\text{Br}_x$ ($0 \leq x \leq 1$) and depositing equimolar ratios of PbBr_2 and MABr to form MAPbBr_3 in DMF solution onto either glass or Glass/ITO/PEDOT:PSS substrates to fabricate the perovskite absorber layer. We found that bandgap tuning of MAPbI_3 can be achieved via substitution of iodide with bromide ions and chemical modification can tune the bandgaps to range between 1.5 and 2.3 eV resulting in colour variation and perovskite power conversion efficiency modulation. Temperature-dependent photoluminescence spectra were measured from 77 to 293 K to explain exciton-related photoluminescence recombination. Optical bandgap values and exciton binding energies of $\text{MAPbI}_{3-x}\text{Br}_x$ ($x = 1$) and MAPbBr_3 are discussed. We show that by harnessing $\text{MAPbI}_{3-x}\text{Br}_x$ perovskites, an avenue for high open-circuit voltage solar cells can be opened.

5.2 Experimental

5.2.1 Materials

Chemicals and solvents were used as received from commercial suppliers, if not stated otherwise. Pre-patterned indium doped tin oxide (ITO) coated glass (15 ohm/cm^2), PbI_2 (99.9%, Sigma Aldrich), PbBr_2 (99.9%, Sigma Aldrich), dimethylformamide (DMF, anhydrous, Sigma Aldrich), poly(3,4-ethylenedioxythiophene) polystyrene sulfonate (PEDOT:PSS) Clevis PH 1000 and Clevis PVP (Al 4083), Zonyl[®]FS-300 fluorosurfactant (40% in H_2O , Fluka), dimethyl sulfoxide (DMSO, AnalR, VWR Chemicals), [6,6]-phenyl-C₆₁-butyric acid methyl ester (PCBM; SolenneBV), chlorobenzene (GPR, VWR Chemicals) chloroform (AnalR, VWR Chemicals), and isopropanol (AnalR, Fisher Chemicals), methylamine (in absolute ethanol, 33 wt%), diethyl ether, hydroiodic acid (aqueous, 57 wt %) and ethanol (absolute), respectively were used. Methylammonium iodide ($\text{CH}_3\text{NH}_3\text{I}$ /MAI) and methylammonium bromide ($\text{CH}_3\text{NH}_3\text{Br}$ /MABr) were synthesized according to a reported literature procedure [9].

5.2.2 Perovskite precursor solutions

Experimental analysis was done using methylammonium lead tribromide, MAPbBr_3 formed from 40 wt% equimolar solution of PbBr_2 and MABr. Mixed halide $\text{MAPbI}_{3-x}\text{Br}_x$ composed of equimolar ratios of PbI_2 and MAI with varying molar ratios of MABr (x). Mixed halide perovskite solutions of 40 wt% 1:1:0.25, 1:1:0.5, 1:1:0.75 and 1:1:1 were prepared in DMF. The solutions were then filtered with a $0.45 \mu\text{m}$ PTFE filter. The final stoichiometry of the perovskites in terms of bromide or iodide/bromide content was not evaluated. The range of precursor stoichiometries was designed to elucidate the role of Br^- . Precursor solutions 1:1 MABr: PbBr_2 and 1:1:1 PbI_2 :MAI:MABr represented as $\text{MAPbI}_{3-x}\text{Br}_x$ ($x = 1$) were employed for further study.

Perovskite solar cells were fabricated and characterized as described in Chapter 3. Photoluminescence and electroluminescence spectra of various devices were measured using a Shamrock SR-303i monochromator and an Andor iDus Si-CCD. Samples were excited at 473 nm (5 mW) using a solid-state laser or a supercontinuum light source (NKT EXB6) connected to a VIS-NIR SuperK Select Box. A set of long-pass filters was used to avoid any distortion of the recorded spectra by the laser light.

5.3 Results and discussion

5.3.1 Device structure

To achieve a high-open circuit voltage in a solar cell, it is necessary to combine a suitable energy band structure of the constituent materials with good charge transfer kinetics. **Figure 5.1** depicts the schematic energy diagrams of $\text{MAPbI}_{3-x}\text{Br}_x$ ($x = 1$) (**Figure 5.1a**) and MAPbBr_3 (**Figure 5.1b**) perovskite solar cells.

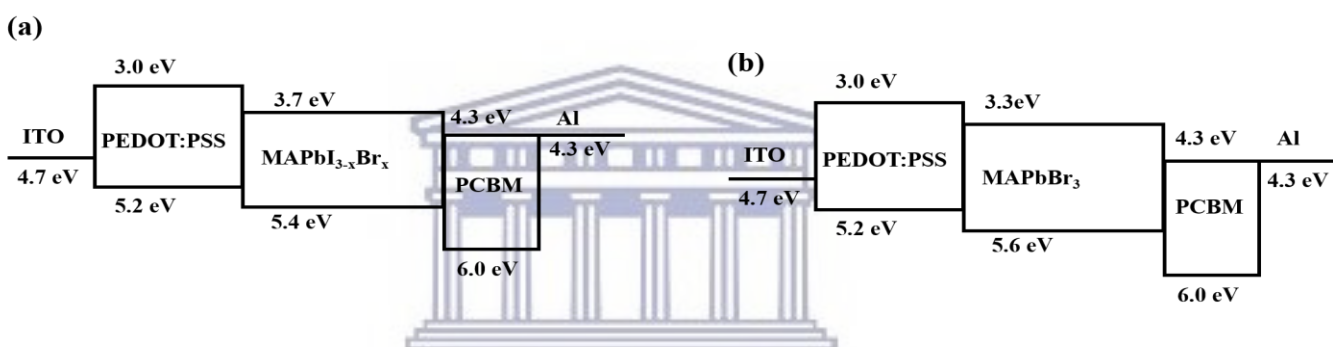


Figure 5.1: Schematics diagrams of approximate energy level alignment in a) $\text{MAPbI}_{3-x}\text{Br}_x$ ($x = 1$) and b) MAPbBr_3 perovskite solar cells [27,32]

Upon illumination, the perovskite absorbs the light and generates electron-hole pairs. The electrons are injected into PCBM and simultaneously the holes are transported to PEDOT:PSS and/or the counter electrode through the perovskite itself [15,33].

Figure 5.1a shows that the valence band maximum (VBM) and conduction band minimum (CBM) of $\text{MAPbI}_{3-x}\text{Br}_x$ ($x = 1$) are 5.4 and 3.7 eV respectively and the highest occupied molecular orbital (HOMO) of PEDOT:PSS is 5.2 eV. In comparison to MAPbBr_3 , **Figure 5.1b**, the favourable alignment between the conduction band minimum of the PCBM and the HOMO of PEDOT:PSS with the conduction band minimum and the valence band maximum of $\text{MAPbI}_{3-x}\text{Br}_x$ ($x = 1$) allows for efficient extraction of photogenerated carriers without inducing excessive interface recombination. The PEDOT:PSS HOMO-LUMO states align relatively poorly with the PbMABr_3 valence and conduction band edges limiting its efficacy as a selective contact for holes.

5.3.2 Perovskite film morphology

The surface morphology of the perovskite films was examined using diascopic illumination optical microscopy and scanning electron microscopy (SEM). **Figure 5.2** shows the morphological differences between $\text{MAPbI}_{3-x}\text{Br}_x$ ($x = 1$) (**Figure 5.2a**) and MAPbBr_3 (**Figure 5.2b**) perovskite films.

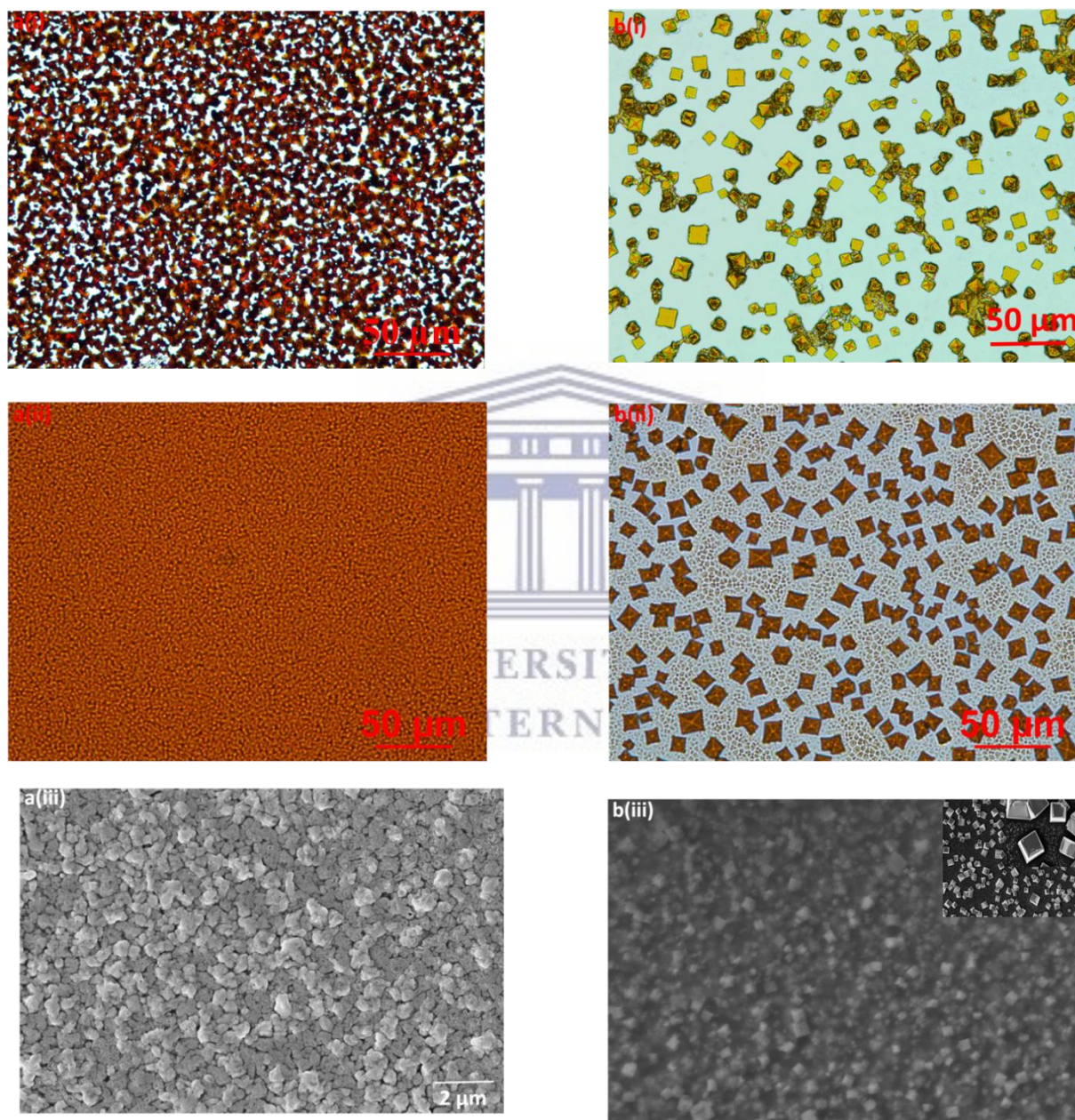


Figure 5.2: Diascopic illumination optical microscopy images on (i) glass and on (ii) glass/ITO/PEDOT:PSS and (iii) SEM images of a) $\text{MAPbI}_{3-x}\text{Br}_x$ ($x = 1$) and b) MAPbBr_3 perovskite films on glass/ITO/PEDOT:PSS.

Both perovskite compositions form films with pinholes and inhomogeneous perovskite film coverage on glass substrates, **Figure 5.2a(i)** and **Figure 5.2b(i)** due to unfavourable interactions between the perovskite solution and the glass substrate. Better wetting of $\text{MAPbI}_{3-x}\text{Br}_x$ perovskite precursor solution on the PEDOT:PSS layer, **Figure 5.2a(ii)** and **Figure 5.2a(iii)** leads to a uniform active layer with relatively complete surface coverage in comparison to MAPbBr_3 which forms a heterogeneous perovskite layer of cuboid-like structures, **Figure 5.2b(ii)** and **Figure 5.2b(iii)**. The growth of mixed-halide iodide-bromide perovskite crystals from a precursor solution tends to be more rapid with increasing bromide content therefore further enhancement in the nucleation rate is necessary for effective decoupling of the nucleation and crystal-growth stages in bromide-rich perovskites, **Figure 2b**.

5.3.3 Absorbance and photoluminescence spectroscopy

To check for variation of the optical properties in the hybrid $\text{MAPbI}_{3-x}\text{Br}_x$ ($0 \leq x \leq 3$), we measured the UV-Vis absorption and photoluminescence spectra of representative perovskite samples on glass. The absorbance and normalized photoluminescence spectra of $\text{MAPbI}_{3-x}\text{Br}_x$ ($0 \leq x \leq 3$) and MAPbBr_3 are shown in **Figure 5.3**.

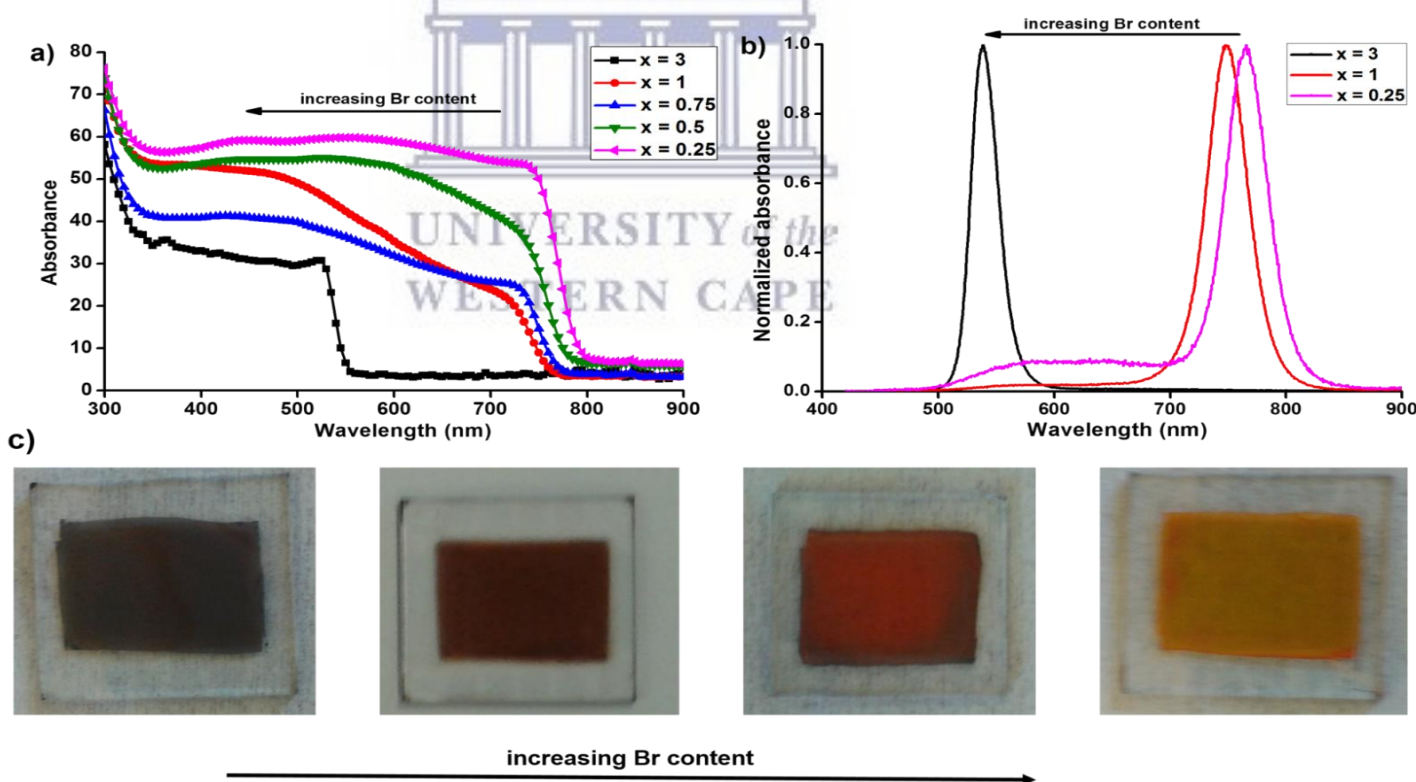
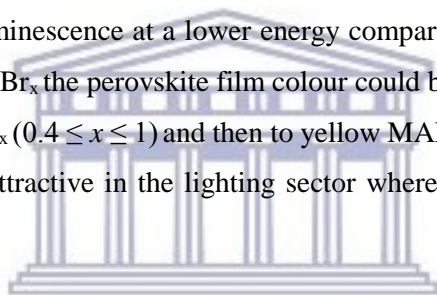


Figure 5.3: a) Absorbance and b) photoluminescence spectra of $\text{MAPbI}_{3-x}\text{Br}_x$ films with different x values and c) Photographs of $\text{MAPbI}_{3-x}\text{Br}_x$ devices from $x = 0$ to $x = 3$ (left to right)

Figure 5.3a shows a continuous blue-shift of absorbance spectra upon increasing bromide content. The different absorption ranges observed in **Figure 5.3a** can be ascribed to the variation of the energy bandgap of those semiconductors arising from the Br-replacement induced structural modification [27] and a strong dependence on the effective exciton mass [34]. It was observed that the absorption of $\text{MAPbI}_{3-x}\text{Br}_x$ ($x \leq 0.3$) extended throughout the UV-Visible region with an absorption onset at ~ 790 nm whereas MAPbBr_3 shows coverage until 550 nm wavelength. **Figure 5.3a** shows that the bandgap of $\text{MAPbI}_{3-x}\text{Br}_x$ can be continuously tuned over the range 1.6-2.3 eV [27] making these materials suitable for single-junction solar cells and for the larger bandgap absorber of tandem solar cells. Our findings are consistent with previous and current reports [35]. The photoluminescence spectra also continuously blue-shift upon increasing bromide content, **Figure 5.3b**. Photoluminescence peaks correspond well to the absorption onsets, suggesting the observed photoluminescence is predominantly from the band gap rather than trap or sub-band states [36]. Photoexcitation in $\text{MAPbI}_{3-x}\text{Br}_x$ with $x \leq 0.3$ induces halide migration resulting in lower-bandgap, iodide-rich domains that pin the photoluminescence at a lower energy compared to MAPbBr_3 [35]. Through the compositional control of $\text{MAPbI}_{3-x}\text{Br}_x$ the perovskite film colour could be tuned from dark brown MAPbI_3 ($x \leq 0.3$) to brown/red $\text{MAPbI}_{3-x}\text{Br}_x$ ($0.4 \leq x \leq 1$) and then to yellow MAPbBr_3 ($x = 3$), **Figure 5.3c**. This in turn makes these materials very attractive in the lighting sector where access to a wide colour range is essential.



5.3.4 Photoluminescence quenching

There is charge transfer from the $\text{MAPbI}_{3-x}\text{Br}_x$ ($x = 1$) perovskite to PEDOT:PSS or to PCBM at the interface shown as photoluminescence quenching in **Figure 5.4**. This quenching is indicative of an efficient exciton diffusion in the perovskite to the dissociating interface, followed by an efficient electron transfer to the fullerene phase. The observed peak shift on introduction of PCBM is attributed to donor-acceptor transitions.

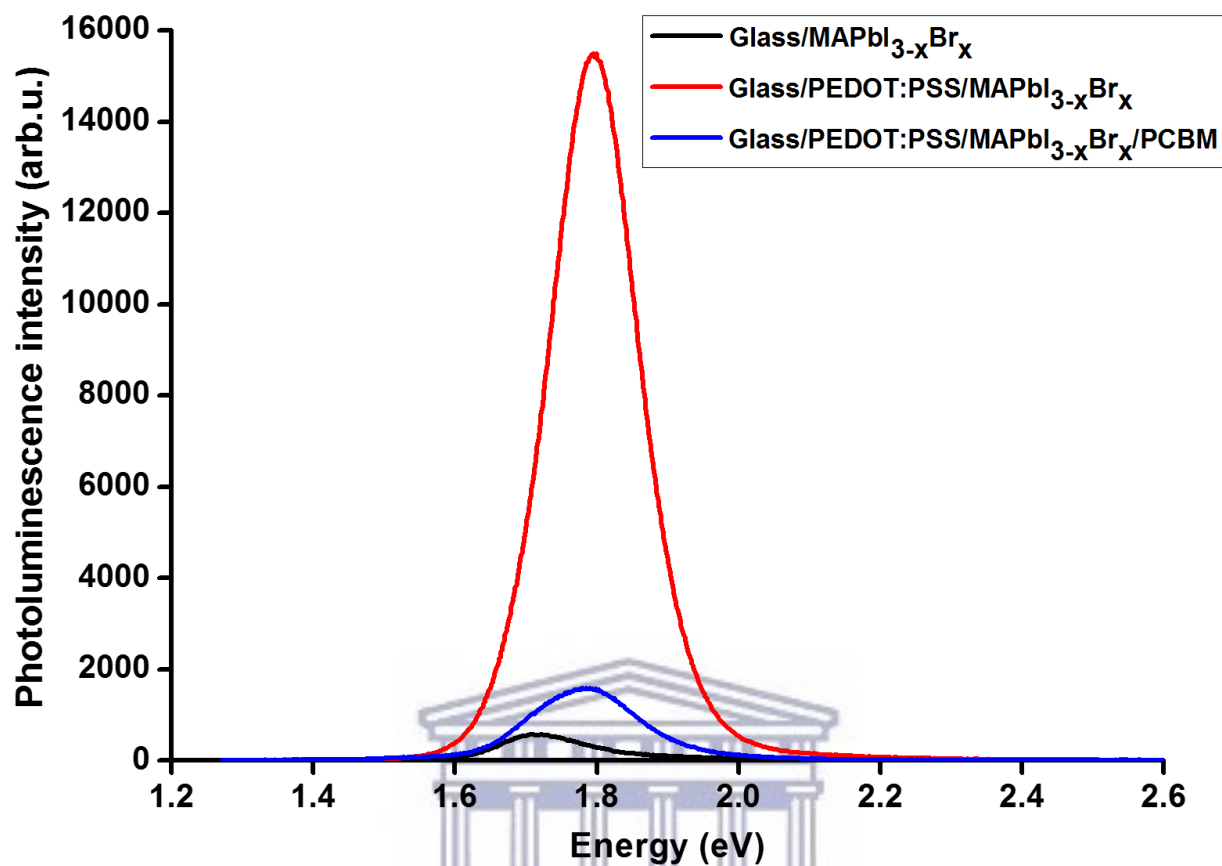


Figure 5.4: Photoluminescence quenching in $\text{MAPbI}_{3-x}\text{Br}_x$ ($x = 1$) perovskite films.

5.3.5 Temperature-dependent photoluminescence spectroscopy

Temperature-dependent photoluminescence spectroscopy was employed to give more information to explicate the exciton-related emission. **Figure 5.5** shows the photoluminescence spectra of $\text{MAPbI}_{3-x}\text{Br}_x$ ($x = 1$) and MAPbBr_3 perovskite films at temperatures ranging from 77 to 293 K. As seen in **Figure 5.5**, both materials exhibit a decrease in PL intensity with increasing temperature. The peak energies of $\text{MAPbI}_{3-x}\text{Br}_x$ ($x = 1$) film in **Figure 5.5a** shift to higher energy and the PL emission linewidths significantly increase with increasing temperature. The PL peak energies of the MAPbBr_3 film in **Figure 5.5b** are only weakly temperature dependent, with no obvious shift and a limited reduction in linewidth. As seen in **Figure 5.5b**, the PL intensities for the MAPbBr_3 perovskite dramatically decrease with increasing temperature indicating thermal quenching of PL emission.

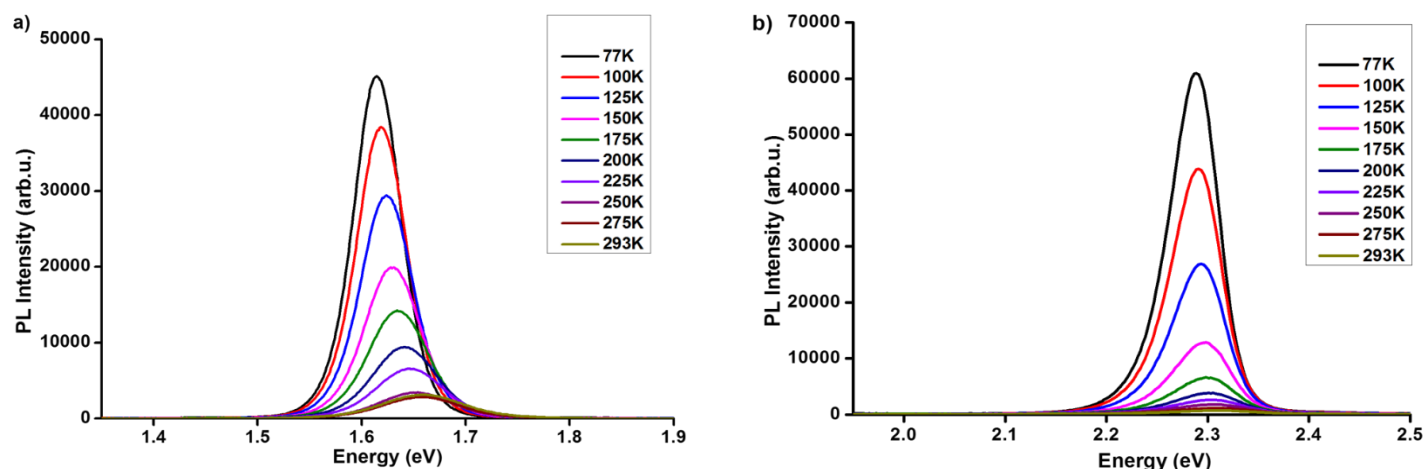


Figure 5.5: Temperature-dependent photoluminescence spectra from 77 K to 293 K of a) $\text{MAPbI}_{3-x}\text{Br}_x$ ($x = 1$) and b) MAPbBr_3 perovskite films on glass.

The shifts in peak energy at various temperatures have been reported to be associated with phase transitions commonly found in lead halide perovskites [37-39], reverse ordering of the band edge [40] or an interplay between the electron-phonon renormalization [41]. The photoluminescence temperature dependence of MAPbBr_3 , **Figure 5.5b**, has been reported to originate from detrapping of carriers from shallow traps and/or from retrapping of electron-hole pairs into exciton states [42].

The peak energies, PL intensities and linewidths of $\text{MAPbI}_{3-x}\text{Br}_x$ ($x = 1$) and MAPbBr_3 films are shown in **Figure 5.6**. **Figure 5.6(i)** shows that the bandgap almost linearly increases from 77 to 293 K. The peak energies of emission of the $\text{MAPbI}_{3-x}\text{Br}_x$ ($x = 1$) and MAPbBr_3 films were found to be 1.69 and 2.28 eV respectively as shown in **Figure 5.6a(i)** and **Figures 5.6b(i)**. This linear bandgap change is similar to that observed by Poglitsch *et al.*, [41], Xing *et al.*, [43] and Dai *et al.*, [44].

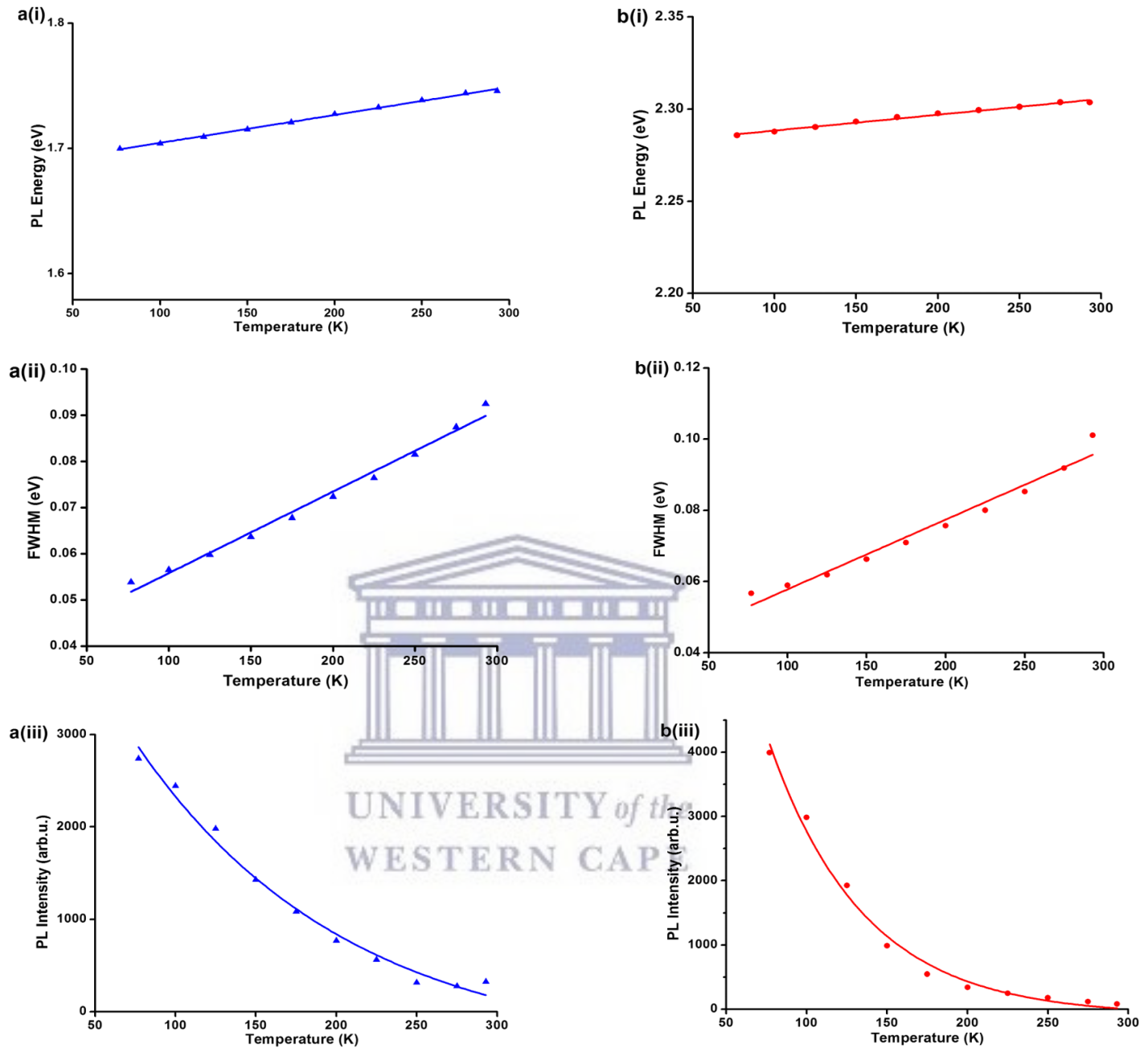


Figure 5.6: Fitted temperature-dependent photoluminescence parameters of a) $\text{MAPbI}_{3-x}\text{Br}_x$ and b) MAPbBr_3 showing the parameters (i) peak energy, (ii) intensity and (iii) temperature-dependent of the full width at half maximum (FWHM).

The PL intensities as a function of temperature shown in **Figure 5.6(ii)** were fitted by using the Arrhenius equation [45,46], **Equation 5.1**:

$$I(T) = \frac{I_0}{1 + Ae^{-\frac{E_B}{k_B T}}} \quad (5.1)$$

in which I_0 is the intensity at 0 K, E_B the binding energy and k_B the Boltzmann constant.

Exciton binding energies of 61.4 ± 4.6 and 103.9 ± 5.9 meV were obtained for $\text{MAPbI}_{3-x}\text{Br}_x$ ($x = 1$) and MAPbBr_3 respectively. It was found that activation energy increases with bromide content. The higher exciton binding energy for MAPbBr_3 is attributed to stronger electron-phonon coupling in the tribromide perovskite than in the iodide-bromide perovskite [47]. Exciton binding energies ranging from 40-113 meV have been reported for MAPbBr_3 [42,44,48,49].

The exciton-phonon coupling of the $\text{MAPbI}_{3-x}\text{Br}_x$ ($x = 1$) and MAPbBr_3 films were studied by measuring the temperature dependence of photoluminescence linewidth broadening, **Figure 5.6a(iii)** and **Figure 5.6b(iii)**. The temperature-dependent linewidth of photoluminescence emission is fitted using the independent Boson model [50], **Equation 5.2**:

$$\Gamma(T) = \Gamma_0 + \sigma T + \frac{\Gamma_{op}}{e^{-\frac{\hbar\omega_{op}}{k_B T}} - 1} \quad (5.2)$$

in which Γ_0 is the inhomogeneous broadening contribution, σ and Γ_{op} are the exciton-acoustic phonon interaction and the exciton-optical phonon contribution to the linewidth broadening respectively, and $\hbar\omega_{op}$ is the optical-phonon energy.

The inhomogeneous broadening contributions, Γ_0 , for $\text{MAPbI}_{3-x}\text{Br}_x$ and MAPbBr_3 were found to be 55.6 ± 0.8 and 75.2 ± 1.1 meV; the exciton-optical phonon contributions, Γ_{op} , 82.4 ± 10.6 and 111.2 ± 9.3 meV and the optical-phonon energies, $\hbar\omega_{op}$, 31.3 ± 3.7 and 42.2 ± 2.6 respectively.

Despite efforts on understanding the photophysical properties of perovskite materials, there are contradicting opinions in literature regarding their emission properties. Several groups have employed photoluminescence spectroscopy to study the relationship between excitons and free carriers in organolead trihalide perovskites. In some steady-state photoluminescence studies, room temperature photoluminescence was attributed to exciton recombination [45,51-53]. Recently, several groups have attributed room temperature PL to free carrier recombination [54-57].

Based on the temperature dependence of PL emissions in MAPbBr_3 we suggest that these emissions result from the recombination of excitons or localized excitons. Our experimental results in **Figure 5.5** and **Figure 5.6** indicate that further studies are needed to improve the thermal stability of MAPbBr_3 perovskites for application in photovoltaics.

5.3.6 Device characterization

5.3.6.1 MAPbI_{3-x}Br_x and MAPbBr₃ photovoltaic characterization

Figure 5.7 shows the photocurrent density-voltage (J - V) curves of the MAPbI_{3-x}Br_x perovskite devices under standard AM 1.5G illumination at 100 mW/cm² (with a scan rate of 20 mV/s). The photovoltaic parameters; open-circuit voltage (V_{oc}), short-circuit current density (J_{sc}), fill factor (FF) and power conversion efficiency (PCE) are tabulated in **Table 5.1**. We performed a scan direction test to check for any hysteresis behavior. Both devices exhibited hysteresis in the J - V curves between forward (J_{sc} to V_{oc}) and reverse (V_{oc} to J_{sc}) scans during the current-voltage measurements, **Figure 5.7**. A reduced anomalous hysteresis in the current-voltage measurement is observed in perovskite solar cells based on MAPbI_{3-x}Br_x ($x = 1$), **Figure 5.7a**, compared to MAPbBr₃, **Figure 5.7b**, which we attribute to improved perovskite morphology, **Figure 5.2**. The inhomogeneous MAPbBr₃ morphology causes leakage current and induced recombination.

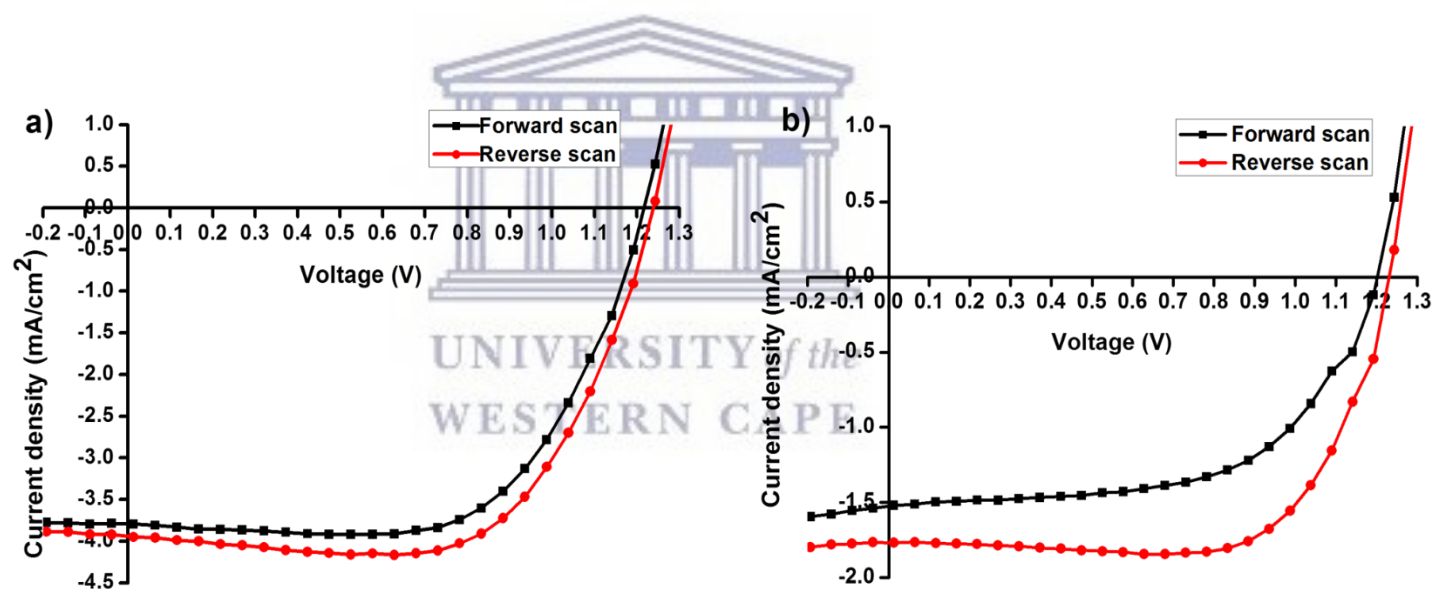


Figure 5.7: Current-voltage curve of the perovskite solar cell, forward and reverse scan 20 mV/s showing minimum hysteric behavior of a) MAPbI_{3-x}Br_x ($x = 1$) and b) MAPbBr₃ perovskite solar cells.

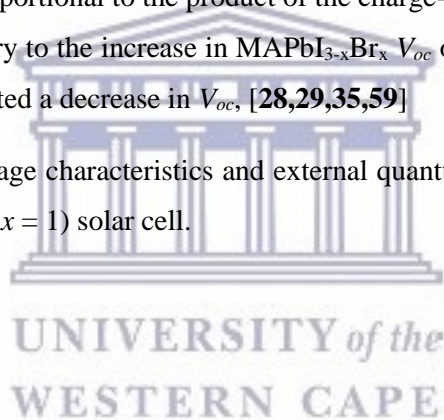
Correlating observations in the absorbance spectra to photovoltaic performance, a change in bandgap in **Figure 5.3**, is expected to result in an increase in V_{oc} assuming no further energetic losses. In comparison to MAPbI_{3-x}Br_x ($x = 1$), **Figure 5.7a**, increasing the bromide fraction further by going all the way to MAPbBr₃ we observe a slight increase in V_{oc} , **Figure 5.7b**. Current-voltage curves taken with increasing voltage (forward scan) tends to exhibit lower currents at each voltage than a curve taken with decreasing voltage (reverse scan) in **Table 5.1**.

Table 5.1: Photovoltaic parameters of measured from reverse (V_{oc} to J_{sc}) and forward (J_{sc} to V_{oc}) scans at 20 mV/s.

x	Scan direction	V_{oc} (V)	J_{sc} (mA/cm ²)	FF	PCE (%)
1	$V_{oc} \rightarrow J_{sc}$	1.240	3.95	0.67	3.2
	$J_{sc} \rightarrow V_{oc}$	1.220	3.79	0.65	3.0
3	$V_{oc} \rightarrow J_{sc}$	1.244	1.767	0.71	1.6
	$J_{sc} \rightarrow V_{oc}$	1.199	1.524	0.59	1.1

The reduction of MAPbBr₃ J_{sc} is directly related to the blue-shift of absorption onset resulting in a short light absorption range, while the improvement in V_{oc} is attributed to the widening bandgap, as explained previously. Relatively lower MAPbBr₃ short-circuit current also indicates that the charge-collection efficiency is low because J_{sc} is proportional to the product of the charge-collection efficiency and the light harvesting efficiency [58]. Contrary to the increase in MAPbI_{3-x}Br_x V_{oc} observed with increasing bromide content, several groups have reported a decrease in V_{oc} , [28,29,35,59]

Figure 5.8 shows the current-voltage characteristics and external quantum efficiency (EQE) spectrum of the best-performing MAPbI_{3-x}Br_x ($x = 1$) solar cell.



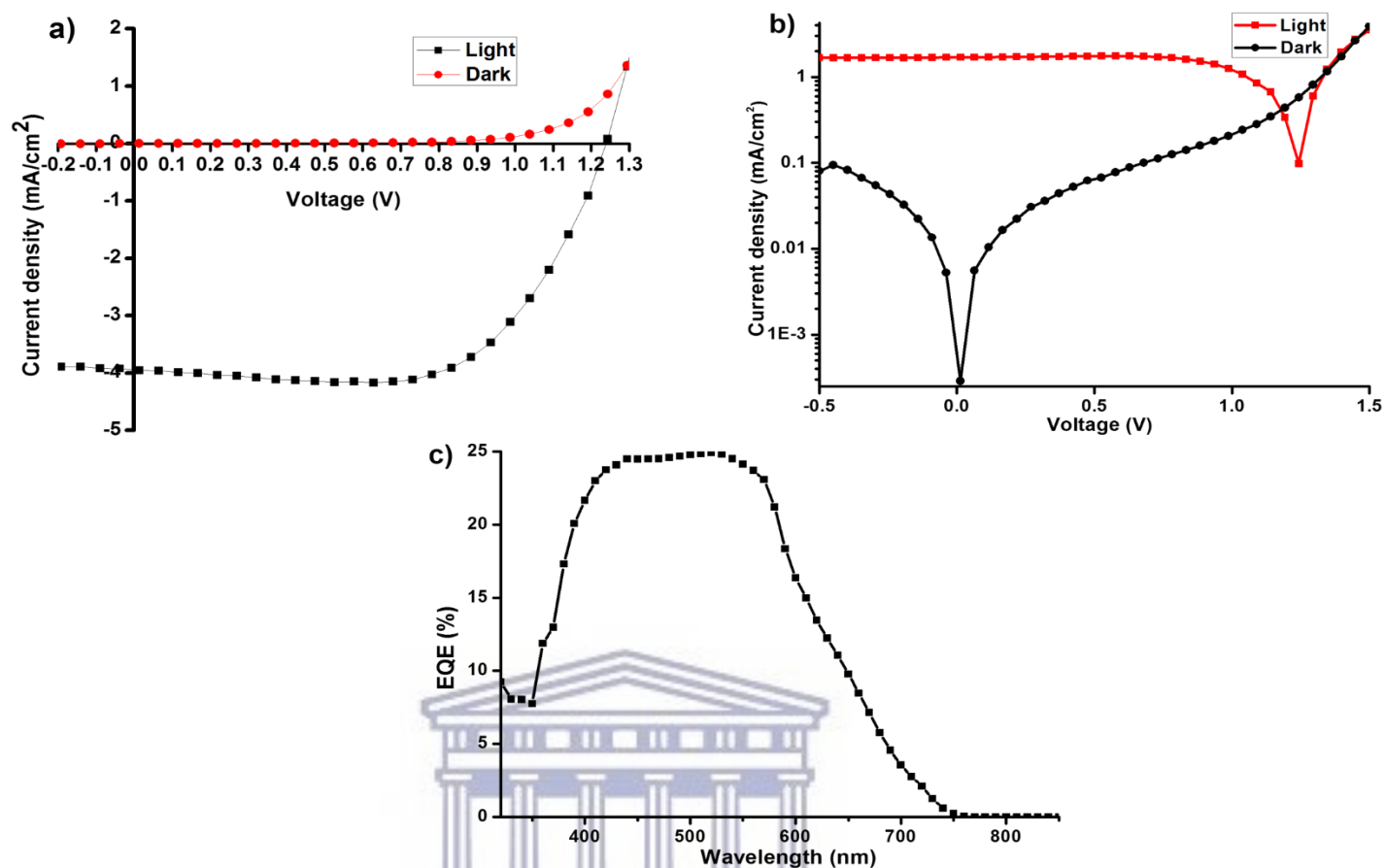


Figure 5.8: a) J - V characteristics, b) the corresponding semi-logarithmic current-voltage characteristics and c) external quantum efficiency (EQE) spectra of $\text{MAPbI}_{3-x}\text{Br}_x$ ($x=1$).

The best performing cell exhibited PCE of 3.2%, V_{oc} of 1.240 V, J_{sc} of 3.95 mA/cm² and FF of 0.67, **Figure 5.8a**. The corresponding semi-logarithmic current-voltage characteristics are shown in **Figure 5.8b** and they exhibit diodes with excellent rectification and low-reverse-bias dark currents. The EQE spectrum reaches a peak value at ~550 nm with a gradual decrease from 600 nm, indicating a photocurrent loss due to either insufficiency in the absorption of the perovskite layer, **Figure 5.8c**. Integration of the EQE spectrum over the AM 1.5G solar emission spectrum yielded a short-circuit photocurrent density of 3.83 mA/cm² which is in good agreement with our J - V photocurrent. The shape of the EQE spectra, **Figure 5.8c**, is in good agreement with the absorption spectra, **Figure 5.3**. The cell also exhibited scan rate- and direction-dependent hysteresis shown in **Figure 5.9**.

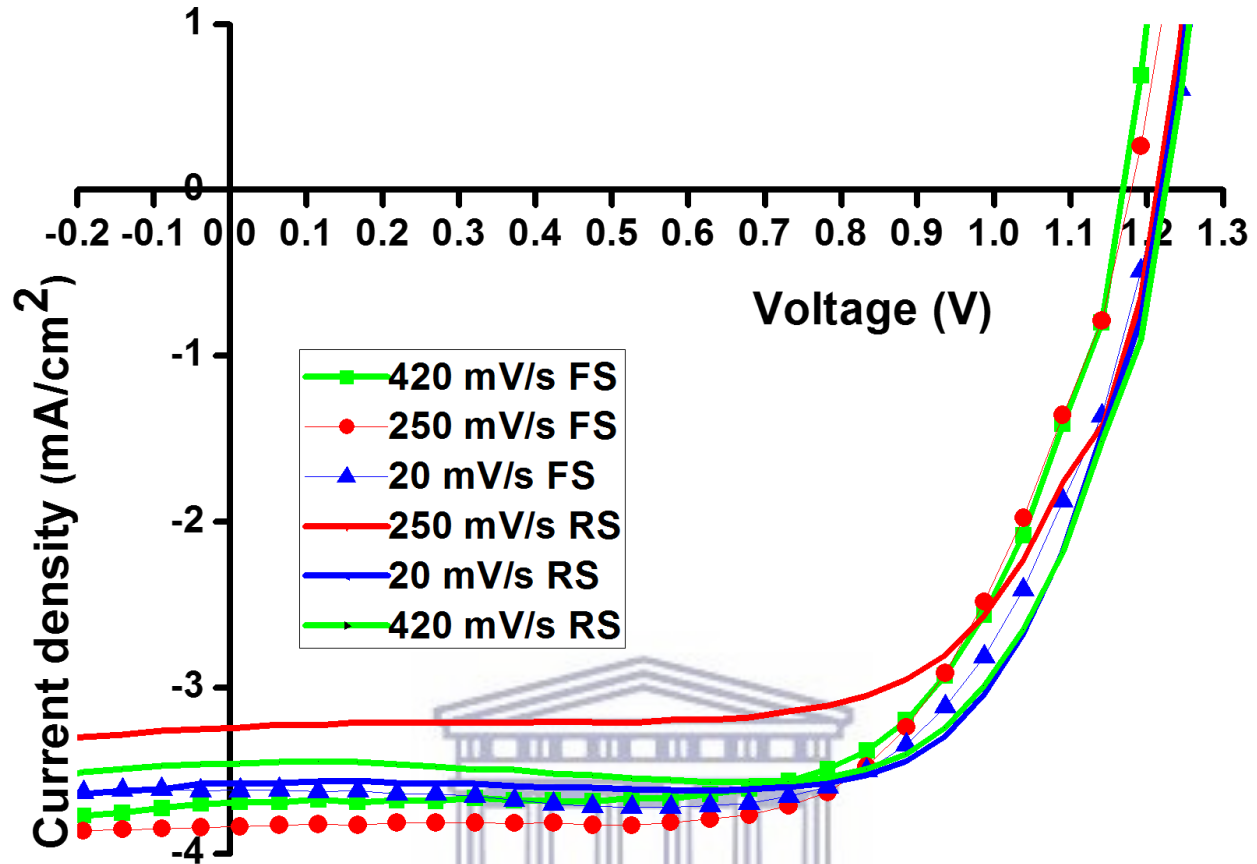


Figure 5.9: Scan rate and direction dependent forward and reverse J - V scans of ITO/PEDOT:PSS/ MAPbI_{3-x}Br_x ($x = 1$)/PCBM/Al solar cell.

UNIVERSITY of the
WESTERN CAPE

5.3.7 Electroluminescence spectroscopy

Figure 5.10 shows the EQE spectrum of a typical device on a logarithmic scale. The EQE decreases rapidly below 1.5 eV suggesting that the number of photoactive states in the absorber band gap is very small. The electroluminescence of the same device is also shown in **Figure 5.10** with a narrow emission peaking at ~ 1.7 eV.

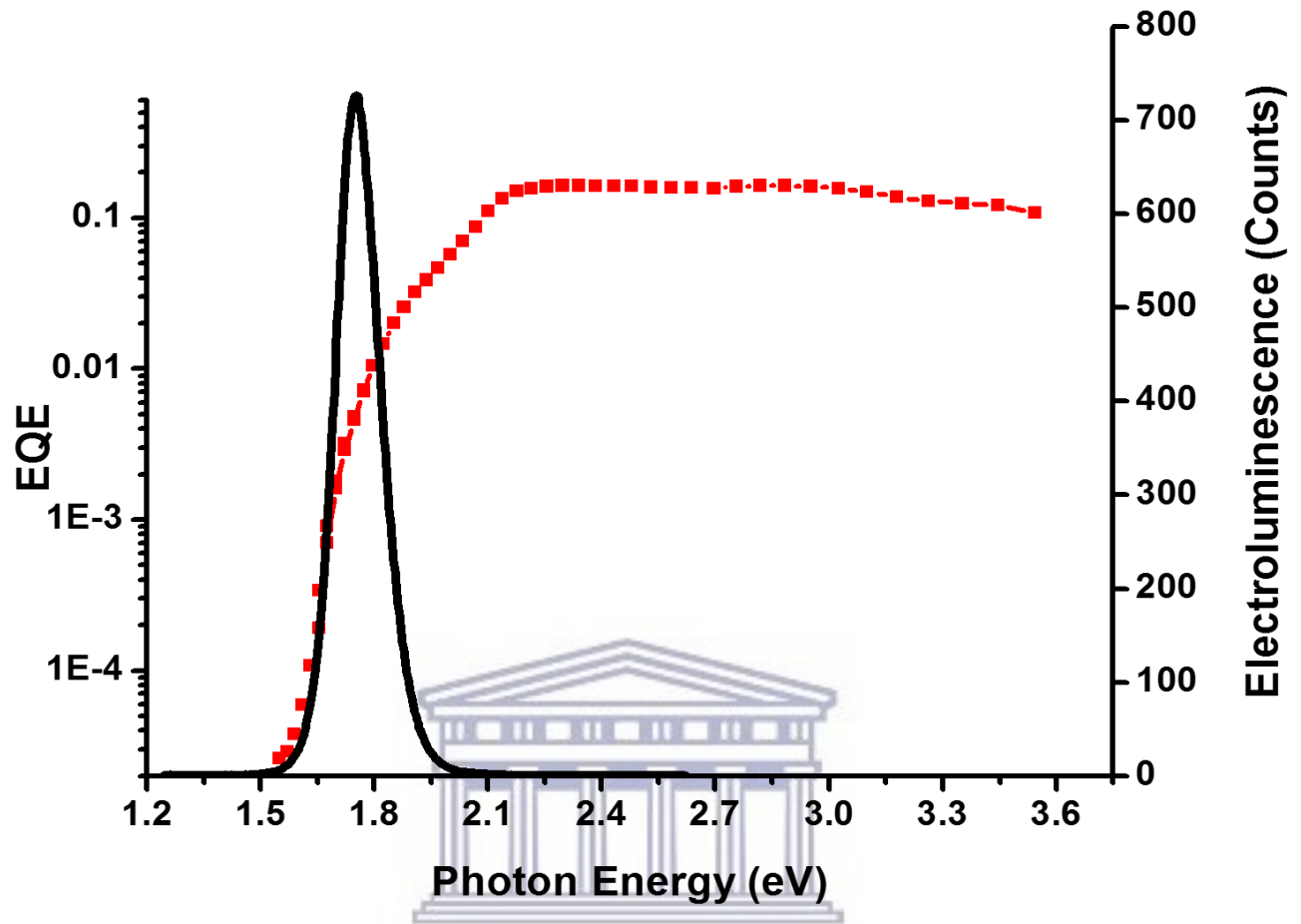


Figure 5.10: EQE spectrum measured into gap and electroluminescence spectrum of the same $\text{MAPbI}_{3-x}\text{Br}_x$ ($x = 1$) perovskite solar cell.

5.3.8 Statistical data analysis

To further check the reproducibility of device performance, **Figure 5.11**, show the statistical analysis from 150 perovskite devices.

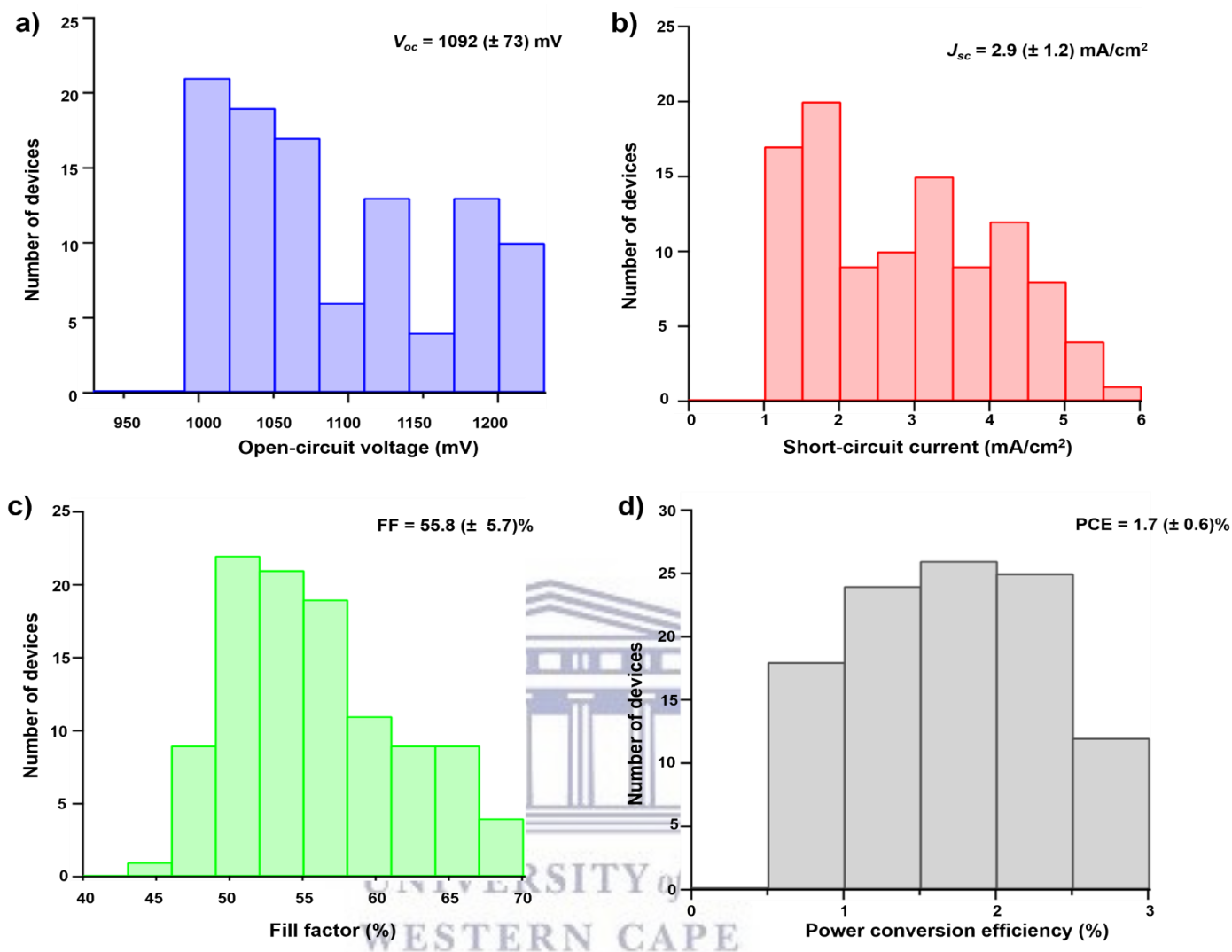


Figure 5.11: Histograms of device parameters a) open-circuit voltage (V_{oc}), b) short-circuit current (J_{sc}), fill factor (FF) and power conversion efficiency (PCE) for 100 separate MAPbI_{3-x}Br_x ($x = 1$) devices.

The MAPbI_{3-x}Br_x ($x = 1$) exhibit considerable reproducibility as indicated by the small standard deviation values although the photovoltaic parameters did not show easily understandable trends.

At this stage factors influencing high voltage MAPbI_{3-x}Br_x ($x \geq 1$) are still not readily understood. More detailed physical and crystallographic studies pertaining to the compositional MAPbI_{3-x}Br_x perovskites which are out of the scope of this work will need to be conducted.

Conclusion

In summary, high open circuit voltage, wide bandgap solution processed mixed iodide-bromide perovskite solar cells with the possible fabrication of colourful solar cells due to tunable bandgap were demonstrated. The thermal stability of perovskite photoluminescence emissions was also studied using steady-state temperature-dependent photoluminescence spectroscopy. Although the demonstrated device performance lags performance of the state-of-the-art devices with similar architecture, findings highlight how perovskite morphology can be controlled by precursor composition and minimizing the complexity of perovskite device fabrication. Deeper insights into ion migration in iodide-bromide perovskites are desired for the understanding of device working mechanism, the suppressing of J - V hysteresis and the enhancement of photovoltaic performance.

References

- [1] A. Kojima, K. Teshima, Y. Shirai and T. Miyasaka, *J. Am. Chem. Soc.*, 2009, 131, 6050-6051
- [2] N.-G. Park, *J. Phys. Chem. Lett.*, 2013, 4, 2423-2429
- [3] H. J. Snaith, *J. Phys. Chem. Lett.*, 2013, 4, 3623-3630
- [4] NREL http://www.nrel.gov/ncpv/images/efficiency_chart.jpg
- [5] F. Giordano, A. Abate, J.-P. C. Baena, M. Saliba, T. Matsui, S. H. Im, S. M. Zakeeruddin, M. K. Nazeeruddin, A. Hagfeldt, M. Grätzel, *Nat. Commun.* 2016, 7, 10379
- [6] M. M. Lee, J. Teuscher, T. Miyasaka, T. N. Murakami, H. J. Snaith, *Science*, 2012, 338, 643-647
- [7] N. G. Park, *Mater. Today*, 2015, 18, 65-72
- [8] Q. Chen, H. Zhou, Z. Hong, S. Luo, H.-S. Duan, H.-H. Wang, Y. Liu, G. Li and Y. Yang, *J. Am. Chem. Soc.*, 2014, 136, 622-625
- [9] J. Burschka, N. Pellet, S.-J. Moon, R. Humphry-Baker, P. Gao, M. K. Nazeeruddin and M. Grätzel, *Nature*, 2013, 499, 316-319
- [10] A. Kojima, M. Ikegama, K. Teshima and T. Miyasaka, *Chem. Lett.*, 2012, 41, 397-399
- [11] E. Edri, S. Kirmayer, D. Cahen, G. Hodes, *J. Phys. Chem. Lett.*, 2013, 4, 897-902
- [12] D. B. Mitzi, C. D. Dimitrakopoulos and L. L. Kosbar, *Chem. Mater.*, 2001, 13, 3728-3740
- [13] D. P. McMeekin, G. Sadoughi, W. Rehman, G. E. Eperon, M. Saliba, M. T. Hörantner, A.-A. Haghighirad, N. Sakai, L. Korte, B. Rech, M. B. Johnston, L. M. Herz and H. J. Snaith, *Science*, 2016, 351, 151-155
- [14] P. Docampo, F. C. Hanusch, S.D. Stranks, M. Döblinger, J. M. Feckl, M. Ehrensperger, N. K. Minar, M. B. Johnston, H. J. Snaith and T. Bein, *Adv. Energy Mater.*, 2014, 4, 1400355
- [15] J. H. Heo, S. H. Im, J. H. Noh, T. N. Mandal, C.-S. Lim, J. A. Chang, Y. H. Lee, H.-J. Kim, A. Sarkar, M. K. Nazeeruddin, M. Grätzel, S. I. Seok, *Nat. Photonics*, 2013, 7, 486-491
- [16] D. Liu and T. L. Kelly, *Nat. Photonics*, 2014, 8, 133-138;
- [17] K. Cao, H. Li, S. Liu, J. Cui, Y. Shen and M. Wang, *Nanoscale*, 2016, 8, 8839-8846
- [18] C. Bi, Y. Yuan, Y. Fang, J. Huang, *Adv. Energy Mater*, 2014, 5, 1401616
- [19] T. Soga, T. Kato, M. Yang, M. Umeno, T. Jimbo, *J. Appl. Phys.* 1995, 78, 4196-4199
- [20] R. Sheng, A. Ho-Baillie, S. Huang, M. Keevers, X. Hao, L. Jiang, Y.-B. Cheng and M. A. Green, *J. Phys. Chem. Lett.*, 2015, 6, 3931-3934
- [21] B. Cai, Y. Xing, Z. Yang, W. H. Zhang, J. Qiu, *Energy Environ. Sci.*, 2013, 6, 1480-1485
- [22] S. Ryu, J. H. Noh, N. J. Jeon, Y. C. Kim, W. S. Yang, J. Seo, S. I. Seok, *Energy Environ. Sci.*, 2014, 7, 2614-2618
- [23] J. H. Heo, D. H. Song and S. H. Im, *Adv. Mater.*, 2014, 26, 8179-8183
- [24] E. Edri, S. Kirmayer, M. Kulbak, G. Hodes and D. Cahen, *J. Phys. Chem. Lett.*, 2014, 5, 429-433

- [25] N. Arora, S. Orlandi, M. I. Dar, S. Aghazada, G. Jacopin, M. Cavazzini, E. Masconi, P. Gratia, F. De Angelis, G. Pozzi, M. Graetzel and M. K. Nazeeruddin, *ACS Energy Lett.*, 2016, 1, 107-112
- [26] N. J. Jeon, J. H. Noh, Y. C. Kim, W. S. Yang, S. Ryu and S. I. Seok, *Nat. Mater.*, 2014, 13, 897-903
- [27] J. H. Noh, S. H. Im, J. H. Heo, T. N. Mandal and S. I. Seok, *Nano Lett.*, 2013, 13, 1764-1769
- [28] B. Suarez, V. Gonzalez-Pedro, T. S. Ripolles, R. S. Sanchez, L. Otero, I. Mora-Sero, *J. Phys. Chem. Lett.*, 2014, 5, 1628-1635
- [29] S. A. Kulkarni, T. Baikie, P. P. Boix, N. Yantara, N. Mathews, S. Mhaisalkar, *J. Mater. Chem. A.* 2014, 2, 9221-9225
- [30] P.-W. Liang, C.-Y. Liao, C.-C. Chueh, F. Zuo, S. T. Williams, X.-K. Xin, J. Lin, A. K. Y. Jen, *Adv. Mater.* 2014, 26, 3748-3754
- [31] M. A. Green, M. J. Keevers, I. Thomas, J. B. Lasich, K. Emery, R. R. King, *Prog. Photovoltaics*, 2015, 6, 685-691
- [32] E. Mosconi, A. Amat, M. K. Nazeeruddin, M. Grätzel, F. D. Angelis, *J. Phys. Chem. C*, 2013, 117, 13902-13913
- [33] L. Etgar, P. Gao, Z. Xue, Q. Peng, A. K. Chandiran, B. Liu, M. K. Nazeeruddin and M. Grätzel, *J. Am. Chem. Soc.*, 2012, 134, 17396-17399
- [34] K. Tanaka, T. Takahashi, T. Ban, T. Kondo, K. Uchida and N. Miura, *Solid State Commun.* 2003, 127, 619-623
- [35] E. T. Hoke, D. J. Slotcavage, E. R. Dohner, A. R. Bowring, M. D. McGehee, H. I. Karunadasa, *Chem. Sci.*, 2015, 6, 613-617
- [36] S. D. Stranks, G. E. Eperon, G. Grancini, C. Menelaou, M. J. P. Alcocer, T. Leijtens, L. M. Herz, A. Petrozza and H. J. Snaith, *Science*, 2013, 342, 341-344
- [37] C. C. Stoumpos, C. D. Malliakas, M. G. Kanatzidis, *Inorg. Chem.*, 2013, 52, 9019-9038
- [38] H.-H. Fang, F. Wang, S. Adjokatse, N. Zhao, J. Even and M. A. Loi, *Light Sci. Appl.* 2016, 5, e16056
- [39] N. Onoda-Yamamuro, T. Matsuo and H. Suga, *J. Phys. Chem. Solids*, 1990, 51, 1383-1395
- [40] R. L. Milot, G. E. Eperon, H. J. Snaith, M. B. Johnston and L. M. Herz, *Adv. Funct. Mater.*, 2015, 25, 6218-6227
- [41] A. Poglitsch, D. Weber, *J. Chem. Phys.* 1987, 87, 6373-6378
- [42] J. Tilchin, D. N. Dirin, G. I. Maikov, A. Sashchiuk, M. V. Kovalenko and E. Lifshitz, *ACS Nano*, 2016, 10, 6363-6371
- [43] J. Xing, X. F. Liu, Q. Zhang, S. T. Ha, Y. W. Yuan, C. Shen, T. C. Sum and Q. Xiong, *Nano Lett.*, 2015, 15, 4571-4
- [44] J. Dai, H. Zheng, C. Zhu, J. Lu and C. Xu, *J. Mater. Chem. C*, 2016, 4, 4408-4413
- [45] T. J. Savenije, C. S. Ponseca, L. Kunneman, M. Abdellah, K. Zheng, Y. Tian, Q. Zhu, S. E. Canton, I. G. Scheblykin, T. Pullerits, A. Yartsev and V. Sundström, *J. Phys. Chem. Lett.*, 2014, 5, 2189-2194
- [46] Z. Chen, C. Yu, K. Shum, J. J. Wang, W. Pfenninger, N. Vockic, J. Midgley and J. T. Kenney, *J. Lumin.*, 2012, 132, 345-349
- [47] A. D. Wright, C. Verdi, R. L. Milot, G. E. Eperon, M. A. Pérez-Osorio, H. J. Snaith, F. Giustino, M. B. Johnston and L. M. Herz, *Nat. Commun.*, 2016, 7, doi:10.1038/ncomms11755
- [48] N. Sestu, M. Cadelano, V. Sarritzu, F. Chen, D. Marongiu, R. Piras, M. Mainas, F. Quochi, M. Saba, A. Mura, G. Bongiovanni, *J. Phys. Chem. Lett.* 2015, 6, 4566-4572
- [49] Y. Yang, M. Yang, Z. Li, R. Crisp, K. Zhu and M. C. Beard, *J. Phys. Chem. Lett.*, 2015, 6, 4688-4692
- [50] S. Rudin, T. L. Reinecke and B. Segall, *Phys. Rev. B: Condens. Mater. Phys.*, 1990, 42, 11218-11231
- [51] S. Sun, T. Salim, N. Mathews, M. Duchamp, C. Boothroyd, G. Xing, T. C. Sum and Y. M. Lam, *Energy Environ. Sci.*, 2014, 7, 399-407
- [52] W. Zhang, M. Saliba, U. Wiesner, Y. Sun, Xian Shi and H. J. Snaith, *Nano Lett.*, 2013, 13, 4505-4510

- [53] H. He, Q. Yu, H. Li, J. Li, J. Si, Y. Jin, N. Wang, J. Wang, J. He, X. Wang, Y. Zhang and Z. Ye, *Nat. Commun.*, 2016, 7, 10896
- [54] F. Deschler, M. Price, S. Pathak, L. E. Klintberg, D.-D. Jarausch, R. Higler, S. Hüttner, T. Leitjens, S. D. Stranks, H.J. Snaith, M. Atatüre, R.T. Phillips, R. H. Friend, *J. Phys. Chem. Lett.*, 2014, 5, 1421-1426
- [55] V. D'Innocenzo, G. Grancini, M. J. P. Alcocer, A. R. S. Kandada, S. D. Stranks, M. M. Lee, G. Lanzani, H. J. Snaith, A. Petrozza, *Nat. Commun.* 2014, 5, 3586-3591
- [56] Y. Yamada, T. Nakamura, M. Endo, A. Wakamiya and Y. Kanemitsu, *J. Am. Chem. Soc.*, 2014, 136, 11610-11613
- [57] Q. Lin, A. Armin, R. C. R. Nagiri, P. L. Burn and P. Meredith, *Nat. Photon.*, 2015, 9, 106-112
- [58] N. J. Jeon, J. H. Noh, W. S. Yang, Y. C. Kim, S. Ryu, J. Seo, S. I. Seok, *Nature*, 2015, 517, 476-480
- [59] G. E. Eperon, S. D. Stranks, C. Menelaou, M. B. Johnston, L. Herz and H. J. Snaith, *Energy Environ. Sci.*, 2014, 7, 982-988



UNIVERSITY of the
WESTERN CAPE

CHAPTER 6

CONCLUSIONS

The work presented in this thesis has aimed to investigate the material-physical-chemical properties of three-dimensional methylammonium lead halide perovskite materials with the ABX_3 structure. We present a systematic study of the effect of halide ions (Cl, Br, I) in a one-step solution deposition approach on the structural, optical and electronic properties of planar heterojunction perovskite solar cells. High efficiency planar heterojunction perovskite solar cells, $MAPbI_{3-x}Y_x$ ($Y = I, Cl, Br$), were fabricated using a low-temperature processing technique for possible large-scale low-cost production and energy payback time.

The study of the single-halide ($MAPbI_3$ and $MAPbBr_3$) and mixed-halide ($MAPbI_{3-x}Cl_x$ and $MAPbI_{3-x}Br_x$) perovskite composition, crystal structure and morphology has enabled an understanding of the formation and degradation of low-temperature solution processed planar heterojunction solar cells. Perovskite morphology was established by diascopic illumination microscopy, surface morphology SEM and surface topography AFM and correlated with photovoltaic performance. Photovoltaic performance was found to be strongly dependent on perovskite film morphology with highly ordered micrometer-sized crystallites delivering the highest efficiency. The presence of perovskite film defects was found detrimental to photovoltaic performance. Further optimization of the perovskite deposition process is most likely to lead to defect-free and uniform perovskite films.

In terms of the perovskite optical properties, we studied the optical absorption and photoluminescence spectroscopy of all perovskite systems. Perovskite optical properties were found to be highly dependent on perovskite composition and morphology which in turn directly affected photovoltaic performance. Further advances in overall power conversion efficiency are expected by extending the absorption onset toward 940 nm as has been reported for formamidinium-based perovskites. The physical parameters of the single- and mixed-halide perovskites such as the exciton binding energy, exciton-phonon interaction and bandgap were also studied via temperature-dependent photoluminescence spectroscopy. We extended our temperature-dependent photoluminescence spectroscopy studied to mixed iodide-bromide compositions which have not yet been analyzed using this technique. A study of these materials has never been performed before and therefore we deemed it of interest to examine their potential properties. However, throughout these studies, exact values of the exciton binding energies could not be determined due to the complexity of the perovskite structure, composition and processing parameters. In addition, a wide range of values have been reported in literature. The results we obtained for the perovskite systems that have been previously reported were in good agreement with most reports and fell within the ranges of generally accepted values obtained through various temperature-dependent spectroscopic techniques.

Chloride or bromide inclusion in the system through either an organic halide source (MAI/ MABr) or an inorganic halide source ($\text{PbCl}_2/\text{PbBr}_2$) modifies the crystallization pathway from precursor-perovskite to precursor-intermediate-perovskite crystallization. This precursor-intermediate-perovskite crystallization has been successfully harnessed in this work using a novel PEDOT:PSS/DMSO activated seed contact layer. The differences observed in the $\text{MAPbI}_{3-x}\text{Y}_x$ ($\text{Y} = \text{Cl}, \text{Br}, \text{I}$) crystalline precursors in this work suggest that modulation of the precursor phase can be achieved by exerting kinetic or thermodynamic control on perovskite formation. However, determining the exact composition of perovskites originating from mixed halide precursor solutions was very challenging and the exact composition was not determined. Composition determining techniques were hampered due to either the solubility of the perovskite structure in aqueous environments or their instability at elevated temperatures. Determination of exact perovskite composition is a subject of on-going debate and many varying precursor compositions of highly efficient perovskite solar cells having been reported in literature, further complicated the issue.

Owing to its complex perovskite device structure, it is challenging to attribute device performance to any one of the different components that constitute the device. To address this issue with regards to charge-transport material as components of the perovskite device we employed PEDOT:PSS and PCBM, *bis*-PCBM and PTCDI as hole- and electron-transport materials respectively. Highly conductive PEDOT:PSS doped with DMSO was found to result in high efficiency solar cells. A central finding of our investigations was that the *mono*-adduct PCBM provides the highest efficiency with higher reproducibility in comparison to the *bis*-adduct *bis*-PCBM and the perylene-based PTCDI examined as electron transport materials. From this study, we concluded that enhancing the light absorption through careful selection of charge transport materials would lead to increased short-circuit current, utilization of highly conductive hole-transport material formulations and better control over the layer thickness would improve the fill factor. Specifically, this study underlines that using three-dimensional perovskites and complementary well-matched hole- and/or electron-transport materials as charge transport materials is key to achieving high efficiency devices.

Wide bandgap methylammonium lead iodide-bromide $\text{MAPbI}_{3-x}\text{Br}_x$ ($0 \leq x \leq 3$) planar heterojunction perovskite solar cells were also studied in this thesis. Methylammonium lead tribromide MAPbBr_3 exhibited a typical bandgap of 2.3 eV. The absence of low-energy photoluminescence features observed in the mixed halide, $\text{MAPbI}_{3-x}\text{Br}_x$, indicated no halide segregation in these materials. However, microscopy results contradicted this finding with evidence of segregated highly crystalline structures in both the tribromide and mixed iodide-bromide perovskites warranting further investigation which could not be carried out due to time constraints. The high open circuit voltage of $\text{MAPbI}_{3-x}\text{Br}_x$ ($0 \leq x \leq 3$) perovskite solar cells is suitable for tandem silicon solar cells in the future with the improvement of fabrication techniques and a deeper understanding of the mixed iodide-bromide perovskite solar cell processing

parameters. The best performing $\text{MAPbI}_{3-x}\text{Br}_x$ device with the highest bromide achieved a power conversion efficiency of 3.2%, the highest of its kind in a low-temperature solution-processed planar heterojunction perovskite solar cell. Morphology control and reproducibility was most challenging in $\text{MAPbI}_{3-x}\text{Br}_x$ in comparison to both MAPbI_3 and $\text{MAPbI}_{3-x}\text{Cl}_x$. Increasing bromide content lead to difficulties in perovskite morphology control. The most straightforward technique is to employ a two-step sequential deposition to solve this problem. However, employment of this deposition technique led to less efficient solar cells.

Advances in methylammonium lead halide perovskites heavily depends on understanding their stability and degradation mechanisms, topics which are under intense investigation. The presence of chloride ions in the $\text{MAPbI}_{3-x}\text{Cl}_x$ perovskite was found to modify the degradation mechanism and showed suppressed perovskite degradation under inert conditions in comparison to the triiodide MAPbI_3 counterparts providing evidence that $\text{MAPbI}_{3-x}\text{Cl}_x$ perovskites retain their perovskite structure longer. It was challenging to determine the degradation mechanisms of perovskites in air since they degraded upon exposure to air. Perovskite solar cell sealing by encapsulation has been used in attempt to stabilize perovskites in air. Even though in our work, perovskite degradation was under inert conditions, we conclude that mere encapsulation will not be sufficient to guarantee their stability because perovskite formation itself is likely a critical component to achieve long-term stability. We conclude that fully understanding perovskite solar cell degradation pathways is crucial to develop effective strategies to improve stability and thus achieve market standards.

The general conclusions from this work are that perovskite structural and optoelectronic properties as well as photovoltaic performances are significantly dependent on perovskite precursor chemistry and growth conditions. Improved photovoltaic performance was achieved by selecting perovskite films deposited with optimized fabrication conditions. In addition to optimizing the perovskite layer, tuning of the contact materials lead to significant improvements in perovskite film morphology and device performance. Good energy alignment was found essential for maximizing the open circuit voltage. Here we show that by harnessing this type of organic-inorganic hybrid planar heterojunction structure, an avenue for high open-circuit voltage solar cells can be opened. The efficiency losses in low-temperature processed perovskite solar cells originated mainly due to charge recombination at imperfect interfaces and structural or chemical defects in perovskite films. Photovoltaic devices fabricated using $\text{MAPbI}_{3-x}\text{Cl}_x$ perovskites exhibited minimal hysteresis with high degree of reproducibility and an average efficiency of ~12%. Even if the material band gap of mixed iodide-chloride remains substantially unchanged with increasing chloride concentration, chloride incorporation dramatically improves charge transport within the perovskite layer, explaining the outstanding performances of perovskite solar cells based on this material. Our findings agree

with previous and current reports suggesting superior transport properties of mixed halide perovskite solar cells, demonstrating the beneficial effect of mixed-halide over the single-halide perovskites.

Optoelectronic characterization attributed the enhanced efficiency to reduced bulk defects and improved charge-carrier mobility in large-grain devices. The methodology studies presented in this work on perovskite precursor solution chemistry and growth kinetics enable an understanding of perovskite film formation and further optimization of the perovskite deposition processes as well as photovoltaic device fabrication. The synergistic effects of tuning perovskite composition revealed in this work signify that perovskites with different compositions in addition to MAPbI₃ deserve more in-depth understanding from physical and crystallographic aspects.

The insights gained from perovskite formation and degradation studies in this thesis are an important step toward developing a complete understanding of these processes and how they might be beneficially controlled. The work presented in this thesis has broad implications for the many potential halide perovskite optoelectronic devices such as light emitting diodes, electrolytic water splitting, transistors and gas sensors, but especially solar cells. This work has demonstrated that not only a new perovskite device architecture with efficient power conversion efficiency but also a useful model system to reveal the correlation between perovskite composition-/structure-dependent properties and the photovoltaic properties of the organic-inorganic hybrid systems is required.

6.1 Outlook

Even though, a good understanding of the microstructure and hence the macroscopic properties of methylammonium lead halide perovskite materials were achieved in this work, a lot of work needs to be done. An improvement of the perovskite photovoltaic efficiency requires a clear understanding of structure-property relationships and numerous challenges related to synthesis of the composite materials and fabrication procedure of the device remain to be overcome. The development of an effective film deposition technique and an interface engineering procedure is of great importance for thin-film perovskite solar cells, as it facilitates the reduction of the loss of light absorption, the decrease of shunt paths, and the minimization of the interface-defect density in planar heterojunction solar cells. An area of great interest is a detailed study of the structural, chemical and physical properties of each component that constitutes the perovskite solar cell, from the substrate, charge transport layers, the photoactive layer to the electrodes. These studies will allow an understanding of the correlation between each material and the photovoltaic device performance. Further improvements in efficiency of solution-processes in perovskite solar cells can be expected by reproducing the perovskite thin-film growth using doctor-blading in a controlled environment, through compositional tuning of the bandgap, and/or selecting hole- and electron-transport materials with

better energy alignment with the perovskite electronic level. However, more detailed physical and crystallographic studies pertaining to the new compositional perovskites would have to be conducted. Through a combination of optimization strategies aimed at fine-tuning the perovskite chemical composition, improving perovskite film quality, tuning the energy levels of charge-extraction materials used in the cell, and harvesting a broader part of the solar spectrum, the power conversion efficiency has the potential to soar past the theoretical 33% limit.

